UNIVERSITY OF GLASGOW

Department of Electronics and Electrical Engineering

Dynamic Modelling and Simulation of Electric Power Systems Using the Newton-Raphson Method

by

Rodrigo Joel Garcia-Valle

A Thesis submitted to the
Department of Electronics and Electrical Engineering
of the
University of Glasgow
for the degree of
Doctor of Philosophy

December, 2007

To my parents and sister,
for their hearten,
trust and love

To my beloved wife, Lorena
as a symbol of my love
and her forbearance
during this years

To my lovely daughter, Valeria
as a gift on her birthday.

Abstract

The research work presented in this thesis is concerned with the development of a dynamic power flow computer algorithm using Newton's method. It addresses both the development of a positive sequence dynamic power flow algorithm for the dynamic study of balanced power systems and a fully-fledged three-phase dynamic power flow algorithm for the dynamic study of power systems exhibiting a significant degree of either structural or operational unbalance.

As a prelude to the research work on dynamic power flows, a three-phase Newton-Raphson power flow algorithm in rectangular co-ordinates with conventional HVDC power plant modelling is presented in this thesis, emphasising the representation of converter control modes. The solution approach takes advantage of the strong numerical convergence afforded by the Newton-Raphson method to yield reliable numerical solutions for combined HVAC-HVDC systems, where power plant and operational imbalances are explicitly taken into account.

The dynamic algorithm is particularly suited to carrying out long-term dynamic simulations and voltage stability assessments. Dynamic model representations of the power plants components and the load tap changing transformer are considered, and to widen the study range of dynamic voltage phenomena using this method, extensions have been made to include induction motor and polynomial load modelling features. Besides, reactive power compensators that base their modus operandi on the switching of power electronic valves, such as the HVDC-VSC and the STATCOM are taken into account. The dynamic power flow algorithm has primarily been developed making use of the positive sequence and dq representations. Extensions are made to developing a three-phase power flows dynamic algorithm.

Test cases for the various dynamic elements developed in this research are presented to show the versatility of the models and simulation tool, including a trip cascading event leading up to a wide-area voltage collapse. Comparisons with the output of a conventional transient stability program carried out where appropriate.

Acknowledgments

The arduous effort that brings out doing a PhD thesis, will not be possible without the unestimated collaboration of many people. To all of you I want to dedicate this space to express my gratitude.

Firstly, I want to acknowledge to my supervisor, Prof. Enrique Acha, for the encourage and commitment given to me during all this period. He has always been up and keen to assist me at any time, giving me the necessary guidance and advice, but also being critic judging my work. I would like to express my thankfulness for his sincere friendship.

The National Council of Science and Technology, CONACyT Mexico, is gratefully acknowledge for the financial support provided during the research project.

I sincerely appreciate the collaboration work carried out by Federico Coffele, Luigi Vanfretti and Rafael Zarate during their work visit at the University of Glasgow; my truthful greet to Pedro Roncero for his fruitful comments about my thesis and his worthwhile advice using LaTeX. I much appreciate their sincere friendliness.

I would like to express my thankfulness to my friends and colleges, Mykhaylo Teplechuk, Sven Soell, Maria Thompson, Damian Vilchis, Enrique Ortega and Carlos Ugalde for the time, talks and outdoors experiences spent together; to the working environment at the power system group at the department of electronics and electrical engineering and to its entire staff.

And last but not least, I also fully appreciate the encourage and credence to me from my parents and sister during this long period. I truly acknowledge to my wife Lorena, for her love, comprehension and encourage during latter years of hard work and sacrifices. And to my daughter Valeria, for helping me to forget about my problem being with you. Without you I would not had done it. THANKS.

Contents

List of Figures

List of Tables

List of Symbols and Acronyms

Capital letters

P	Active power
P_{ag}	Active power at the air-gap
P_l	Active load power
P_{dR}	Active power at the rectifier
K_a	Amplifier gain
T_a	Amplifier time constant
A^e	First ceiling coefficient
B^e	Second ceiling coefficient
S_e	Ceiling function
I	Complex current
S	Complex power
V	Complex voltage
I_q	Quadrature axis current
I_{dq}	Axis armature current
I_d	Direct axis current

I_{dc}	Current at the dc link
I_a	Phase a current
D	Damping coefficient
$\Delta - Y$	Delta-star connection
T_e	Field circuit time constant
BC_1	Fire intensity
BC_2	Auxiliary variable
K	Governor gain
P_{gov}	Governor power
T_1	Governor time constant
Z_l	Series impedance
Y_l	Shunt impedance
H	Inertia constant
$\mathbf{J}$	Jacobian matrix
T_r	Measurement time constant
M_g	Angular momentum
abc	abc frame of reference
P_e	Electrical power
P_a	Power of the synchronous generator
P_m	Mechanical power
P_M	Equivalent mechanical input powers
P_{km}	Active power through the phase shifter
P_{set}	Power set point

Q	Reactive power
Q_{ag}	Reactive power at the air-gap
Q_{dI}	Reactive power at the inverter
Q_l	Reactive load power
X_r	Rotors' reactance
R_r	Rotors' resistance
Y_{sc}	Short-circuit admittance matrix
K_f	Stabiliser gain
T_f	Stabiliser time constant
$Y - \Delta$	Star-delta connection
$Y - Y$	Star-star connection
SF	Steam production
T_k	Tap ratio
A	Tap changer position
H_T	Taps' servomotor inertia
P_0	Target active power
V_0	Target voltage magnitude
DP	Throttle pressure
T'_{do}	Transient time constant at the d axis
T''_{do}	Sub-transient time constant at the d axis
T'_{qo}	Transient time constant at the q axis
T''_{qo}	Sub-transient time constant at the q axis
F_{HP}	High pressure turbine power fraction

P_{HP}	High pressure turbine power
F_{IP}	Intermediate pressure turbine power fraction
P_{IP}	Intermediate pressure turbine power
F_{LP}	Low pressure turbine power fraction
P_{LP}	Low pressure turbine power
T_{CH}	Steam chest time constant
T_{CO}	Cross-over or steam storage time constant
T_{RH}	Reheat time constant
V_d	Voltage magnitude at the d axis
E_a	Excitation or behind the reactance voltage
E'_d	Flux linkage voltage at the d axis
E'_q	Flux linkage voltage at the q axis
V_{dI}	Voltage at the inverter
V_q	Voltage magnitude at the q axis
V_{dR}	Voltage at the rectifier
V_r	Regulator voltage

Lowercase letters

r_a	Armature resistance
k_3	Boiler gain
$dq0$	$dq0$ frame of reference
e	Real part of the voltage
f	Imaginary part of the voltage

f_{ag}	Imaginary voltage at the air-gap
it	Iterations
nbus	Number of buses
ngen	Number of synchronous generators
j	Mathematical complex operator $\sqrt{-1}$
k_1	Constant associated with commutation overlap
x'_d	Transient quadrature reactance at the d axis
x_d	Direct axis reactance
x''_d	Sub-transient quadrature reactance at the d axis
x'_q	Transient quadrature reactance at the q axis
x_q	Quadrature axis reactance
x''_q	Sub-transient quadrature reactance at the q axis
e_{ag}	Real voltage at the air-gap
s	Rotor' slip
$\dot{y}$	State variable
f_0	Synchronous frequency
x	Vector of integrable algebraic variables
y	Vector of non-integrable algebraic variables

Greek symbols

σ	Acceleration
α	Firing angle
Δ	Increment

ε	Round-off error
γ	Extinction angle
μ	Exponential load model constant
ν	Exponential load model constant
ρ	Denote phases a, b, c
θ	Phase angle
ϕ_k	Phase angle mechanism on the primary side
δ	Power or rotor angle
δ_0	Initial power angle
ω	Synchronous generator speed
ω_0	Synchronous speed

Acronyms

ABB	Asea Brown Boveri
AC	Alternate Current
AVR	Automatic Voltage Generator
CCC	Capacitor Commutated Converter
CIGRÉ	Conseil International des GrandsRéseaux Électriques
CPF	Continuation Power Flows
FPC	Federal Power Commission
NYPP	New York Power Pool
CPU	Central Processing Unit
DAE	Differential-Algebraic Equations

DC	Direct Current
DLTC	Dynamic Load Tap Changer
FACTS	Flexible Alternate Current Transmission Systems
GTO	Gate Turn-Off thyristor
SVC	Static VAR Compensator
HVDC	High Voltage Direct Current
IEEE	The Institute of Electrical and Electronics Engineers
IGBT	Insulated Gate Polar Transistor
LCC	Line Commutated Current
LTC	Load Tap Changer
NERC	North American Electric Reliability Council
ODE	Ordinary Differential Equation
OEL	Over Excitation Limiter
PES	Power Engineering Society
PSAT	Power System Analysis Toolbox
QSS	Quasi-Static Simulation
USA	United States of America
VSC	Voltage Source Converter

Chapter 1

Introduction

1.1 Overview

Electric power systems around the world are all of different sizes; each having its own generation, mix transmission structure and load capacity to serve. Nevertheless, all of them share similar construction and operating principles, with four main elements becoming, at first sight, more visible, namely generating units, transmission lines, transformers and loads. Control and protection equipment have a vital function to play and they also constitute essential elements of the electric power system. Arguably, from a dynamic viewpoint, generating units and loads are the most important elements of the electric power system.

Electric power is generated mainly using synchronous machines, which are driven by turbines of various kinds, such as steam, hydro, diesel, nuclear and internal combustion. The generator voltages are in the range of 11 to 35 kV [Kundur, 1994]. The generating stations may be far away from consumers centres and transmission lines make up the link between distribution systems, where the loads are, and generating units. The transmission system is said to be the backbone of any electric power system and operates at high voltage levels (commonly, 230 kV-400 kV). Distribution voltage levels are typically in the range 4 kV - 34.5 kV. Industrial consumers are fed from primary feeders at these voltage levels; residential and

commercial consumers are supplied from secondary distribution feeders where the voltage levels are 400 volts for the three-phase fed customers and 230 for the single phase ones (UK system). Figure 1.1 shows a one-line diagram with the basic elements of a power system.

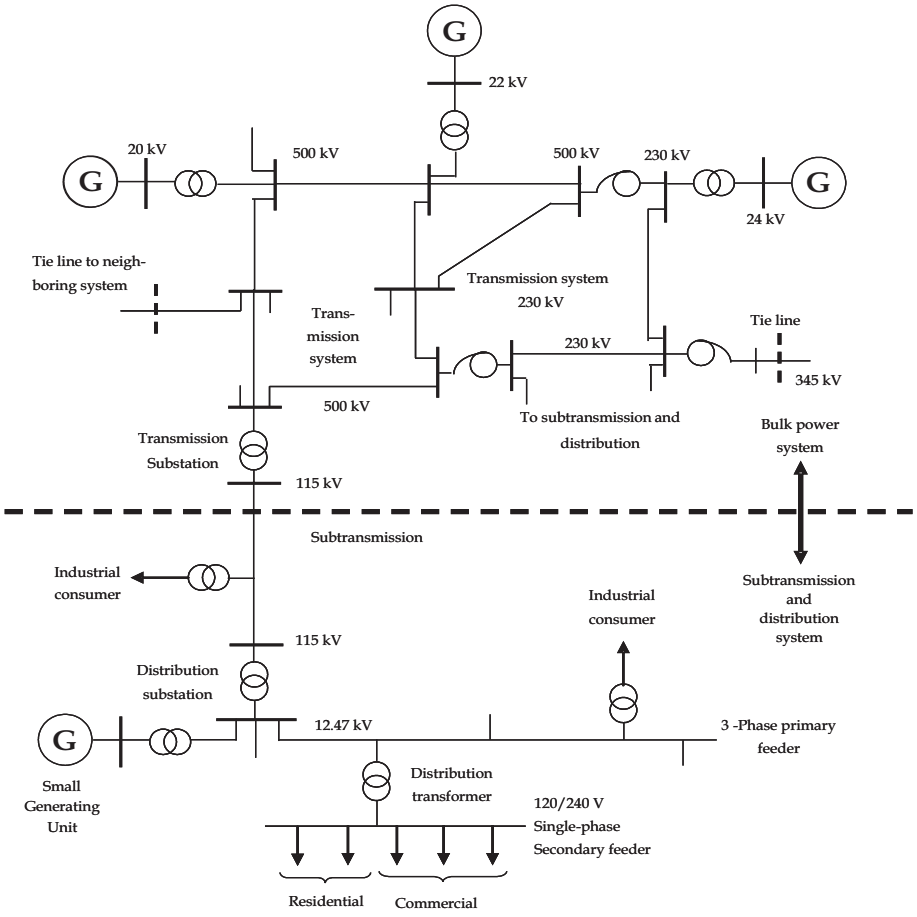

Figure 1.1: *Basic elements of a power system.*

The general perception is that transmission system used to be over-engineered but that this is rapidly coming to an end, owing to financial and regulatory pressures which are thwarting the network expansion plans of many utilities around the world. As a consequence, transmission assets are being operated closer to their limits than ever before, a fact that weakens the network and makes it prone to developing voltage collapse conditions. Essentially, the limited supply of reactive power from synchronous generators and marked increases in system

load are factors that contribute to increase the likelihood of voltage instabilities. If at a given point in time and space, these adverse matters come together and the situation is not managed appropriately, a local voltage instability may reach neighbouring equipment becoming more widespread and leading to a voltage collapse. In extreme cases, the voltage collapse may engulf the entire power system or a large geographical area encompassing neighbouring systems; an instance know by the public at large as a "blackout". Owing to the high social and economic costs that instances of voltage collapse carry, the power engineering community has made the study of this phenomenon a high profile issue.

Based on recent experience, gained from carrying out very detailed post-mortum analyses of a series of major operational disasters which took place in the Autumn of 2003, the North American Electric Reliability Council (NERC) developed system and planning operator standards for controlling and avoiding such undesirable situations. The key recommendations of the NERC document are summarised as follows:

1. Generation and demand must balance continuously.
2. Reactive power supply and demand must balance to maintain scheduled voltages.
3. Monitor power flows transmission lines and other equipment to ensure that thermal (heating) limits are not exceeded.
4. Keep the system in a stable condition.
5. Operate the system in such a way that it remains in a reliable condition even if a contingency were to occur, such as the loss of a key generation or transmission facility.
6. Plan, design, and maintain the system in such a way that it operates reliably.
7. Prepare for emergencies.

Despite the techniques and methodologies available to keep blackouts and outages at

bay, most practising engineers concur that the most practical way to prevent blackouts from happening is to carry out comprehensive long-term voltage stability simulations.

Excessive imbalances in the phase voltages or currents of a three-phase power system have always been a concern to power engineers. Moreover, a typical power system may contain untransposed transmission lines and feeders, single and unbalanced three-phase static loads, single and three-phase dynamic loads such as induction motors, co-generators, transformers, capacitors banks and more advanced power electronics systems, such as FACTS devices. To try to incorporate a suitable representation of the impact that excessive imbalances have in the power system, a three-phase dynamic power flow algorithm which considers the complete power system is developed in this research work.

The solution algorithm combines the differential equations that represent the network dynamic with the algebraic equations that represent the static part, in such a way that a simultaneous method becomes possible. The technique possesses the advantage of being numerically stable. It is robust and capable of handling islanding and simultaneous faults. It must be said that the conventional methods of power systems simulation (transient stability-like algorithms) are known to incur problems when network islanding arises [Kundur, 1994, Machowski et al., 1997]. Such key advantage of the dynamic simulator developed in this research will be exploited to study blackouts and long-term dynamic assessments.

1.2 Objectives of the Project

The main objective of this PhD project is to conduct research on the dynamic modelling, simulation and assessment long-term power system dynamics using the Newton-Raphson method in rectangular co-ordinates.

A key aspect of paramount importance in this research is the development of new mathematical models and methods coded into software to carry out effective dynamic analyses of power networks. The software is robust and flexible enough to solve power networks undergo-

ing different circumstances, including steady-state operating conditions, electromechanical-type transients and slow voltage oscillations.

On the main, this PhD thesis is developed within the broad context of voltage stability, focusing on aspects of dynamic modelling of power plat components. These models are suitably combined with those of conventional sources of reactive power such as synchronous generators and those pertaining to a new bread of reactive power compensators that base their modus operandi on the switching of power electronic valves, such as HVDC-VSC and FACTS controllers. It describes fundamental concepts regarding power systems stability analysis, time domain dynamics simulations of non-linear power systems in the combined use of the positive sequence and dq representations. The software developed is aimed at the study of long-term power systems dynamic when unfavourable conditions of the system are present. The FACTS devices, including HVDC-VSC control, the load modelling and the synchronous machines have been all selected and modelled to be amenable with the objective of this research work.

It has been observed in practice that voltage collapse phenomena may evolve over time scales that are several times the orders of magnitude of power systems phenomena studied with well-established transient stability application methods, such as those looking at first and second swing assessments. Hence, in order to ensure numerically stable solutions, even when rather large integration time steps are used, which may become necessary in the kind of studies that fall within the remit of this research; a simultaneous approach that uses the implicit trapezoidal rule in conjunction with the Newton-Raphson method is applied to carry out the time domain simulations. Again this contrast with the solution methods used in conventional transient stability application programs where the time-dependent nodal currents at the generator nodes are injected into a nodal impedance matrix.

The software developed in this research provides a flexible and robust test bed where the impact of traditional and emerging power system controllers on long-term dynamic simulations can be tested with ease.

1.3 Contributions

The main contributions of the research work are summarised below:

- A complete methodology for a developing dynamic power flow algorithm using Newton's method in rectangular co-ordinates has been developed. A flexible digital computer program has been written in MATLAB. This is a flexible simulation tool for the study of dynamic reactive power assessments and voltage stability phenomena.

- A general framework of reference for the solution of unified dynamic power flow solutions problems is presented.

- A *dq* model of the synchronous generator with saliency and flux decay has been implemented within the dynamic power flow algorithm, to enable suitable representation of the fast dynamic effects contributed by the synchronous generators.

- To widen the study range of dynamic voltage phenomena using the dynamic power flow algorithm, induction motor modelling features have been developed. For completeness, voltage and frequency dependant load models have also implemented.

- A discrete dynamic LTC transformer model suitable for the dynamic power flow algorithm has also been developed, implemented and applied to assess its impact on the voltage collapse phenomena.

- A Static Synchronous Compensator model which takes account of the dynamics of the device is developed and suitably included into the dynamic power flow algorithm.

- The implementation of a High Voltage Direct Current link model based on voltage-source converter is presented. In general, VSC-FACTS controllers are devices of great flexibility and speed of response, which aid the power system response during both normal and abnormal operation, as shown in this research.

- A fully-fledged three-phase dynamic power flow algorithm using *abc* co-ordinates is developed to study power networks with significant degree of unbalance.
- A comprehensive and robust three-phase power flow algorithm in rectangular co-ordinates is developed.
- Conventional LCC-HVDC controllers with different control operating modes have been introduced.

1.4 Outline of the thesis

This PhD thesis is organised in 8 chapters, including this introductory chapter, taking the following structure.

Chapter 2 outlines the main concepts involved in power system stability, describing the main kinds of stability and their importance in power systems planning and operation. A global definition of the power system stability is given. In addition, the modelling and data required to carry out voltage stability assessments are discussed. The all-important problem of contingency analyses is brought into discussion. The justification for selecting a dynamic modelling approach to study power system contingencies and related problems of voltage stability is given. The integration method applied in this research to solve the differential equations that characterise the electrical power systems is described.

Chapter 3 presents the theory of phase domain power flows using rectangular co-ordinates. Starting from first principles, it derives the nodal power flows equations, the Jacobian matrix entries and the linearised three-phase power flow equations. In order to expand the flexibility representation of contemporary power systems, LCC-HVDC are modelled on a three-phase basis. To make this representation more realistic, three different control strategies for LCC-HVDC links are developed. Test cases of unbalanced multi-phase power networks are solved, using different control modes.

Chapter 4 focuses on the dynamic power flow algorithm using the Newton-Raphson method in rectangular co-ordinates. The traditional power system elements and the conventional synchronous machine representation with its classical controllers such as governor, turbine, automatic voltage regulator and boiler are considered and suitably modelled within the dynamic power flow algorithm. An advanced synchronous machine model which considers the transient saliency and flux linkages in each axis of the synchronous machine is implemented. A realistic tap changer transformer model for dynamic assessments taking due account of the discrete nature of the transformer tap, is developed. The basic dynamic power flow algorithm is discussed in a comprehensive manner in this chapter. A classical transient stability study, validation results for the solution technique and some test cases are included.

Chapter 5 deals with power system load modelling. It stresses the importance of load modelling in dynamic studies, and critically assesses the most popular static and dynamic load models used in stability analyses. An induction motor load model and its inclusion into the dynamic power flow algorithm, is put forward. Several case studies are presented using different load representations. An assessment of the response of the static load models and that of an induction motor model is presented.

Chapter 6 is dedicated to the modelling and simulation of FACTS devices based on voltage source converters. The STATCOM and HVDC-VSC are single out for development and their inclusion into the dynamic power flow algorithm. Several tests cases are solved, where the control improvements in the power system response when the STATCOM and HVDC controllers are used, is clearly shown.

Chapter 7 deals with the extension of the basic dynamic power flow algorithm into a full three-phase dynamic power flow algorithm in ABC co-ordinates. The algorithm is suitably applied to the dynamic assessments of unbalanced power systems. The dynamic load tap changer and the static and dynamic load models are expressed in ABC co-ordinates and implemented in the three-phase dynamic power flow algorithm.

Chapter 8 draws overall conclusions for this research work and suggests directions for

future research work in this timely area of electric power systems.

1.5 Publications

During the process of this doctoral thesis and as part of it, the following publications have been generated.

- F. Coffele, R. Garcia-Valle and E. Acha, "The Inclusion of HVDC Control Modes in a Three-Phase Newton-Raphson Power Flow Algorithm". Paper presented at the IEEE Power Tech Conference, Lausanne, Switzerland, July 2007.

- R. Garcia-Valle and E. Acha, "The Incorporation of a Discrete, Dynamic LTC Transformer Model in a Dynamic Power Flow Algorithm". Paper presented at the Power and Energy Systems EuroPES Conference IASTED, Palma de Mallorca, Spain, August 2007.

Chapter 2

Dynamic Assessment

2.1 Introduction

The maintenance of stability between the rotating masses of all the synchronous generators in the power network and system load is an essential requirement for the operation any electrical power system. Within its limits, all the equipment in the network naturally tends to operate in synchronism, and it is very important to understand where the limits lays and how close to such limits the system can be pushed and still maintain normal operation.

Stability studies, such as small signal, transient rotor angle and voltage stability studies are effective tools for the evaluation of power system performance under abnormal operating conditions. Besides, the usefulness of these studies is in the design and implementation of control strategies for the enhancement of the overall stability of the system.

To be able to carry out these studies, it becomes first necessary to use the adequate mathematical models of synchronous machines, prime movers, voltage regulators and the broad number of control systems involved in the dynamic operation of power systems. Thus, the results derived from any stability simulation directly relies on the mathematical models of each one of the devices taken into consideration.

This chapter deals with general aspects of power system stability. A background and lit-

erature on the subject are presented to lay the ground for the description and classification of power system stability phenomena, together with the modelling and data set required to carry out voltage stability assessments are presented. The justification for the dynamic modelling, simulation and analyses is presented towards the end of the chapter. The Chapter concludes with a brief description of the trapezoidal method of integration. The integration method applied to solve the differential equations that characterise the electrical power systems is reported.

2.2 Background Review

Power systems around the world are being faced with great many challenges concerning overall system security, reliability and stability issues because of the unprecedented increase in electricity demand, limited transmission expansion, and the fact that new power plants are not being built close to the population centers because of environmental, land availability and economic constraints. Several major blackouts [US - Canada Power System Outage Task Force, 2004, Knight, 2001], exemplify these issues rather well.

One of the most sever power failures in history was experienced in November 1965 in the United Stated. This blackout lasted for about 19 hours, affecting millions of people.

The main technical reason behind the disturbance was the faulty setting of a relay and the resulting tripping of one of five heavily loaded 230-kilovolts transmission lines [IEEE Power Engineering Review, 1991].

After such a disaster the Federal Power Commission (FPC), which was the regulatory body overseeing the American power system at the time, prepared a report for the president of the USA, with a recommendations to create the Northeast Reliability Council (NERC) and the New York Power Pool (NYPP). Both institutions have developed industry standards for equipment testing and reserve generation capacity, as well as promoted the reliability of bulk electric utility systems in North America.

Notwithstanding all this effort, a new outage occurred in 1977 in New York city. The new blackout was a consequence of a combination of natural phenomena, mal operation of protective devices, inadequate presentation of data to system dispatchers and communication difficulties [Corwin and Miles, 1998]. Such adverse combination of conditions led to a wide-area voltage collapse in the Consolidated Edison system; the Consolidate Edison system is one of the 8 members of the New york Power Pool (NYPP) and it supplies electricity to five regions of New York city Manhattan, the Bronx, Brooklyn, Queen and Westchester Country.

Following on the steps of these two large blackouts, many others wide-area voltage collapses have happened in the USA, fortunately the consequences were not as severe as the previous two. Nevertheless, in the months of July and August of 1996, events turned for the worst; the USA underwent another two large-scale blackouts. These system failures took the industry by surprise since generation from the Pacific Northwest had been at its all time peak.

For the case of the July's blackout, the main reason was a flashover in a tree and near a 345-kV line, the faulty operation of a ground unit of an analogue electronic relay, and a voltage depression in the Southern Idaho system. All of this led to the new fatal blackout.

In August 1996, the generation capability and the power transfer from Canada to the USA was at almost peak value but the weather was very warm. Over a period of time, the power grid started to overload due to insufficient generation. This outage affected more that 4 million people in the USA and even in some parts of Mexico.

Within the last five years, a series of blackouts have struck many countries around the world. A case in point is Italy, which is a country highly dependent on electricity supplies from neighbouring countries. The blackout occurred due to branches of a tree falling on a 380-kV transmission line coming from neighbouring Switzerland, resulting the remaining lines in corridor becoming overloaded. Furthermore, two transmission lines coming from France came out of operation. Following these events, the whole of Italy suffered a power outage, with the exception of the island of Sardinia [Commission de Régulation de L'énergie, 2004].

Another recent, is the blackout that took place in London, where the system failure was traced to a wrongly installed fuse at a key power station. [National Grid, 2003].

The latest most recent blackout took place, once more in the USA. This outage has been attributed to the loss of generation in Cleveland power station which was, in turn, due to the sequential loss of three overloaded 345-kV transmission lines in Ohio, South of Cleveland. The unbalance between load and generation produced a cascading effect leading to the blackout [US - Canada Power System Outage Task Force, 2004].

Other key aspects which are making the system more fragile, is the way in which the interconnected system is being operated, transferring power in large blocks from generation excess areas to generation deficit points, thus leading to increased transmission congestion problems. Power system operators are constantly dealing with the challenge of operating their systems in a secure manner, while taking into account the uncertainty in demand and supply and the availability of enough security margins. Thus, off-line system studies are performed to ensure the overall system security ahead of time. In addition to the static application studies dealing with the constrained optimal operation of the network, dynamic studies are also carried out. These are mainly classified into voltage stability analysis and angle stability analysis, based on short-, mid- and long-term stability studies. These dynamic studies are based on power system models that are represented by differential-algebraic equations (DAEs); by necessity, these mathematical models are based on approximate system representation and limited data, since obtaining comprehensive and reliable data for a power system is a rather troublesome task [Concordia and Ihara, 1982].

In spite of the many investigations into methods of assessing voltage stability such as, Liapunov's method, continuation power flows, extended equal-area criterion, bifurcation analyses, a different way to approach this issue is the use of simultaneously solution techniques. This method is numerically more stable than the traditionally solution algorithms, robust and inherent capable of handling islanding and fault analyses [Gear, 1971b, Rafian et al., 1987].

This thesis studies various issues regarding off-line modelling of power system, i.e. long-term stability analysis, which are associated with phenomena that may lead to significant problems in power systems. The possibility of predicting the voltage collapse using these system simultaneous solution technique combined with the Newton-Raphson method is explored, as the dynamic effect of the different system plant components, load modelling and FACTS devices models on the unified frame-of-reference.

2.3 Literature Review

Over the years, various computational methods have been developed to carry out off-line and on-line security assessments of the power system enabling prediction and corrective actions of problematic dynamic system instances.

These tools have been developed to carry out more realistic dynamic reactive power system margins and voltage collapse assessments. The existing computer programs use one of the following approaches: Quasi-Static Simulation (QSS), Continuation Power Flows (CPF). The QSS uses a suitable combination of detailed dynamic models and simplified steady state models [Van Cutsem and Vournas, 1998]. The s-domain is used to access the problem of voltage collapse from a dynamic perspective; carrying out sensitivity analyses to determine the nature of the equilibrium point with data information obtained from a state estimator [IEEE Power Engineering Society, 2002]. Continuation power flows takes the approach of tracing the PV-curves to determine the critical equilibrium point [Qin et al., 2006].

In spite of the great numerical robustness, modelling capabilities and software flexibilities of these application tools, they may not be able to take into account the full dynamics of power system elements. Besides, these simulation approaches may not be able to incorporate protection action, the long term dynamics response of the system after short-circuit events and when islanding conditions. These factors are important issues to be considered when carrying out voltage stability assessments.

An alternative solution approach for the study of voltage phenomena based on full time domain simulations is developed in this thesis. It is a unified framework where the power flows representation of the network is combined with the dynamic models of the power system to enable combined solutions at pre-defined discrete time steps using the Newton-Raphson method. The result is a dynamic power flows algorithm where all dynamic components in the power system are fully taken into account.

These off-line tools may be used by system operators to gain information on available security margins and in taking proper corrective actions to overcome system problems.

2.4 Stability Evaluation

Power system stability is a term denoting a condition in which the various synchronous machines of the system remain in synchronism with one another [Kimbark, 1948a]. The IEEE/CIGRÉ joint Task Force on stability [IEEE/CIGRE Joint Task Force on Stability Terms and Definitions, 2004] has defined the problem of power system stability as follows:

"Power system stability is the ability of an electric power system, for a given initial operating condition, to regain a state of operating equilibrium after being subjected to a physical disturbance, with most system variables bounded so that practically the entire system remains intact."

Power system stability has always been recognized as an important issue for secure system operation [IEEE/CIGRE Joint Task Force on Stability Terms and Definitions, 2004], and the many blackouts caused by system instability highlight the importance of the problem [IEEE Power Engineering Review, 1991, Anderson et al., 2005]. As power systems have evolved through continuing growth in voltage and power rating and interconnections have sprawled, different forms of stability have emerged. Hence, a classification of the problem of power system stability has become necessary. This is a key issue which needs to be clearly understood to be able to properly design, operate and control an electrical power system.

The current steady-state stability consensus is that power system stability can be classified into steady-state stability, transient stability and dynamic stability.

2.4.1 Steady-state stability

During the normal operation of a power system, the total load is undergoing constant and relatively small fluctuations, the generators adjusting to maintain the load at the specified frequency. When the loading of a power system is greater than the normal working level, the fluctuations become more significant. A limit is reached when the transfer of synchronism power cannot increase and a further small increase in loading causes a loss in synchronism between generators or groups of them. This point is known as the steady-state stability limit. The power transfer between two machines varies, approximately, with terminal voltage and the size of the angle between the voltages and inversely with the transfer impedance as described in Eq. 2.1. This approximation is known as the power angle characteristic.

$$P \simeq \frac{V_1 V_2}{X} sin\delta \tag{2.1}$$

From Eq. 2.1, when the angle δ takes the value of zero there is no power transferred between the associated elements. As soon as a power transferred conditions exists, the angle is increased and after a certain angle, normally 90°, an additional increment in angle will produce a reduction in power transferred [Kundur, 1994]. Thus, there is a maximum steady-state transfer capability between the involved elements. This condition is only valid when there is no more than two elements, i.e. a synchronous generator and a static load. For the case when more than two elements are considered, the power power transferred and the angular deviation are a function of generation and load distribution. At this point, an angular separation of 90 degrees between any two synchronous generators has no particular significance [Stevenson Jr, 1982, Kundur, 1994].

The damping of a generator is also a very important factor in maintenance stability. When

the damping is positive, transients due to load fluctuations die out; when it has a value equal to zero, the machines could remain stable and when negative, the oscillations increase and the angle between voltages eventually exceed the limit.

The addition of an automatic voltage regulator improves the stability of a synchronous generator. By making excitation a function of the power output, the terminal voltage is varies, which in turn varied the steady-state stability limit.

2.4.2 Transient stability

When a change in load occurs, the synchronous generator cannot respond immediately, due to the inertia of its rotating parts. To identify if the system is stable after a disturbance it is necessary to solve the generator's swing equation. The system is unstable if the angle of a synchronous generator or between any two of them tends to increase without limit. On the other hand, if the angle reaches a maximum value and then decrease, the system may be stable. There is a simple and direct method for assessing the stability of the system, but it may only apply to systems of no more than generators. It is know as the equal-area stability criterion [Kimbark, 1948a, Stevenson Jr, 1982] and does not require an explicit solution of the generator's swing equation. Some simplifying assumptions are:

- The mechanical power is constant
- The synchronous generator is represented by a voltage source of constant magnitude behind a transient reactance.

The swing equation describes the synchronous generator rotor dynamics through a differential equation of the form:

$$M\frac{d^2\delta}{dt^2} = P_a \tag{2.2}$$

$$P_a = P_m - P_e \tag{2.3}$$

where

δ is the rotor angle.

M is the inertia constant.

P_a is the accelerating power.

P_m is the mechanical power.

P_e is the electrical power.

The key concept behind the equal-area criterion is illustrated in Fig. 2.1 where an unstable and a stable condition are presented. In the unstable case, δ increases indefinitely with time and the machine loses synchronism. In contrast, the stable case undergoes oscillations, which eventually disappear because of damping. It is clear that in the stable case the gradient od the δ-curve reaches a value of 0, i.e. $\frac{d\delta}{dt} = 0$.

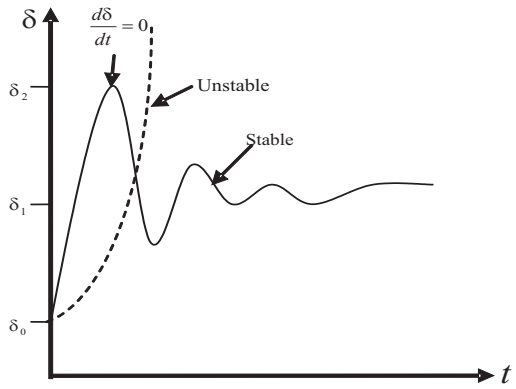

Figure 2.1: *Stable and unstable system.*

Therefore the stability is checked by monitoring the rotor speed deviation $\frac{d\delta}{dt}$, with respect to the synchronous speed, which must be zero at some point, this means that:

$$\int_{\delta_0}^{\delta} P_a d\delta = 0 \tag{2.4}$$

This condition requires that, for stability, the area under the graph of accelerating power P_a versus δ must be zero for some value of δ. Assuming the inertia of the synchronous machine to be constant and a slight value of damping, the positive (or accelerating) area under the graph must be identical to the negative (or decelerating) area [Nasar and Trutt, 1999].

$$A_1 = A_2 \tag{2.5}$$

The method is illustrated with reference to Fig. 2.2. Point a, corresponding to δ_0, the initial steady-state operating point. At this position, the input power to the machine, P_{i0}, is equal to the developed power P_{e0}. When a sudden increase of the input power P_i occurs due to a large change in the network, the accelerating power, P_a, becomes positive and the rotor moves towards point b. It is assumed that the machine is connected to a large power system and there is also a constant field current which maintains the internal voltage constant. Thus, the rotor accelerates and the power angle begins to increase, at point b, $P_i = P_e$ and $\delta = \delta_0$. At this moment, P_a is negative and δ finally reaches a maximum value δ_2 or point c and then swings backwards b. Hence, the rotor establishes to the point b, which is the new steady-state stable operating point.

For the criterion for stability stability given by Eq. 2.5 and with reference to Fig. 2.2 it can be stablished that

$$\int_{\delta_0}^{\delta_i} (P_i - P_{max} \sin\delta)\, d\delta = \int_{\delta_1}^{\delta_2} (P_{max} \sin\delta - P_i)\, d\delta \tag{2.6}$$

In a multi-machine system a definite criterion for stability is not so easily defined. Frequent drifts of generators do occur and whilst each machine considered individually would be appeared to be unstable, the system as a whole is relatively stable [Kundur, 1994, Pavella

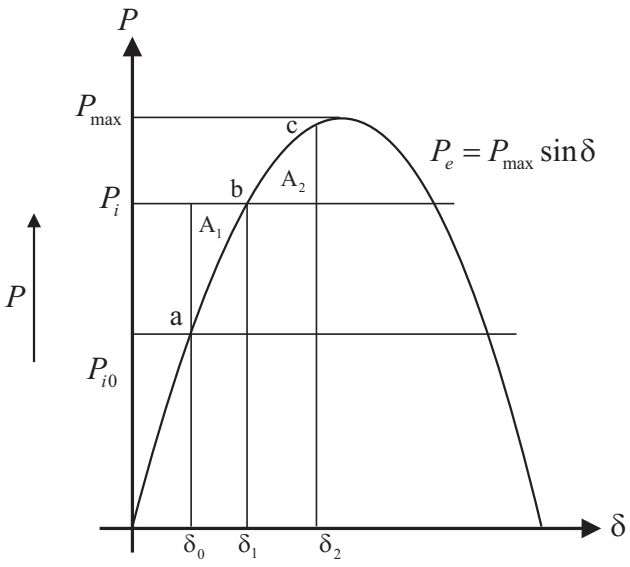

Figure 2.2: *Power angle characteristics.*

and Murthy, 1995, Machowski et al., 1997].

Transient stability studies are usually performed for a frame time of a few seconds following the disturbance. In the case of two machine systems, if the system first-swing is stable, then stability is usually assured. For multi-machine systems, it is necessary to prolong the study to ensure that interactions between synchronous generator swinging do not induce instabilities in other generators during the second or third swing. By the end of the the third swing, the amplitude of the oscillations are usually diminishing and if the system is still stable there is little chance of later instability.

The problem of stability during the transient period is usually most acute when faults occur in the electrical network. The most common fault is that of a single-phase being short-circuited to ground, but the most onerous is normally a three-phase short-circuit.

When a fault occurs the transfer impedance rises instantaneously to a new value and the power-angle curve changes. The generators accelerate because of power unbalance between the mechanical and the electrical powers. Normally faults are cleared quickly by opening the circuit breakers before the clearing critical time.

2.4.3 Dynamic stability

When a system is working close to the stability limit even or when operating in a dynamically stable region, small perturbations such as those normally experienced in a power-system, may cause instability. This situation has become more pronounced recently as large blocks of power are transmitted over very long distances. The model of the system for dynamic stability studies must be very accurate and the software used for the study must include components not normally modelled in software used for transient stability studies. In studies of this type the simulation time is very long, lasting up to tens of minutes of time phenomena representation.

If for any reason the transfer impedance between the synchronous generators and an induction motor load increases, then a voltage reduction occurs which causes the motor to slow down. This will cause an increment of current and reactive power flowing into the motors and a further voltage decrement will follow. It is possible in a situation like this that the voltage may collapse in the vicinity of the load. This is a voltage instability phenomena.

Stable operation of a power system depends on the ability to continuously match the electrical output of generating units to the electrical load of the system. Dynamic stability of power systems is a non-linear phenomenon which arises from the fact that generators are operated in a parallel structure and during steady-state they are operated in synchronism. The evaluation of a power systems' ability to cope with large disturbances and to survive transitions to normal or acceptable operating conditions it is termed transient stability assessment. A transient period occurs when this equilibrium state is disturbed by a sudden change in input, load, structure, or in a sequence of such changes; the system is transiently stable if after a transient period, the system returns to a steady condition, maintaining synchronism. If it does not, it is unstable and the system may be divided into disconnected subsystems, which in turn may experience further instability.

During the dynamic stability, there is a very common scenery called outages of voltage

collapse. This outages can be divided into two major groups, planned and unplanned outages.

The first ones are mainly related to the maintenance of equipment or upgrade of the power network, whereas the latter ones are described by unscheduled events such as wrong relay co-ordination scheme, unfavourable weather conditions or poor reactive power supply.

2.5 Off-line Functional Requirements

2.5.1 Modelling and data conditions

Experimentation with power system components is expensive and time consuming, therefore, simulations are a fast and economic method to conduct studies in order to analyse the system performance and this type of devices. Power system elements should be designed to endure overvoltages and faults. Due to the great electrical and mechanical stress that these devices support during transient conditions, the design of these components relies on the dynamic characteristics of these elements. Modelling and simulation are issues of paramount importance in the design and operation of any power system.

Correct modelling selection, should bare in mind the time-scale for the problem at hand. Fig. 2.3 shows the main areas for the power systems' dynamic assessment [Arrillaga and Watson, 2002]. In principle at least, it is possible to develop a simulation model which consider all the dynamic phenomena, from the fast inductive/capacitive effects of the network, to the slow effects associated with plant dispatch, but this would be a very hard task and it is not done in practice.

Traditionally, power system engineers have used two main classes of programs for analyses of bulk power systems performance: 1) power flows and 2) transient stability.

Historically, power and reactive power flow problems have been analysed using static power flow programs. This approach was satisfactory since these problems have been governed by essentially static or time-independent factors. Power flow analyses allows simulation of a snapshot of time.

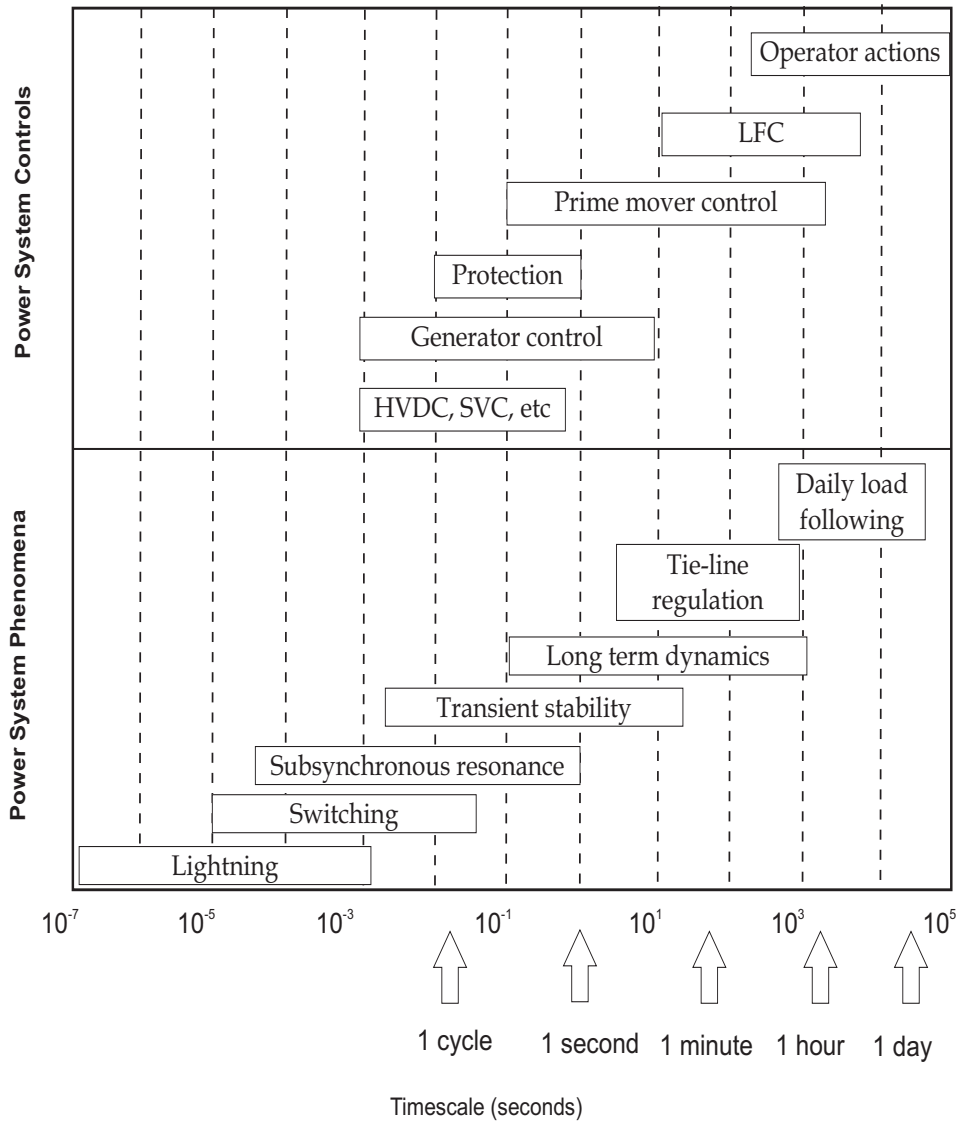

Figure 2.3: *Time frame of various transient phenomena.*

Static analyses involve only the solution of algebraic equations and are therefore, computationally much more efficient than dynamic analyses. Static analyses are ideal for the bulk of studies in which voltage stability limits for many pre-contingency and post-contingency cases must be determined.

Dynamic issues, such as first swing transient stability problems have normally been ad-

dressed using transient stability programs. These programs ordinarily include dynamic models of the synchronous machines with excitation systems, turbines and governors, as well as other dynamic models, such as loads and fast acting devices. These component models and the accompanying solution algorithms are suitable for analyses of phenomena from tens of milliseconds up to several seconds.

With the evolution of modern, heavily compensated power systems, voltage stability has emerged as the limiting consideration in many systems. The phenomenon of voltage collapse is dynamic, yet frequently evolves very slowly, from the perspective of a transient stability program. It has been argued that slower acting devices such as generator over excitation limiters (OEL) and the characteristics of the system loads will contribute to the evolution of a voltage collapse [IEEE Power Engineering Society, 2002, Sekine and Ohtsuki, 1990, Hill, 1993, Anrborg et al., 1998]. Power flow analysis will take into account all these effects, by enforcement of their steady-state response, which is based on algebraic considerations. Conversely, transient stability analysis will typically assume that these phenomena are slow, and corresponding variables will remain constant. In actual practice, neither of these assumptions can be relied upon, thus leaving voltage collapse in a no-mans-land between these two analytical domains.

The recent emergence of a new class of computer simulation software provides utility engineers with powerful tools for analysis of long-term dynamic phenomena. The ability to perform long-term dynamic simulations with detailed dynamic modelling permits more accurate assessment of critical power system problems than what it is possible with conventional power flows and transient stability programs. However, time-domain simulations are time consuming in terms of CPU and are essentially for post-mortem analyses and the coordination of protection and control. Therefore, the most effective approach for studying voltage instability is to make use of an analytical technique which consider the full dynamics of an electrical power network.

Conventional analytical tools, including power flows and transients stability programs may

not be particularly well suited to the analyses of all voltage stability problems. Specifically, long term dynamic simulations require good models of the slow dynamics associated with voltage collapse and also the modelling of important slow acting controls and protective devices. This modelling technique will give utility engineers the ability to conduct studies that reflect the behaviour of the systems in a more realistic manner. Moreover, the interaction of customer loads and system equipment such as generator protection, load tap-changer transformer control and shunt compensation plays a key role in the progress of a voltage collapse.

The dynamic nature of the aggregate system load, that is, the change in characteristics between the transient and the long-term period, has important consequences for analyses of voltage stability. Modelling of frequency dependence of the loads may therefore be as important as voltage dependence. So then, load behaviour is a main part of long-term dynamic modelling.

There is a strong relationship between the load modelling and the modelling of other system components, in terms of the overall system response. High fidelity simulations are dependent on good representation of all these elements.

2.5.2 Contingency analyses

A contingency consists of one or more events happening simultaneously or at different instants of time, with each event resulting in a change in the state of one or more power system elements. A contingency may be initiated by a small disturbance, which may be a fault, or a switching action.

It is impractical and unnecessary to analyse in detail the impact of every conceivable contingency. Generally, only a limited number of contingencies might impose a immediate threat to voltage stability and these might be different from the ones impacting on transient stability. It is required therefore to define a reliable list of contingencies and provide the capability to screen and select those most likely to cause problems, so that they will be

addressed in detail.

The following types of switching operations should be considered as a contingency:

- Breaker opening/closing,
- Generator tripping,
- Load shedding.

For contingency analyses, the dynamic simulation should be able to analyse both fast and slow dynamics, preferably with automatic time step adjustment. Besides, it should contain generator and governor dynamics, tap changing time delays and prime mover dynamics mainly.

2.6 Dynamic Modelling Philosophy

Before it is possible to study the methods of solving the electrical power-system stability problem, it is necessary to adequately define the elements of the system in such a manner that a time solution is both feasible and practical.

Engineering judgement must be used to establish the approximations, which can safely be made in order that the model behaves in a similar manner to the actual system. Some of the approximations have self-cancelling effects and can be justified, while others can be made only where it leads to a pessimistic result.

The approximations are necessary harder to avoid the expense of an over-elaborate model which would require an unduly large programme using excessive computer storage and execution time.

Another reason for the approximations is that data on the elements of the power-system is limited and the models should reflect this limitation.

The classical model of a synchronous machine is that of a fixed voltage magnitude behind a reactance. This model was adequate for investigations of multi-machine stability performance

before the advent of digital computers. It led to pessimistic results often indicated that the system was unstable when in practice it maintained stability. Models of machines close to large disturbances were made more accurate accounting for changes in the flux linkages in the field winding. This together with the inclusion of automatic voltage regulators (AVR) actions, improved results by a considered margin. When digital computers became available it was possible to further improve the results by including damper winding and speed governor models. To compensate for the increased accuracy of the generator models, the representation of loads was also improved, moving on from the constant impedance representation to include constant power and constant current types. Moreover, large induction motors were beginning to be modelled in a similar fashion to synchronous machines.

If only steady-state performance of the networks is on interest, it is standard to model the networks by a set of non-linear equations, corresponding to the active and reactive powers injected at the nodes of the network. The set of equations that describe the system for stability studies may be more involved, and may be divided into two groups. Differential equations are used to describe the rotational motion of synchronous generators and induction motors, the slowly changing voltages representing the internal characteristics of the machines, and their controllers.

The electrical network responds very rapidly to changes and a good assumption is that the response is instantaneous. Algebraic equations therefore describe the network very well for the range of phenomena which are of concern in this research. These equations are linearised around a base operating point determined by the system load powers and the mechanical/electrical power contributed by the generators in the system.

Variables associated with the differential equations must be solved using a suitable integration method and may be referred to as integrable variables. Similarly variables associated with the algebraic equations may be referred to as algebraic or non-integrable variables.

Combing the two sets of equations, yields an algebraic-differential initial described as:

$$\dot{y} = F(y, x) \tag{2.7}$$

$$0 = G(x, y) \tag{2.8}$$

where x and y are vectors of integrable and non-integrable algebraic variables. The starting conditions for the stability simulations are determined by using only the algebraic set Eq. 2.8. This is followed by a combined solution of Eq. 2.7 and Eq. 2.8 as a function of time, to be able to carry out the dynamic assessments.

In consequence, the objective of the dynamic assessment is to solve x and y as a function of time.

Equation 2.7, comprises the differential equations of all synchronous generators and their controllers. Since each generator is coupled to the power plants only through a single connecting bus of the network, Eq. 2.7 is a collection of separate subsets. Eq. 2.8 consists of network equations and the stator equations of all synchronous generators transformed into the network reference frame. The two set of equations are co-dependent so then the solution technique should be a simultaneous one for high solution reliability. The open literature offers a rich list of solution techniques [Kundur, 1994, Machowski et al., 1997, Pavella and Murthy, 1995, Arrillaga, 1998, Van Cutsem and Vournas, 1998, Claudio A. Cañizares, 1995]. In power system research there are two main approaches proposed to carry out the solution of Eq. 2.7 and Eq. 2.8 [Stott, 1979]. In the first approach the solution of the algebraic and differential equations is carried out in an independent fashion, and it is termed partitioned method. The other solution approach consists in solving the algebraic and differential equations at the same time. The differential equations are transformed into algebraic equations and combined with the network algebraic equations. This approach is termed simultaneous approach method. The most common way of solving the sets of Eq. 2.7 and Eq. 2.8 to carry out power system dynamic assessments, is to use the partitioned method. This remark

applies to both academic and commercial software alike. there are two notable exceptions, where the simultaneous method is applied very elegantly [Rafian et al., 1987, Van Cutsem and Vournas, 1998].

For instance, Van Cutsem [Van Cutsem and Vournas, 1998], developed a technique for voltage stability using a simultaneously method. This technique approaches the problem by modelling only the slow dynamics, while the fast dynamics are neglected, converting them into algebraic equations, enabling quasi-static simulation (QSS), as referred to by the author.

The solution technique adopted for voltage stability assessment in this work is a simultaneous method, which is based mainly in the simultaneous solution of the differential-algebraic equations (DAEs) [Gear, 1971b, Rafian et al., 1987].

As a first approach, a dynamic power flow algorithm using the trapezoidal rule and the Newton-Raphson technique has been developed. Moreover, this algorithm has been extended to the phase co-ordinates system to cover situation of natural imbalances in the power network and also cases of unbalanced loading. In either case, the balanced of the unbalanced solution approach, the differential equations are discretised and transformed into algebraic equations ensuing that the discretised equations are in such a way that can be solved in conjunction with the algebraic equations.

The most important power plant components which should be modelled dynamically for dynamic voltage assessments are: the synchronous generators and their controls (AVR, turbine-governor, boiler), dynamic loads, load tap-changers and phase-shifters, and FACTS controllers, bring out a reliable simultaneously technique for voltage stability assessment.

Figure 2.4 depicts the general algorithm developed during this research project. It contains four main blocks. The first one makes provisions for all the relevant data related to the power network, such as generation, loads, load-tap changers and FACTS equipment. The second block encompasses a list of faults and perturbations which are pre-defined during the simulation study.

In the third block, the solution of static power flows in rectangular co-ordinates is carried

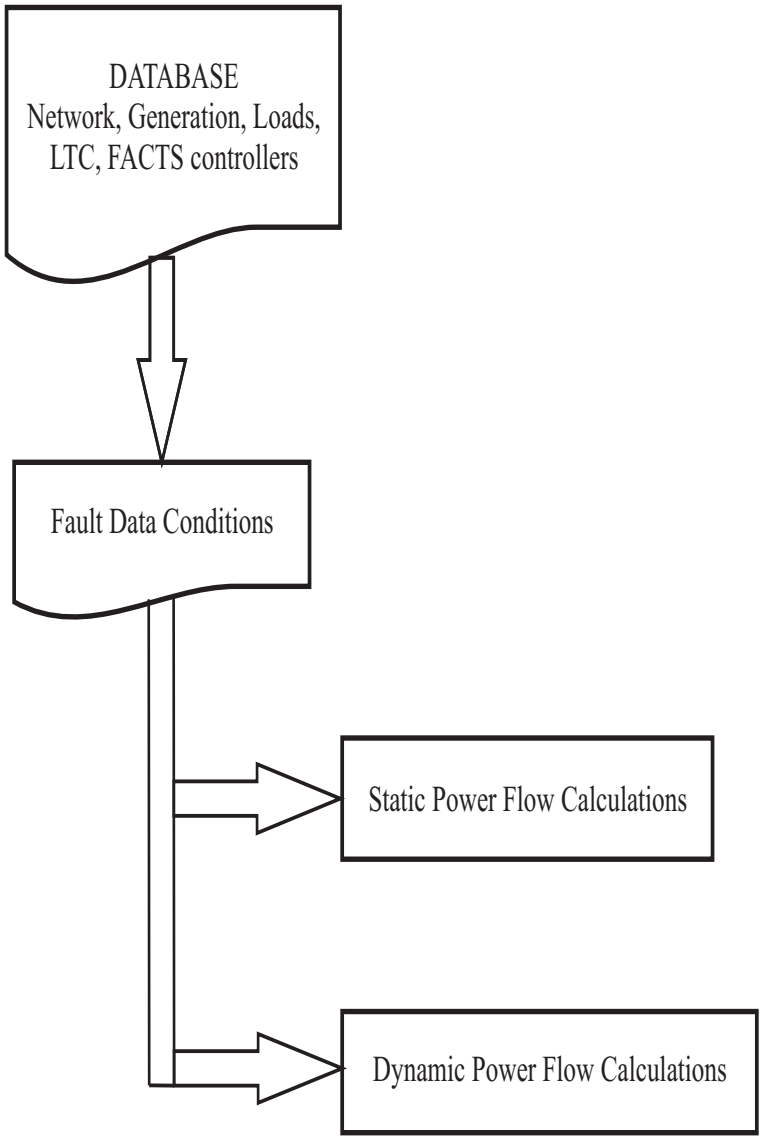

Figure 2.4: *Software environment to carry out static and dynamic power flows calculations.*

out. This block is further described in the following chapter. The last block describes the dynamic power flow algorithm. Fig. 2.5 presents a more descriptive diagram of it. At this flow diagram, the blocks where the differential equations are discretised using the trapezoidal rule are established.

Besides, the dynamic assessment block presented in Fig. 2.5, block represented by Fig.

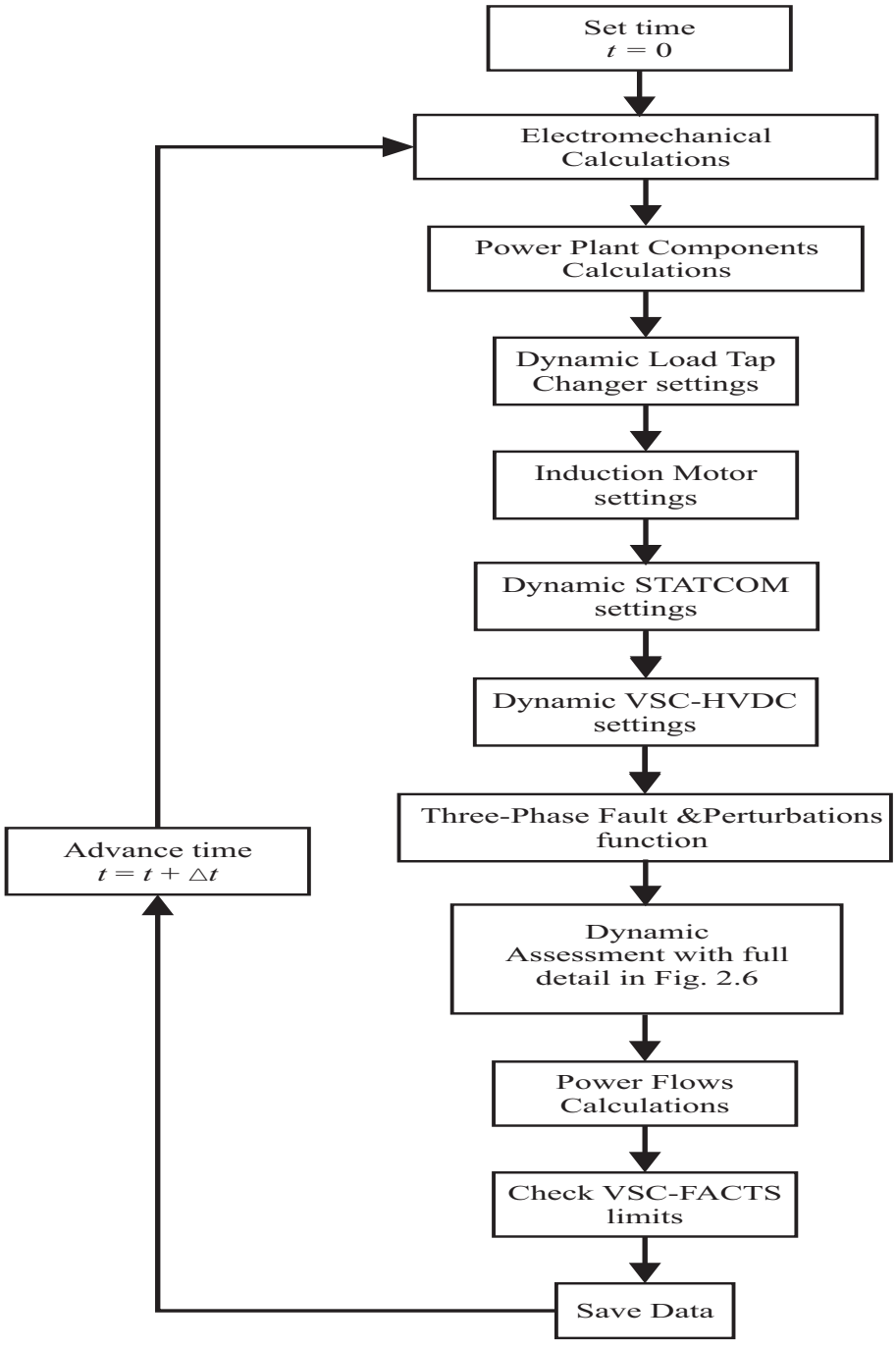

Figure 2.5: *Flow diagram for dynamic power flows studies.*

2.6 presents the Newton-Raphson algorithm for the dynamic process.

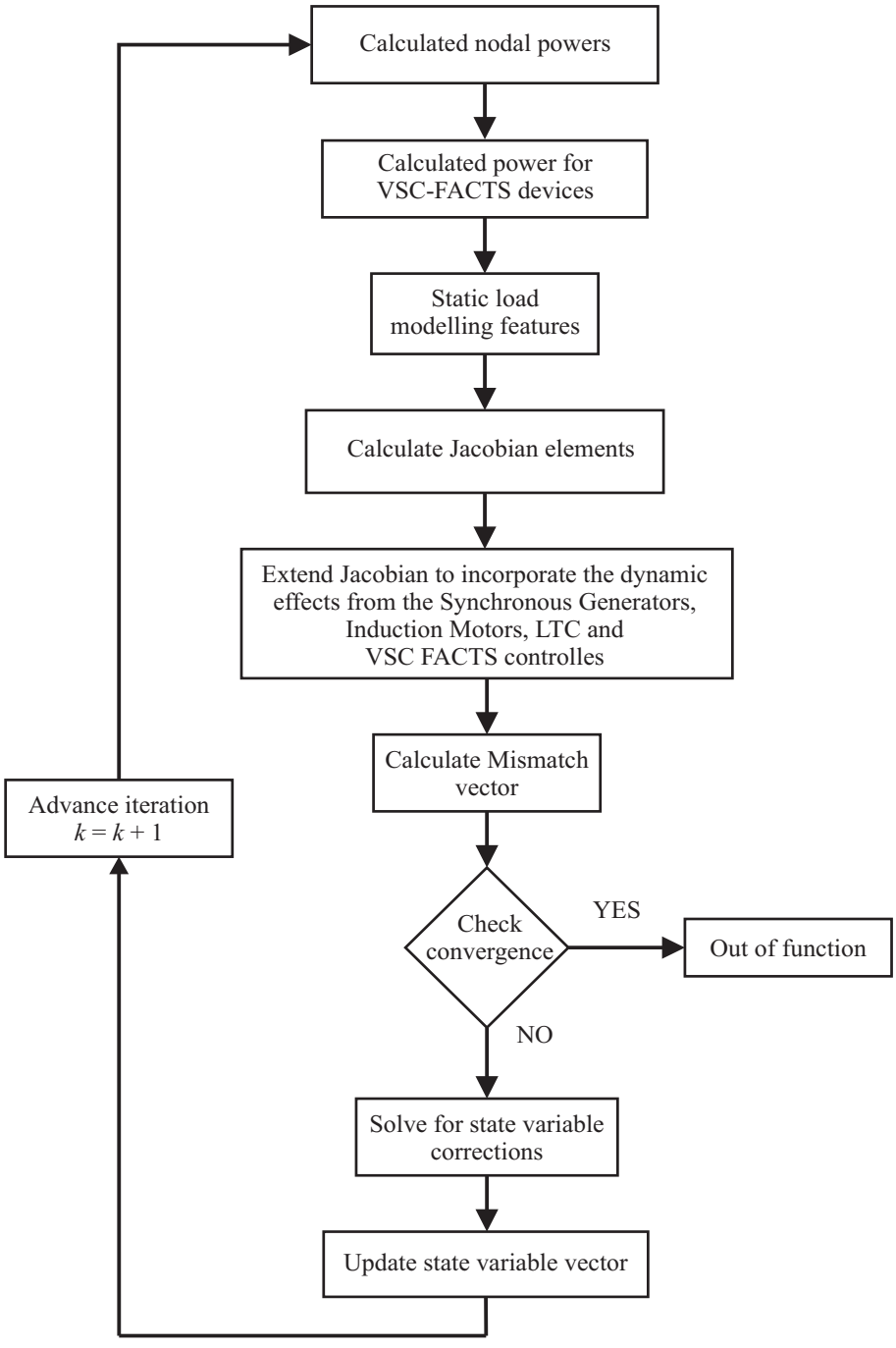

Figure 2.6: *Newton-Raphson flow diagram for dynamic power flows calculations.*

2.7 The Trapezoidal Method

Prior to the advent of digital computers only a few methods of solving ordinary differential equations (ODEs) were practical. Hand calculation precluded the use of complex formulae and also made large system studies impossible.

Since then, numerical analyses has become very important, not only to the mathematicians but also to the scientists and engineers. Each problem requires special consideration in order to get the best available solution method. This is specially true in the solution of ODEs where the choice of method can make the difference between good and bad results.

The stability of a method for the solution of ODEs is of great importance and has received a great deal of attention [Gear, 1971b, Gear, 1971a, Lapidus and Seinfeld, 1971, Williams, 1972]. The implicit trapezoidal integration method has been used as a method of solving the multi-machine transient stability problem [Dommel and Sato, 1972], and has gained recognition as a very powerful method, having great advantages over the more traditional methods such as Gauss, Gauss-Seidel, Runge-Kutta and Euler.

The trapezoidal method is derived from the general multi-step equation,

$$\sum_{i=0}^{k} \alpha_i \; y_{n-i+1} + h \sum_{i=0}^{k} \beta_i \; \dot{y}_{n-i+1} = 0 \tag{2.9}$$

where α_i and β_i are constant, and with k equal to unity it becomes a single step method. The solution at the end of $n+1$ steps is given by:

$$y_{n+1} = y_n + \frac{h_{n+1}}{2} \left(\dot{y}_{n+1} + \dot{y}_n \right) \tag{2.10}$$

This is implicit and requires an iterative solution. The solution can be made directly if the derivative can be replaced by the differential equations, forming an algebraic equation.

The accuracy of the method may be determined by expanding each term in Eq. 2.9 by a Taylor's series. The lowest non-zero coefficient is for $y_n^{(3)}$ and is $-\frac{1}{12}h^3$. Thus the trapezoidal

method has second order accuracy and the true solution may be given as:

$$y(x_{n+1}) = y_n + \frac{h}{2}\left(y_{n+1}^{(1)} + y_n^{(1)}\right) + 0(h^3) + \varepsilon_{n+1} \tag{2.11}$$

where ε_{n+1} represents the round-off error at the $n+1^{th}$ step.

The characteristic root of the method when applied to the ordinary differential equations is,

$$\dot{y} = \lambda y \tag{2.12}$$

with $y(0) = y_0$ is

$$z_1 = (1 - 2b_{n+1}) \tag{2.13}$$

where

$$b_{n+1} = \frac{h_{n+1}}{\left(h_{n+1} - \frac{2}{\lambda}\right)} \tag{2.14}$$

If $\Re(\lambda) < 0$ then $0 \leq b_{n+1} \leq 1$ and $|z_1| \leq 1$. The trapezoidal method is therefore A-stable. This means that the method has an infinite stability boundary (unconditionally stable). The trapezoidal method is linear and thus in a multi-variable problem, like the power system stability problem, the method is sigma-stable (multi-variable version of A-stability). The two are equivalent when the method is linear but may not be equivalent otherwise. Back Euler and the trapezoidal method are sigma-stable, single step methods.

The great advantage of this method is that the solution of all the variables is simultaneous. With the more traditional methods, using explicit integration methods, interface errors occurred due to the out of step solution of the two groups of variables in the problem.

2.8 Summary

This chapter has outlined the issues of power system dynamics, emphasising current agreement on the classification of power system stability phenomena and its importance in power plants modelling development. The main tools available for voltage stability assessments and their main drawbacks compared to the models and algorithms developed in this research work.

Key concepts regarding dynamic stability studies, focusing on voltage stability assessment, are described within the context of the current research project. The main requirements for off-line analyses of electric power networks are assessed. Besides, the great importance of equipment modelled for voltage stability simulation is remark.

The data modelling which is an issue of noteworthiness for voltage stability studies is addressed. The definition of contingency for voltage stability studies and the significance of slow and fast dynamics are described.

The modelling philosophy adopted to tackle the voltage stability problem is described. The difference between this approach and the conventional techniques to solve the problem are stated. Moreover, a clear explanation about the integration method used to discretised the differential equations is introduced.

Chapter 3

Newton-Raphson Power Flow Algorithm in *abc* Rectangular Co-ordinates

3.1 Introduction

Modern system interconnections enable the safe exchange of electric power between regions or countries, taking advantage of load diversity in time and space leading to a more economical and environmental way of supplying electricity to consumers. The key advantages of interconnected systems are [Arrillaga et al., 2007]:

1. the pooling of generation capability with the opportunity to utilise diverse primary energy resources;

2. the creation of larger markets, which enable economies of scale to be realised in the operation of power plants and in accommodating demand growth;

3. significant flexibility for the introduction of competition into electricity supply.

Such advantages have been conventionally alighted by the use of additional AC lines between the various interconnected systems, in order to reinforce the interconnections. Nevertheless, with the increasing complexity of power systems and consumers' appetite for electricity, the reliability of power supply has deteriorated, bringing about, as a consequence, a great number of blackouts in various parts of the world [Knight, 2001]. Consequently, strengthening the transmission system is vital to the reliability of block power interchanges among interconnected power systems.

It is argued by HVDC enthusiasts that the probability to decrease blackouts and bottlenecks in power systems can be substantially alleviated with the use of HVDC interconnection.

The thrust of this chapter is the development and modelling of three-phase power AC-DC networks making use of the Newton-Raphson method in rectangular co-ordinates.

3.2 Power Flows Concepts

Power flows solutions is the most frequently performed kind of study in power systems engineering. The power flow formulation is at the heart of power system analyses and is closely associated with voltage stability analyses [Taylor, 1994].

The classical Newton [Tinney and Hart, 1967] and fast decoupled load flow [Stott and Alsac, 1974] have been extensively used in power flow analyses for the last decades. The steady-state conditions relating to transmission systems are obtained by assuming balanced operation in most cases. However, the proposals and developments of algorithms for three-phase power flows calculation for unbalanced power system conditions are increasing [Arrillaga and Watson, 2001, Wilsun Xu and Dommel, 1991, Smith and Arrillaga, 1998, Zhang, 1996].

To solve the power flow problem, the most general and reliable algorithm is the Newton-Raphson method. The basis of this iterative method relies on successive linearization of the non-linear set of equations that represent the electrical power network using only the first

term of the Taylor's series expansion.

The Newton-Raphson method, as applied to the three-phase power flow problem in rectangular co-ordinates, is dealt with detail in this chapter.

The Newton-Raphson method in rectangular co-ordinates, as opposed to the one in polar co-ordinates, is less well-known but it is equally effective and it goes on well with the method of dynamic power flows which is the central focus of this thesis.

3.2.1 The power flow problem formulation

The main object of the power flow solution is to obtain the nodal phase voltages at all buses of the network corresponding to specified system level of generation and load patterns. In power flow analyses using rectangular co-ordinates, the nodal voltages are expressed as a function of their real and imaginary parts. The complex voltages, expressed as real and imaginary parts are the state variables rather than the magnitude and phase angles used in the polar co-ordinate analyses.

As voltage magnitudes and angles are involved, it follows that for each bus, six independent constraints are required in order to solve for the six unknowns. These constraints are different for different types of buses. The two main types are load and generators buses, with the slack bus being treated as a special case of the generator bus.

Despite the fact that the number of equations and variables involved in the solution of power flows in rectangular co-ordinates is greater than in polar co-ordinates, when sparsity techniques are applied, such an increase in size is of little significance. Each iteration carried out in rectangular co-ordinates analyses is faster than in polar co-ordinates because no trigonometric operations are involved [Stagg and El-Abiad, 1968, Arrillaga and Watson, 2001].

3.2.2 Power flow equations

The power balance equation for a three-phase transmission line component, as shown in Fig. 3.1, can be written as,

$$S^{a,b,c} = P^{a,b,c} + \mathrm{j}Q^{a,b,c} = V^{a,b,c}(I^{a,b,c})^* \tag{3.1}$$

where

$S^{a,b,c}$ is the complex power injected into the three-phase bus.

$P^{a,b,c}$ is the active power injected into the three-phase bus.

$Q^{a,b,c}$ is the reactive power injected into the three-phase bus.

$V^{a,b,c}$ is the voltage at the three-phase bus.

$I^{a,b,c}$ is the current at the three-phase bus.

with a, b, c referring to the three phases of the system.

In rectangular co-ordinates analyses, the bus voltages and the admittances are expressed as,

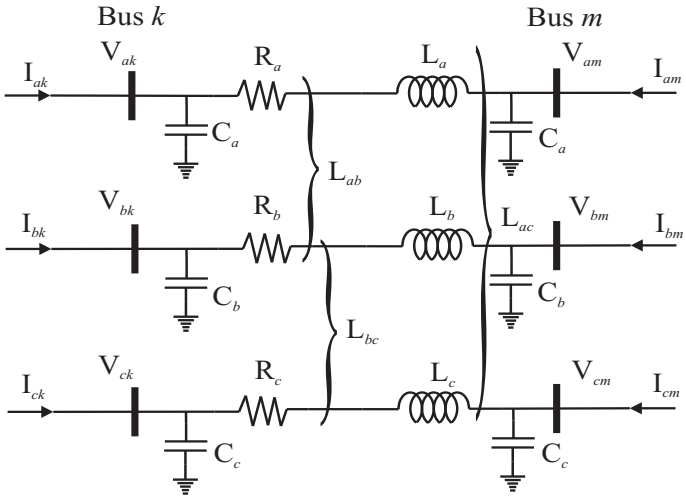

Figure 3.1: *Three-phase transmission line diagram.*

$$V_k^{\rho} = \begin{bmatrix} e_k^b + \mathrm{j}f_k^b \\ e_k^b + \mathrm{j}f_k^b \\ e_k^c + \mathrm{j}f_k^c \end{bmatrix} \tag{3.2}$$

and

$$Y_{km}^{\rho\rho} = \begin{bmatrix} Y_{km}^{aa} & Y_{km}^{ab} & Y_{km}^{ac} \\ Y_{km}^{ba} & Y_{km}^{bb} & Y_{km}^{bc} \\ Y_{km}^{ca} & Y_{km}^{cb} & Y_{km}^{cc} \end{bmatrix} = \begin{bmatrix} G_{km}^{aa} + \mathrm{j}B_{km}^{aa} & G_{km}^{ab} + \mathrm{j}B_{km}^{ab} & G_{km}^{ac} + \mathrm{j}B_{km}^{ac} \\ G_{km}^{ba} + \mathrm{j}B_{km}^{ba} & G_{km}^{bb} + \mathrm{j}B_{km}^{bb} & G_{km}^{bc} + \mathrm{j}B_{km}^{bc} \\ G_{km}^{ca} + \mathrm{j}B_{km}^{ca} & G_{km}^{cb} + \mathrm{j}B_{km}^{cb} & G_{km}^{cc} + \mathrm{j}B_{km}^{cc} \end{bmatrix} \tag{3.3}$$

Separating the real and imaginary parts of Eq. 3.1, in expanded form, leads to nodal active and reactive power expressions for phase ρ,

$$P_k{}^{\rho} = e_k^{\rho} \sum_{i=k,m} \sum_{j=a,b,c} \left(G_{ki}^{\rho j} e_i^j - B_{ki}^{\rho j} f_i^j \right) + f_k^{\rho} \sum_{i=k,m} \sum_{j=a,b,c} \left(G_{ki}^{\rho j} f_i^j + B_{ki}^{\rho j} e_i^j \right) \tag{3.4}$$

$$Q_k{}^{\rho} = f_k^{\rho} \sum_{i=k,m} \sum_{j=a,b,c} \left(G_{ki}^{\rho j} e_i^j - B_{ki}^{\rho j} f_i^j \right) - e_k^{\rho} \sum_{i=k,m} \sum_{j=a,b,c} \left(G_{ki}^{\rho j} f_i^j + B_{ki}^{\rho j} e_i^j \right) \tag{3.5}$$

where ρ is used to denote phases a, b and c. Expressions for the active and reactive power injected at node m are similar in form with subscript m replacing k and viceversa.

3.2.3 The Jacobian matrix formation

The linearised three-phase power flow expression using rectangular co-ordinates is constructed using the real and imaginary parts of the voltage to form the Jacobian matrix and the mismatch voltages vector.

$$\begin{bmatrix} \Delta P_1^a \\ \vdots \\ \Delta P_{nbus}^c \\ \Delta Q_1^a \\ \vdots \\ \Delta Q_{nbus}^c \end{bmatrix} = \begin{bmatrix} \frac{\partial P_1^a}{\partial e_1^a} & \cdots & \frac{\partial P_1^a}{\partial e_{nbus}^c} & \frac{\partial P_1^a}{\partial f_1^a} & \cdots & \frac{\partial P_1^a}{\partial f_{nbus}^c} \\ \vdots & \ddots & \vdots & \vdots & \ddots & \vdots \\ \frac{\partial P_{nbus}^c}{\partial e_1^a} & \cdots & \frac{\partial P_{nbus}^c}{\partial e_{nbus}^c} & \frac{\partial P_{nbus}^c}{\partial f_1^a} & \cdots & \frac{\partial P_{nbus}^c}{\partial f_{nbus}^c} \\ \frac{\partial Q_1^a}{\partial e_1^a} & \cdots & \frac{\partial Q_1^a}{\partial e_{nbus}^c} & \frac{\partial Q_1^a}{\partial f_1^a} & \cdots & \frac{\partial Q_1^a}{\partial f_{nbus}^c} \\ \vdots & \ddots & \vdots & \vdots & \ddots & \vdots \\ \frac{\partial Q_{nbus}^c}{\partial e_1^a} & \cdots & \frac{\partial Q_{nbus}^c}{\partial e_{nbus}^c} & \frac{\partial Q_{nbus}^c}{\partial f_1^a} & \cdots & \frac{\partial Q_{nbus}^c}{\partial f_{nbus}^c} \end{bmatrix} \begin{bmatrix} \Delta e_1^a \\ \vdots \\ \Delta e_{nbus}^1 \\ \Delta f_1^a \\ \vdots \\ \Delta f_{nbus}^c \end{bmatrix} \tag{3.6}$$

Each element of the Jacobian matrix in rectangular co-ordinates may take one of the following forms:

$$\begin{matrix} \frac{\partial P_{k,m}^{\rho 1}}{\partial e_{k,m}^{\rho 2}} & \frac{\partial P_{k,m}^{\rho 1}}{\partial f_{k,m}^{\rho 2}} \\ \frac{\partial Q_{k,m}^{\rho 1}}{\partial e_{k,m}^{\rho 2}} & \frac{\partial Q_{k,m}^{\rho 1}}{\partial f_{k,m}^{\rho 2}} \end{matrix} \tag{3.7}$$

where $\rho 1$ and $\rho 2$ refer to the a, b and c phases. Each one of the elements of Eq. 3.7 is a 3x3 matrix; with the matrix being symmetric if it represents a geometrically balanced network, otherwise it becomes an asymmetric matrix.

Consider the i^{th} transmission element connected between buses k and m in Eq. 3.6, for which self and mutual Jacobian terms are given below.

For $k \neq m$

$$\frac{\partial P_{k,i}^{\rho 1}}{\partial e_{m,i}^{\rho 2}} = \left(G_{km}^{\rho 1 \rho 2} e_k^{\rho 1} + B_{km}^{\rho 1 \rho 2} f_k^{\rho 1} \right) \tag{3.8}$$

$$\frac{\partial P_{k,i}^{\rho 1}}{\partial f_{m,i}^{\rho 2}} = \left(G_{km}^{\rho 1 \rho 2} f_k^{\rho 1} - B_{km}^{\rho 1 \rho 2} e_k^{\rho 1} \right) \tag{3.9}$$

$$\frac{\partial Q_{k,i}^{\rho 1}}{\partial e_{m,i}^{\rho 2}} = \left(G_{km}^{\rho 1 \rho 2} f_k^{\rho 1} - B_{km}^{\rho 1 \rho 2} e_k^{\rho 1} \right) \tag{3.10}$$

$$\frac{\partial Q_{k,i}^{\rho 1}}{\partial f_{m,i}^{\rho 2}} = - \left(G_{km}^{\rho 1 \rho 2} e_k^{\rho 1} + B_{km}^{\rho 1 \rho 2} f_k^{\rho 1} \right) \tag{3.11}$$

For $k = m$, with $\rho 1 = \rho 2$

$$\frac{\partial P_{k,i}^{\rho 1}}{\partial e_{k,i}^{\rho 2}} = \left(G_{kk}^{\rho 1 \rho 2} e_k^{\rho 1} + B_{kk}^{\rho 1 \rho 2} f_k^{\rho 1} \right) + \Re \left(I_k^{\rho 1} \right) \tag{3.12}$$

$$\frac{\partial P_{k,i}^{\rho 1}}{\partial f_{k,i}^{\rho 2}} = \left(G_{kk}^{\rho 1 \rho 2} f_k^{\rho 1} - B_{kk}^{\rho 1 \rho 2} e_k^{\rho 1} \right) + \Im \left(I_k^{\rho 1} \right) \tag{3.13}$$

$$\frac{\partial Q_{k,i}^{\rho 1}}{\partial e_{k,i}^{\rho 2}} = \left(G_{kk}^{\rho 1 \rho 2} f_k^{\rho 1} - B_{kk}^{\rho 1 \rho 2} e_k^{\rho 1} \right) - \Im \left(I_k^{\rho 1} \right) \tag{3.14}$$

$$\frac{\partial Q_{k,i}^{\rho 1}}{\partial f_{k,i}^{\rho 2}} = - \left(G_{kk}^{\rho 1 \rho 2} e_k^{\rho 1} + B_{kk}^{\rho 1 \rho 2} f_k^{\rho 1} \right) + \Re \left(I_k^{\rho 1} \right) \tag{3.15}$$

For $\rho 1 \neq \rho 2$

$$\frac{\partial P_{k,i}^{\rho 1}}{\partial e_{k,i}^{\rho 2}} = \left(G_{kk}^{\rho 1\rho 2} e_k^{\rho 1} + B_{kk}^{\rho 1\rho 2} f_k^{\rho 1}\right) \tag{3.16}$$

$$\frac{\partial P_{k,i}^{\rho 1}}{\partial f_{k,i}^{\rho 2}} = \left(G_{kk}^{\rho 1\rho 2} f_k^{\rho 1} - B_{kk}^{\rho 1\rho 2} e_k^{\rho 1}\right) \tag{3.17}$$

$$\frac{\partial Q_{k,i}^{\rho 1}}{\partial e_{k,i}^{\rho 2}} = \left(G_{kk}^{\rho 1\rho 2} f_k^{\rho 1} - B_{kk}^{\rho 1\rho 2} e_k^{\rho 1}\right) \tag{3.18}$$

$$\frac{\partial Q_{k,i}^{\rho 1}}{\partial f_{k,i}^{\rho 2}} = -\left(G_{kk}^{\rho 1\rho 2} e_k^{\rho 1} + B_{kk}^{\rho 1\rho 2} f_k^{\rho 1}\right) \tag{3.19}$$

where the current $I_{i,j}^{\rho 1}$ is:

$$I_{k,i}^{\rho 1} = \sum_{l=k,m} \sum_{\rho 2=a,b,c} \left[\left(G_{kl}^{\rho 1\rho 2} e_l^{\rho 2} - B_{kl}^{\rho 1\rho 2} f_l^{\rho 2}\right) + \mathrm{j}\left(B_{kl}^{\rho 1\rho 2} e_l^{\rho 2} + G_{kl}^{\rho 1\rho 2} f_l^{\rho 1}\right)\right] \tag{3.20}$$

The Jacobian matrix and mismatch vector are evaluated at each iteration. The generic power mismatch equations at bus k are:

$$\Delta P_{k,m}^{\rho} = \left(P_{k,m}^{\rho}\right)^{sp} - \left(P_{k,m}^{\rho}\right)^{cal,it} \tag{3.21}$$

$$\Delta Q_{k,m}^{\rho} = \left(Q_{k,m}^{\rho}\right)^{sp} - \left(Q_{k,m}^{\rho}\right)^{cal,it} \tag{3.22}$$

where $\left(P_{k,m}^{\rho}\right)^{sp}$ and $\left(Q_{k,m}^{\rho}\right)^{sp}$ are the specified active and reactive power injections determined by the net amount of power generation and load connected to the bus, and $\left(P_{k,m}^{\rho}\right)^{cal,it}$ and $\left(Q_{k,m}^{\rho}\right)^{cal,it}$ are the calculated active and reactive injections at the bus using the corresponding nodal voltages, $(e^{\rho} + \mathrm{j}f^{\rho})^{it}$. Normally, the nodal voltage for phase a is initialised at one and zero for real and imaginary part, respectively, while phases b and c are initialised at $-\frac{1}{2} - \mathrm{j}\frac{\sqrt{3}}{2}$ and $-\frac{1}{2} + \mathrm{j}\frac{\sqrt{3}}{2}$ respectively. At each iteration the nodal voltages are updated

according to the following expression.

$$(e^{\rho} + \mathrm{j}f^{\rho})^{it+1} = \left[\left(e_k^{\rho}\right)^{it} + \left(\Delta e_k^{\rho}\right)^{it}\right] + \mathrm{j}\left[\left(f_k^{\rho}\right)^{it} + \left(\Delta f_k^{\rho}\right)^{it}\right] \tag{3.23}$$

The process is repeated until the complex power mismatches are within a specified tolerance, e.g. $1\mathrm{e}-12$.

3.2.4 Voltage controlled bus

In the Newton-Raphson method using rectangular co-ordinates, a nodal voltage magnitude mismatch equation is needed for each PV-type bus [Stagg and El-Abiad, 1968]. The equation for a voltage-controlled bus become,

$$P_k^{\rho 1} = \sum_{m=1}^{nbus}\left[e_k^{\rho 1}\left(G_{km}^{\rho 1\rho 2}e_m^{\rho 2} - B_{km}^{\rho 1\rho 2}f_m^{\rho 2}\right) + f_m^{\rho 1}\left(G_{km}^{\rho 1\rho 2}f_m^{\rho 2} + B_{km}^{\rho 1\rho 2}e_m^{\rho 2}\right)\right] \tag{3.24}$$

$$\left(V_k^{\rho 1}\right)^2 = \left(e_k^{\rho 1}\right)^2 + \left(f_k^{\rho 1}\right)^2 \tag{3.25}$$

Accordingly, new types of Jacobian elements are needed for the Jacobian matrix in rectangular co-ordinates where:

$$\frac{\partial\left(V_{k,m}^{\rho 1}\right)^2}{\partial e_{k,m}^{\rho 2}} \tag{3.26}$$

and

$$\frac{\partial\left(V_{k,m}^{\rho 1}\right)^2}{\partial f_{k,m}^{\rho 2}} \tag{3.27}$$

For the i^{th} element connected to a PV-type bus, say k, the Jacobian elements are:

$$\frac{\partial \left(V_{k,i}^{\rho 1}\right)^2}{\partial e_{k,i}^{\rho 2}} = 2e_{k,i}^{\rho} \tag{3.28}$$

$$\frac{\partial \left(V_{k,i}^{\rho 1}\right)^2}{\partial f_{k,i}^{\rho 2}} = 2f_{k,i}^{\rho} \tag{3.29}$$

$$\frac{\partial \left(V_{k,i}^{\rho 1}\right)^2}{\partial e_{m,i}^{\rho 2}} = 0 \tag{3.30}$$

$$\frac{\partial \left(V_{k,i}^{\rho 1}\right)^2}{\partial f_{m,i}^{\rho 2}} = 0 \tag{3.31}$$

Changes in voltage magnitude for the RV-type buses at iteration it are calculated as follows:

$$\Delta \left[\left(V_k^{\rho}\right)^2\right]^i t = \left[\left(V_{k(scheduled)}^{\rho}\right)\right]^i t - \left[\left(V_k^{\rho}\right)^2\right]^i t \tag{3.32}$$

At iteration it the reactive power at each voltage controlled bus is reviewed using Eq. 3.5 to calculate reactive power and to check its limits. If the source of reactive power exceeds the limits the bus changes to a load bus with fixed reactive power, equal to the violated limit.

The process is repeated until complex power mismatches are within a specified tolerance, e.g. $1e-12$.

Fig. 3.2 depicts the flow diagram for three-phase power flows using the Newton-Raphson method in rectangular co-ordinates.

3.3 Power System Loads

Load modelling has a significant influence on power systems operation, simulation and analyses. Usually, the power system loads are modelled as constant three-phase power sink, which can be connected either in an star or delta arrangement [Chen and Dillon, 1974],

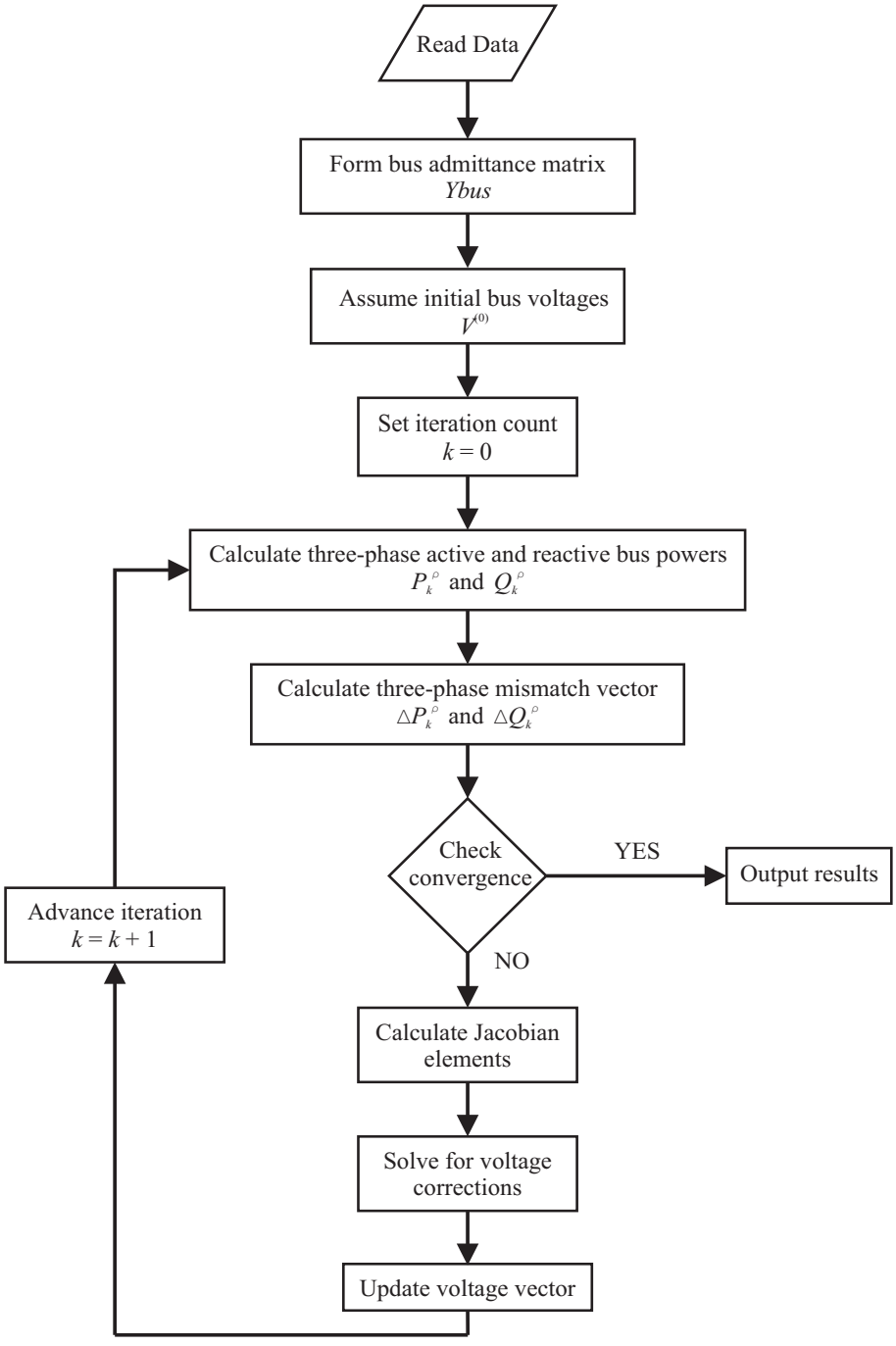

Figure 3.2: *Flow diagram for three-phase power flows using the Newton-Raphson method in rectangular co-ordinates.*

$$S_l^\rho = P_l^\rho + \mathrm{j}Q_l^\rho \tag{3.33}$$

where P_l and Q_l are the active and reactive load powers; a, b and c are phases of the load system represented by the superscript ρ.

However, this kind of model is inadequate for some power system studies such as dynamic and voltage collapse studies.

Temporary the unbalance between the power generation and the power demand reduce systems security margins and increase the risks unsafe operation. In order to reduce such risks, system studies have to be carried out with more realistic models for all systems components, including load models.

A very substantial part of the system load actually consists of induction motors. Hence, if data is available induction motor modelling must be considered and carry out.

For power system analyses, the load is refer as the active and reactive power delivered to specific buses of the network at subtransmission and distribution level.

In spite of the fact, that it very simple to model certain types of loads, usually it is very difficult to find the exact composition of the load. In common practice, the load is modelled as (a) constant power, (b) constant current and (c) constant impedance, and sometimes it is modelled as a combination of (a), (b) and (c).

Normally the load power varies with respect to the voltage and frequency. The effect of voltage angle on reactive load power is zero whilst its effect on the active load power is of a transient nature which persists for less than a second [IEEE Working Group on Power Plant Response to Load Changes, 1973].

The mathematical load model that includes the effect of the voltage magnitude may be approximated by

$$S = P_0 \left(\frac{|V|}{|V_0|}\right)^n + \mathrm{j}Q_0 \left(\frac{|V|}{|V_0|}\right)^m \tag{3.34}$$

where

P_0 is the active power at initial voltage.

Q_0 is the reactive power at initial voltage.

V_0 is initial voltage.

n and m are the rational coefficients representing the degree of dependency of active and reactive power with voltage magnitude.

In Chapter 5, a more detailed description for the power loads is presented.

3.4 Numerical Evaluation of a Multiphase Power Network

The three-phase power flow algorithm using the Newton-Raphson method in rectangular co-ordinates is used to solve a simple three-phase network, the nine-bus system shown at Fig. 3.3 [Anderson and Fouad, 1997].

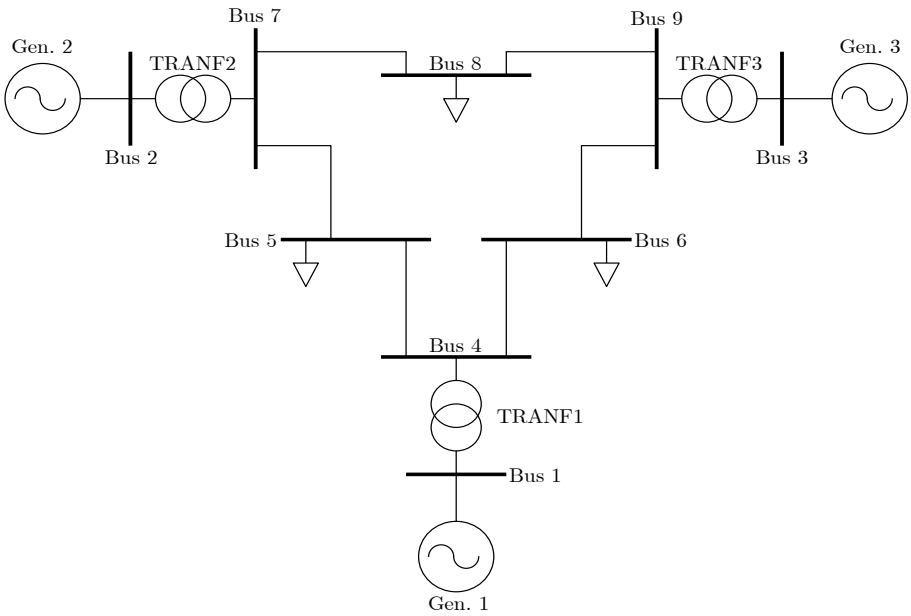

Figure 3.3: *One-line schematic representation of the* 3 *generators* 9 *buses power system.*

The three-phase loads are represented by their static load model.

The unbalanced complex three-phase powers in per unit, connected at buses 5, 6 and 8 are shown in Table 3.4.

Table 3.1: *Unbalanced complex power loads.*

	Phase a	Phase b	Phase c
S_5	$1.25 + \text{j}0.50$	$1.10 + \text{j}0.25$	$1.40 + \text{j}0.70$
S_6	$0.75 + \text{j}0.45$	$0.90 + \text{j}0.30$	$1.10 + \text{j}0.15$
S_8	$1.00 + \text{j}0.35$	$0.90 + \text{j}0.50$	$1.15 + \text{j}0.15$

In this study the generator Bus 1 is taken as the compensator Bus (or slack Bus), its specified voltage magnitude is 1.04 pu; generators Buses 2 and 3 located at Buses 2 and 3, respectively, are nominated as voltage controlled buses (PV Buses) and their nodal voltage magnitudes are both maintained at 1.0253 pu. Fig. 3.4 depicts the bus voltage profile for unbalanced power loads conditions. It is observed in Fig. 3.4, that the lowest voltage magnitude is at phase c of Bus 5, being 0.996 pu, and the highest voltage magnitude is for phase b of Bus 4 being 1.0481 pu. It is clearly observed the unbalanced voltage response of the system due to the unbalanced loading condition.

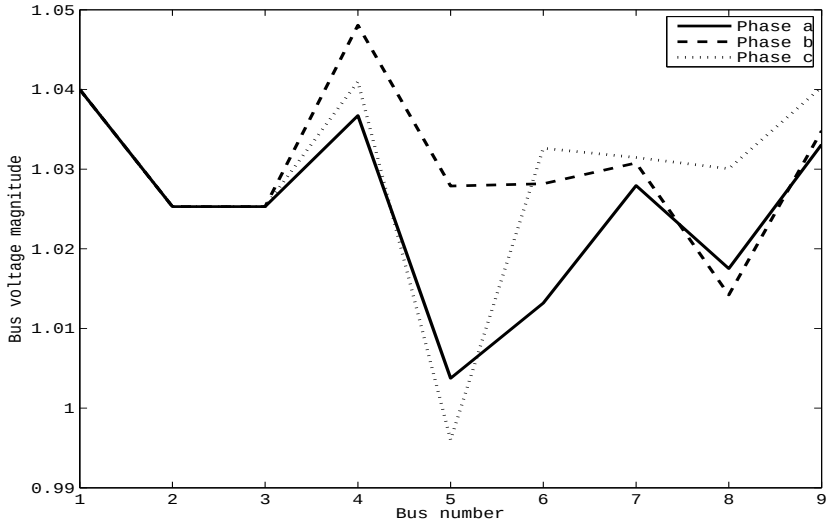

Figure 3.4: *Bus voltage magnitude for unbalanced loading conditions.*

In this study, by virtue of the strong convergence characteristics of the Newton-Raphson method, the solutions were achieved in 6 iterations to a power mismatch tolerance of $1e-12$.

3.5 HVDC Transmission Systems

Over many years, interest in HVDC technology for bulk power transmission, and other more specialised applications, has remained strong. Further to the traditional HVDC technology, termed line commutated current (LCC), based on the use of conventional thyristors; two other lines of development in HVDC technology have appeared, capacitor commutated converters (CCC), which is an upgrading of the traditional technology, and voltage source converters (VSC) with insulated gate bipolar transistor (IGBT) and pulse width modulation (PWM) control. In each of these applications, manufacturers have taken maximum benefits from the accelerated pace of power electronics technology. It is believed that in a few years time, HVDC-VSC-based systems, will take over a large portion of the traditional HVDC market. However, at present, bulk power DC transmission remains the realm of thyristor-based HVDC technology [Carlsson, 2002].

The HVDC-LCC converter technology of today dates back to the mid 1970s, when thyristor valves were taking over the mercury arc valves; but dramatics developments have taken place in the reliability and in the performance of HVDC equipment and systems. An HVDC link can be configured in many ways. In order of increasing complexity, the simplest is the back-to-back interconnection in which the two converters are located in the same site and there is no transmission line. The two units are identical and each can be used on the rectification or inversion modes, as ordered by the system control. In the monopolar link, the two converter stations are joined by a single conductor line, and earth or the sea is used as the returning conductor, requiring two electrodes capable of carrying the full current. Next, the bipolar link which consists of two monopolar systems combined, one at positive and the other at negative polarity with respect to ground (middle). Each monopolar side can operate on its

own with ground return, but if the two poles have equal currents, they cancel out each other's ground current to practically zero. In such cases, the ground path is used for limited periods in emergency, when one pole is temporarily out of service. Other more complex configurations are possible such as multiterminal links and series connections. The central components of any HVDC-LCC converter are the thyristor valves, used to perform the conversion from AC to DC and vice versa. The thyristor valves are made of highly pure monocrystalline silicon. The high performance thyristors installed in HVDC plants today are characterized by silicon wafer diameters of up to 125 mm, blocking voltages up to 8kV and current carrying capacities of up to 4kA DC [Siemens AG Power Transmission and Distribution High Voltage Division, 2007].

The converter stations are connected to the AC busbars by means of converter transformer, which scale-down the voltage of the grid to the required entry voltage of the converter. The converter transformer is equipped with an on-load tap changer.

A large inductance (smoothing reactor) is installed on the DC side current to prevent resonance in the DC circuit, to reduce the ripple in the direct current and to limit telephone interference. In addition, a DC filter is needed to reduce the level of harmonic currents in the DC overhead line.

On the AC side, harmonics current are prevented from entering the AC network by using AC filters, i.e. resonant circuits comprising capacitors, reactors and resistors. The reactive power consumption of an HVDC converter is a function of active power, transformer reactances and control angle. It increases with increasing active power. Full reactive power compensation is a standard requirement in a converter station; with part of the reactive power produced by filters and the rest by shunt capacitor banks or synchronous condensers when dynamic compensating is deemed necessary [Siemens AG Power Transmission and Distribution High Voltage Division, 2007].

3.5.1 Converter steady state modelling

The monopolar HVDC transmission system scheme, shown in Fig. 3.5, is used to explain the model developed and its inclusion in a three-phase power flow using the full Newton-Raphson method. The approach can easily be expanded to include some of the most common HVDC configurations, such as bipolar HVDC systems.

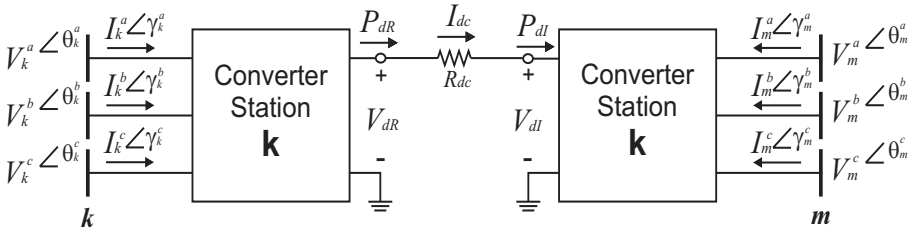

Figure 3.5: *Monopolar HVDC system.*

In the monopolar HVDC link, two converter stations are joined together by a line conductor, and the earth (sea) is used as the return path, requiring two electrodes capable of carrying the full current. In addition to the six pulse bridge, each converter station comprises a three-phase tap changing transformer (LTC), as illustrated in Fig. 3.6, where A_k is the LTC's tap ratio.

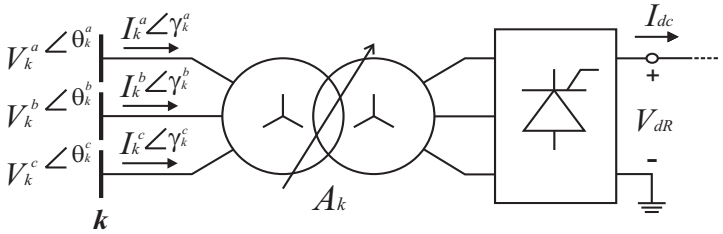

Figure 3.6: *HVDC-LCC monopolar converter station.*

Practical systems rarely have perfectly balanced loads, currents, voltages or impedances in all three phases. In the unbalanced case, to analyse the HVDC-LCC converters, the unbalanced three-phase voltages of the terminal buses are considered, Fig. 3.7.

To control the firing or extinction angles in a real system, where the voltages are not

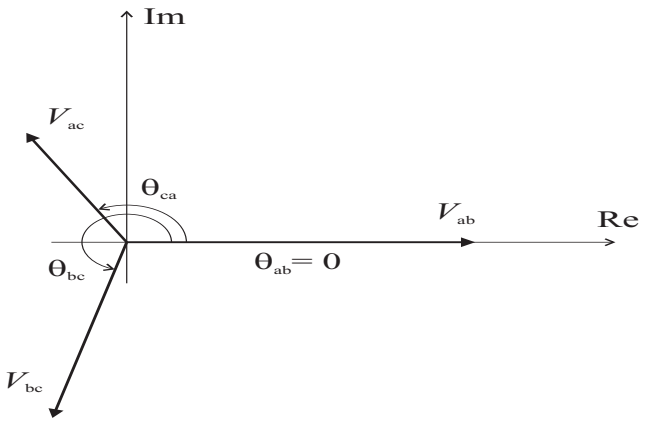

Figure 3.7: *Asymmetric three-phase voltages.*

symmetrical, there are two basically different control methods:

- Individual phase control,
- Equidistant firing control.

The first approach is used in the early HVDC-LCC converters. The firing instants are determined individually for each valve, so a constant delay (or extinction) angle is maintained for all the valves in steady state with respect to the voltage crossing.

Operating difficulties encountered in this method indicated that the distorted converter current cause AC-voltage distortion which can influence the firing pulse spacing and often reinforce the original distortion [Harker and Arrillaga, 1979, Arrillaga and Callaghan, 1991].

In theory, this situation can be improved by placing control filters between the AC system and the control system, so as to attenuate the harmonics. However, the use of control filters has disadvantages too, like the filter's inherent phase error, which varies with system frequency, and its inability to attenuate negative sequence fundamental voltages, the effect of which is precisely to cause irregular firing-pulse spacing. Moreover, with filters included, the control system will ignore the presence of harmonics on the AC voltages, whereas the

valves will respond to the actual voltages reaching them, including harmonics [Rashid and Maswood, 1988, Harker and Arrillaga, 1979, Arrillaga and Callaghan, 1991, Ainsworth, 1988].

The difficulties encountered with the individual phase control system encouraged the development of an alternative control philosophy which could get away from the voltage waveform dependence, the equidistant firing control system.

The basis of this control system for the rectifier is to find the voltage crossing for the first phase and to define when it produces a short pulse to turn on the valve, adding the firing control α. Then, the complete set of six pulses normally occurs at successive intervals of 60°, as shown in Fig. 3.8. Similarly the pulses for inverter operation of the converter are obtained [Ainsworth, 1988, Arrillaga, 1998].

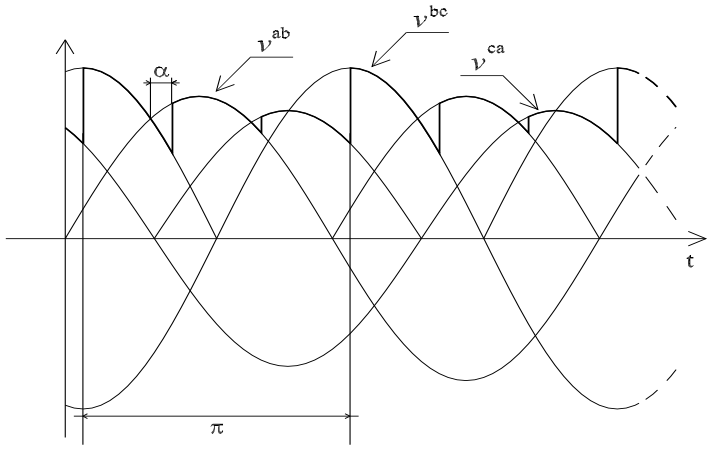

Figure 3.8: *Unbalanced converter voltage waveform.*

3.5.2 Three-Phase Power Equations

To derive the power flow Newton-Rapshon model, the three-phase power consumed by the converters is written as a function of AC voltages and DC variables.

$$P_k^{\rho} = f\left(V_k^{a,b,c}, \theta_k^{a,b,c}, X\right) \tag{3.35}$$

$$P_m^{\rho} = f\left(V_m^{a,b,c}, \theta_m^{a,b,c}, X\right) \tag{3.36}$$

where P_k and P_m are active powers at buses k and m, respectively; V_k and θ_k and V_m and θ_m are the voltage magnitudes and phase angles, respectively, at the sending and receiving buses k and m; ρ denotes the a, b, and c phases of the system. X represents, in generic form at this stage, the DC variables.

The reactive powers are,

$$Q_k^{\rho} = \sqrt{(S_k^{\rho})^2 - (P_k^{\rho})^2} = \sqrt{\frac{\left(k_1 A_k V_k^{\rho} I_{dc}\right)^2}{3} - (P_k^{\rho})^2} \tag{3.37}$$

$$Q_m^{\rho} = \sqrt{(S_m^{\rho})^2 - (P_m^{\rho})^2} = \sqrt{\frac{\left(k_1 A_m V_m^{\rho} I_{dc}\right)^2}{3} - (P_m^{\rho})^2} \tag{3.38}$$

where S_k, S_m and Q_k, Q_m are the complex and reactive powers at buses k and m respectively; k_1 is a constant associated with the commutation overlap, A_k and A_m are the tap changers positions at buses k and m, respectively; and I_{dc} is the current in the dc-link. The full derivation is given in Appendix A.

3.5.3 Linearised power equations

A three-phase power network with n-buses is described by $6 \times (n-1)$ non linear equations. The inclusion of one HVDC link in the network model augments the number of equations by six. The solution of the combined system of non-linear equations is carried out by iteration using the full Newton-Raphson method.

The power through the dc-link can be controlled by varying the DC-voltages as indicated

by the following two basic relations:

$$P_{dR} = V_{dR} I_{dc} \tag{3.39}$$

$$P_{dI} = V_{dI} I_{dc} \tag{3.40}$$

where P_{dR} and P_{dI} are the DC powers at the inverter and rectifier ends, respectively; and V_{dR} and V_{dI} are the DC voltages, at the rectifier and inverter, respectively.

The DC-voltages can be controlled either with the transformers tap ratios or with the converters control angles. At the rectifier, the control angle is the firing angle α; and at the inverter, the control angle is the extinction angle, γ. An increase in the control angle gives a decrease in DC-voltage, an increase in reactive power consumption (since the current will lag the voltage) and an increase in harmonics generation. The latter is clearly undesirable and there is thus some benefit in keeping the control angles at low values [Arrillaga, 1998].

There are several modes of operation in converter control. The first one, when the firing angle α, the extinction angle γ, V_{dI} and P_{dI} are specified, is called control mode A. The converter transformer taps are varied in order to meet these specifications. In control mode B, the extinction angle γ, is kept at its lower limit at the inverter and the transformer taps and the power P_{dI} are specified. The power is controlled by varying the firing angle α at the rectifier. The firing angle rather than the tap transformer is preferred for control, since the tap changer control is too slow compared to the firing angle. In control mode C, α is fixed to its minimum value and γ is regulated to maintain constant power.

If the current I_{dc} is kept constant instead of the power P_{dI}, three other control modes are defined. In this paper only the mode A, B and C with constant power are addressed.

The Jacobian used in conventional power flows is suitably extended to take account of the new elements contributed by the HVDC link. The set of linearised power flow equations for the complete system is,

$$\begin{bmatrix} \Delta P \\ \Delta Q \\ -- \\ \Delta P_{dR} \\ \Delta P_{dI} \end{bmatrix} = \begin{bmatrix} \mathbf{J_{11}} & | & \mathbf{J_{12}} \\ -- & + & -- \\ \mathbf{J_{21}} & | & \mathbf{J_{22}} \end{bmatrix} \begin{bmatrix} \Delta\theta \\ \frac{\Delta V}{V} \\ -- \\ \Delta X_1 \\ \Delta X_2 \end{bmatrix} \tag{3.41}$$

where

$\Delta P = [\Delta P_1^\rho, \cdots, \Delta P_n^\rho]^t$

$\Delta Q = [\Delta Q_1^\rho, \cdots, \Delta Q_n^\rho]^t$

$\Delta\theta = [\Delta\theta_1^\rho, \cdots, \Delta\theta_n^\rho]^t$

$\frac{\Delta V}{V} = \left[\frac{\Delta V_1^\rho}{V_1^\rho}, \cdots, \frac{\Delta V_n^\rho}{V_n^\rho}\right]^t$

ΔP and ΔQ are the normal power mismatch equations, and $\Delta\theta$ and $\frac{\Delta V}{V}$ are voltage increments of phase angle and magnitude, respectively.

There are two additional state variables X_1 and X_2, (i.e. $X_{1,2}$), and two power mismatch equations introduced by the HVDC link,

$$\Delta P_{dR} = P_{dR}^{sch} - P_{dR}^{cal} \tag{3.42}$$

$$\Delta P_{dI} = P_{dI}^{sch} - P_{dI}^{cal} \tag{3.43}$$

P^{sch} and P^{cal} are the scheduled and calculated powers for the HVDC link.

The power mismatches for buses k and m, where the HVDC link is connected to become:

$$\Delta P_k = P_{Gk} - P_{Lk} - P_{Nk}(\theta, V) - P_{dR}(V_k, V_m, X_{1,2}) \tag{3.44}$$

$$\Delta P_m = P_{Gm} - P_{Lm} - P_{Nm}(\theta, V) - P_{dI}(V_k, V_m, X_{1,2}) \tag{3.45}$$

$$\Delta Q_k = Q_{Gk} - Q_{Lk} - Q_{Nk}(\theta, V) - Q_{dR}(V_k, V_m, X_{1,2}) \tag{3.46}$$

$$\Delta Q_m = Q_{Gm} - Q_{Lm} - Q_{Nm}(\theta, V) - Q_{dI}(V_k, V_m, X_{1,2}) \tag{3.47}$$

where P_{Gk}, Q_{Gk} and P_{Gm} and Q_{Gm} represent the active and reactive powers injected by the generator at buses k and m, respectively; P_{Lk}, Q_{Lk} and P_{Lm} and Q_{Lm} represent the active and reactive powers drawn by the load at buses k and m, respectively;

The $\mathbf{J_{11}}$ matrix corresponding to the AC network at buses k and m

$$\begin{bmatrix} \frac{\partial P_k^\rho}{\partial \theta_k^\rho} & \frac{\partial P_k^\rho}{\partial V_k^\rho} V_k^\rho & \frac{\partial P_k^\rho}{\partial \theta_m^\rho} & \frac{\partial P_k^\rho}{\partial V_m^\rho} V_m^\rho \\ \frac{\partial Q_k^\rho}{\partial \theta_k^\rho} & \frac{\partial Q_k^\rho}{\partial V_k^\rho} V_k^\rho & \frac{\partial Q_k^\rho}{\partial \theta_m^\rho} & \frac{\partial Q_k^\rho}{\partial V_m^\rho} V_m^\rho \\ \frac{\partial P_m^\rho}{\partial \theta_k^\rho} & \frac{\partial P_m^\rho}{\partial V_k^\rho} V_k^\rho & \frac{\partial P_m^\rho}{\partial \theta_m^\rho} & \frac{\partial P_m^\rho}{\partial V_m^\rho} V_m^\rho \\ \frac{\partial Q_m^\rho}{\partial \theta_k^\rho} & \frac{\partial Q_m^\rho}{\partial V_k^\rho} V_k^\rho & \frac{\partial Q_m^\rho}{\partial \theta_m^\rho} & \frac{\partial Q_m^\rho}{\partial V_m^\rho} V_m^\rho \end{bmatrix} \tag{3.48}$$

is augmented with the partial derivatives of the active and reactive powers contributions by the HVDC link.

Matrix $\mathbf{J_{12}}$ includes the partial derivatives of the three-phase powers $P_{k,m}^\rho$ and $Q_{m,n}^\rho$ with respect to the HVDC link state variables and $\mathbf{J_{21}}$ represents the partial derivatives of P_{dR} and P_{dI} with respect to the three-phase voltage angles and magnitudes $\theta_{k,m}^\rho$ and $V_{k,m}^\rho$. Moreover, $\mathbf{J_{22}}$ represents the self partial derivatives of the HVDC link.

3.5.4 Control mode A

In control mode A, the variables α, γ, V_{dI} and P_{dI} are specified, making it possible to calculate the current I_{dc}, the voltage V_{dI} and the power P_{dR}:

$$I_{dc} = \frac{P_{dI}}{V_{dI}} \tag{3.49}$$

$$V_{dR} = V_{dI} + R_{DC} I_{dc} \tag{3.50}$$

$$P_{dR} = V_{dR} I_{dc} \tag{3.51}$$

The new state variables for this control mode are the tap changers, A_k and A_m, with the Jacobian elements $\mathbf{J_{12}}$, $\mathbf{J_{21}}$ and $\mathbf{J_{22}}$ having the following structure:

$$\mathbf{J_{12}} = \begin{bmatrix} \frac{\partial P_k^\rho}{\partial A_k} & \frac{\partial P_k^\rho}{\partial A_m} \\ \frac{\partial Q_k^\rho}{\partial A_k} & \frac{\partial Q_k^\rho}{\partial A_m} \\ \frac{\partial P_m^\rho}{\partial A_k} & \frac{\partial P_m^\rho}{\partial A_m} \\ \frac{\partial Q_m^\rho}{\partial A_k} & \frac{\partial Q_m^\rho}{\partial A_m} \end{bmatrix} \tag{3.52}$$

$$\mathbf{J_{21}} = \begin{bmatrix} \frac{\partial P_{dR}}{\partial \theta_k^\rho} & \frac{\partial P_{dR}}{\partial V_k^\rho} V_k^\rho & \frac{\partial P_{dR}}{\partial \theta_m^\rho} & \frac{\partial P_{dR}}{\partial \theta_m^\rho} V_m^\rho \\ \frac{\partial P_{dI}}{\partial \theta_k^\rho} & \frac{\partial P_{dI}}{\partial V_k^\rho} V_k^\rho & \frac{\partial P_{dI}}{\partial \theta_m^\rho} & \frac{\partial P_{dI}}{\partial \theta_m^\rho} V_m^\rho \end{bmatrix} \tag{3.53}$$

$$\mathbf{J_{22}} = \begin{bmatrix} \frac{\partial P_{dR}}{\partial A_k} & \frac{\partial P_{dR}}{\partial A_m} \\ \frac{\partial P_{dI}}{\partial A_k} & \frac{\partial P_{dI}}{\partial A_m} \end{bmatrix} \tag{3.54}$$

It should be noted that a single tap changer is used to regulate voltage magnitude at all three phases.

3.5.5 Control mode B

In control mode B, the variables a_k, a_m, γ and P_{dI} are specified and the new state variables are the current I_{dc} and the firing angle α. For this control mode, $\mathbf{J_{21}}$ has the same structure as in control mode A. The other two terms of the Jacobian are:

$$\mathbf{J_{12}} = \begin{bmatrix} \frac{\partial P_k^\rho}{\partial \alpha} & \frac{\partial P_k^\rho}{\partial I_{dc}} \\ \frac{\partial Q_k^\rho}{\partial \alpha} & \frac{\partial Q_k^\rho}{\partial I_{dc}} \\ \frac{\partial P_m^\rho}{\partial \alpha} & \frac{\partial P_m^\rho}{\partial I_{dc}} \\ \frac{\partial Q_m^\rho}{\partial \alpha} & \frac{\partial Q_m^\rho}{\partial I_{dc}} \end{bmatrix} \tag{3.55}$$

$$\mathbf{J_{22}} = \begin{bmatrix} \frac{\partial P_{dR}}{\partial \alpha} & \frac{\partial P_{dR}}{\partial I_{dc}} \\ \frac{\partial P_{dI}}{\partial \alpha} & \frac{\partial P_{dI}}{\partial I_{dc}} \end{bmatrix} \tag{3.56}$$

3.5.6 Control mode C

In control mode C, the variables a_k, a_m, α and P_{dI} are specified and the new state variables are the current I_{dc} and the extinction angle γ. Matrix $\mathbf{J_{21}}$ has the same structure as in the previous control modes, whereas matrices $\mathbf{J_{12}}$ and $\mathbf{J_{22}}$ take the following structure,

$$\mathbf{J_{12}} = \begin{bmatrix} \frac{\partial P_k^\rho}{\partial I_{dc}} & \frac{\partial P_k^\rho}{\partial \gamma} \\ \frac{\partial Q_k^\rho}{\partial I_{dc}} & \frac{\partial Q_k^\rho}{\partial \gamma} \\ \frac{\partial P_m^\rho}{\partial I_{dc}} & \frac{\partial P_m^\rho}{\partial \gamma} \\ \frac{\partial Q_m^\rho}{\partial I_{dc}} & \frac{\partial Q_m^\rho}{\partial \gamma} \end{bmatrix} \tag{3.57}$$

$$\mathbf{J_{22}} = \begin{bmatrix} \frac{\partial P_{dR}}{\partial I_{dc}} & \frac{\partial P_{dR}}{\partial \gamma} \\ \frac{\partial P_{dI}}{\partial I_{dc}} & \frac{\partial P_{dI}}{\partial \gamma} \end{bmatrix} \tag{3.58}$$

It is important to remark that this is a three-phase formulation, and that all elements in the above equations are vectors of order 3×1, except for $\mathbf{J_{11}}$ which are vectors of order 3×3 and $\mathbf{J_{22}}$ which are single terms.

3.6 HVDC-LCC Numerical Evaluation

3.6.1 Test Case 1

To show the applicability of the proposed approach, the five-bus network depicted in Fig. 3.9 is used. All necessary data to carry out a balanced three-phase AC power flow is taken from [Acha et al., 2004].

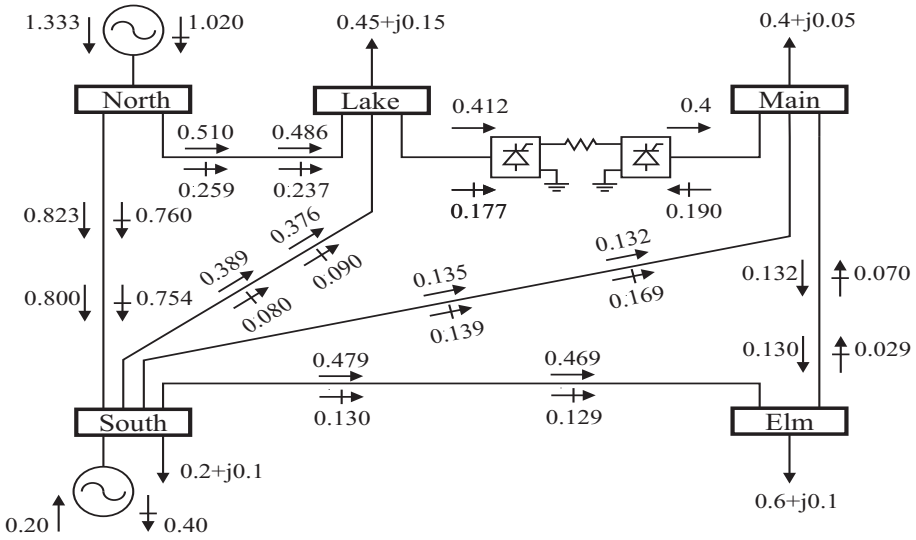

Figure 3.9: *Five-bus test network for three-phase balanced conditions.*

The five-bus network is modified to include one HVDC link connected between Lake and Main buses. In this contrived example, the AC network and HVDC converters are assumed to work under three-phase balanced conditions. The HVDC link is made to operate in control mode A.

The data used for the HVDC link is given at Table 3.2 and the three-phase nodal voltage magnitudes and phase angles are given in Table 3.3. Notice that voltage values are given in per unit and angles are given in degrees.

Table 3.4 shows the generated powers in the North and South buses, and the powers in both the rectifier and the inverter, which are connected to Lake and Main, respectively. All

Table 3.2: *Data for the HVDC link.*

Transformer reactances	0.051 pu
D.C. link resistance	0.10 pu
Firing angle for the rectifier	15 deg
Extinction angle for the inverter	18 deg
Transmitted power	0.4 pu per phase

Table 3.3: *Bus voltages and generation results.*

Bus name	Phase A		Phase B		Phase C	
	Voltage	Angle	Voltage	Angle	Voltage	Angle
North	1.060	0	1.060	-120	1.060	120
South	1.000	-1.8126	1.000	-121.8126	1.000	118.1874
Lake	0.9610	-5.5998	0.9610	-125.5998	0.9610	114.4002
Main	0.9634	-2.6911	0.9634	-122.6911	0.9634	117.3089
Elm	0.9648	-4.8845	0.9648	-124.8845	0.9648	115.1155

other active and reactive power flows are shown in Fig. 3.9, for phase A only.

Table 3.4: *Powers from generator buses and HVDC converters.*

	HVDC converter				Generator buses			
	Main		Lake		North		South	
	P	Q	P	Q	P	Q	P	Q
Phase A	0.40	0.1902	0.412	0.1772	1.333	1.02	0.20	-0.4053
Phase B	0.40	0.1902	0.412	0.1772	1.333	1.02	0.20	-0.4053
Phase C	0.40	0.1902	0.412	0.1772	1.333	1.02	0.20	-0.4053

3.6.2 Test Case 2

To show the wider applicability of this technique, the test system [Chow, 1982], which consists of 68 nodes, 16 generators and 86 transmission lines, is used.

The system has been modified to include three HVDC links, each operating with a different

operational control mode, as shown in Fig. 3.10 and described in Table 3.5.

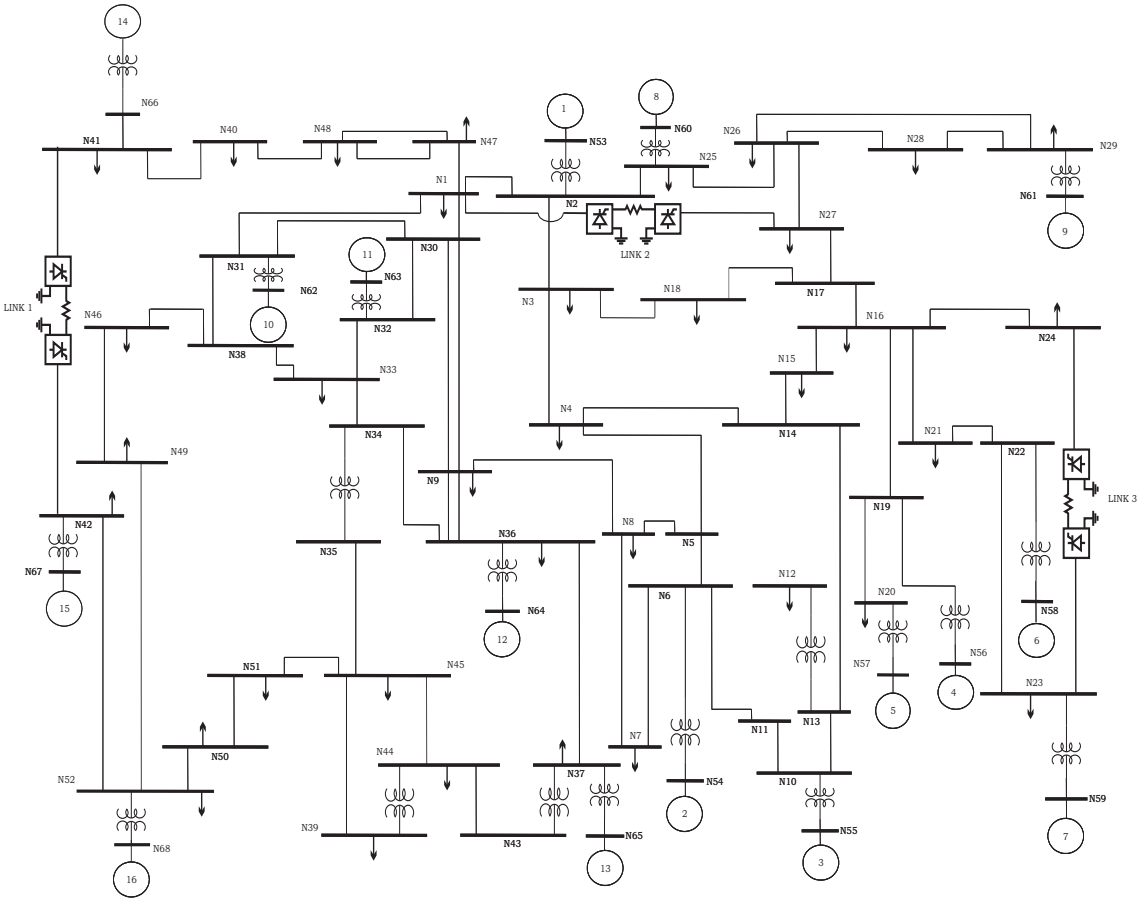

Figure 3.10: *Modified* 16 *generators power network.*

Table 3.5: *HVDC link control modes.*

Bus code	from	to	Control mode
Link 1	bus 41	bus 42	C
Link 2	bus 1	bus 27	A
Link 3	bus 23	bus 24	B

Imbalances are introduced into the network by changing the active and reactive power loads at the buses where the HVDC stations connect, by ±10% with respect to the balanced

case. Phase A is subtracted 10%, Phase B is added 10% and Phase C is kept unchanged.

Tables 3.6, 3.7 and 3.8 show the unbalanced three-phase voltage profiles and the active and reactive powers for each HVDC converter. The solution was achieved in 6 iterations to a power mismatch tolerance of $1e^{-12}$.

Table 3.6: *Parameters of Link* 1.

	Sending Node			Receiving Node		
	A	B	C	A	B	C
$\|V\|$	0.9941	0.9942	0.9941	0.9973	0.9976	0.9966
θ	47.1452	-71.7897	167.0982	18.8528	-102.6938	136.3634
P	0.4428	0.4401	0.4430	0.3940	0.4012	0.4048
Q	0.3255	0.3292	0.3253	0.3857	0.3784	0.3737

Table 3.7: *Parameters of Link* 2.

	Sending Node			Receiving Node		
	A	B	C	A	B	C
$\|V\|$	0.9992	1.0015	1.0024	0.9845	1.0014	0.9899
θ	-5.6705	-125.4563	114.6696	-6.6707	-124.6575	116.1454
P	0.3561	0.3566	0.3567	0.3342	0.3361	0.3297
Q	0.2196	0.2205	0.2211	0.2234	0.2329	0.2338

Table 3.8: *Parameters of Link* 3.

	Sending Node			Receiving Node		
	A	B	C	A	B	C
$\|V\|$	1.0113	1.0142	1.0142	0.9696	0.9822	0.9749
θ	9.0899	-109.0112	131.4502	-6.1403	-124.4343	116.5493
P	0.6372	0.6295	0.6270	0.5354	0.5374	0.5272
Q	0.6252	0.6366	0.6391	0.5692	0.5812	0.5826

The three HVDC links are set to operate with different control schemes and the state variables are A_k and A_m (control mode A) for link 1; α and I_{dc} (control mode B) for link 2;

and γ and I_{dc} (control mode C) for link 3.

Figures 3.11, 3.12 and 3.13 show the behaviour towards the convergence for each state variable during the power flow solution.

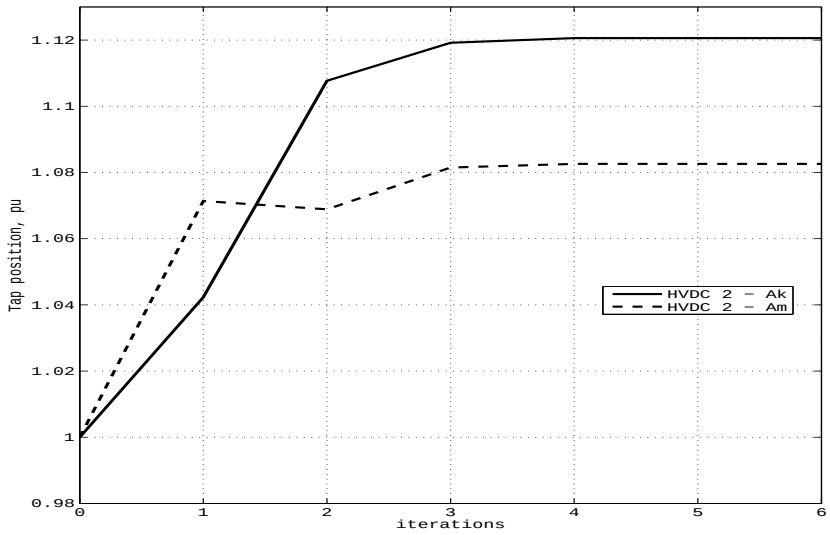

Figure 3.11: *Tap position of link* 2*, Control Mode A.*

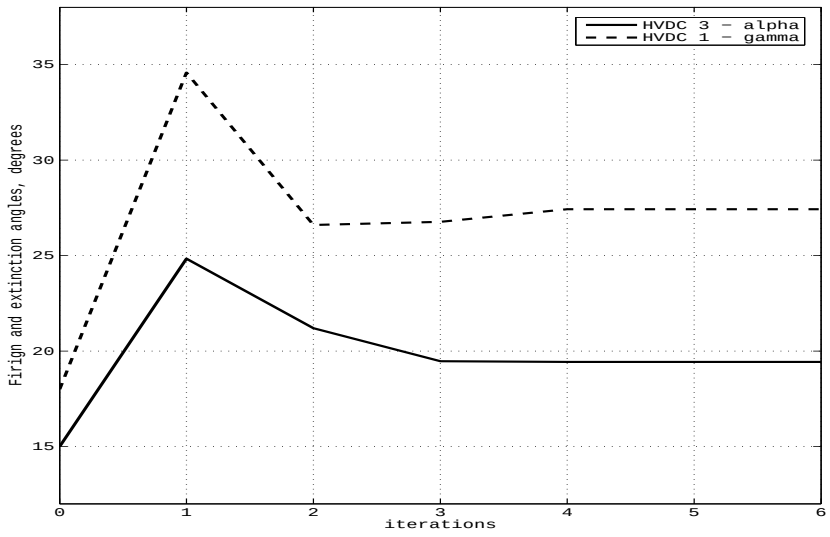

Figure 3.12: *Firing and extinction angles of links 3 and 1, Control Mode B and C, respectively.*

It should be noticed that the state variables A_k, A_m and I_{dc} have initial values of 1 per

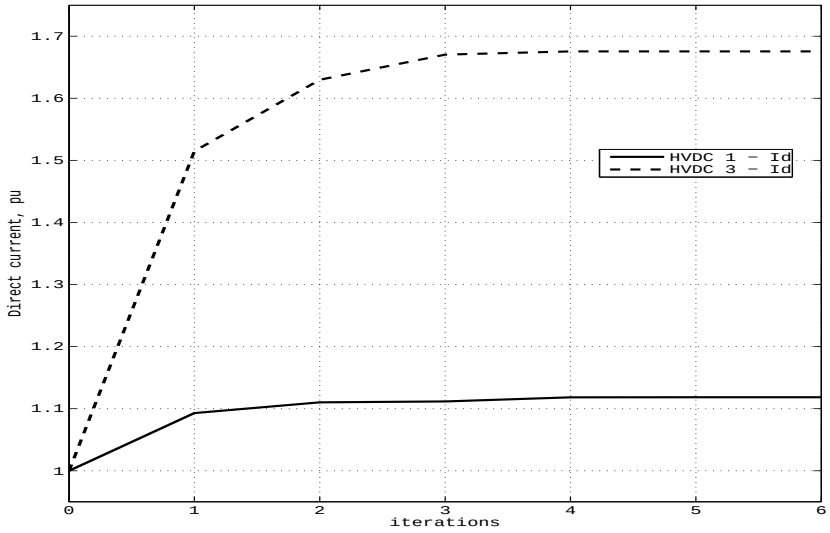

Figure 3.13: *Direct current of links 1 and 3, Control Mode B and C, respectively.*

unit, and upon convergence, settle to final values. For the remaining state variables, α and γ, are given values of 15° and 18° degrees, respectively, which are typical specified control angles [Smed, 1989, Arrillaga and Arnold, 1990].

3.7 Summary

This chapter presents the theory and modelling to carry out three-phase power flows analyses in rectangular co-ordinates making use of the Newton-Raphson method.

The problem formulation, the Jacobian formation and its power equations, in three-phase rectangular co-ordinates making use of the Newton-Raphson method is mentioned.

The adopted technique posses the quadratic convergence capability given by the Newton-Raphson method. Despite of the number of equations to solve the load flow problem in rectangular co-ordinates are increased in comparison with the polar algorithm, the problem can be alleviated using sparsity techniques.

Moreover, this chapter presents a three-phase power flow method to include conventional HVDC link models where several control modes are applied. The approach takes advantage of the strong convergence characteristics of the Newton-Raphson technique to ensure reliable iterative solutions. A test case is presented for a large network including unbalanced loading and three HVDC links; each operating with its own control mode.

Chapter 4

Dynamic Power Flows in Rectangular Co-ordinates

4.1 Introduction

Power flows in a power network can be assessed very affectively by modelling the power system as a set of non-linear algebraic equations corresponding to active and reactive nodal injections, valid for a pre-defined set of system generation and load.

For dynamic power system assessments, the mathematical model which described the dynamic plant components such as generators and their controls are represented by a set of differential equations.

By suitable combination of both sets of equations the complete power system model, aimed to at time response calculations of large-scale power networks, can be reduced to an algebraic-differential problem of the form,

$$\dot{y} = F(y, x) \tag{4.1}$$

$$0 = G(x,\, y) \tag{4.2}$$

where y and x are vectors of integrable and non-integrable algebraic variables. Generally, F and G are non-linear vector functions and thus the non-integrable network variables cannot be eliminated algebraically. Equations 4.1 and 4.2 must be solved simultaneously as a function of time [Gear, 1971b, Stott, 1979, Hill and Mareels, 1990].

The objective of the unified framework is to solve y and x as a function of time. Equations 4.1, comprises the differential equations of all synchronous generators, since each generator is coupled to the power plants only through the network, Eq. 4.1 is a collection of separate subsets. Equations 4.2, consists of network equations and the stator equations of each machine, transformed into the network reference frame. This set of equations is independent so then the solution technique must provide a simultaneous solution.

The **Jacobian** matrix, Eq. 4.3, takes into account the network elements and generators variables, whereupon the **Jacobian** from conventional power flows must be modified to include the appropriate elements of the other components.

$$\begin{bmatrix} \Delta P \\ \Delta Q \\ -- \\ \Delta F(\dot{y}) \end{bmatrix} = \begin{bmatrix} & & | & \frac{\partial P}{\partial e} & \frac{\partial P}{\partial f} \\ & \textbf{Jacobian} & | & \frac{\partial Q}{\partial e} & \frac{\partial Q}{\partial f} \\ -- & & + & -- & -- \\ \frac{\partial F(\dot{y})}{\partial e} & \frac{\partial F(\dot{y})}{\partial f} & | & \frac{\partial F(\dot{y})}{\partial y} & \frac{\partial F(\dot{y})}{\partial y} \end{bmatrix} \begin{bmatrix} \Delta e \\ \Delta f \\ -- \\ \Delta y \end{bmatrix} \tag{4.3}$$

The important feature of the task in hand being the solution of a dynamic stability analysis in combination with numerical techniques to get a simultaneous solution of coupled differential and algebraic equations.

4.2 Synchronous Machine Model - Classical Representation

Synchronous generators are the most important and principal sources of electric energy at any power system. The power system stability problem is mainly related keeping to interconnected synchronous machines in synchronism. However, power system dynamic problems are basically those of the synchronous machines. There are many kinds of power system dynamics problems, like high or low frequency oscillations, large or small system disturbances, and so on. Owing to the wide range of dynamic phenomena, several synchronous machine models have been put forward in the open literature.

The mechanical equations of synchronous machines are well established [Weedy, 1967, Elgerd, 1971, Stevenson Jr, 1982, Chapman, 1991], so they are only briefly outlined. Three basic assumptions are made in deriving the equations:

1. Machine rotor speed does not vary greatly from synchronous speed.
2. Machine rotational losses due to windage and friction are neglected.
3. Mechanical power shaft is smooth; it means the power which comes from the shaft is constant except for the action of a speed governor.

From the previous assumptions, in particular from the second one, the power of the machine P_a is the difference between the shaft power P_m as supplied by the prime mover and the electrical power P_e. The acceleration is thus:

$$\sigma = \frac{P_a}{M_g} = \frac{P_m - P_e}{M_g} \tag{4.4}$$

where σ represents the acceleration of the machine, M_g is the angular momentum and the powers are given in per unit.

It is convenient to choose a synchronously rotating reference to define the rotor angle δ. Thus,

$$\frac{d^2\delta}{dt^2} = \frac{P_m - P_e}{M_g} \tag{4.5}$$

The angular momentum may be further defined by the inertia constant M_g which is relatively constant regardless of the size of the machine.

$$M_g = \frac{H}{\pi f_0} \tag{4.6}$$

In the above equation f_0 represents the system base frequency.

Eddy currents induced in the rotor iron or in the damping windings produce torques which opposes the motion of the rotor relative to the synchronous speed. A deceleration power can be introduced into the mechanical equation to account for this damping, leading to

$$\frac{d^2\delta}{dt^2} = \frac{1}{M_g}\left(P_m - P_e - D\frac{d\delta}{dt}\right) \tag{4.7}$$

This section describes a classical representation of the synchronous machines assuming constant flux linkages in both axis and neglecting transient saliency. An internal voltage behind the *d*-axis transient reactance is defined and its magnitude is assumed constant. This model neglects the effects of damper circuits, it means the axis armature current I_{dq} do not fluctuate during the transient period.

In the approach used in this research, the **Jacobian** matrix of a conventional power flow method [Stagg and El-Abiad, 1968] is expanded to include, in suitable form the network dynamic equations. It is argued that the method is numerically stable, robust and inherently capable of handling islanding and fault analyses [Rafian et al., 1987].

Bearing in mind the fact that the problem of stability involves the rotors of synchronous machines, it is mandatory to use the swing equation of each machine in the system Eq. 4.7, in the solution.

Equation 4.7 can be discomposed into two first order differential equations,

$$\dot{\omega} = \frac{\pi f_0}{H} \left[P_m - P_e - D \left(\omega - \omega_0 \right) \right] \tag{4.8}$$

$$\dot{\delta} = \omega - \omega_0 \tag{4.9}$$

where

H is the inertia constant, MW*s/MVA.

P_m is the mechanical input power, pu.

P_e is the electrical output power, pu.

D is the damping coefficient, s/rad.

f_0 is the synchronous frequency, Hz.

δ is the load angle, rad.

The classical derivation of the voltages and reactances which exists in a synchronous machine are well established [Kimbark, 1948b, Concordia, 1951]. The electrical quantities will be defined under the following assumptions:

1. All inductances are independent of the current.
2. Machine winding can be represented as constants.
3. Distributed windings may be represented as concentrated windings.
4. The machine is represented by a voltage behind the reactance.
5. There are no hysteresis losses in the iron.
6. The leakage reactance occurs only in the stator.

Using these assumptions the classical model for a synchronous machine is constructed.

With reference to Fig. 4.1, assuming balanced conditions, the algebraic equations that describe generator voltage relations can be written by a set of equations based on direct and quadrature axis parameters,

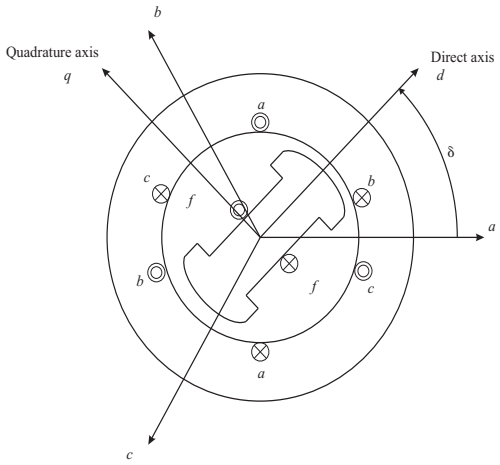

Figure 4.1: *Synchronous machine scheme.*

$$E_a = V + r_a I_a + \mathrm{j} x_d I_d + \mathrm{j} x_q I_q \tag{4.10}$$

$$I_a = I_d + \mathrm{j} I_q \tag{4.11}$$

where

V is the terminal voltage of phase a.

E_a is the excitation voltage.

r_a is the armature resistance for phase a.

x_d is the direct axis reactance.

x_q is the quadrature axis reactance.

I_d is the direct axis current.

I_q is the quadrature axis current.

I_a is the phase a current.

Another manner to calculate the voltage source behind the transient reactance where the effects of saliency and changes in field flux linkages are neglected is,

$$E_a = |E| \left(\cos \delta_E + \mathrm{j} \sin \delta_E\right) \tag{4.12}$$

4.3 Synchronous Machines Controllers

Power-generating plants consist of various components involved in energy conversion from mechanical to electrical. The main elements involved in most dynamic voltage stability analyses are the generators, voltage regulators, governors, turbines, boilers, and auxiliary equipment.

This section illustrates suitable models for voltage stability assessment.

4.3.1 Governor

The governor is a frequency controller which plays an important role in power system operations. It has three main functions which are:

1. To keep the generator speed as close as possible to its nominal value.
2. To guarantee a fast and automatic participation of the generator to any change in generation, which is required in order to maintain a balanced generation-load in the system.
3. To offer a way to adapt the active power production of the unit, via speed-changer adjustments.

The governor adjusts the steam or water input to the turbine. To achieve this, it senses the difference between the actual rotor speed and the angular frequency and adjusts accordingly the turbine valve.

Figure 4.2 shows the block diagram adopted to represent the speed governing system for steam generators. This is the simplified model proposed in [IEEE Committee Report, 1973].

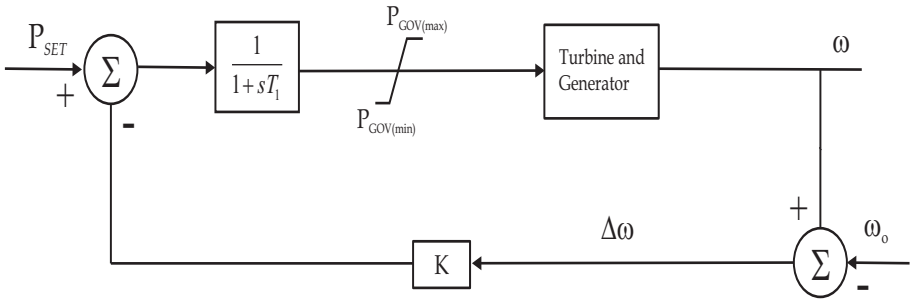

Figure 4.2: *IEEE simplified speed governor model.*

From Figure 4.2 we derive the following mathematical expression,

$$\dot{P}_g = \frac{\Delta P - P_g}{T_1} \tag{4.13}$$

with,

$$\Delta\omega = \omega - \omega_o$$

$$\Delta P = P_{SET} - K\Delta\omega$$

where

K is the governor gain.

P_{set} is the power set point.

T_1 is the governor time constant.

4.3.2 Turbine

All compound steam turbine systems utilize governor-controlled valves at the inlet to the high pressure or in some cases very high pressure turbine to control steam flow. The steam chest and inlet piping to the first turbine cylinder and reheaters and crossover piping downstream all introduce delays between valves movement and change in steam flow. The

main objective in modelling the steam system for stability studies is to consider these delays. Flows into and out of any steam vessel are related by simple time constant.

Pressure changes at the entrance to the governor-controlled valves may also be important in stability studies. Boiler controls are designed to regulate valve pressure, but the controlled boiler response is not fast enough to compensate for pressure variations due to the movements of governor-controlled valves.

For steam turbines the model is selected from the IEEE committee report [IEEE Committee Report, 1973].

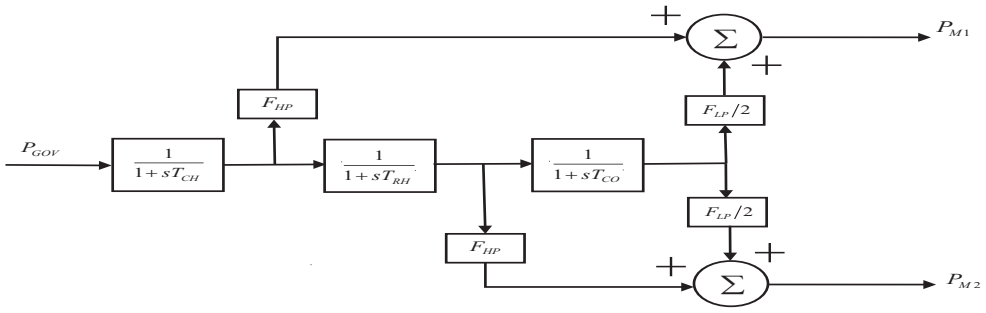

Figure 4.3: *IEEE steam turbine model.*

Figure 4.3 shows the block diagram of a cross compound, single reheat steam turbine system. The mathematical equations corresponding to this diagram are,

$$\dot{P_{HP}} = \frac{P_g - P_{HP}}{T_{CH}} \tag{4.14}$$

$$\dot{P_{IP}} = \frac{P_{HP} - P_{IP}}{T_{RH}} \tag{4.15}$$

$$\dot{P_{LP}} = \frac{P_{IP} - P_{LP}}{T_{CO}} \tag{4.16}$$

$$P_M = P_{HP}F_{HP} + P_{IP}F_{IP} + P_{LP}F_{LP} \tag{4.17}$$

From Figure 4.3 we have that,

P_{GOV} is the output power of the control valve.

T_{CH} is the steam chest time constant (including the high-pressure (HP) stage of the turbine time constant).

T_{RH} is the reheater time constant (including the intermediate-pressure (IP) stage of the turbine time constant).

T_{CO} is the steam storage or cross-over time constant (including the low-pressure (LP) stage of the turbine time constant).

F_{HP} is the HP turbine power fraction.

F_{IP} is the IP turbine power fraction.

F_{LP} is the LP turbine power fraction.

P_{M1} and P_{M2} are the equivalent generator input mechanical powers.

4.3.3 Automatic voltage regulator

The basic function of an AVR is to provide direct current to the field winding of a synchronous machine. In addition, the excitation system can provide a broad number of control and protection functions necessary for the satisfactory performance of the machine and the power system by means of the control of the field voltage. The protective functions ensure that the capacity limits of both synchronous machine and excitation control system will not be exceeded.

Several Automatic Voltage Regulator (AVR) models have been developed for transient stability studies. The model adopted in this simulation tool, is the STA1 IEEE model [Energy Development and Power Generating Committe of the PES, 2003, IEEE Committee Report, 1981].

The main objective of an AVR is to provide an effective control of the generator terminal voltage and, hence, the enhancement of system stability.

From Figure 4.4, the following expressions are derived:

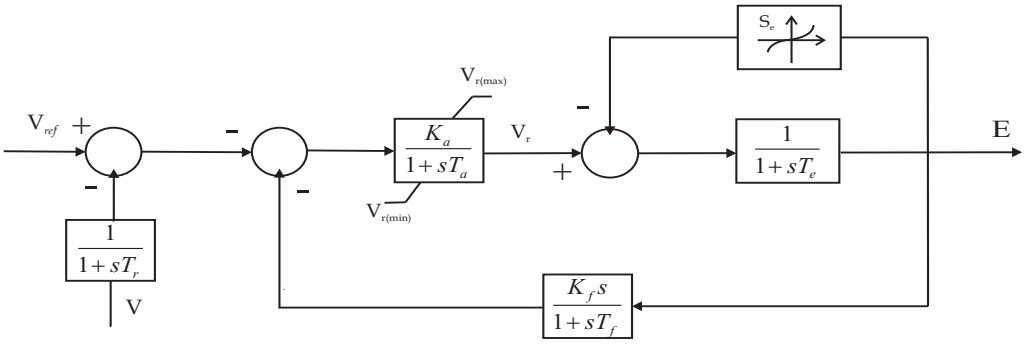

Figure 4.4: *STA1 IEEE AVR model.*

$$\dot{V_m} = \frac{V - V_m}{T_r} \tag{4.18}$$

$$\dot{V_{r1}} = \frac{K_a \left(V_{ref} - V_m - V_{r2} - \frac{K_f}{T_f} V_f\right) - V_{r1}}{T_a} \tag{4.19}$$

$$\dot{V_{r2}} = -\frac{\frac{K_f}{T_f} V_f + V_{r2}}{T_f} \tag{4.20}$$

$$\dot{V_f} = -\frac{(V_f\,(1 + S_e(V_f)) - V_r)}{T_e} \tag{4.21}$$

where the ceiling function S_e is defined as:

$$S_e(V_f) = A_e \left(e^{B_e |V_f|} - 1\right) \tag{4.22}$$

where,

$V_{r\,max}$ is the maximum regulator voltage, pu.

$V_{r\,min}$ is the minimum regulator voltage, pu.

K_a is the amplifier gain, pu.

T_a is the amplifier time constant, sec.

K_f is the stabiliser gain, pu.

T_f is the stabiliser time constant, sec.

T_e is the field circuit time constant, sec.

T_r is the measurement time constant, sec.

A^e is the 1^{st} ceiling coefficient.

B^e is the 2^{nd} ceiling coefficient.

4.3.4 Boiler

The boiler model presented here is a simple model which takes into account the slow plant response. The equations that formulate the boiler storage, throttle pressure, and the change in the flow of the steam into the steam chest according to the boiler response are:

$$\Delta \dot{DP} = \frac{SF - \Delta P_{HP}}{C_B} \tag{4.23}$$

$$\Delta P_{HP} = P_{HP} - (P_{set} - k_3 \Delta\omega) \tag{4.24}$$

$$\dot{P_{HP}} = \frac{P_g + k_1 \Delta DP - P_{HP}}{T_{CH}} \tag{4.25}$$

where,

DP is the throttle pressure.

SF is the steam production.

k_3 is the gain factor to regulate the effect of frequency deviation on boiler response.

Equation 4.25 will replace Eq. B.12 to allow the effects of pressure change in the boiler an the steam flow into the turbine.

4.4 Synchronous Machine Model - Advanced Representation

In early stability studies calculations the generators were commonly represented by a simple model, assuming constant flux linkages in each axis and neglecting transient saliency [Stagg and El-Abiad, 1968]. In these simple models an internal voltage behind the d-axis

transient reactance x_d is determined and its magnitude is assumed constant.

Due to the inertia of the flux linkages, faster changes in the conditions external to the synchronous machine are presented, and these changes are not reflected throughout the whole of the model immediately.

In order to get a more realistic representation of the power system behaviour, it is essential to consider transient saliency and the flux linkages in each axis of the synchronous machine. Figure 4.5 depicts the phasor diagram of synchronous machine in the transient state.

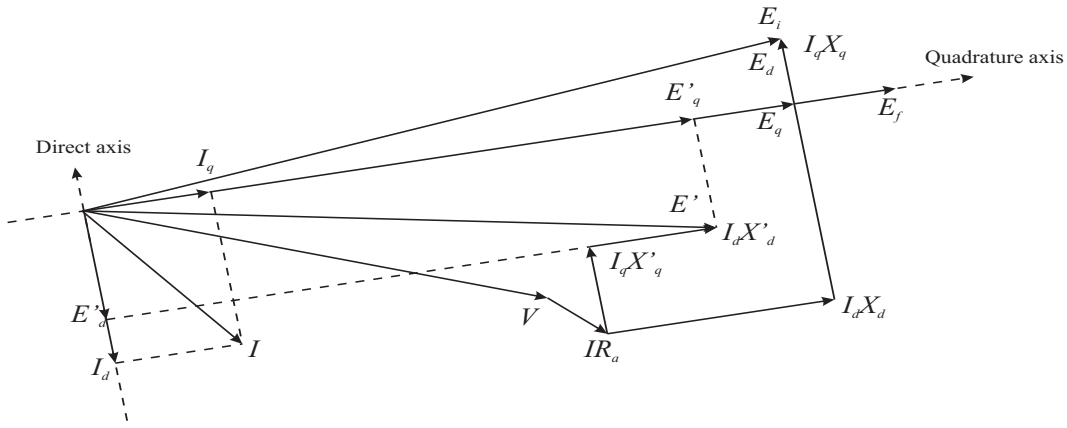

Figure 4.5: *Phasor diagram of synchronous generator in the transient state.*

Thus, the voltage behind synchronous reactance E_a, should be obtained with the voltages, E'_d and E'_q. To obtain these voltages, it is necessary to obtain the voltages which will represent the flux linkages of the rotor windings.

The differential equations that describe the variation in time of the rotor flux linkages are:

$$\dot{E}'_q = \frac{E_a + (x_d - x'_d)\, I_d - E'_q}{T'_{do}} \tag{4.26}$$

$$\dot{E}'_d = \frac{-E'_d - \left(x_q - x'_q\right) I_q}{T'_{qo}} \tag{4.27}$$

where E'_q, E'_d and are obtained as follow,

$$E'_q - V_q = r_a I_q - x'_d I_d$$
$$E'_d - V_d = r_a I_d + x'_q I_q$$

If a more detailed synchronous machine model representation is required, then the sub-transient synchronous machine model is used.

$$\ddot{E}'_q = \frac{E'_q + (x'_d - x''_d)\, I_d - E''_q}{T''_{do}} \tag{4.28}$$
$$\ddot{E}'_d = \frac{E'_d - \left(x'_q - x''_q\right) I_q - E''_d}{T''_{qo}} \tag{4.29}$$
$$E''_q - V_q = r_a I_q - x''_d I_d \tag{4.30}$$
$$E''_d - V_d = r_a I_d + x''_q I_q \tag{4.31}$$

This sub-transient synchronous model is derived assuming that the transient time constant are large compared to the sub-transients ones [Arrillaga and Arnold, 1990]. Figure 4.6 shows the phasor diagram for this sub-transient condition.

4.5 Network Modelling

The basic form of the power flows equations for balanced three-phase power systems involve the set of non-linear algebraic equations which represent the network under steady state. The expressions for active and reactive powers used to form the term **Jacobian**, Eq. 4.3, for bus k are,

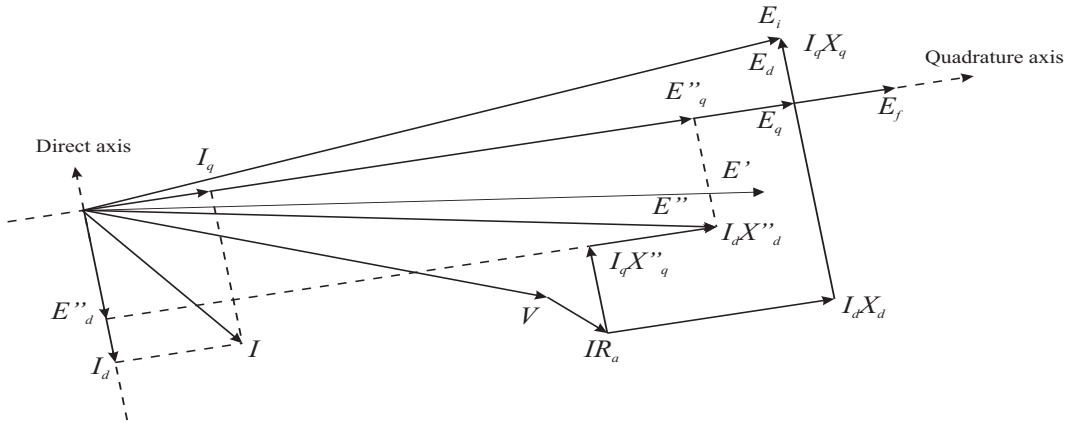

Figure 4.6: *Phasor diagram of synchronous generator in the sub-transient state.*

$$P_k = e_k \sum_{m=1,n} (G_{km}e_m - B_{km}f_m) + f_k \sum_{m=1,n} (G_{km}f_m + B_{km}e_m) \tag{4.32}$$

$$Q_k = f_k \sum_{m=1,n} (G_{km}e_m - B_{km}f_m) - e_k \sum_{m=1,n} (G_{km}f_m + B_{km}e_m) \tag{4.33}$$

where P_k and Q_k are the active and reactive powers injected at bus k, e_k and f_k are the voltage's real and imaginary parts at bus k, G_{km} and B_{km} are the real and imaginary parts of the nodal admittance relating buses k and m. It should be noted that $k = m$ corresponds to the self admittance of bus k. As shown below, each plant component of the power network is represented by its own form of nodal admittance elements G_{kk}, B_{kk}, G_{km} and B_{km}.

4.6 Transmission Line Model

In power system studies it is common to represent a transmission line by its nominal π circuit, shown in Fig. 4.7.

corresponding to a transmission line l of series impedance Z_l and shunt admittance Y_l. The transmission line is connected between buses k and m, giving rise to the following transfer

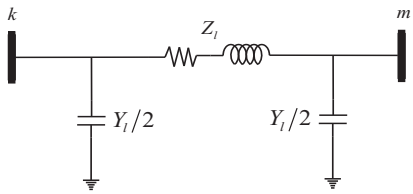

Figure 4.7: *Transmission line representation.*

admittance matrix:

$$\begin{pmatrix} Y_{kk} & Y_{km} \\ Y_{mk} & Y_{mm} \end{pmatrix} = \begin{pmatrix} Z_l^{-1} + \frac{Y_l}{2} & -Z_l^{-1} \\ -Z_l^{-1} & Z_l^{-1} + \frac{Y_l}{2} \end{pmatrix} \tag{4.34}$$

where $Y_{kk} = Y_{mm} = G_{kk} + \mathrm{j}B_{kk}$ are the nodal self admittances at buses k and m, respectively, and $Y_{km} = Y_{mk} = G_{km} + \mathrm{j}B_{km}$ are the mutual admittances between buses k and m and m and k, respectively.

4.7 Dynamic Load Tap Changer and Phase Shifting Transformer Modelling

Power transformers are essentials plant components of the power system. In addition to those that perform the basic functions of transforming an AC supply voltage into one or more different AC voltages and providing electrical insulation between the supply voltage and the user's equipment, there are power transformers that are provided with an on-load tap changing mechanism to regulate voltage magnitude at a specified point of the network or to control the amount of active power that flows through the transformer. They are known as tap-changing and phase-shifting transformers, respectively.

The nodal transfer admittance matrix of a tap-changing transformer of impedance Z_l, with the tap mechanism located on the primary side T_k, and connected between buses k and m is as shown in Fig 4.8.

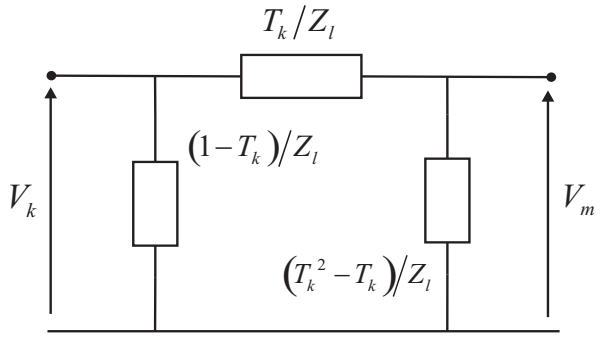

Figure 4.8: *Tap-changer transformer equivalent circuit.*

The transfer admittance matrix for this equivalent circuit is:

$$\begin{pmatrix} Y_{kk} & Y_{km} \\ Y_{mk} & Y_{mm} \end{pmatrix} = \begin{pmatrix} Z_l^{-1} & -T_k Z_l^{-1} \\ -T_k Z_l^{-1} & T_k^2 Z_l^{-1} \end{pmatrix} \tag{4.35}$$

The tap's dynamic is represented by the following first-order differential equation, according to the block diagram of Fig. 4.9.

$$\dot{T_k} = \frac{1}{H_T}\left(\sqrt{e_k^2 + f_k^2} - V_0\right) \tag{4.36}$$

where H_T is the tap's servomotor inertia, e_k and f_k are the real and imaginary parts of the voltage at the regulated bus, V_0 is the target voltage magnitude.

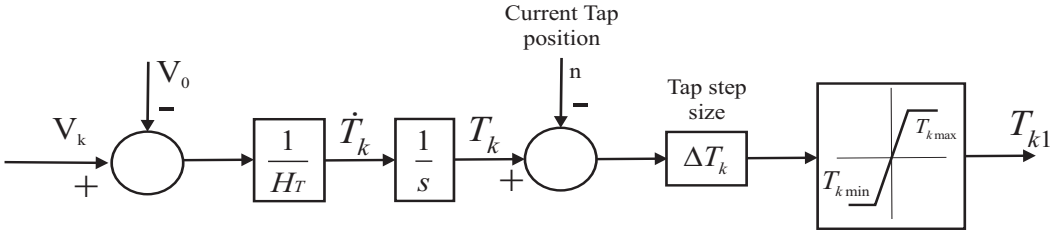

Figure 4.9: *Dynamic load tap changer model.*

As indicated in Fig. 4.10 the transformer tap is discrete, and it will be varying over the time, according to the values of e_k and f_k, the tap step size ΔT_k and its pre-defined operating

range.

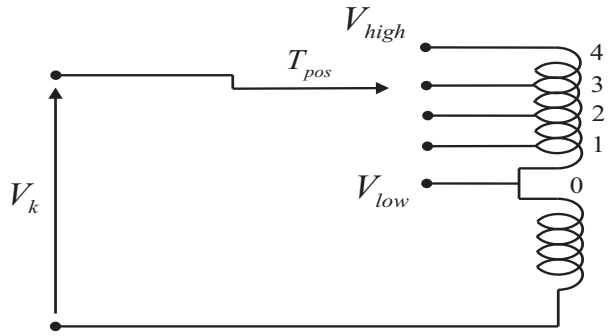

Figure 4.10: *Discrete tap.*

The nodal transfer admittance matrix of a phase-changing transformer of impedance Z_l, with the phase angle mechanism located on the primary side ϕ_k, and connected between buses k and m, is:

$$\begin{pmatrix} Y_{kk} & Y_{km} \\ Y_{mk} & Y_{mm} \end{pmatrix} = \begin{pmatrix} Z_l^{-1} & -Z_l^{-1}(\cos\phi_k + \mathrm{j}\sin\phi_k) \\ -Z_l^{-1}(\cos\phi_k - \mathrm{j}\sin\phi_k) & T_k^2 Z_l^{-1} \end{pmatrix} \tag{4.37}$$

The tap's dynamic is represented by the following first order differential equation:

$$\dot{\phi_k} = \frac{1}{H_\phi}\left(P_{km} - P_0\right) \tag{4.38}$$

where H_ϕ is the phase shifter's servomotor inertia, P_{km} is the active power through the phase shifter, P_0 is the target active power.

4.8 Numerical Solution Technique

The set of algebraic and differential equations that describe each plant component of the power network are interdependent and it has been suggested that their simultaneous calcu-

lation provides for a more stable numerical solution [Rafian et al., 1987]. To this end, the differential equations are transformed into algebraic equations and appended to the existing set of algebraic equations for a unified solution. One way of ensuring a numerically stable transformation is to use the implicit trapezoidal method, a technique known for giving reasonably accurate results even when relatively large integration time steps are selected [Kundur, 1994, Machowski et al., 1997].

The first step in the application of the trapezoidal method is to express the system differential equations in the form of Eq. 4.2. To exemplify the procedure, the method is applied to dynamic Eqs. 4.8 and 4.9:

$$\omega_{(t)} - \omega_{(t-\Delta t)} = \frac{\Delta t}{2}\left[\frac{\pi f_0}{H}\left(P_m - P_{e(t)} - D\left(\omega_{(t)} - \omega_0\right)\right)\right.$$
$$\left. + \frac{\pi f_0}{H}\left(P_m - P_{e(t-\Delta t)} - D\left(\omega_{(t-\Delta t)} - \omega_0\right)\right)\right] \tag{4.39}$$

$$\delta_{(t)} - \delta_{(t-\Delta t)} = \frac{\Delta t}{2}\left(\dot{\delta}_{(t)} + \dot{\delta}_{(t-\Delta t)}\right) \tag{4.40}$$

Substituting in Eq. 4.39 the expression of electrical power P_e, where the effects of saliency and flux decay are considered, but assuming constant P_m, we have,

$$\begin{aligned}
\omega_{(t)} - \omega_{(t-\Delta t)} = \frac{\Delta t}{2}\Bigg[\big(\frac{\pi f_0}{H} P_m \\
+(E'_{d(t)} - r_a I_{d(t)} + (X'_q - X_l) I_{q(t)}) I_{d(t)} \\
+(E'_{q(t)} - r_a I_{q(t)} + (X'_d - X_l) I_{d(t)}) I_{q(t)} \\
-D\left(\omega_{(t)} - \omega_0\right)\big) + \frac{\pi f_0}{H}\big(P_m \\
+(E'_{d(t-\Delta t)} - r_a I_{d(t-\Delta t)} + (X'_q - X_l) I_{q(t-\Delta t)}) I_{d(t-\Delta t)} \\
+(E'_{q(t-\Delta t)} - r_a I_{q(t-\Delta t)} + (X'_d - X_l) I_{d(t-\Delta t)}) I_{q(t-\Delta t)} \\
-D\left(\omega_{(t-\Delta t)} - \omega_0\right)\big)\Bigg]
\end{aligned} \tag{4.41}$$

Notice that in this equation only the transient effects have been represented, as opposed to sub-transient ones, to keep the expression at a manageable level.

Re-arranging terms, leads to a more compact expression,

$$F_\omega = F_{\omega(t)} + F_{\omega(t-\Delta t)} + C_\omega = 0 \tag{4.42}$$

$$F_\delta = F_{\delta(t)} + F_{\delta(t-\Delta t)} + C_\delta = 0 \tag{4.43}$$

where

$$\begin{aligned}
F_{\omega(t)} &= \omega_{(t)} + \frac{\Delta \pi f_0}{2H}\left(P_{e(t)} + D\omega_{(t)}\right) \\
F_{\omega(t-\Delta t)} &= -\omega_{(t-\Delta t)} + \frac{\Delta \pi f_0}{2H}\left(P_{e(t-\Delta t)} + D\omega_{(t-\Delta t)}\right) \\
C_\omega &= -\frac{\Delta t \pi f_0}{H}\left(P_m + D\omega_0\right)
\end{aligned}$$

Likewise, expression 4.42 is re-arranged,

$$
\begin{aligned}
F_{\delta(t)} &= \delta_{(t)} - \frac{\Delta t}{2}\omega_{(t)} \\
F_{\delta(t-\Delta t)} &= -\delta_{(t-\Delta t)} - \frac{\Delta t}{2}\omega_{(t-\Delta t)} \\
C_{\delta} &= 2\pi f_0 \Delta t
\end{aligned}
$$

Equations 4.32 and 4.33, describing the active and reactive powers injected in the network buses, are augmented to incorporate explicitly the active and reactive powers contributed by all generators in the network. Hence, at generator buses only, including the slack bus,

$$
\begin{aligned}
&P_k + P_{e,l} \\
&Q_k + Q_{e,l}
\end{aligned}
\tag{4.44}
$$

for $k = 1, ..., l, ..., nbus$ and $l = 1, ..., ngen$.

Equations 4.32, 4.33 and 4.44 for load buses and Eq. 4.42 to Eq. 4.44 for generator buses form the necessary set with which to carry out dynamic power flow solutions of a power system. One option to achieve this is to solve the equation set, which is non-linear, using the Newton-Raphson method. Hence, the following linearised equation, around a base point, provides the computing engine with which to carry out the solution by iteration:

$$\begin{bmatrix} \boldsymbol{\Delta P} \\ \boldsymbol{\Delta Q} \\ -- \\ \boldsymbol{F_{\omega}} \\ \boldsymbol{F_{\delta}} \\ \boldsymbol{F_{E'_d}} \\ \boldsymbol{F_{E'_q}} \\ \boldsymbol{F_{E''_d}} \\ \boldsymbol{F_{E''_q}} \end{bmatrix} = \begin{bmatrix} \mathbf{J_{11}} & | & \mathbf{J_{12}} \\ -- & + & -- \\ \mathbf{J_{21}} & | & \mathbf{J_{22}} \end{bmatrix} \begin{bmatrix} \boldsymbol{\Delta e} \\ \boldsymbol{\Delta f} \\ -- \\ \boldsymbol{\Delta \omega} \\ \boldsymbol{\Delta \delta} \\ \boldsymbol{\Delta E'_d} \\ \boldsymbol{\Delta E'_q} \\ \boldsymbol{\Delta E''_d} \\ \boldsymbol{\Delta E''_q} \end{bmatrix} \tag{4.45}$$

where

$$\Delta P = [\Delta P_1, \ldots, \Delta P_n]^t$$

$$\Delta Q = [\Delta Q_1, \ldots, \Delta Q_n]^t$$

$$\Delta e = [\Delta e_1, \ldots, \Delta e_n]^t$$

$$\Delta f = [\Delta f_1, \ldots, \Delta f_n]^t$$

$$\Delta \omega = [\Delta \omega_1, \ldots, \Delta \omega_m]^t$$

$$\Delta \delta = [\Delta \delta_1, \ldots, \Delta + \delta_m]^t$$

$$\Delta E'_d = \left[\Delta E'_{d_1}, \ldots, \Delta E'_{d_m}\right]^t$$

$$\Delta E'_q = \left[\Delta E'_{q_1}, \ldots, \Delta E'_{q_m}\right]^t$$

$$\Delta E''_d = \left[\Delta E''_{d_1}, \ldots, \Delta E'_{d_m}\right]^t$$

$$\Delta E''_q = \left[\Delta E''_{q_1}, \ldots, \Delta E'_{q_m}\right]^t$$

$$F_\omega = [F_{\omega_1}, \ldots, F_{\omega_m}]^t$$

$$F_\delta = [F_{\delta_1}, \ldots, F_{\delta_m}]^t$$

$$F_{E'_d} = \left[F_{E'_{d_1}}, \ldots, F_{E'_{d_m}}\right]^t$$

$$F_{E'_q} = \left[F_{E'_{q_1}}, \ldots, F_{E'_{q_m}}\right]^t$$

$$F_{E''_d} = \left[F_{E''_{d_1}}, \ldots, F_{E''_{d_m}}\right]^t$$

$$F_{E''_q} = \left[F_{E''_{q_1}}, \ldots, F_{E''_{q_m}}\right]^t$$

$$\mathbf{J_{11}} = \begin{bmatrix} \left(\frac{\partial P_1}{\partial e_1} + \frac{\partial P_{e_1}}{\partial e_1}\right) & \left(\frac{\partial P_1}{\partial f_1} + \frac{\partial P_{e_1}}{\partial f_1}\right) & \cdots & \frac{\partial P_1}{\partial e_n} & \frac{\partial P_1}{\partial f_n} \\ \left(\frac{\partial Q_1}{\partial e_1} + \frac{\partial Q_{e_1}}{\partial e_1}\right) & \left(\frac{\partial Q_1}{\partial f_1} + \frac{\partial Q_{e_1}}{\partial f_1}\right) & \cdots & \frac{\partial Q_1}{\partial e_n} & \frac{\partial Q_1}{\partial f_n} \\ \vdots & \vdots & \ddots & \vdots & \vdots \\ \frac{\partial P_n}{\partial e_1} & \frac{\partial P_n}{\partial f_1} & \cdots & \frac{\partial P_n}{\partial e_n} & \frac{\partial P_n}{\partial f_n} \\ \frac{\partial Q_n}{\partial e_1} & \frac{\partial Q_n}{\partial e_1} & \cdots & \frac{\partial Q_n}{\partial e_n} & \frac{\partial Q_n}{\partial f_n} \end{bmatrix}$$

$$\mathbf{J_{22}} = \begin{bmatrix} \frac{\partial F_{\omega_1}}{\partial \omega_1} & \frac{\partial F_{\omega_1}}{\partial \delta_1} & \frac{\partial F_{\omega_1}}{\partial E'_{d_1}} & \frac{\partial F_{\omega_1}}{\partial E'_{q_1}} & \frac{\partial F_{\omega_1}}{\partial E''_{d_1}} & \frac{\partial F_{\omega_1}}{\partial E''_{q_1}} \\ \frac{\partial F_{\delta_1}}{\partial \omega_1} & \frac{\partial F_{\delta_1}}{\partial \delta_1} & \frac{\partial F_{\delta_1}}{\partial E'_{d_1}} & \frac{\partial F_{\delta_1}}{\partial E'_{q_1}} & \frac{\partial F_{\delta_1}}{\partial E''_{d_1}} & \frac{\partial F_{\delta_1}}{\partial E''_{q_1}} \\ \frac{\partial F_{E'_{d_1}}}{\partial \omega_1} & \frac{\partial F_{E'_{d_1}}}{\partial \delta_1} & \frac{\partial F_{E'_{d_1}}}{\partial E'_{d_1}} & \frac{\partial F_{E'_{d_1}}}{\partial E'_{q_1}} & \frac{\partial F_{E'_{d_1}}}{\partial E''_{d_1}} & \frac{\partial F_{E'_{d_1}}}{\partial E''_{q_1}} \\ \frac{\partial F_{E'_{q_1}}}{\partial \omega_1} & \frac{\partial F_{E'_{q_1}}}{\partial \delta_1} & \frac{\partial F_{E'_{q_1}}}{\partial E'_{d_1}} & \frac{\partial F_{E'_{q_1}}}{\partial E'_{q_1}} & \frac{\partial F_{E'_{q_1}}}{\partial E''_{d_1}} & \frac{\partial F_{E'_{q_1}}}{\partial E''_{q_1}} \\ \frac{\partial F_{E''_{d_1}}}{\partial \omega_1} & \frac{\partial F_{E''_{d_1}}}{\partial \delta_1} & \frac{\partial F_{E''_{d_1}}}{\partial E'_{d_1}} & \frac{\partial F_{E''_{d_1}}}{\partial E'_{q_1}} & \frac{\partial F_{E''_{d_1}}}{\partial E''_{d_1}} & \frac{\partial F_{E''_{d_1}}}{\partial E''_{q_1}} \\ \frac{\partial F_{E''_{q_1}}}{\partial \omega_1} & \frac{\partial F_{E''_{q_1}}}{\partial \delta_1} & \frac{\partial F_{E''_{q_1}}}{\partial E'_{d_1}} & \frac{\partial F_{E''_{q_1}}}{\partial E'_{q_1}} & \frac{\partial F_{E''_{q_1}}}{\partial E''_{d_1}} & \frac{\partial F_{E''_{q_1}}}{\partial E''_{q_1}} \end{bmatrix}$$

$$\mathbf{J_{12}} = \begin{bmatrix} \frac{\partial P_1}{\partial \omega_1} & \frac{\partial P_1}{\partial \delta_1} & \frac{\partial P_1}{\partial E'_{d_1}} & \frac{\partial P_1}{\partial E'_{q_1}} & \frac{\partial P_1}{\partial E''_{d}} & \frac{\partial P_1}{\partial E''_{q}} \\ \frac{\partial Q_1}{\partial \omega_1} & \frac{\partial Q_1}{\partial \delta_1} & \frac{\partial Q_1}{\partial E'_{d_1}} & \frac{\partial Q_1}{\partial E'_{q_1}} & \frac{\partial Q_1}{\partial E''_{q}} & \frac{\partial Q_1}{\partial E''_{q}} \\ \vdots & \vdots & \vdots & \vdots & \vdots & \vdots \\ 0_n & 0_n & 0_n & 0_n & 0_n & 0_n \\ 0_n & 0_n & 0_n & 0_n & 0_n & 0_n \end{bmatrix}$$

$$\mathbf{J_{21}} = \begin{bmatrix} \frac{\partial F_{\omega_1}}{\partial e_1} & \frac{\partial F_{\omega_1}}{\partial f_1} & \cdots & 0_n & 0_n \\ \frac{\partial F_{\delta_1}}{\partial e_1} & \frac{\partial F_{\delta_1}}{\partial f_1} & \cdots & 0_n & 0_n \\ \frac{\partial F_{E'_{d_1}}}{\partial e_1} & \frac{\partial F_{E'_{d_1}}}{\partial f_1} & \cdots & 0_n & 0_n \\ \frac{\partial F_{E'_{d_1}}}{\partial e_1} & \frac{\partial F_{E'_{d_1}}}{\partial f_1} & \cdots & 0_n & 0_n \\ \frac{\partial F_{E''_{d_1}}}{\partial e_1} & \frac{\partial F_{E''_{d_1}}}{\partial f_1} & \cdots & 0_n & 0_n \\ \frac{\partial F_{E''_{q_1}}}{\partial e_1} & \frac{\partial F_{E''_{q_1}}}{\partial f_1} & \cdots & 0_n & 0_n \end{bmatrix}$$

$\mathbf{J_{11}}$ is a matrix of first order partial derivatives of the active and reactive power, P and Q, with respect to nodal voltages, e,f. The active and reactive powers contributed by the generators are taken into consideration in the Jacobian term, $\mathbf{J_{11}}$. $\mathbf{J_{22}}$ is a matrix of partial derivatives of generators discretised functions of the form of Eq. 4.42 and Eq. 4.43, with respect to generator state variables ω, δ, E'_d, E'_q, E''_d and E''_q. $\mathbf{J_{12}}$ is a matrix of first order partial derivatives of active and reactive power at generator buses with respect to generator state variables. $\mathbf{J_{21}}$ is a matrix of first order partial derivatives of generator discretised functions of the form of Eq. 4.42 and Eq. 4.43, with respect to nodal voltages e,f.

Equation 4.45 may be seen as an extended Newton-Raphson power flow formulation in rectangular coordinates, where the generating plant equations, in discretised form, are linearised and solved together with the normal power flow equations, including those of the slack bus generator. In the overall Jacobian, in addition to the entries corresponding to the generating plant itself there are mutual terms corresponding to the interface between the network and the generating plant.

It should be remarked that in Eq. 4.45 the mechanical power P_m contributed by the boiler-turbine-governor set has been taken to remain constant, for the sake of simplifying the equation. In practice, however, the boiler-turbine-governor set is an important dynamic element in power systems long term dynamics and the linearised Eq. 4.45 should be suitably expanded to accommodate an expression of the form:

$$F_{P_{HP}} = F_{P_{HP}(t)} + F_{P_{HP}(t-\Delta t)} + C_{P_{HP}} = 0$$

$$F_{P_{IP}} = F_{P_{IP}(t)} + F_{P_{IP}(t-\Delta t)} + C_{P_{IP}} = 0$$

$$F_{P_{LP}} = F_{P_{LP}(t)} + F_{P_{LP}(t-\Delta t)} + C_{P_{LP}} = 0$$

$$F_{P_{gov}} = F_{P_{gov}(t)} + F_{P_{gov}(t-\Delta t)} + C_{P_{gov}} = 0$$

$$F_{DP} = F_{DP(t)} + F_{DP(t-\Delta t)} + C_{DP} = 0$$

$$F_{BC_1} = F_{BC_1(t)} + F_{BC_1(t-\Delta t)} + C_{BC_1} = 0$$

$$F_{BC_2} = F_{BC_2(t)} + F_{BC_2(t-\Delta t)} + C_{BC_2} = 0$$

$$F_{SF} = F_{SF(t)} + F_{SF(t-\Delta t)} + C_{SF} = 0$$

$$P_m = P_{HP}F_{HP} + P_{IP}F_{IP} + P_{LP}P_{LP}$$

where P_{HP} is the equivalent power from the high pressure stage of the turbine, P_{IP} is the equivalent power from the intermediate pressure stage, P_{LP} is the equivalent power from the low pressure stage, P_{gov} is the equivalent input power to the turbine, BC_1 is the fire intensity, BC_2 is an auxiliary variable, SF is the steam production, DP is the throttle pressure and P_m is the mechanical power.

4.9 Time Domain Simulations

4.9.1 Validation

To validate the solution technique, a time domain simulation has been carried out and compared with PSAT [Milano, 2007, Milano, 2005, Milano, 2006]. The test system used is the nine-bus, three-machine power system depicted at Fig. 4.16 [Chow, 1982, Anderson and Fouad, 1997].

The synchronous generators are presented by their 4^{th} order model with no controls, load are modelled by their static representation and tap changing transformers are not considered.

The scenario considered for this study is a load change at Bus 8. A load of 10MW is added at $t = 1$s, using a 10 pu resistive impedance. The simulation runs for five seconds.

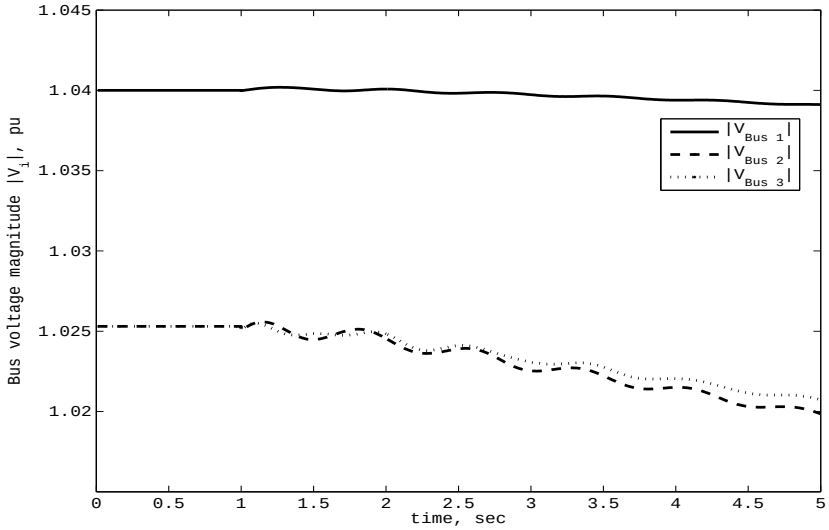

Figure 4.11: *Bus voltage response to a load change.*

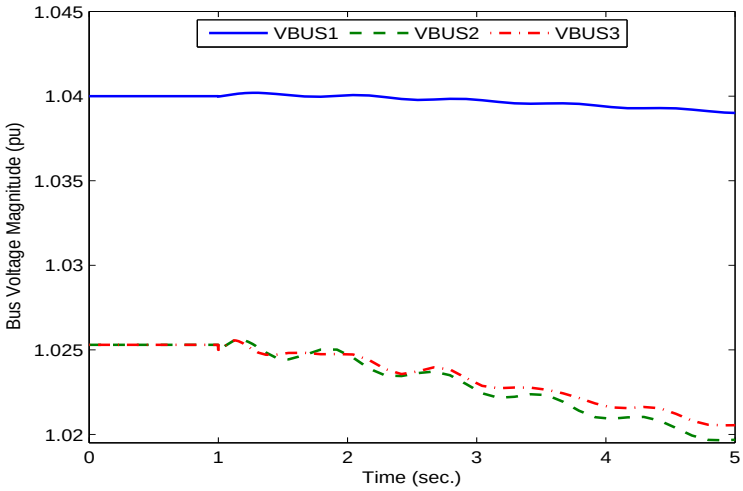

Figure 4.12: *PSAT simulation - Bus voltage response to a load change.*

It should be noted from Fig. 4.11 and Fig. 4.12, that the system response at Bus 1, is more damped than those at Buses 2 and 3. This is due to the fact that former buses are closer to the perturbation point.

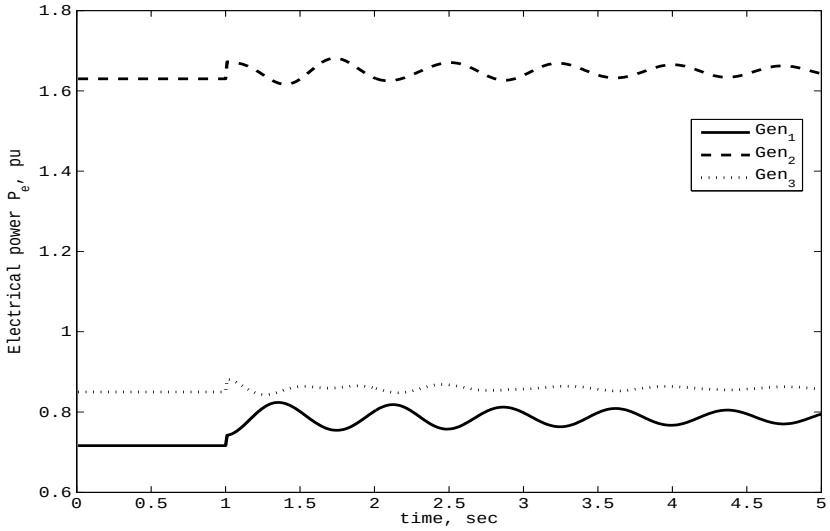

Figure 4.13: *Electrical power deliver by generators.*

Fig. 4.13 shows the electrical power delivered by the generators during the transient simulation. Fig. 4.14 presents the machines angle differences. It is noted that the angular differences of the machines are small, thus, the system will remain stable after the disturbance.

Fig. 4.15 shows the speed deviation for the synchronous generators.

4.9.2 A classical stability study

Even when the simultaneous solution technique adopted is particularly suited to carrying out long-term assessments of voltage stability in power systems, it can also handle transient stability analyses. So then, the solution technique is illustrated by solving the classical transient stability study depicted at [Anderson and Fouad, 1997].

The nine-bus system [Chow, 1982, Anderson and Fouad, 1997], shown at Fig. 4.16, is used to conduct this analyses.

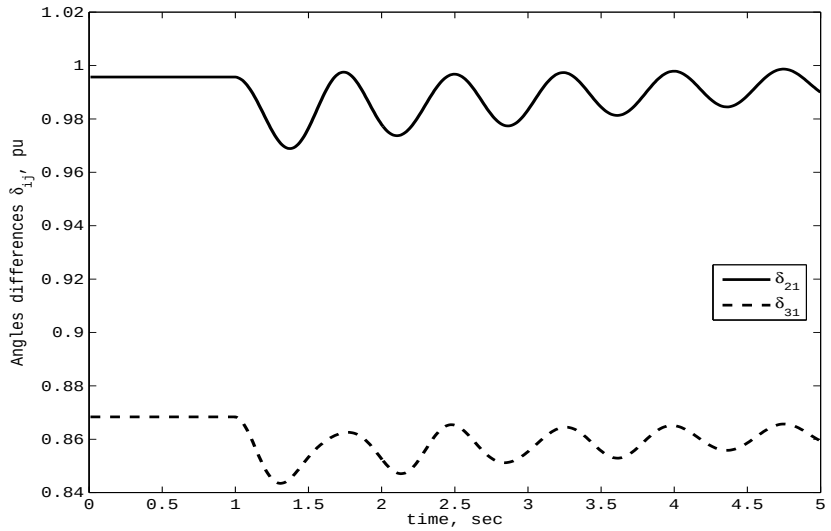

Figure 4.14: $\delta_i - \delta_1$ *response to the load change.*

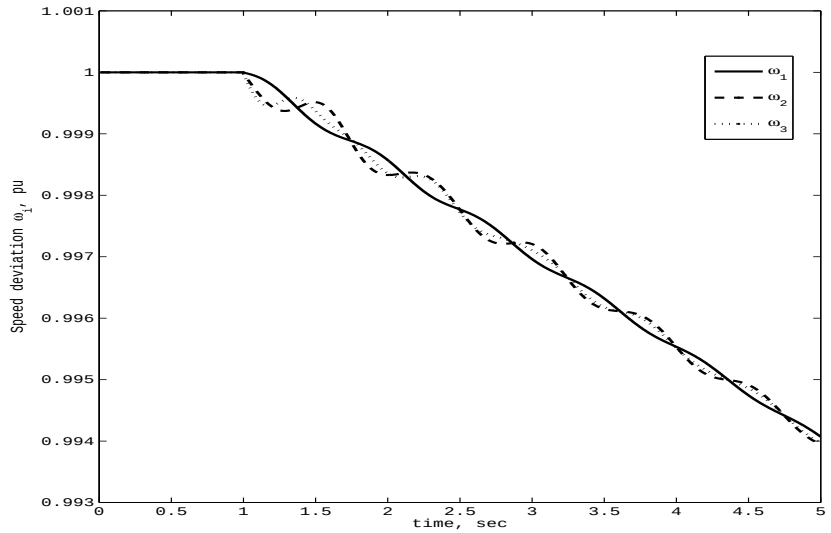

Figure 4.15: *Synchronous generators' angular velocity.*

The disturbance is initiated by a symmetric three-phase fault occurring near Bus 7 at the end of line 5-7. The fault is cleared by opening line 5-7 through the breaker approximately 5 cycles after the fault occurred. It is assumed for this analyses that the base operating frequency is 50 Hz.

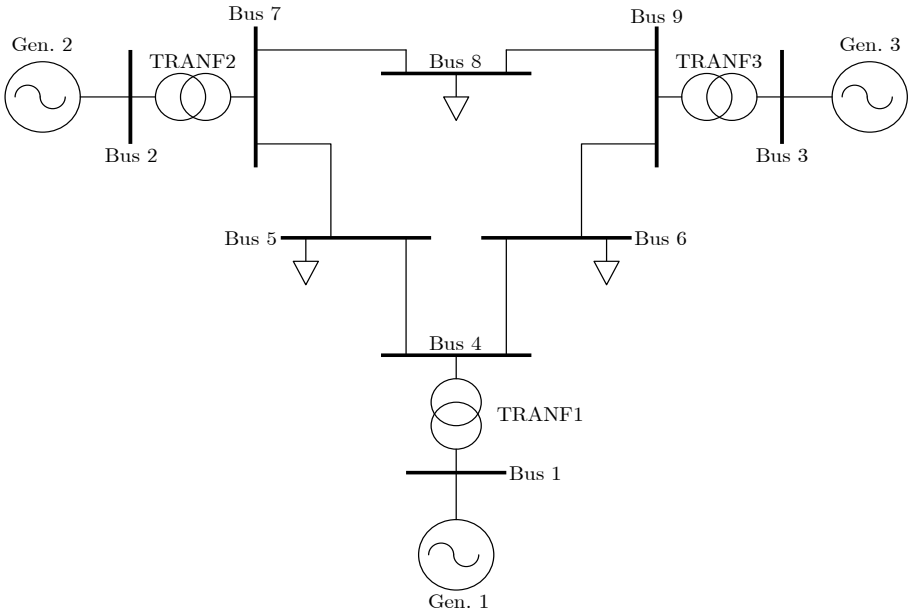

Figure 4.16: 3 *Generators* 9 *buses power system.*

For this stability assessment, synchronous generator are modelled by their classical representation with no controls.

The variables plotted are the generator's speed, ω_i, generator's rotor angle, δ_i, and the buses voltage magnitude, $|V_i|$.

Figures 4.17-4.21 show the result for this dynamic assessment, with Fig. 4.17 showing the voltage magnitude at the system buses. In Fig. 4.18 the response of the machine's rotor angle, δ_i, is presented. Fig. 4.19 gives the angle differences between machines, namely, $\delta_{21} = \delta_2 - \delta_1$ and $\delta_{31} = \delta_3 - \delta_1$. This plot indicates that the system remains stable. This fact is clearly indicated by the angular differences of the machines which are not divergent even though their response is oscillatory.

Figure 4.20 shows the speed deviation for the synchronous generators, and Fig. 4.21 shows the voltage magnitude for the buses where the synchronous generators are connected to.

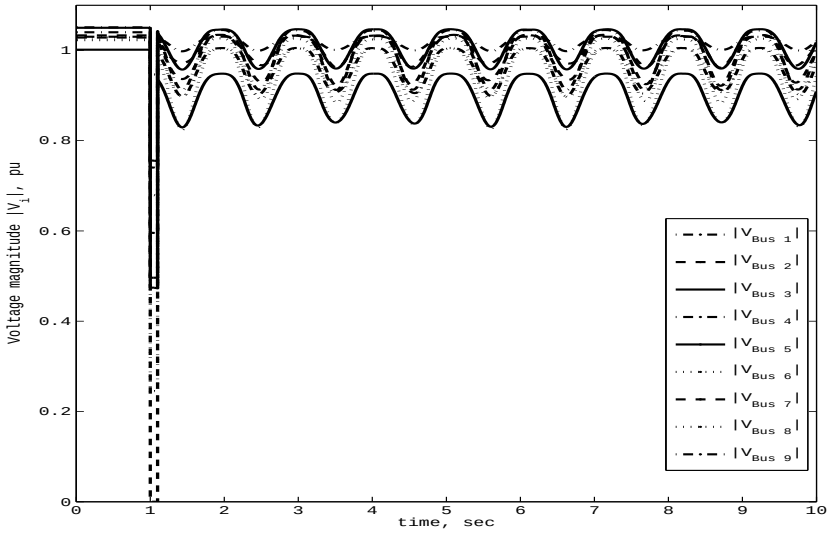

Figure 4.17: *Bus voltage response to the fault.*

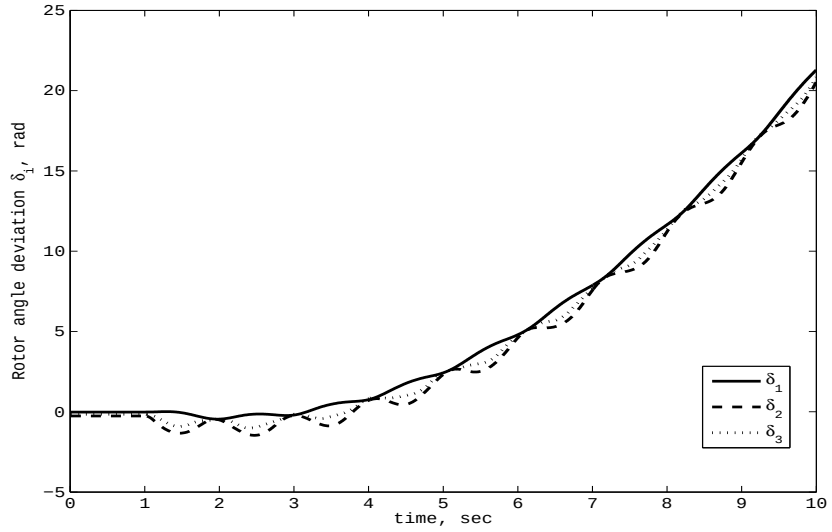

Figure 4.18: δ_i *responses to the fault.*

4.9.3 Test case 1

To demonstrate the applicability of the dynamic power flow algorithm, the load connected at Bus 8 is increased by 50%. For this simulation, the boiler-turbine-governor set model is included. The simulation period is 10 minutes.

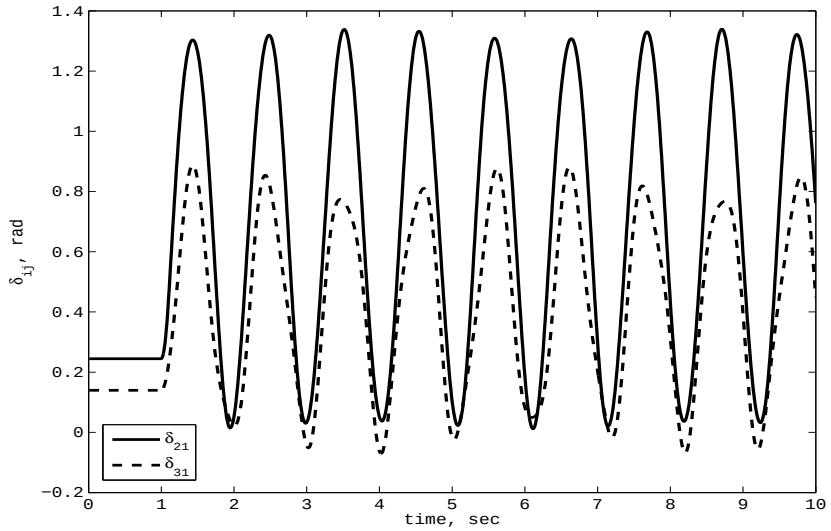

Figure 4.19: *δ_{ij} differences.*

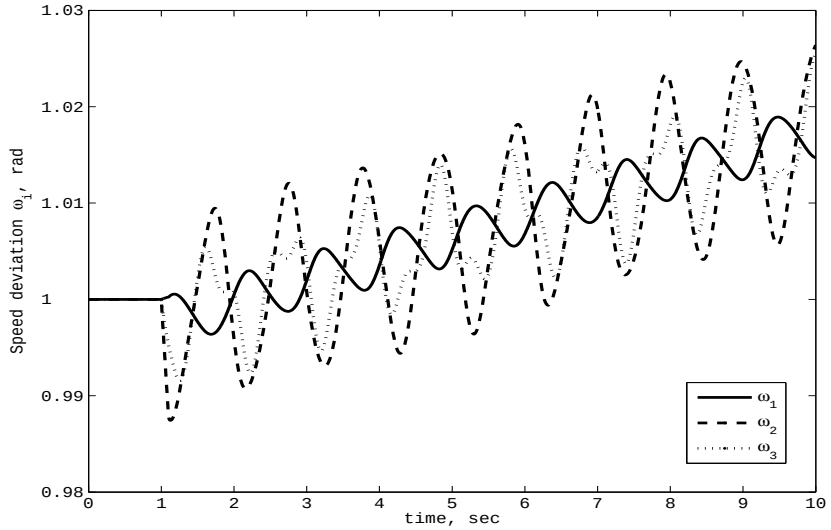

Figure 4.20: *Speed deviation ω_i response to the fault.*

Fig. 4.22 shows the system with a mechanical power P_m constant, continuous line, whereas the dash line represents the mechanical power associated with the boiler-turbine-governor set model.

As in the previous case the synchronous generators are modelled in detail by means of

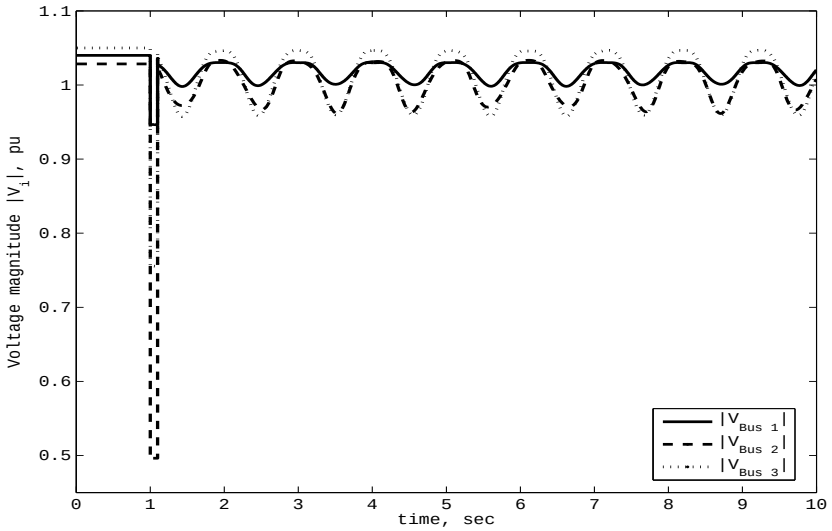

Figure 4.21: *Voltage magnitude for generator buses.*

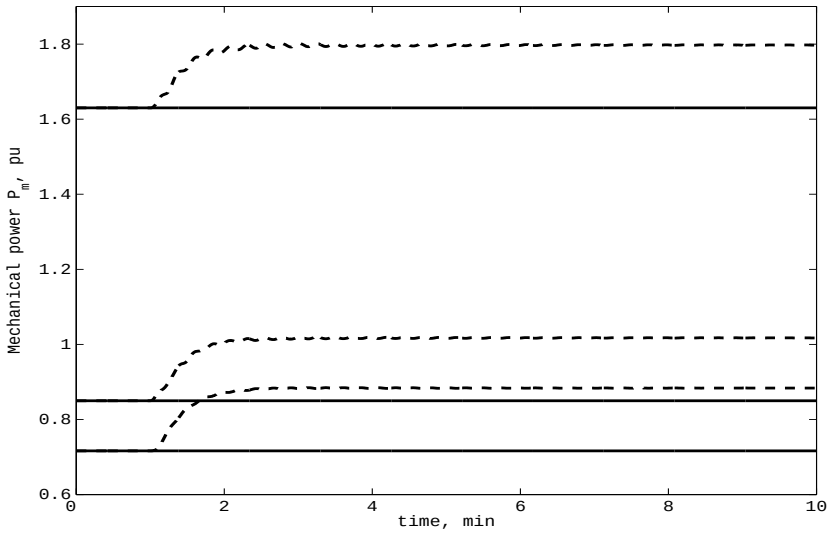

Figure 4.22: *Synchronous generators' mechanical power.*

the subtransient model. Fig 4.23 shows the excitation voltage $|E_f|$ for the case when the boiler-turbine-governor set is considered. Fig 4.24 depicts the voltage magnitudes for the systems' buses.

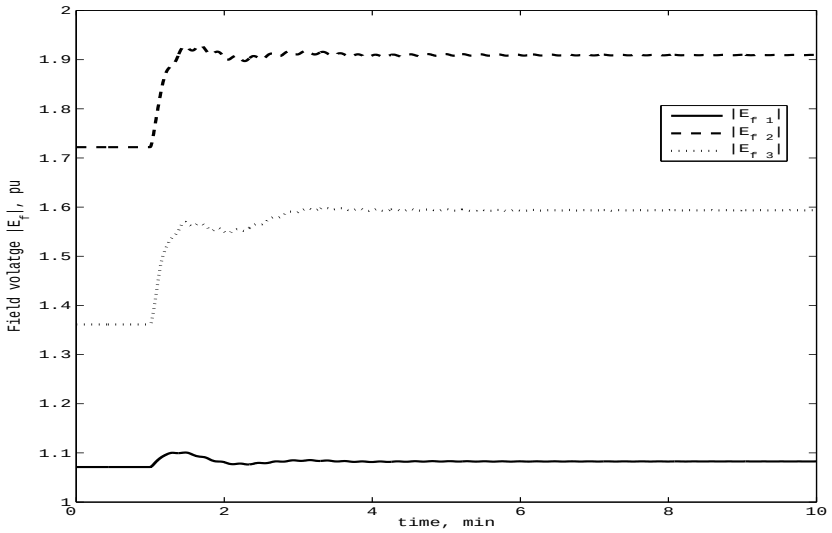

Figure 4.23: *Synchronous generators' excitation voltage.*

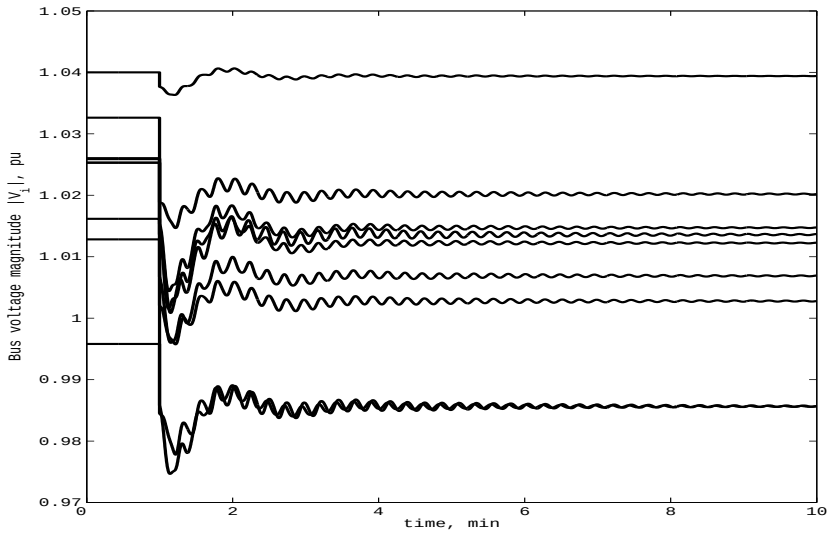

Figure 4.24: *Bus voltage magnitude.*

4.9.4 Test case 2

To assess the performance of the dynamic LTC transformer model, a separate test case is carried out. A load increment in Bus 8 is used as the source of the perturbation. Fig. 4.25 shows the LTC performance following the perturbation. Dynamic tap-changers 2 and 3 are

closer to the perturbation point and their action is more pronounced than the dynamic LTC 1 which is farther away; it is noted that after an initial drop, it returns to a value closer to its pre-disturbance value.

Fig. 4.26 gives the voltage profiles at buses where the load tap changers are connected to. When the load tap changer is active, 'ON', given by the continuous line, and when the load tap changer is inactive, 'OFF', given by the dashed line.

In this test case, the dynamic load tap changer plays a very important role in improving the voltage profile at these specific points of the system.

4.9.5 Test case 3

To show the wider applicability of the proposed approach, the New England system [Chow, 1982] depicted in Fig. 5.21, is used.

The system has been modified to include one tap-changing transformer between buses 40 and 3.

At first, transmission lines which connect Bus 17 with buses 27, 16 and 18 are tripped; as

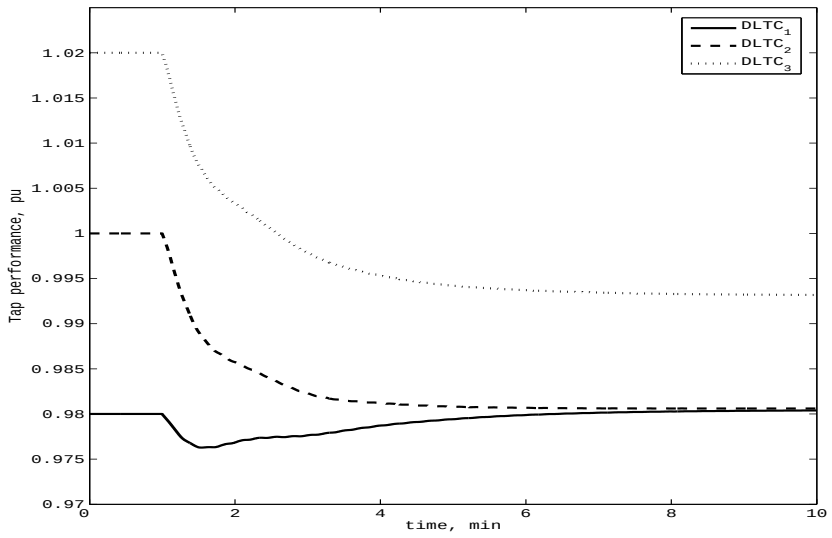

Figure 4.25: *Dynamic Load Tap-Changer (DLTC) performance.*

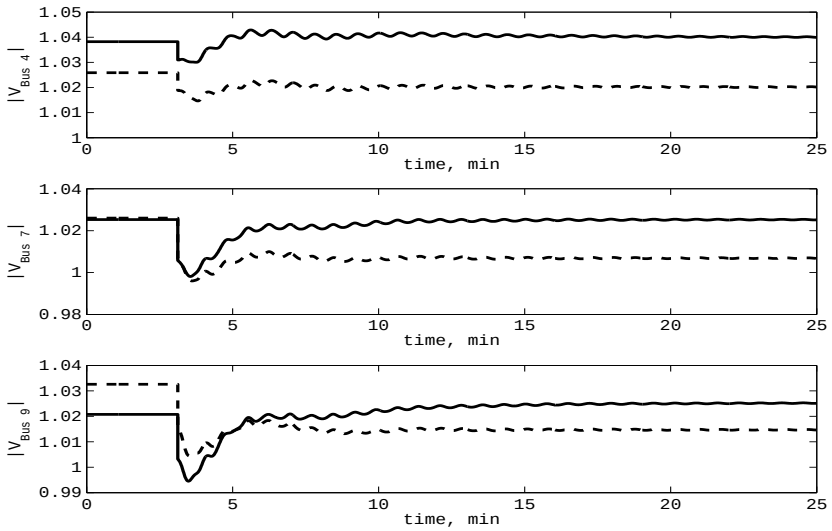

Figure 4.26: *Voltage magnitude at Buses* 4, 7 *and* 9.

a consequence Bus 17 including its load, is isolated from the system, producing a voltage drop at the majority of nodes. Next, the transmission line connecting buses 3 and 18 is taken out of service, causing that node 18 and its load become separated from the system, bringing a recovery of system voltages. This is followed by a tripping of the transmission line connecting buses 3 to 4; an event that triggers a voltage collapse of the entire system.

Fig. 4.28 shows the voltage magnitudes in the remaining 37 buses of the system. Fig. 4.29 shows the discrete response of the tap-changer under abrupt voltage changes. It can be seen that this device works in its pre-specified working range, which is from 0.90 to 1.10. The tap changer performance can be observed in Fig. 4.29.

Fig. 4.30 shows the voltage profile at the bus where the voltage is controlled by the tap-changer. As shown, the tap-changer transformer is able to control the voltage around its specified value, 1 p.u., even when the system is undergoing unfavourable conditions.

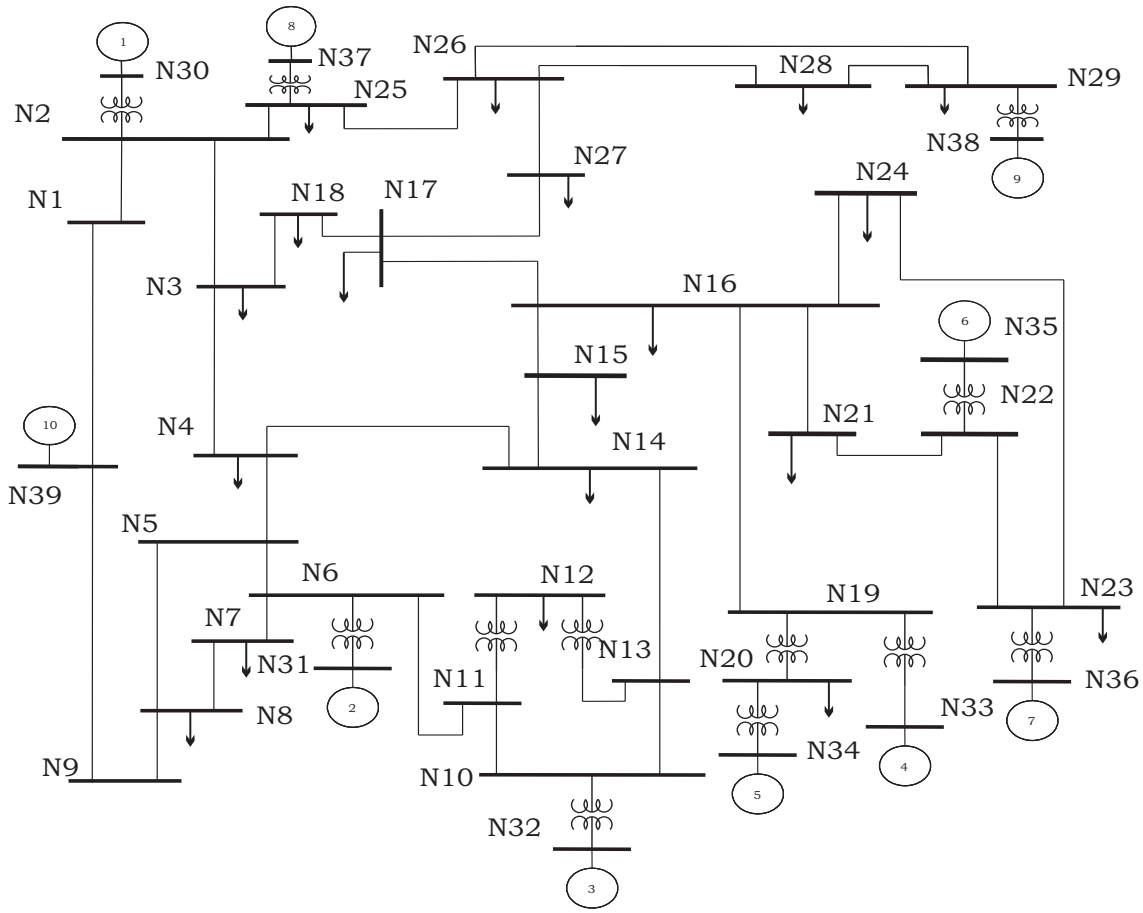

Figure 4.27: *One-line New England test system diagram.*

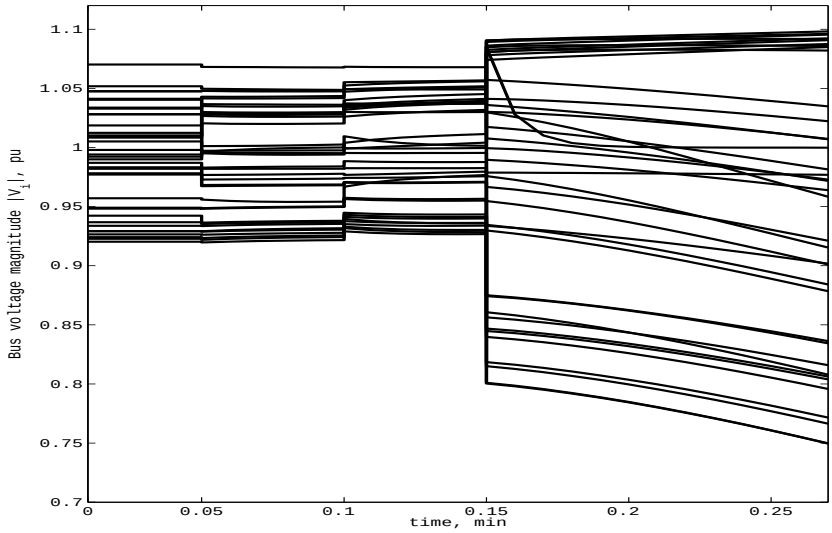

Figure 4.28: *Bus voltages' response.*

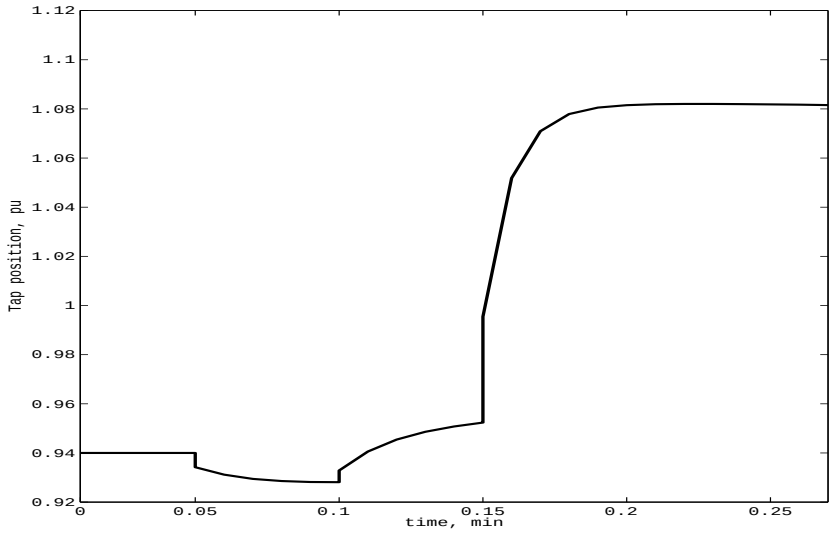

Figure 4.29: *Dynamic load tap changer performance.*

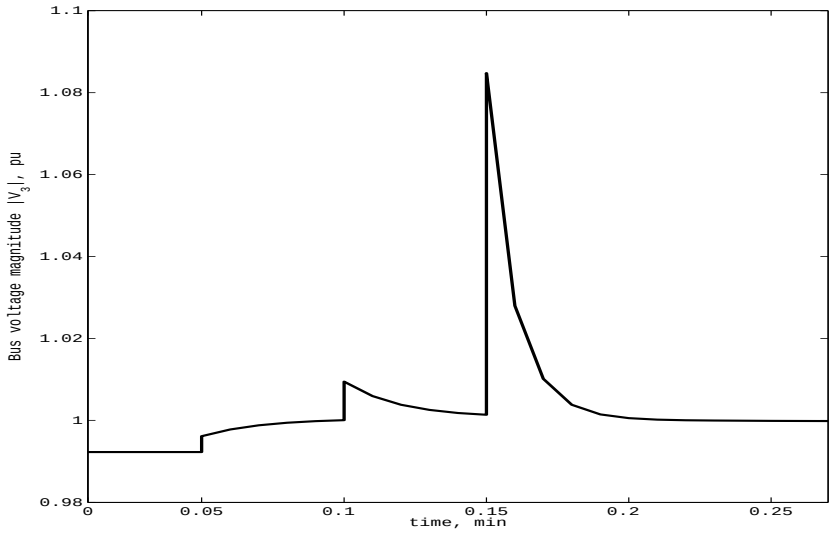

Figure 4.30: *Voltage magnitude at Bus* 3.

4.10 Summary

This chapter focuses on the dynamic model of generating plants. For the purpose of this research, dynamic stability assessment, mathematical models of the classical synchronous machine model and the advanced representation of it, with automatic voltage regulator, turbine, speed-governor and boiler, in a balanced three-phase frame of reference have been developed. A set of ordinary differential equations describing the components was obtained for each generating plant component. In each case, the differential equations of each component are transformed into an algebraic form taking advantage of the implicit trapezoidal rule. The differential-algebraic model of the network has been coded in software to carry out time domain analyses of power networks with combined dynamic and static elements. An implicit trapezoidal integration method embedded with a Newton-Raphson iteration technique has been selected to solve simultaneously, the differential and static system equations. The models and the solution method have been proven capable of performing adequately the long-term dynamic assessment of power systems. The trapezoidal rule is applied to discretise the dynamic equations corresponding to all the synchronous generators' variables and power plant components.

Several network disturbances, such as tripping lines, load variations and balanced three-phase faults have been studied using the developed algorithm. Where appropriate, the results reported are compared with the output of PSAT [Milano, 2007,Milano, 2005,Milano, 2006], a widely used transient stability simulation package within the academic community, yielding satisfactory agreement.

Chapter 5

Power System Loads Modelling

5.1 Load Modelling Concepts

5.1.1 Introduction

Over the past several years, the increasing concern over voltage stability has lead to an enormous effort in industry to develop acceptable techniques and tools for analysis of this phenomena [Taylor, 1994,IEEE Power Engineering Society, 2002,Morison et al., 1993]. Since voltage stability is characteristically different from other forms of stability, such as transient stability or small signal stability, new analytical and modeling approaches were required. Both steady-state (static) analyses methods (such as PV curves and modal analyses) and dynamic analyses (such as time-domain simulation) have gained industry acceptance and are now widely used.

An important step in the development of analyses methods involves identifying and developing models for system components, devices, and controls which are key to the voltage stability phenomenon. These include such examples as the modelling of reactive capability of generators including over-excitation limiters, Static Var Systems, automatic under-load tap-changer transformers, automatically switched capacitors, and load-shedding schemes. In gen-

eral, these can be considered deterministic modelling issues; the device structures/functions are not explicitly time-varying and once known, can be modelled with a reasonable degree of certainty. However, the driving force for voltage instability is usually the loads, which can be considered highly statistical in nature and, therefore, much more of a challenge when developing practical models which are generically applicable. Studies have shown that the results of stability simulations can be drastically affected by variations in load models; this is particularly true for voltage stability studies in which loads may be subjected to large variations in system voltages and in which short-term and long-term non-linear load characteristics may come into play. While there has been significant attention given to load modelling in industry [IEEE Load Task Force, 1993, IEEE Task Force on Load Representation, 1995, Xu and Mansour, 1994, Hagajos and Danai, 1998], including numerous IEEE and CIGRE publications, for most engineers, it remains a challenge to properly develop load models which can be used with confidence in practical day-to-day studies.

Power system engineers base decisions concerning system performance in large part on the results of power flow and stability simulation studies. In performing power system analyses, models must be developed for all relevant system components, including generating station, transmission and distribution equipment and load devices.

Much attention has been given to models for generation and transmission/distribution equipment as described in Chapter 4, and load representation has received a lack of attention and continues to be an area of greater uncertainty.

Many studies have shown that load representation can have a significant impact on analyses result [IEEE Load Task Force, 1993, IEEE Task Force on Load Representation, 1995]. Therefore, load modelling is of major importance and should be address and considered for dynamic performance analyses.

For purposes of system studies, the term "load" refers to the equivalent representation of the aggregate effects of many individual load devices and the interconnecting distribution and subtransmission systems that are not explicitly represented in the system model [IEEE

Power Engineering Society, 2002].

Load characteristics affect the dynamic behaviour of a power system and the importance of proper representation of loads in power system stability studies has long been recognized [Concordia and Ihara, 1982].

Load modelling for dynamic performance analyses has been greatly advanced in the past few years. A bibliographical review [IEEE Task Force on Load Representation, 1995] published in 1995 contained 118 references on the subject. However, the representation of loads for voltage stability analyses involves several aspects not required for conventional stability studies. The modelling of these effects is not well-established and is still the subject of ongoing investigation [IEEE Power Engineering Society, 2002].

For stability studies load representation is very common to be denoted by a load bus which represents incandescent and fluorescent lamps, heaters, air conditioner, ovens, refrigerators, motors, arc furnaces and so on. Induction motors constitute a major portion of the system load. The precise representation of load is difficult to estimate. Even when the precise representation of load is known, there are many other factors like time (hour, day, season), weather conditions and the state of the economy that prevent the load modelling in power systems [Kundur, 1994]. Hence, load representation in stability studies is based on a considerable amount of simplifications. The active and reactive power consumed by the load could be represented by a simple mathematical model, and the load models can be divided into two main categories:

a Static load model,

b Dynamic load model.

5.2 Static Load Model

In transient stability studies simulations, loads are typically modelled as purely static, (algebraic) functions according to their time responses to voltage and frequency variations in the system.

The load model can be defined as a mathematical representation of the relation between the active or reactive power (or the current injection) in a load bus and the complex voltage of this same bus.

Regularly, static models were used in earlier attempts to model load elements. However, to simplify the mathematical load expression frequency was considered constant, leading it to a load expression where only the voltage dependency is considered.

5.2.1 Polynomial representation

Typically both active and reactive power loads are represented by quadratic polynomials given by

$$P = P_0 \left[a_0 \left(\frac{|V|}{|V_0|} \right)^2 + a_1 \left(\frac{|V|}{|V_0|} \right) + a_2 \right] \tag{5.1}$$

$$Q = Q_0 \left[b_0 \left(\frac{|V|}{|V_0|} \right)^2 + b_1 \left(\frac{|V|}{|V_0|} \right) + b_2 \right] \tag{5.2}$$

where V_0, P_0 and Q_0 are normally taken as initial operating conditions.

Fig. 5.1 shows this load model representation.

The load elements were divided into:

i Constant impedance "Z",

ii Constant current "I" and

iii Constant power "P".

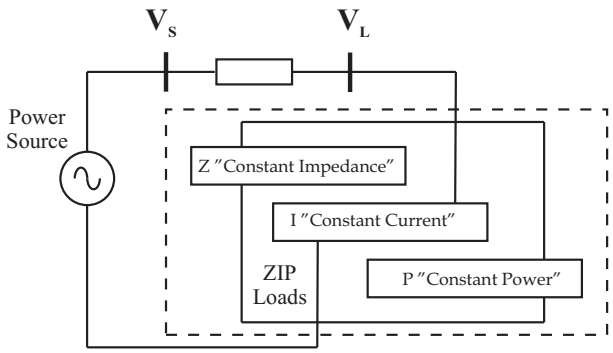

Figure 5.1: *Simple load representation as ZIP loads.*

The coefficients $a_{0,1,2}$ and $b_{0,1,2}$ are fractions of the constant power, constant current and constant impedance components in the active power loads. A constraint is imposed:

$$a_0 + a_1 + a_2 = 1$$

$$b_0 + b_1 + b_2 = 1$$

This load representation in not appropriate for cases involving large voltage variations.

5.2.2 Exponential representation

This load model has a voltage dependence of load characteristics and expresses the characteristics of the load at any instant or time as algebraic functions of the bus voltage magnitude at that moment [IEEE Load Task Force, 1993]. It is represented by,

$$P = P_o \left(\frac{|V|}{|V_o|} \right)^{np} \tag{5.3}$$

$$Q = Q_o \left(\frac{|V|}{|V_o|} \right)^{nq} \tag{5.4}$$

Note that by setting the exponents np and nq to 0, 1 or 2, the model represents con-

stant power, constant current or constant impedance characteristics, respectively. Exponents greater than 2 or less than 0 may be appropriate for some types of loads [IEEE Load Task Force, 1993].

For constant power model, the voltage is invariant and allows loads to be represented with a stiff voltage characteristic. The constant current model gives a load demand that varies linearly with voltage $np \approx nq \approx 1$. This is a practical representation of the real power demand as a mixture of resistance and motor devices. Finally, for constant impedance model, the load power changes proportionally $np \approx nq \approx 2$. This model represents lighting loads but it does not model stiff loads satisfactorily.

5.3 Frequency Load Model

For this load modelling, a static load model representation may includes frequency dependance. This is usually represented by expressing either a polynomial or exponential load model multiplied by a factor of the following form,

$$(1 + a_{pf}\Delta f)$$

where Δf is the frequency deviation, given by,

$$(f - f_0)$$

where f is the frequency of the bus voltage, f_0 is the rated frequency.

The value of a_{pf} normally ranges from 0 to 3.0 for the active contribution and from -2.0 to 0 for the reactive power contribution [Concordia and Ihara, 1982].

Usually, the bus voltage frequency is not an inherent state variable of the system however, it can be computed by taking the numerical derivative of the bus voltage angle.

5.4 Dynamic Load Model

Despite the effort to get more accurate load models where the voltage/frequency dependance is present [Hill, 1993, Anrborg et al., 1998], these models do not take into account the dynamic of the load and are still being modelled as static loads. Thus, to modelled the dynamic load behaviour in more detail where the voltage/frequency parameters and the dynamic itself of any electrical power system could be represented, an induction motor load representation is more than necessary.

In today's power systems, the motors consume a large fraction of the electricity generated. Hence, accurate modelling of these motors is required to capture the dynamics associated with the motors.

There is wide-ranging agreement that load characteristics have a marked influence on system stability, in general, and that induction motor loads play a dominate role during the initial stages of a voltage instability occurrence [Sekine and Ohtsuki, 1990, Hill, 1993], in particular.

5.4.1 Induction motor modelling

A simple and yet realistic model of the induction motor is used in the dynamic power flows algorithm. It is based on the equivalent circuit shown in Fig. 5.2, and corresponds to a single cage induction motor.

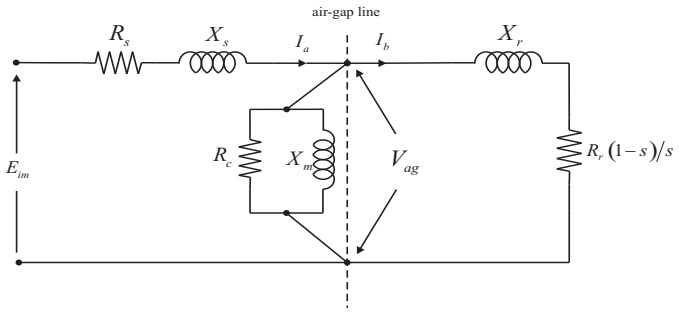

Figure 5.2: *Induction motor equivalent circuit.*

Where R_s and X_s are the resistance and reactance of the stator, respectively, R_c stands for core loses, X_m represents the magnetizing reactance, R_r and X_r are the rotor's resistance and reactance, respectively, and s is the slip. The applied voltage of the induction machine is $E_{im} = V_{im}e^{\mathrm{j}\theta_{im}}$, while I_a and I_b are the currents through stator and rotor, respectively.

The induction motor's stator and magnetizing branch impedances may be lumped together with the impedances of the transmission network and only the rotor is taken to be the dynamic element of it, with the air-gap line providing the interface between the two circuits. Hence, the rotor model consists of a first order differential equation where the rotor slip s is the state variable, and equations for active and reactive powers at the air-gap line are:

$$\dot{s} = \frac{1}{2H_{im}}\left(\frac{P_{im}}{1-s} - P_{ag}\right) \tag{5.5}$$

$$P_{ag} = \left(\frac{sR_r}{R_r^2 + s^2X_r^2}\right)(e_{ag}^2 + f_{ag}^2) \tag{5.6}$$

$$Q_{ag} = \left(\frac{s^2X_r}{R_r^2 + s^2X_r^2}\right)(e_{ag}^2 + f_{ag}^2) \tag{5.7}$$

where $s = (\omega_0 - \omega_r)/\omega_0$, $\omega_0 = 2\pi f$ is the synchronous speed, f is the base operating frequency, ω_r is the rotor speed, H_{im} is the induction motor's inertia constant, P_{im} is the mechanical output power, P_{ag} and Q_{ag} are the active and reactive powers at the air-gap line, e_{ag} and f_{ag} are the real and imaginary components of the air-gap voltage, R_r and X_r are the rotor's resistance and reactance, respectively.

As already has been described at Section 4.8, the set of DAE describing each plant component of the power network are interdependent and the simultaneous calculation provides for a more stable numerical solution.

The same procedure applied at Chapter 4 is applied for the differential equation of the induction motor, Eq. 5.5,

$$s_{(t)} - s_{(t-\Delta t)} = \frac{\Delta t}{2}\left[\frac{1}{2H_{im}}\left(\frac{P_m}{1-s_{(t)}} - P_{ag(t)}\right) + \frac{1}{2H_{im}}\left(\frac{P_m}{1-s_{(t-\Delta t)}} - P_{ag(t-\Delta t)}\right)\right] \quad (5.8)$$

in a compact way, it can be re-written as follow,

$$F_s = F_{s(t)} + F_{s(t-\Delta t)} + C_s = 0 \quad (5.9)$$

where

$$F_{s(t)} = s_{(t)} + \frac{\Delta t}{2}\left[\frac{1}{2H_{im}}\left(\frac{P_m}{1-s_{(t)}} - P_{ag(t)}\right)\right]$$
$$F_{s(t-\Delta t)} = -s_{(t-\Delta t)} + \frac{\Delta t}{2}\left[\frac{1}{2H_{im}}\left(\frac{P_m}{1-s_{(t-\Delta t)}} - P_{ag(t-\Delta t)}\right)\right]$$
$$C_s = 0$$

Equations 4.32 and 4.33 describing the active and reactive powers injected in the network buses reported at Section 4.5, are augmented to incorporate explicitly the active and reactive powers contributed by all induction motors and generators in the network, respectively. Hence, at generator buses and load buses with an induction motor load representation,

$$P_{(k)} + P_{e(genbus(l))} \quad (5.10)$$
$$Q_{(k)} + Q_{e(genbus(l))}$$

$$P_{(m)} + P_{ag(imbus(n))} \quad (5.11)$$
$$Q_{(m)} + Q_{ag(imbus(n))}$$

for k=1,...,nbus and l=1,...,ngen, where $genbus(l)$ is an array of generator-connected buses and for m=1,...,nbus and n=1,...,nim, where $imbus(n)$ is an array of induction motor-connected buses.

When induction motors are considered, Eqs. 4.32, 4.33 and Eq. 4.44 for load buses, Eq. 4.42 to Eq. 4.44 for generator buses and Equation 5.9 for induction motors form the necessary set with which to carry out dynamic power flows solutions of a power system with induction motor loads. To solve the equation set, the Newton-Raphson method may be used to carry out the solution using a linearised system of equations. For this case, Eq. 4.45 must be modified to include the dynamic effects of the induction motor, yielding to the following linearised system of equations:

$$\begin{bmatrix} \boldsymbol{\Delta P} \\ \boldsymbol{\Delta Q} \\ -- \\ \boldsymbol{F_{\omega}} \\ \boldsymbol{F_{\delta}} \\ \boldsymbol{F_{E'_d}} \\ \boldsymbol{F_{E'_q}} \\ \boldsymbol{F_{E''_d}} \\ \boldsymbol{F_{E''_q}} \\ -- \\ \boldsymbol{F_s} \end{bmatrix} = \begin{bmatrix} \mathbf{J_{11}} & | & \mathbf{J_{12}} & | & \mathbf{J_{13}} \\ -- & + & -- & + & -- \\ \mathbf{J_{21}} & | & \mathbf{J_{22}} & | & \mathbf{J_{23}} \\ -- & + & -- & + & -- \\ \mathbf{J_{31}} & | & \mathbf{J_{32}} & | & \mathbf{J_{33}} \end{bmatrix} \begin{bmatrix} \boldsymbol{\Delta e} \\ \boldsymbol{\Delta f} \\ -- \\ \boldsymbol{\Delta \omega} \\ \boldsymbol{\Delta \delta} \\ \boldsymbol{\Delta E'_d} \\ \boldsymbol{\Delta E'_q} \\ \boldsymbol{\Delta E''_d} \\ \boldsymbol{\Delta E''_q} \\ -- \\ \boldsymbol{\Delta s} \end{bmatrix} \tag{5.12}$$

where

$$\Delta P = [\Delta P_g, \ldots, \Delta P_n]^t$$
$$\Delta Q = [\Delta Q_g, \ldots, \Delta Q_n]^t$$
$$\Delta e = [\Delta e_g, \ldots, \Delta e_n]^t$$
$$\Delta f = [\Delta f_g, \ldots, \Delta f_n]^t$$
$$\Delta \omega = [\Delta \omega_g, \ldots, \Delta \omega_r]^t$$
$$\Delta \delta = [\Delta \delta_g, \ldots, \Delta \delta_r]^t$$
$$\Delta E'_d = \left[\Delta E'_{d_g}, \ldots, \Delta E'_{d_r}\right]^t$$
$$\Delta E'_q = \left[\Delta E'_{q_g}, \ldots, \Delta E'_{q_r}\right]^t$$
$$\Delta E''_d = \left[\Delta E''_{d_g}, \ldots, \Delta E''_{d_r}\right]^t$$
$$\Delta E''_q = \left[\Delta E''_{q_g}, \ldots, \Delta E''_{q_r}\right]^t$$
$$\Delta s = [\Delta s_j, \ldots, \Delta s_m]^t$$
$$F_\omega = \left[F_{\omega_g}, \ldots, F_{\omega_r}\right]^t$$
$$F_\delta = \left[F_{\delta_g}, \ldots, F_{\delta_r}\right]^t$$
$$F_{E'_d} = \left[F_{E'_{d_g}}, \ldots, F_{E'_{d_r}}\right]^t$$
$$F_{E'_q} = \left[F_{E'_{q_g}}, \ldots, F_{E'_{q_r}}\right]^t$$
$$F_{E''_d} = \left[F_{E''_{d_g}}, \ldots, F_{E''_{d_r}}\right]^t$$
$$F_{E''_q} = \left[F_{E''_{q_g}}, \ldots, F_{E''_{q_r}}\right]^t$$
$$F_s = \left[F_{s_j}, \ldots, F_{s_m}\right]^t$$

with the various Jacobian entries defined as:

$$\mathbf{J_{11}} = \begin{bmatrix}
\left(\frac{\partial P_g}{\partial e_g} + \frac{\partial P_{eg}}{\partial e_g}\right) & \left(\frac{\partial P_g}{\partial f_g} + \frac{\partial P_{eg}}{\partial f_g}\right) & \cdots & \frac{\partial P_g}{\partial e_l} & \frac{\partial P_g}{\partial f_l} & \cdots & \frac{\partial P_g}{\partial e_m} & \frac{\partial P_g}{\partial f_m} \\
\left(\frac{\partial Q_g}{\partial e_g} + \frac{\partial Q_{eg}}{\partial e_g}\right) & \left(\frac{\partial Q_g}{\partial f_g} + \frac{\partial Q_{eg}}{\partial f_g}\right) & \cdots & \frac{\partial P_g}{\partial e_l} & \frac{\partial P_g}{\partial f_l} & \cdots & \frac{\partial Q_g}{\partial e_m} & \frac{\partial Q_g}{\partial f_m} \\
\vdots & \vdots & \ddots & \vdots & \vdots & \ddots & \vdots & \vdots \\
\frac{\partial P_l}{\partial e_g} & \frac{\partial P_l}{\partial f_g} & \cdots & \frac{\partial P_l}{\partial e_l} & \frac{\partial P_l}{\partial f_l} & \cdots & \frac{\partial P_l}{\partial e_m} & \frac{\partial P_l}{\partial f_m} \\
\frac{\partial Q_l}{\partial e_g} & \frac{\partial Q_l}{\partial f_g} & \cdots & \frac{\partial P_l}{\partial e_l} & \frac{\partial P_l}{\partial f_l} & \cdots & \frac{\partial Q_l}{\partial e_m} & \frac{\partial Q_l}{\partial f_m} \\
\vdots & \vdots & \ddots & \vdots & \vdots & \ddots & \vdots & \vdots \\
\frac{\partial P_m}{\partial e_g} & \frac{\partial P_m}{\partial f_g} & \cdots & \frac{\partial P_m}{\partial e_l} & \frac{\partial P_m}{\partial f_l} & \cdots & \left(\frac{\partial P_m}{\partial e_m} + \frac{\partial P_{em}}{\partial e_m}\right) & \left(\frac{\partial P_m}{\partial f_m} + \frac{\partial P_{em}}{\partial f_m}\right) \\
\frac{\partial Q_m}{\partial e_g} & \frac{\partial Q_m}{\partial f_g} & \cdots & \frac{\partial Q_m}{\partial e_l} & \frac{\partial P_m}{\partial f_l} & \cdots & \left(\frac{\partial P_m}{\partial e_m} + \frac{\partial P_{em}}{\partial e_m}\right) & \left(\frac{\partial P_m}{\partial f_m} + \frac{\partial P_{em}}{\partial f_m}\right)
\end{bmatrix}$$

Entry $\mathbf{J_{11}}$ is essentially the Jacobian matrix of the conventional Newton-Raphson method in rectangular coordinates but with the following extensions: (i) full contribution of the slack bus is included; (ii) the Jacobian terms of the generator stator powers are added to the self elements contributed by the network at generator buses (bus g in matrix $\mathbf{J_{11}}$, where $g = 1, \ldots,$ngen); (iii) the Jacobian terms of the induction motor stator powers are added to the self elements contributed by the network at induction motor buses (bus m in matrix $\mathbf{J_{11}}$, where $m = 1, \ldots,$nim). It should be noted that in matrix $\mathbf{J_{11}}$, load buses with no induction motor load are termed l.

$$\mathbf{J_{22}} = \begin{bmatrix}
\frac{\partial F_{\omega g}}{\partial \omega_g} & \frac{\partial F_{\omega g}}{\partial \delta_g} & \frac{\partial F_{\omega g}}{\partial E'_{dg}} & \frac{\partial F_{\omega g}}{\partial E'_{qg}} & \frac{\partial F_{\omega g}}{\partial E''_{dg}} & \frac{\partial F_{\omega g}}{\partial E''_{qg}} \\
\frac{\partial F_{\delta g}}{\partial \omega_g} & \frac{\partial F_{\delta g}}{\partial \delta_g} & \frac{\partial F_{\delta g}}{\partial E'_{dg}} & \frac{\partial F_{\delta g}}{\partial E'_{qg}} & \frac{\partial F_{\delta g}}{\partial E''_{dg}} & \frac{\partial F_{\delta g}}{\partial E''_{qg}} \\
\frac{\partial F_{E'_{dg}}}{\partial \omega_g} & \frac{\partial F_{E'_{dg}}}{\partial \delta_g} & \frac{\partial F_{E'_{dg}}}{\partial E'_{dg}} & \frac{\partial F_{E'_{dg}}}{\partial E'_{qg}} & \frac{\partial F_{E'_{dg}}}{\partial E''_{dg}} & \frac{\partial F_{E'_{dg}}}{\partial E''_{qg}} \\
\frac{\partial F_{E'_{qg}}}{\partial \omega_g} & \frac{\partial F_{E'_{qg}}}{\partial \delta_g} & \frac{\partial F_{E'_{qg}}}{\partial E'_{dg}} & \frac{\partial F_{E'_{qg}}}{\partial E'_{qg}} & \frac{\partial F_{E'_{qg}}}{\partial E''_{dg}} & \frac{\partial F_{E'_{qg}}}{\partial E''_{qg}} \\
\frac{\partial F_{E''_{dg}}}{\partial \omega_g} & \frac{\partial F_{E''_{dg}}}{\partial \delta_g} & \frac{\partial F_{E''_{dg}}}{\partial E'_{dg}} & \frac{\partial F_{E''_{dg}}}{\partial E'_{qg}} & \frac{\partial F_{E''_{dg}}}{\partial E''_{dg}} & \frac{\partial F_{E''_{dg}}}{\partial E''_{qg}} \\
\frac{\partial F_{E''_{qg}}}{\partial \omega_g} & \frac{\partial F_{E''_{qg}}}{\partial \delta_g} & \frac{\partial F_{E''_{qg}}}{\partial E'_{dg}} & \frac{\partial F_{E''_{qg}}}{\partial E'_{qg}} & \frac{\partial F_{E''_{qg}}}{\partial E''_{dg}} & \frac{\partial F_{E''_{qg}}}{\partial E''_{qg}}
\end{bmatrix}$$

$$\mathbf{J_{33}} = \left[\begin{array}{c} \frac{\partial F_{s_{im}}}{\partial s_{im}} \end{array} \right]$$

$$\mathbf{J_{12}} = \left[\begin{array}{cccccc} \frac{\partial P_g}{\partial \omega_g} & \frac{\partial P_g}{\partial \delta_g} & \frac{\partial P_g}{\partial E'_{d_g}} & \frac{\partial P_g}{\partial E'_{q_g}} & \frac{\partial P_g}{\partial E''_{d_g}} & \frac{\partial P_g}{\partial E''_{q_g}} \\ \frac{\partial Q_g}{\partial \omega_g} & \frac{\partial Q_g}{\partial \delta_g} & \frac{\partial Q_g}{\partial E'_{d_g}} & \frac{\partial Q_g}{\partial E'_{q_g}} & \frac{\partial Q_g}{\partial E''_{d_g}} & \frac{\partial Q_g}{\partial E''_{q_g}} \\ \vdots & \vdots & \vdots & \vdots & \vdots & \vdots \\ \mathbf{0} & \mathbf{0} & \mathbf{0} & \mathbf{0} & \mathbf{0} & \mathbf{0} \end{array} \right]$$

$$\mathbf{J_{21}} = \left[\begin{array}{ccc} \frac{\partial F_{\omega_g}}{\partial e_g} & \frac{\partial F_{\omega_g}}{\partial f_g} & \cdots \; \mathbf{0} \\ \frac{\partial F_{\delta_g}}{\partial e_g} & \frac{\partial F_{\delta_g}}{\partial f_g} & \cdots \; \mathbf{0} \\ \frac{\partial F_{E'_{d_g}}}{\partial e_g} & \frac{\partial F_{E'_{d_g}}}{\partial f_g} & \cdots \; \mathbf{0} \\ \frac{\partial F_{E'_{q_g}}}{\partial e_g} & \frac{\partial F_{E'_{q_g}}}{\partial f_g} & \cdots \; \mathbf{0} \\ \frac{\partial F_{E''_{d_g}}}{\partial e_g} & \frac{\partial F_{E''_{d_g}}}{\partial f_g} & \cdots \; \mathbf{0} \\ \frac{\partial F_{E''_{q_g}}}{\partial e_g} & \frac{\partial F_{E''_{q_g}}}{\partial f_g} & \cdots \; \mathbf{0} \end{array} \right]$$

$$\mathbf{J_{23}} = \left[\begin{array}{cc} \frac{\partial F_{\omega_1}}{\partial s_1} & \cdots \; \mathbf{0} \\ \frac{\partial F_{\delta_1}}{\partial s_1} & \cdots \; \mathbf{0} \\ \frac{\partial F_{E'_{d_1}}}{\partial s_1} & \cdots \; \mathbf{0} \\ \frac{\partial F_{E'_{q_1}}}{\partial s_1} & \cdots \; \mathbf{0} \\ \frac{\partial F_{E''_{d_1}}}{\partial s_1} & \cdots \; \mathbf{0} \\ \frac{\partial F_{E''_{q_1}}}{\partial s_1} & \cdots \; \mathbf{0} \end{array} \right]$$

$$\mathbf{J_{32}} = \begin{bmatrix} \frac{\partial F_{s_{im}}}{\partial \omega_g} & \frac{\partial F_{s_{im}}}{\partial \delta_g} & \frac{\partial F_{s_{im}}}{\partial E'_{dg}} & \frac{\partial F_{s_{im}}}{\partial E'_{qg}} & \frac{\partial F_{s_{im}}}{\partial E''_{dg}} & \frac{\partial F_{s_{im}}}{\partial E''_{qg}} \end{bmatrix}$$

$$\mathbf{J_{13}} = \begin{bmatrix} \frac{\partial P_g}{\partial s_{im}} \\ \frac{\partial Q_g}{\partial s_{im}} \\ \vdots \\ \mathbf{0} \end{bmatrix}$$

$$\mathbf{J_{31}} = \begin{bmatrix} \frac{\partial F_{s_{im}}}{\partial e_g} & \frac{\partial F_{s_{im}}}{\partial f_g} & \cdots & \mathbf{0} \end{bmatrix}$$

In matrix entries $\mathbf{J_{12}}$, $\mathbf{J_{21}}$, $\mathbf{J_{13}}$ and $\mathbf{J_{31}}$ all zero terms are null vectors of suitable dimensions required to pad out the various matrix entries. Notice also that if no induction motors and generators share the same bus, matrix entries $\mathbf{J_{23}}$ and $\mathbf{J_{32}}$ are null entries.

In addition to the entries corresponding to the generating plant itself the Jacobian also considers mutual terms corresponding to the interface between the network and the generating plant.

5.5 Results

5.5.1 Test case 1

To validate the induction motor model, a time domain simulation has been carried out and compared with a dynamic simulation where the load is represented by its voltage/frequency dependence load model [Concordia and Ihara, 1982,IEEE Task Force on Load Representation, 1995].

The test system used for the induction motor validation is depicted at Fig. 5.3.

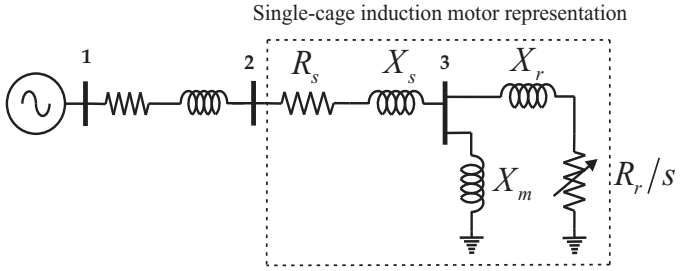

Figure 5.3: *Single-cage induction motor representation.*

To fully model the induction motor as depicted at Fig. 5.2, the induction motor's stator impedances, $R_s + \mathrm{j}X_s$, and the magnetizing branch, X_m are grouped with the impedances of the transmission network and only the rotor is modelled according to Eq. 5.7. The core resistance, R_c of Fig. 5.2 is neglected.

For validation purposes, the circuit delimited by the dashed line of Fig. 5.3, is replaced by a load represented by its voltage/frequency dependance load model, as shown in Fig. 5.4. There is the notion that the exponential representation with index equal to 1 may be used to good effect to represent an induction motor load.

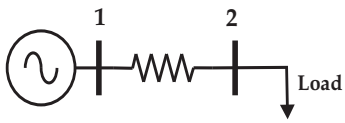

Figure 5.4: *Static load model representation.*

The scenario considered for this study is a load aggregation at Bus 2. A load is added at $t = 0.05$m, using a 0.25 pu resistive impedance. The simulation is carried out with a 200kW induction machine [Pedra et al., 2005] described in Table 5.5.1. The simulation is run for five minutes.

Fig. 5.5 shows the bus voltage profile for the induction motor load model and the voltage/frequency dependence load model at Bus 2.

Fig. 5.6 and 5.7 depict the active and reactive consumed powers at Bus 2, for the induction

Table 5.1: *Induction Motor Parameters*

Rated output power,	500kW
Rated voltage,	400V
Rated frequency,	50Hz
$R_s = 0.00360$ pu	$X_s = 0.08179$ pu
$R_r = 0.00719$ pu	$X_r = 0.08179$ pu
$X_m = 2.2940$ pu	

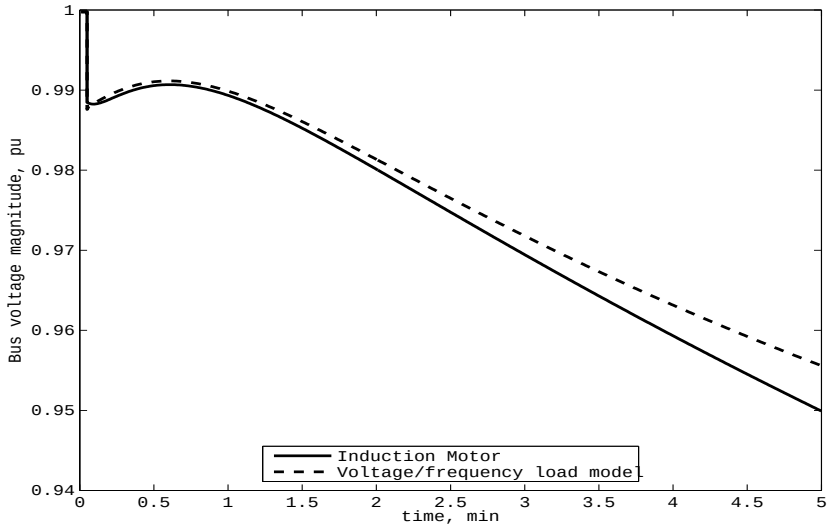

Figure 5.5: *Bus voltage magnitude at Bus* 2.

motor load model and the voltage/frequency dependance load model.

As expected, the response between the induction motor model representation and the voltage/frequency load model representation agree on well for the steady-state period but they do so how to have a slightly different dynamic behaviour.

Fig. 5.8 and Fig. 5.9 show the slip performance, s and the voltage profile at the air-gap line, V_{ag}. 5.2. Fig. 5.10 shows the voltage frequency deviation at Bus 2.

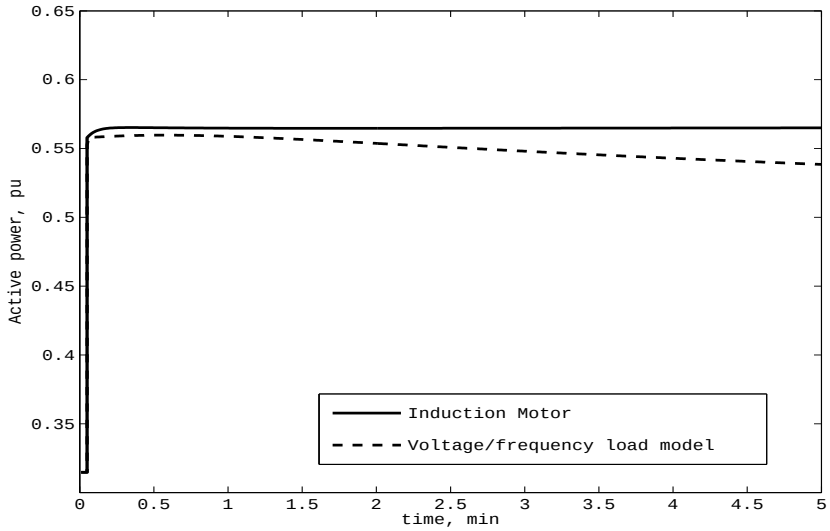

Figure 5.6: *Active power injection at Bus* 2.

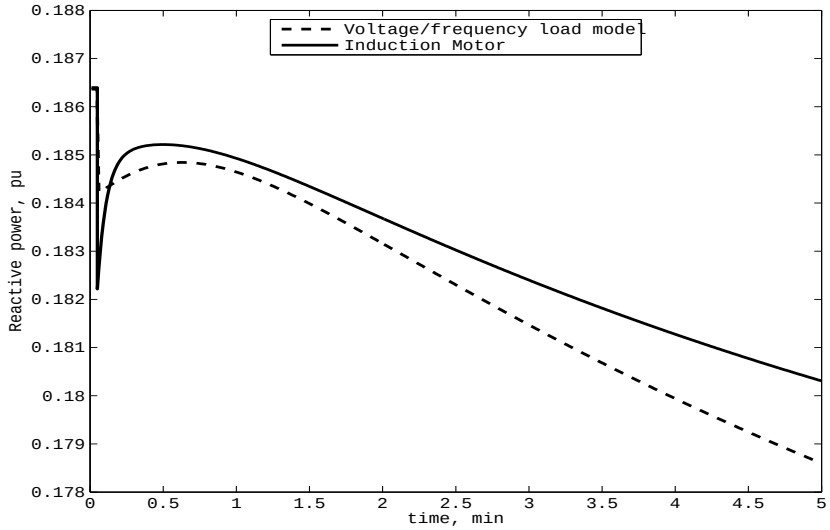

Figure 5.7: *Reactive power injection at Bus* 2.

5.5.2 Test case 2

The dynamic behaviour of the induction motor is assessed more fully. The test system used is the nine-bus, three-machine power system depicted at Fig. 4.16 [Chow, 1982,Anderson and Fouad, 1997].

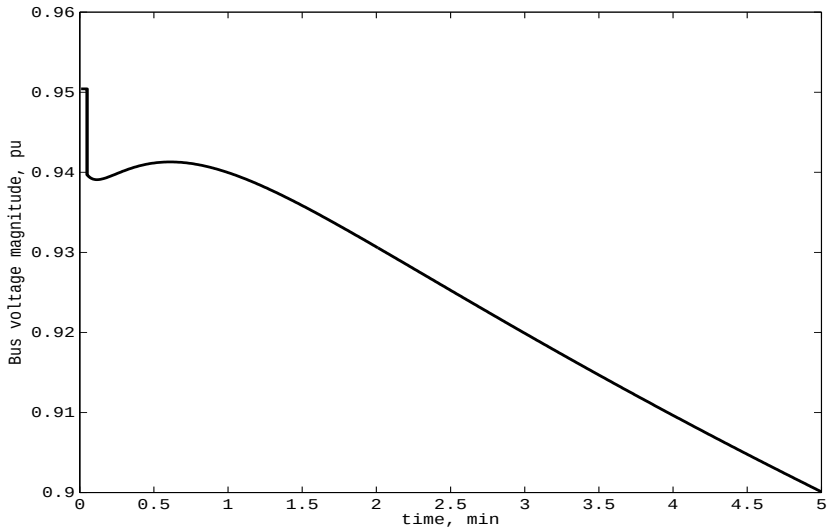

Figure 5.8: *Air-gap voltage profile.*

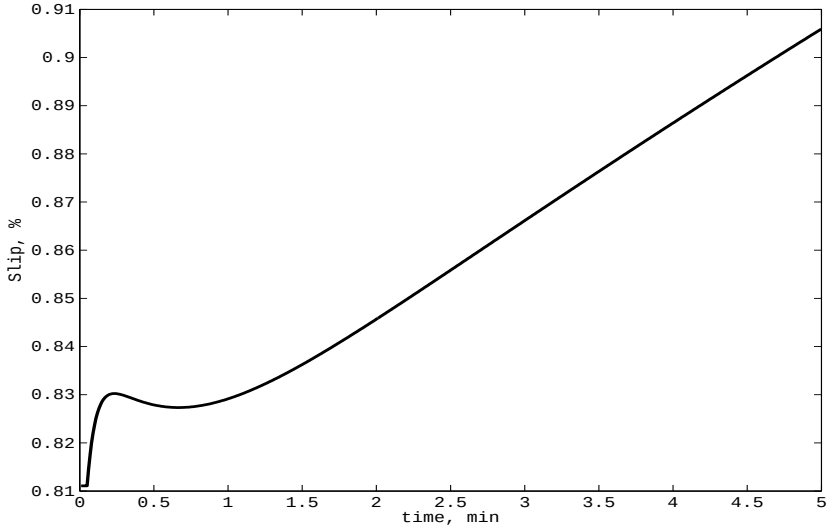

Figure 5.9: *Slip performance.*

To demonstrate the applicability and versatility of the dynamic power flows tool and the induction motor modelling, the loads of Buses 5 and 6 of Fig. 4.16 have been replaced for two small industrial induction motors [Kundur, 1994]. The load connected at Bus 8 remains as an static load. There is a 35% load increment of phase c at this bus at time 1 min. The

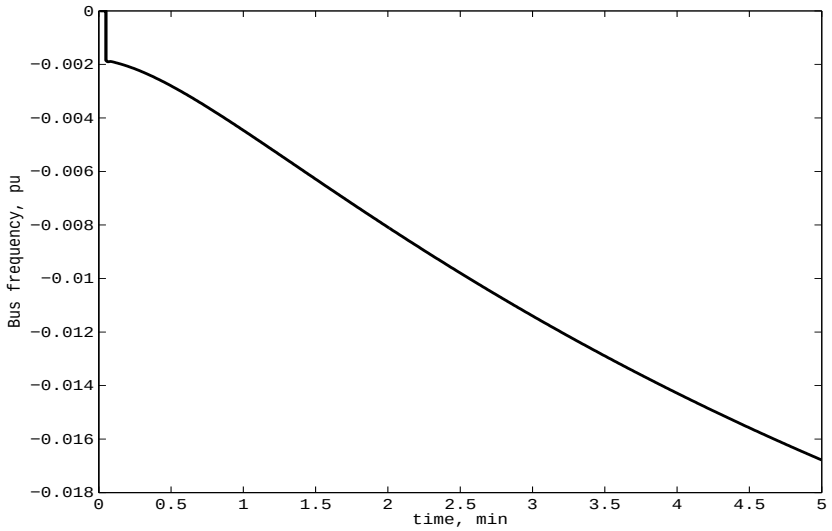

Figure 5.10: *Bus frequency deviation.*

simulation is run for 10 minutes.

Figure 5.11 and Fig. 5.12 show active and reactive power consumed by the induction motors, respectively.

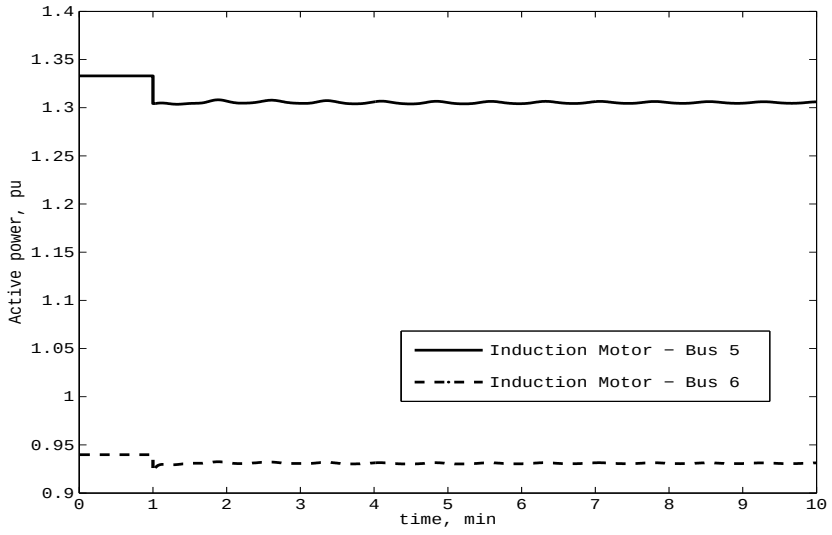

Figure 5.11: *Active power consumption by the induction motors.*

Fig. 5.13 depicts the slip performance for the induction motor during the transient sim-

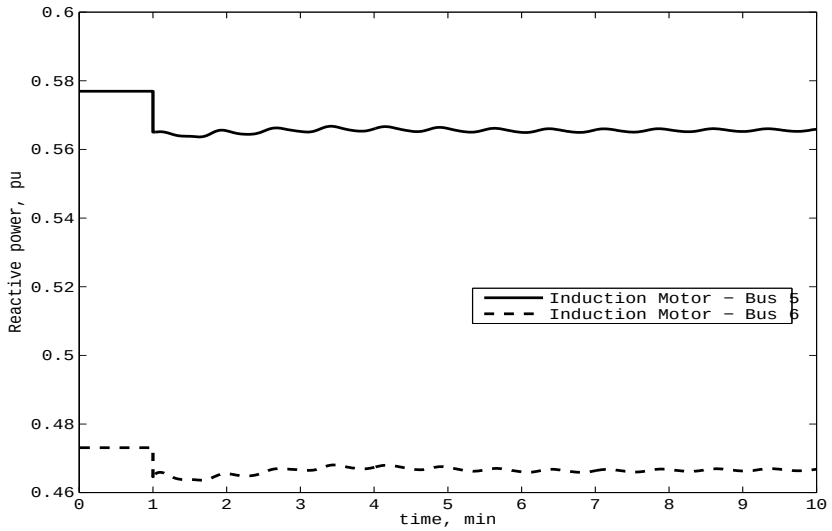

Figure 5.12: *Reactive power consumption by the induction motors.*

ulation.

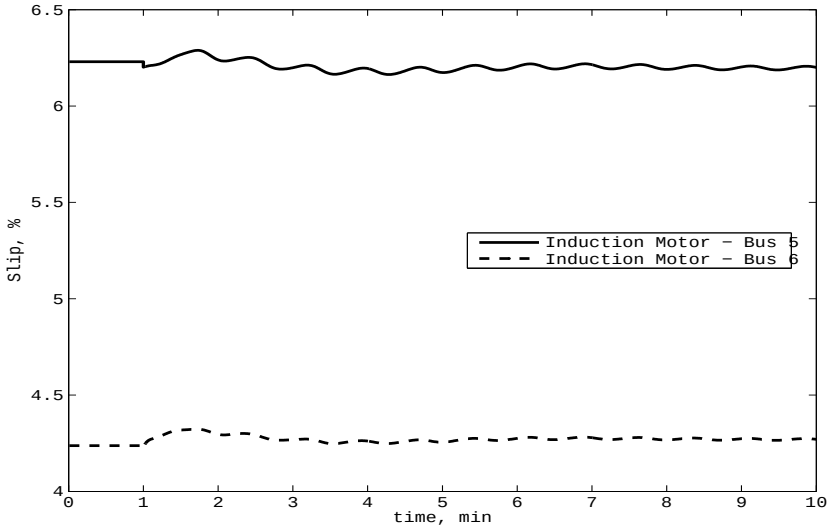

Figure 5.13: *Slip performance.*

Fig. 5.14 depicts the bus voltage magnitude at load-connected buses. The voltage magnitude at the induction motor-connected buses is also affected by the load variation perturbation however, it drops less than at the affected bus, as is shown in Fig. 5.14. Due to load mod-

ification, it brings about a generators' field voltage E_f increment, as depicted at Fig. 5.15. From Fig. 5.15, it can be said, that the synchronous generators connected at Buses 2 and 3 supply more energy than the one connected at Bus 1, due to the former ones being closer to the perturbation point.

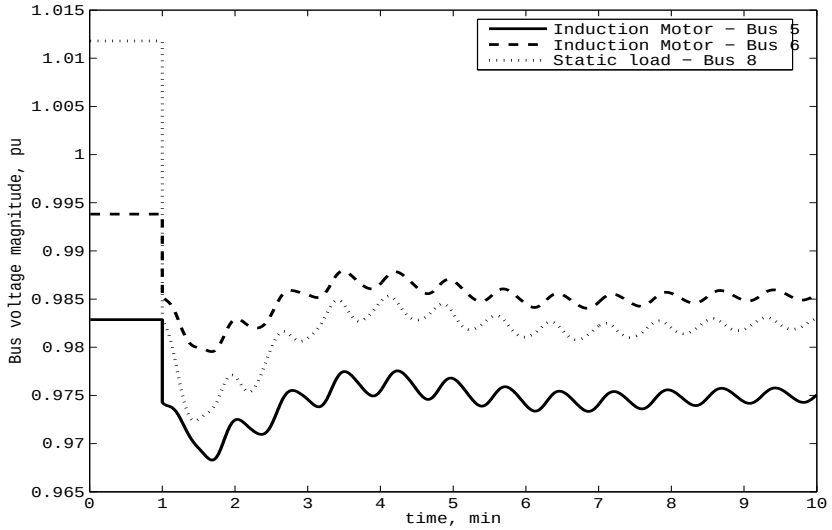

Figure 5.14: *Bus voltage magnitude at load-connected buses.*

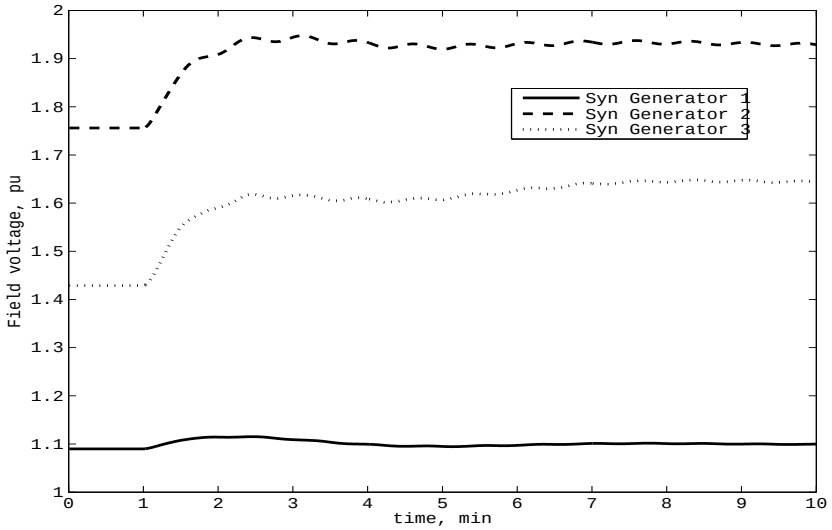

Figure 5.15: *Generators' field voltage.*

5.5.3 Test case 3

The dynamic behaviour of the induction motor load is assessed further in this section, with an induction motor with parameter data corresponding to a large industrial motor [Kundur, 1994], replacing the load connected at Bus 5. The perturbation consists in increasing the torque of this induction motor by 25%. Figs. 5.16 and 5.17 show the active and reactive powers drawn by the induction motor, where the former jumps from just over 1.3 pu in steady-state to a new value of 1.66 pu, an increase of approximately 27%. Likewise, the reactive power consumption goes from 0.39 pu to 0.46 pu, an increase of almost 18%.

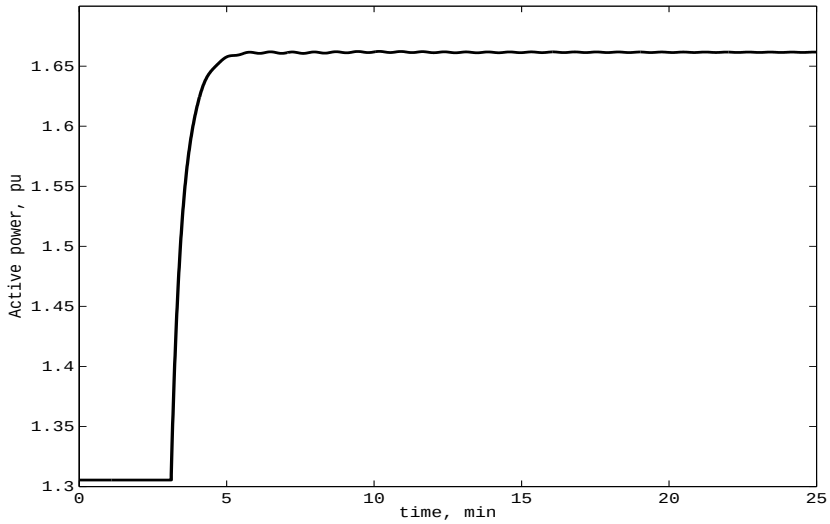

Figure 5.16: *Active power consumption of the induction motor.*

As shown in Fig. 5.18, the slip has an initial value of 8.1% and following the perturbation it settles to a value of 10.75%. Fig 5.19 depicts the bus voltage magnitude for all buses. It it shown, that after a bus voltage drop at all buses the system remains stable. Fig 5.20 shows the angular velocity for the three generators.

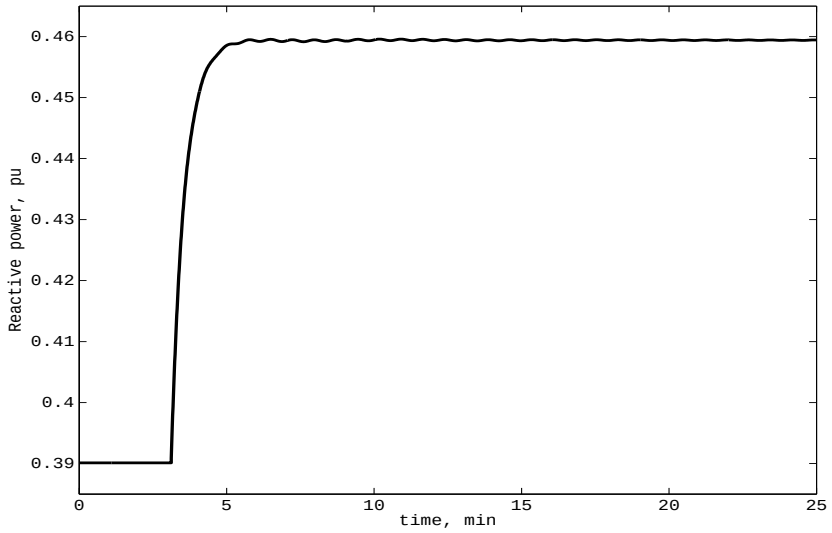

Figure 5.17: *Reactive power consumption of the induction motor.*

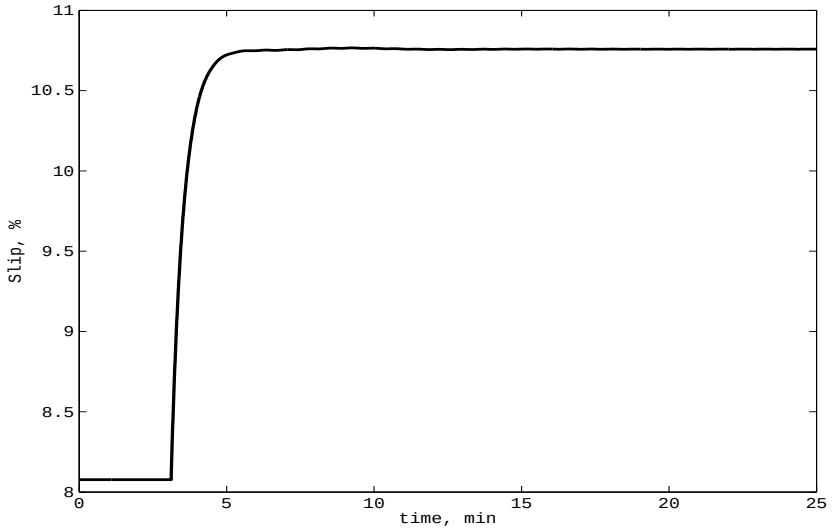

Figure 5.18: *Slip performance of the induction motor.*

5.5.4 Test case 4

The dynamic power flows algorithm is used to analyse the dynamic response of the New England test system [Chow, 1982], depicted in Fig. 5.21. It consists of 39 buses, 10 generators, 36 transmission lines and 10 transformers. Four distinct simulation studies are conducted in

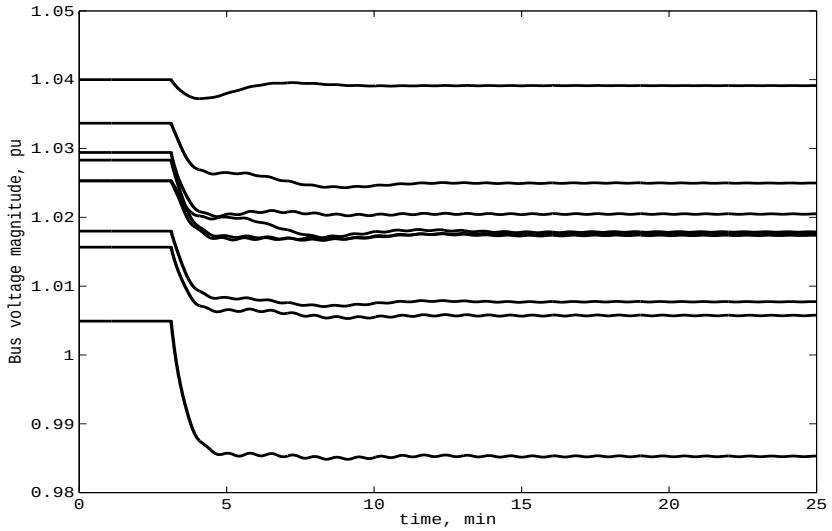

Figure 5.19: *Bus voltage profile.*

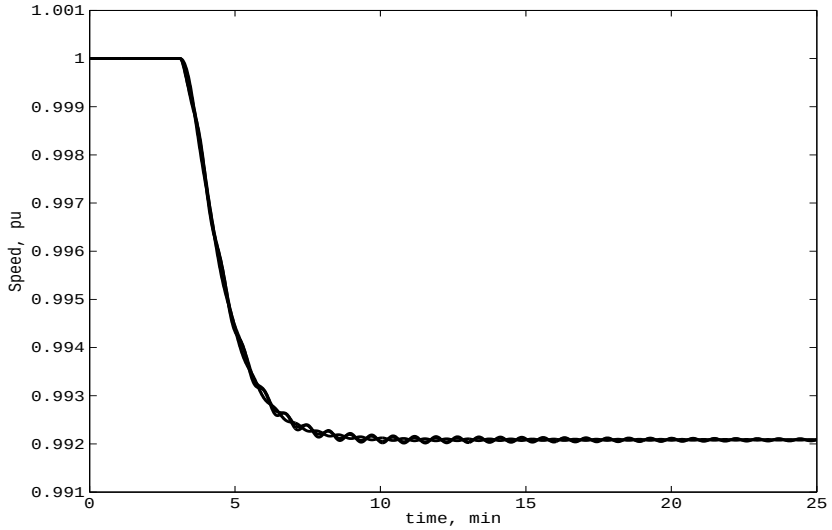

Figure 5.20: *Generators' speed.*

this section, each relating to a different kind of load representation, namely induction motor and exponential load model with indices 0, 1 and 2, respectively. In each case, all loads are assumed to be of the same kind. The aim is to carry out a series of planned outages which have the effect of pushing the system into a state of voltage instability. At the simulation

level, such outages lead to very low voltages at several nodes of the network, and it comes a point during the simulation that the dynamic power flows algorithm fails to converge.

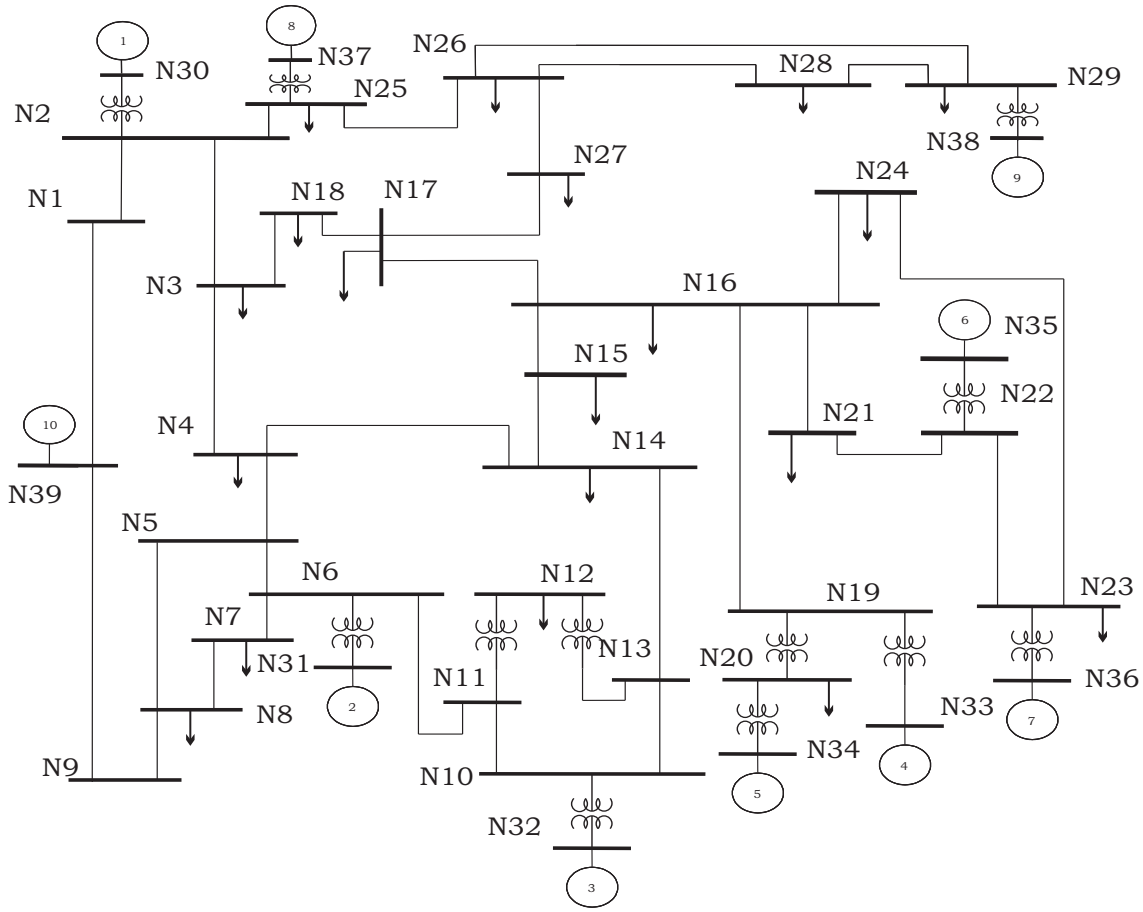

Figure 5.21: *One-line New England test system diagram.*

The sequence of planned outage events is as follows: at time 0.05 s, transmission lines connecting Bus N17 and buses N27, N16 and N18 are tripped; as a consequence of this, Bus N17, including its load, becomes isolated from the system, producing voltage drops in the majority of buses, as shown in Fig. 5.23. Later on, at time 0.1 s, the transmission line connecting buses N3 and N18 is disconnected, causing Bus N18 and its load to separate from the system, resulting in an overall recovery of system voltages, as shown in Fig. 5.23. This is followed by the tripping of transmission line connecting buses N3 and N4, at time 0.15 s; an

event which to a greater or lesser extent reduces voltages at all buses. This trend accentuates with time and in several buses, when the system load is represented by induction motors, the voltages drop below 0.93 p.u. at a time 0.25 s. Just after 0.42 s, the voltage at Bus N14, which has shown to be the weakest bus, reaches a value of 0.85 p.u. and the dynamic power flows algorithm can not reach convergence any longer. The results in Fig. 5.22 corresponds to the case when all loads are assumed to be induction motors with parameter data corresponding to a large industrial motor [Kundur, 1994].

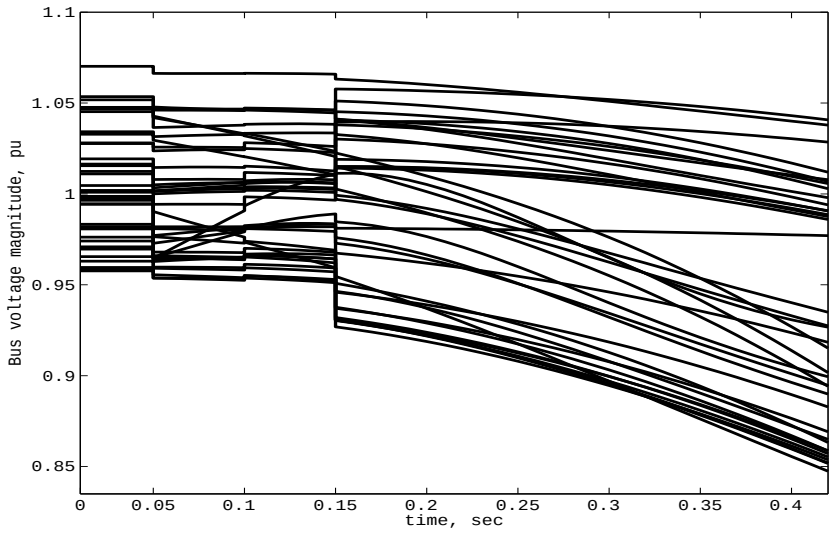

Figure 5.22: *Bus voltage profile - Loads as induction motors.*

In Fig. 5.23 it is shown how the overall system voltage perform when the load is exponential with index 1. The simulation seems to be slightly more robust with the static load representation with exponential index 1 than with the dynamic load representation; the simulation runs for almost 0.50 s but the downward trend of system voltage is very much in line with that observed in Fig. 5.22 for the case of induction motor load. A more detailed assessment is made with reference to Fig. 5.26, where nodal voltages are shown for Bus N14; the weakest bus in the network. Four different results are shown, corresponding to the four kinds of load representation used in the study. At this particular bus, the dynamic load voltage

response exhibits the higher profile and this is followed by the static load representations with exponential indices 0, 1 and 2, respectively. The load representation with exponential index 2 is too pessimistic and posses the biggest challenge to the dynamic power flow algorithm. The solution is halted at just after 0.37 s. The load representation with exponential index 1 posses the least challenge to the algorithm but the nodal voltages are still well below those of the induction motor and the static load representation with exponential index 0.

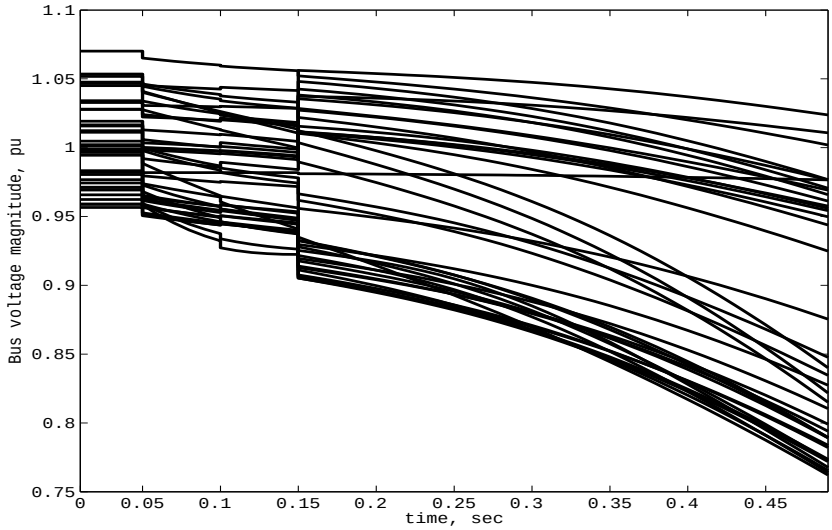

Figure 5.23: *Bus voltage profile - Loads with exponential indices equal to* 1.

Moreover, the active and reactive power consumed by the induction motors are depicted at Fig. 5.24 and 5.25, respectively.

For completeness, Fig. 5.28 shows the slip behaviour of the induction motor connected to Bus N14 and Fig. 5.27 shows slip performance for all the induction motors. The figures clearly shows that at time 0.15 s, following the tripping of transmission line N3-N4, the slip for most of the induction motors exhibits a relatively large swing.

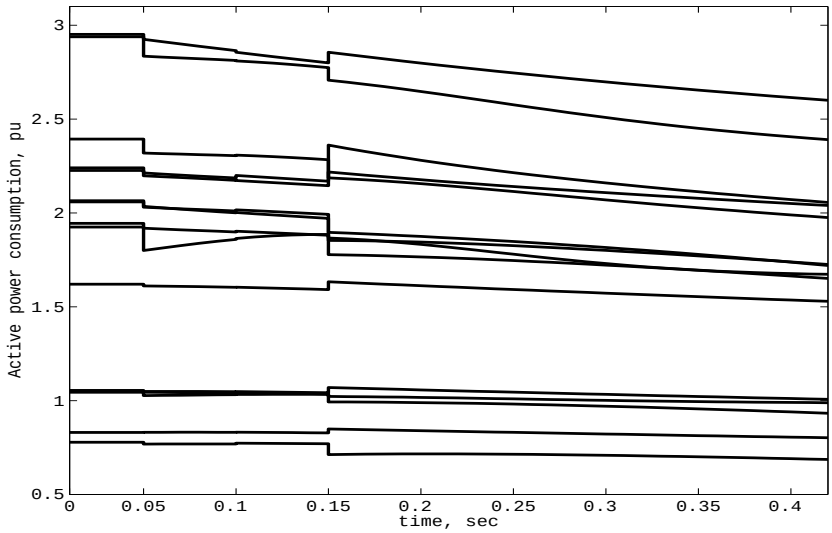

Figure 5.24: *Active power consumed by the induction motors.*

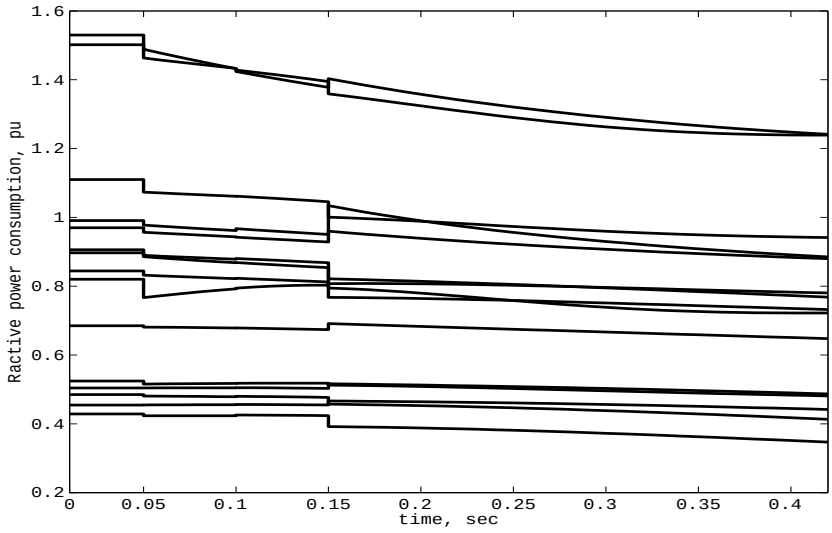

Figure 5.25: *Reactive power consumed by the induction motors..*

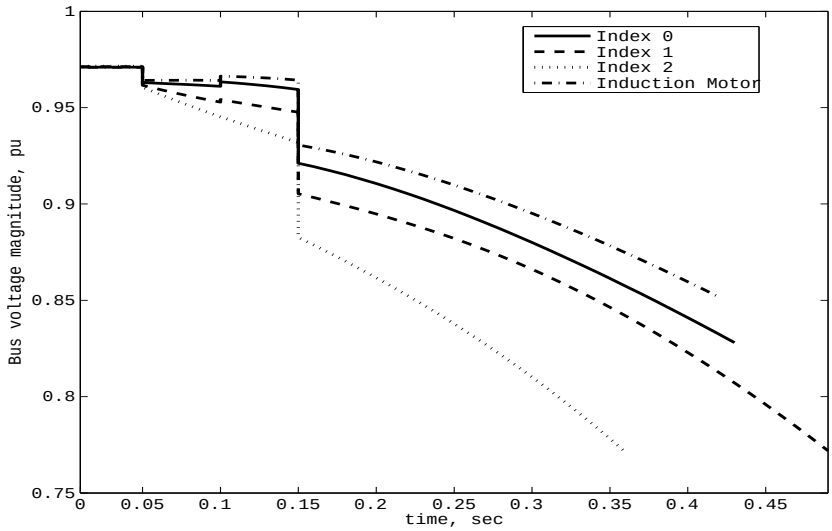

Figure 5.26: *Voltage magnitudes at N*14*.*

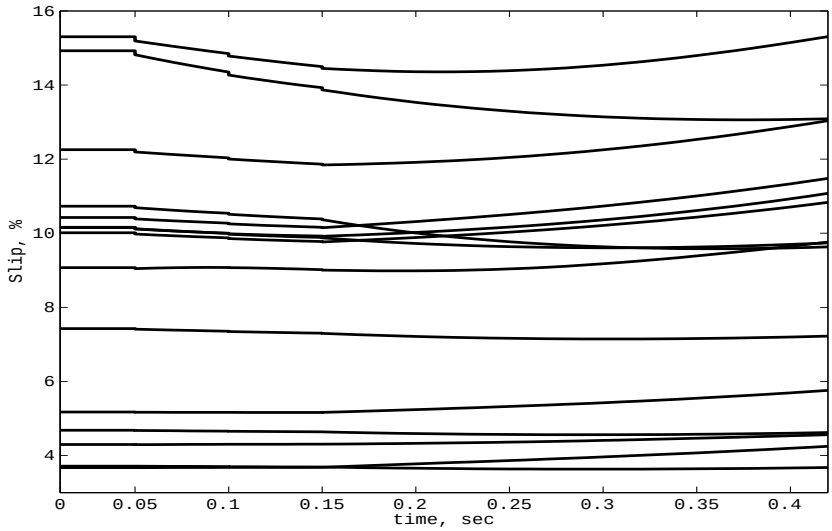

Figure 5.27: *Slip performance.*

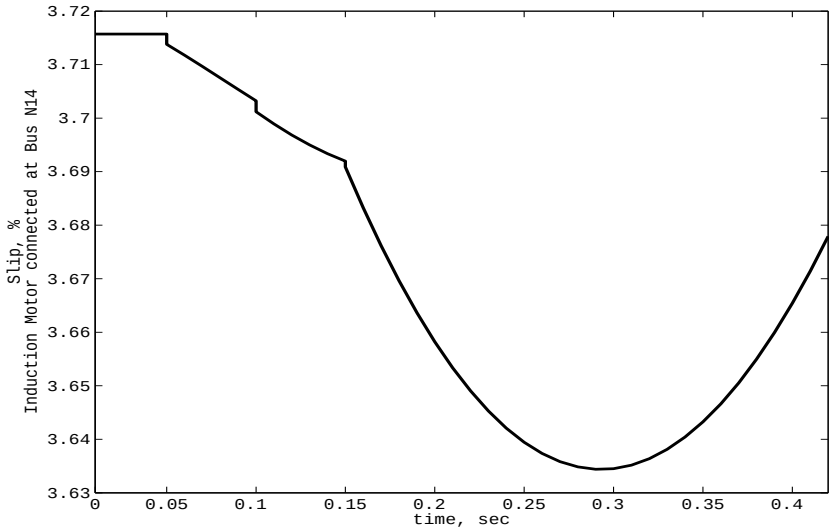

Figure 5.28: *Slip performance.*

5.6 Summary

This chapter relies mainly, on the development, analyses and implementation of the loads' behaviour in a dynamic power flow algorithm.

The dynamic power flows computer program has been extended to encompass static and dynamic load modelling including induction motor loads, to enable the study of a wide range of dynamic voltage phenomena in power systems. The upgraded software is well suited to carrying out comprehensive studies of wide-area dynamic voltage collapse, as demonstrated by numerical example. The overall method blends seamlessly the algebraic-differential equation set which represent the power system by using repeated linearization and the trapezoidal rule, resulting in a unified frame-of-reference with which to carry out reliable numerical solutions using the Newton-Raphson method.

In a nutshell, this is a dynamic power flows algorithm which enables dynamic assessments of the power system, with strong convergence characteristics and flexible network representation. Besides presenting a detailed description of how high-order synchronous generator and induction motor models are incorporated into the dynamic power flows algorithm, the thrust of this chapter is on system load modelling, and the responses of static load representations are compared with those of induction motors, and general conclusions are drawn.

Chapter 6

Modelling of FACTS Controllers

6.1 Introduction

Voltage stability and control are increasingly becoming a limiting factor in the planning and operation of power systems, mainly in weakly interconnected ones. However, for a number of economical and environmental reasons the construction of new transmission lines is suffering delays. This has resulted in the need to maximise the use of existing transmission facilities. During steady state operation, bus voltages must be controlled on a specified range. A suitable voltage and reactive power control allows to obtain important benefits in the power system operation, such as reduction of voltage gradients, efficient transmission capacity utilisation and increase of stability margins. Applying various control equipment and methods, the voltage control objectives in transmission system can be achieved. Some controllers work on the basis of injecting a series voltage injection an others on injecting a shunt reactive current at the point of connection with the power system. Following a disturbance, changes in the system voltage take place and restoration to the reference values depends very much on the dynamic response of the excitation systems and the other voltage controllers. In the last decade commercial availability of Gate Turn-Off thyristor (GTO) devices with high power handling capability, and the rapid progress of other power-semiconductor devices such as

IGBT, have led to the development of controllable reactive power sources utilising electronic switching converter technology [Nabavi-Niaki, 1996]. These technologies offer considerable advantages over the existing ones such as static VAR compensators in terms of smaller footprints and operational performance. GTOs and IGBTs enable the design of solid-state shunt reactive compensation equipment based upon switching converter technology.

The advent of Flexible AC Transmission Systems (FACTS) has given rise to a new family of power electronic equipment for controlling and optimising the performance of a power system, e.g. STATCOM, SSSC and UPFC. The voltage-source converter (VSC) is widely accepted to be the next generation of reactive power controller to the SVC, made up by thyristor-switched capacitors (TSC) and thyristor controlled reactors (TCR).

Researchers are directing their efforts at the application of FACTS to enhance the economic operational and the dynamic response of the power system. The major areas of dynamic applications are: voltage stability enhancement, damping torsional oscillations, power system voltage control, and power system stability improvement. These applications require of suitable control schemes implementation (voltage magnitude and phase angle control) [Banerjee and Verghese, 2001, Kassakian et al., 1991, IEEE, 2000].

6.2 Static Synchronous Compensator (STATCOM)

The Static Synchronous Compensator (STATCOM) is a shunt connected reactive compensator capable of generating or absorbing reactive power in a dynamic fashion. The STATCOM possesses operating characteristics similar to those of the rotating synchronous compensator but with no mechanical inertia. The STATCOM employs solid state power switching devices, providing rapid controllability of the voltage magnitude.

The STATCOM contains a step-down transformer, with a leakage reactance, a GTO or IGBT voltage source inverter (VSI), a DC capacitor and a control structure. The AC voltage difference across the leakage reactance is regulated to produced reactive power exchange

between the STATCOM and the power system, the objective being to regulate the AC voltage at the bus bar in order to improve the voltage profile of the power system. Moreover, a secondary damping function may be added to the STATCOM for damping power system oscillations [IEEE, 2000]. The basic voltage-source inverter representation for reactive power generation is shown schematically in Fig. 6.1.

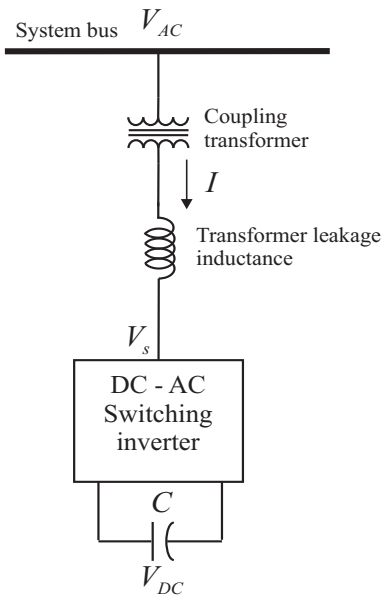

Figure 6.1: *STATCOM one-line diagram.*

The basic principle of STATCOM operation is as follows. The VSI generates a controllable AC voltage source behind the leakage reactance. This voltage is compared with the AC bus voltage system; when the AC bus voltage magnitude is above that of the VSI voltage magnitude, the AC system sees the STATCOM as an equivalent inductor connected to its terminals. Otherwise, if the VSI voltage magnitude is above that of the AC bus voltage magnitude, the AC system sees the STATCOM as a capacitor. If the voltage magnitudes are equal, the reactive power exchange is zero. If the STATCOM has a DC source or energy storage device on its DC side, it can supply active power to the power system. This active power exchange can be achieved by adjusting the phase angle of the STATCOM terminal

and the phase angle of the AC power system. When the phase angle of the AC power system leads the VSI phase angle, the STATCOM absorbs active power from the AC system; if the phase angle of the AC power system lags the VSI phase angle, the STATCOM supplies active power to AC system [Padiyar and Kulkarni, 1997, Lehn and Iravani, 1998, Lehn and Iravani, 2002]. Typical applications of the STATCOM are:

- Effective voltage regulation and control,
- Reduction of temporary overvoltages,
- Improvement of steady-state power transfer capacity
- Improvement of transient stability margin,
- Damping of power system oscillations,
- Damping of subsynchronous power system oscillations,
- Flicker control,
- Power quality improvement,

The voltage source converter is the building block of a STATCOM and other FACTS devices. A simple two-level converter produces a square voltage waveform as it switches the direct voltage source on and off. The basic objective of a VSC is to produce a sinusoidal AC voltage with minimal harmonic distortion from a DC voltage. Three basic techniques are used for reducing harmonics in the converter output voltage. Harmonic neutralisation using magnetic coupling (multi-pulse converter configurations), harmonic reduction using multi-level converter configurations and control.

6.3 STATCOM Modelling

STATCOM is a FACTS controller that is used in power systems to regulate the line voltage, enhance the power transmission capacity and extend the transient stability margin. A STATCOM essentially a voltage-source converter aimed at proving reactive power support for voltage control.

Assuming balanced, fundamental frequency voltages, the controller can be accurately represented in stability studies using the voltage source model shown in Fig. 6.2 together with the block diagram control law in Fig. 6.3.

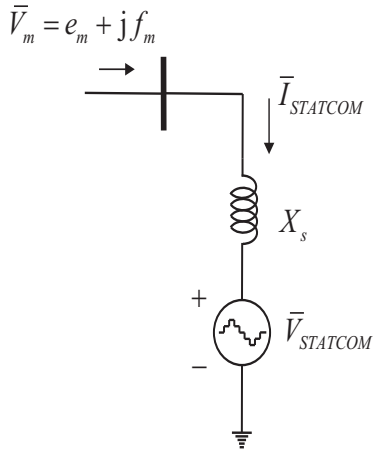

Figure 6.2: *STATCOM model.*

The differential equation corresponding to this model can be written as follows:

$$\dot{V_{STAT}} = \frac{K_{STAT}\,(V_{ref} - V_m) - V_r}{T_{STAT}} \tag{6.1}$$

where V_r is the STATCOM voltage target, K_r is the gain for the STATCOM, V_{ref} is the voltage reference, T_r is the control time constant, and V_m is the bus voltage magnitude where the STATCOM is connected to.

The complex power equation for the STATCOM is derived by first establishing the STATCOM current, I_{STAT},

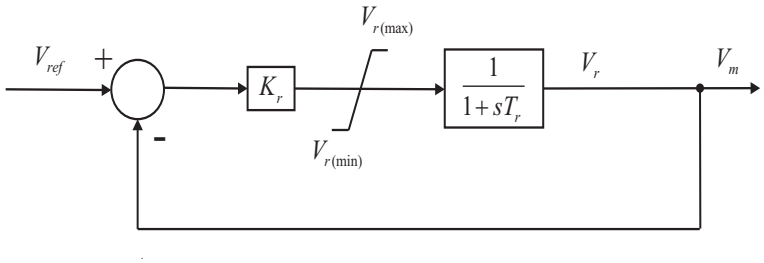

Figure 6.3: *STATCOM block diagram.*

$$I_{STAT} = \left[(V_m - V_{STAT}) \left(-\mathrm{j}\frac{1}{X_s} \right) \right]^*$$

$$S_{STAT} = V_{STAT} I^*_{STAT}$$

S_{STAT} and V_{STAT} are the complex power and the voltage magnitude for the STATCOM respectively, V_m is the bus voltage magnitude where the STATCOM is connected to, and X_s is the transformer reactance.

Separating the real and imaginary parts of the complex power, we obtain the expression for the STATCOM active and reactive powers:

$$P_{STAT} = \frac{V_{STAT} \left(f_m \cos \delta_{STAT} - e_m \sin \delta_{STAT} \right)}{X_s} \tag{6.2}$$

$$Q_{STAT} = \frac{V_{STAT} \left(e_m \cos \delta_{STAT} + f_m \sin \delta_{STAT} \right) - V^2_{STAT}}{X_s} \tag{6.3}$$

The differential equation 6.1 is transformed into an algebraic equation by means of the trapezoidal rule and appended to the existing set of algebraic equations representing the network for a unified solution. This ensures a numerically stable transformation since the implicit trapezoidal method, described at Section 2.7 is well known for giving reasonably accurate results even when relatively large integration time steps are selected [Kundur, 1994,

Machowski et al., 1997].

The trapezoidal method is applied to the differential Eq. 6.1 as follows,

$$V_{STAT(t)} - V_{STAT(t-\Delta t)} = \frac{\Delta t}{2\ T_{STAT}}\Big[K_{STAT}\big(V_{ref} - V_{m(t)}\big) - V_{STAT(t)} + \big(V_{ref} - V_{m(t-\Delta t)}\big) - V_{STAT(t-\Delta t)}\Big] \tag{6.4}$$

Re-arranging terms, leads to a more compact expression,

$$F_{STAT} = F_{STAT(t)} + F_{STAT(t-\Delta t)} + C_{STAT} = 0$$

where

$$\begin{aligned} F_{STAT(t)} &= V_{STAT(t)}\left[1 - \frac{\Delta t}{2\ T_{STAT}}\right] - \frac{\Delta t}{2\ T_{STAT}} K_{STAT} V_{m(t)} \\ F_{STAT(t-\Delta t)} &= -V_{STAT(t-\Delta t)}\left[1 - \frac{\Delta t}{2\ T_{STAT}}\right] - \frac{\Delta t}{2\ T_{STAT}} K_{STAT} V_{m(t-\Delta t)} \\ C_{STAT} &= \frac{\Delta t}{T_{STAT}} K_{STAT} V_{ref} \end{aligned}$$

Equation 6.2 and Eq. 6.3, describing the active and reactive powers contributions for the STATCOM, are explicitly incorporated into the active and reactive powers injected in the network buses and the powers contributed by all generators in the network:

$$\begin{aligned} &P_k + P_{e,l} + P_{STAT,m} \\ &Q_k + Q_{e,l} + Q_{STAT,m} \end{aligned} \tag{6.5}$$

for $k = 1, \ldots, l, \ldots, nbus$, $l = 1, \ldots, ngen$ and $m = 1, \ldots, n_{STAT}$.

6.4 Numerical Evaluation of Power Networks with STATCOM Controller

6.4.1 Test case 1

In this section the STATCOM controller is used to improve the bus voltage profile and the general performance of test networks.

The nine-bus, three-machine power system depicted on Fig. 4.16, is used as test case.

From a standard static power flow calculation, it is noted that the lowest voltage magnitude is at Bus 5. Hence, the STATCOM is placed at this node to improve the voltage at this bus.

Table 6.4.1 shows the parameters of the STATCOM.

Table 6.1: *STATCOM parameters*

Transformer reactance, X_s	0.06
Reference Voltage	1.00
Control Gain, K_{STAT}	100
Time constant, T_{STAT}	0.10

The source of perturbation is a 50% load increase at Bus 8.

Figure 6.4 shows the voltage profile at Bus 5 for two different conditions. When no STATCOM is connected, represented by a dashed line, and the condition when STATCOM is connected, represented by the solid line.

It is observed that when no STATCOM is connected the bus voltage magnitude drops until a value around 0.977 pu, whereas for the condition when the STATCOM is connected the voltage magnitude has a sudden voltage drop at the time of the perturbation reaching a value of around 0.993, but the fast response of the STATCOM controller improves the voltage magnitude to the desired value condition.

Figure 6.5 and Fig. 6.6 depict the reactive power and the STATCOM injected voltage,

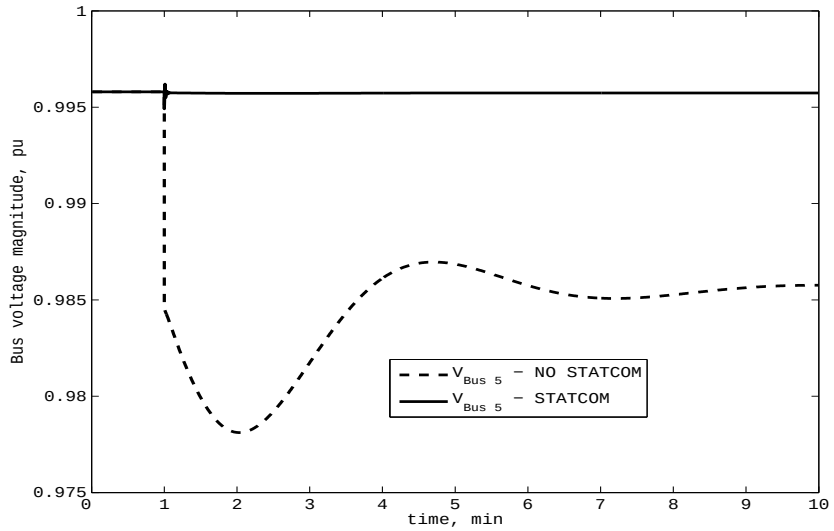

Figure 6.4: *Bus voltage response to a load change.*

needed to improve the voltage at Bus 5.

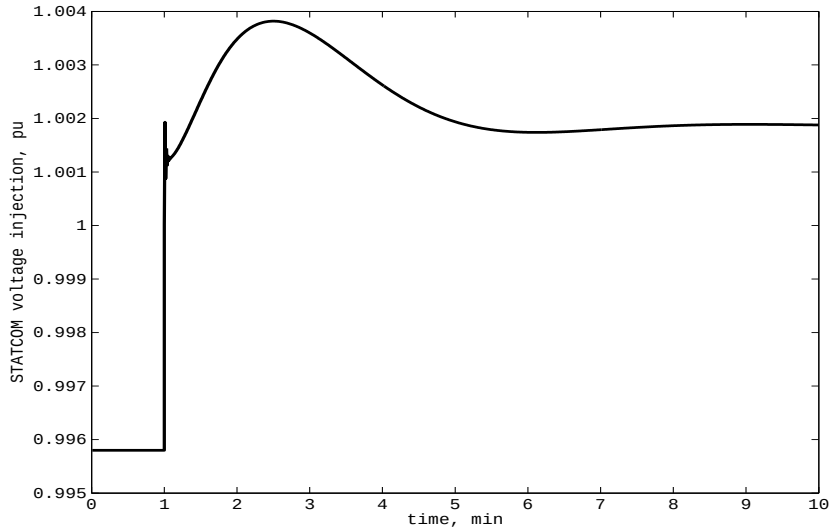

Figure 6.5: *STATCOM voltage injection.*

Priori to the disturbance, the reactive power injected by the STATCOM is null but once the system is subjected to the load variation, the STATCOM starts injecting the necessary amount of reactive power to control the voltage at the specified level, as shown in Fig. 6.6. A

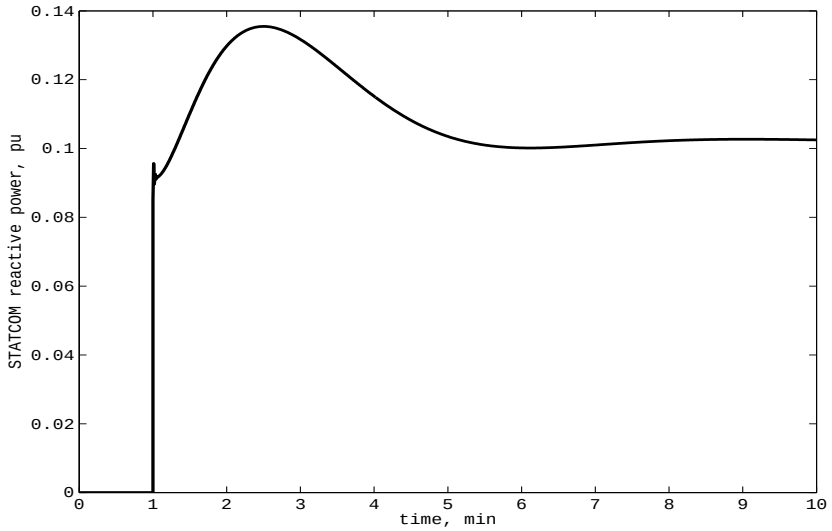

Figure 6.6: *STATCOM reactive power injection.*

similar situation arises with the voltage provided by the STATCOM, however, the STATCOM voltage is close to 0.996 pu prior to the disturbance, and reaches a maximum value of around 1.003 pu during the transient period.

6.4.2 Test case 2

The dynamic behavior of the STATCOM is assessed further in this section.

The disturbance is initiated by a symmetric three-phase fault occurring near Bus 7, at the end of line 5-7. The fault is cleared by opening line 5-7 through the breaker approximately 3 cycles after the fault occurred.

The dynamic voltage response is shown in Fig. 6.7, where large voltage swings follow the fault clearance. Notice that the voltage drops below 0.6 pu at Bus 8 at time 1.6 min. To improve the system response to this kind of faults, a STATCOM is connected at this bus, and a vastly improved response is shown in Fig. 6.8.

As expected, the bus voltage profile for the complete system is improved by the inclusion of the STATCOM device.

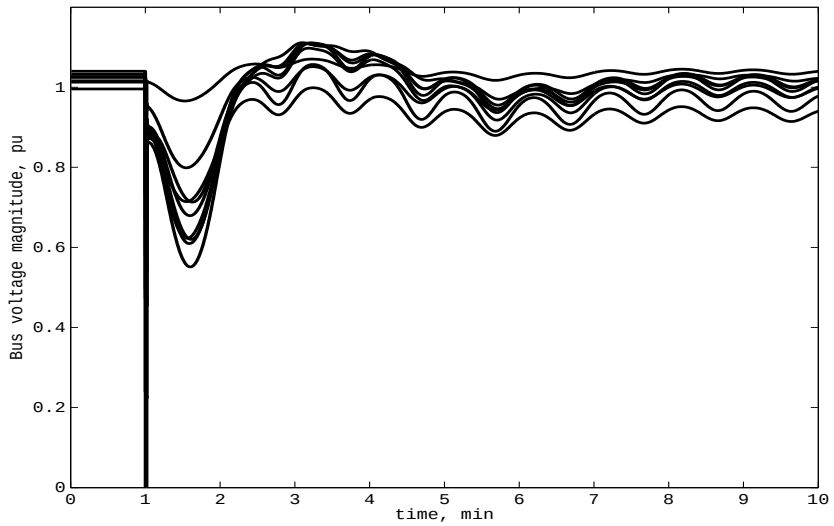

Figure 6.7: *Bus voltage profile for condition when NO STATCOM is placed.*

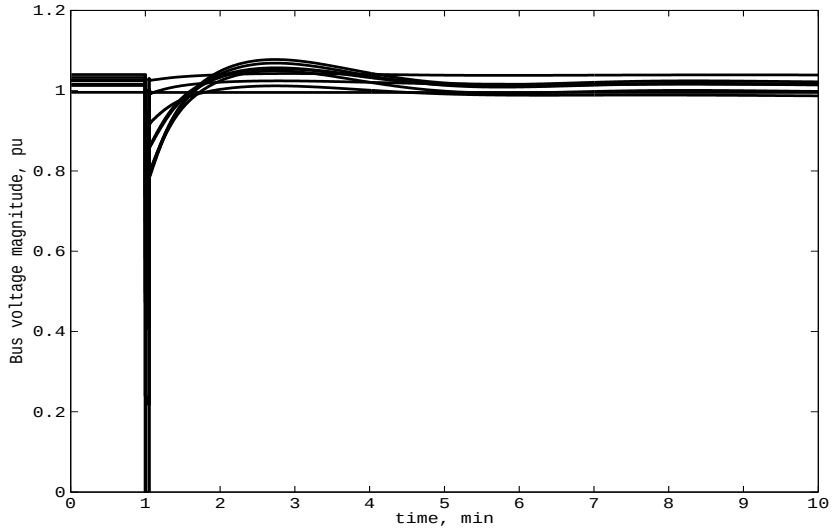

Figure 6.8: *Bus voltage profile for condition when STATCOM is placed.*

Figure 6.9 shows the reactive power injected by the STATCOM to improve the bus voltage profile of the system and Fig. 6.10 depicts the magnitude of the STATCOM voltage injection.

Figure 6.11 depicts the current injection of the STATCOM. In a similar manner as for the reactive power injection, prior to the three-phase fault, both the reactive power and

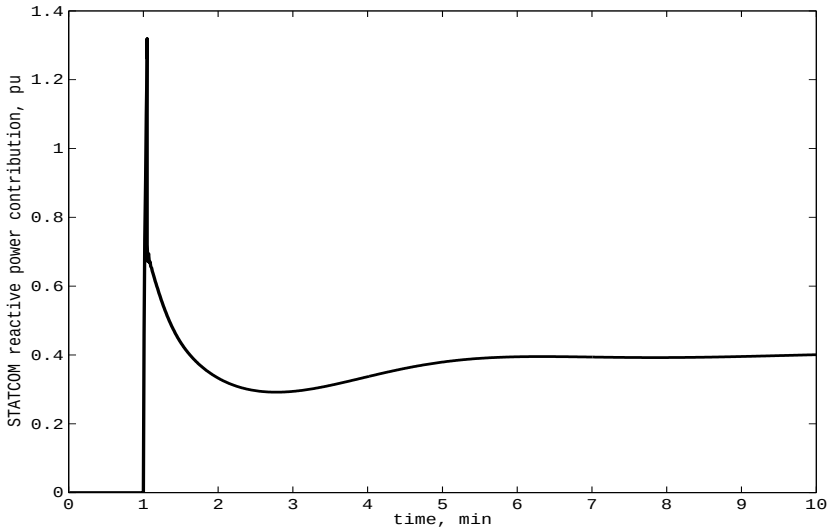

Figure 6.9: *Reactive power injection of the STATCOM.*

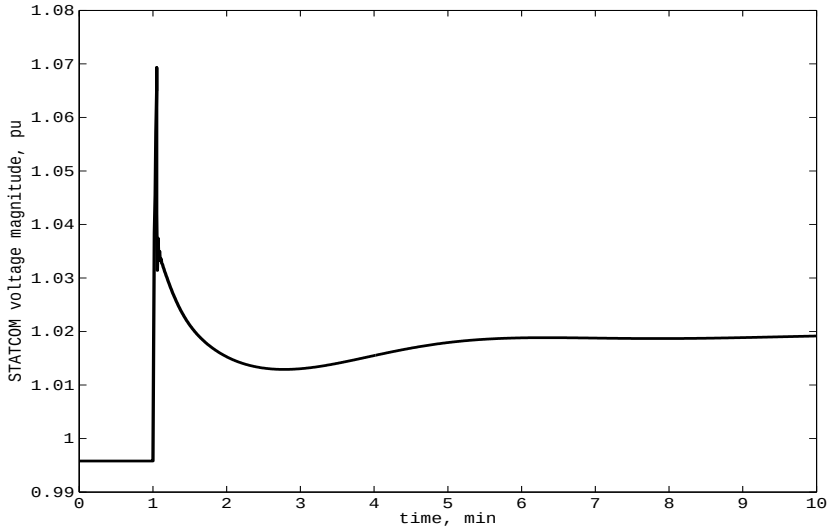

Figure 6.10: *Voltage magnitude injection of the STATCOM.*

current injected by the STATCOM are null, however once the fault occurs, the STATCOM starts injecting the required amount of current and reactive power to control and improve the voltage of the power network.

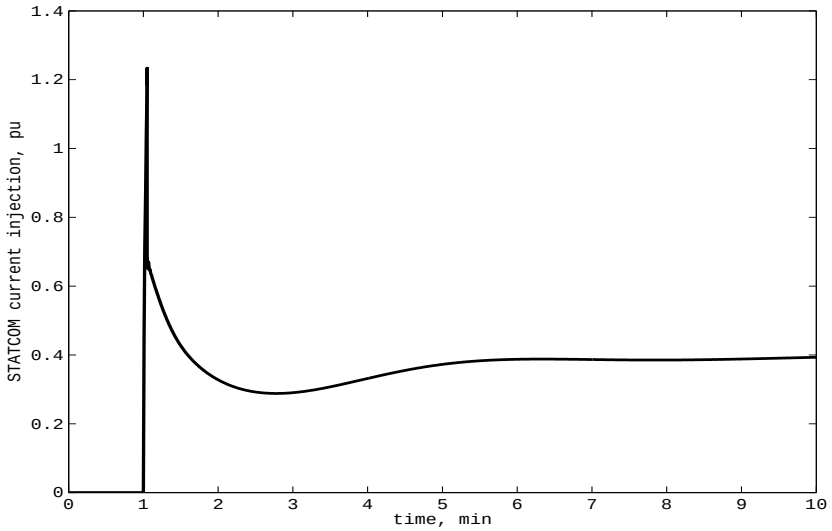

Figure 6.11: *STATCOM current absorbtion.*

6.4.3 Test case 3

The New England test system [Chow, 1982], which consists of 39 buses, 10 generators, 36 transmission lines and 10 transformers depicted in Fig. 5.21 is used to further assess the STATCOM controller.

The FACTS device is connected at Bus 14. Two perturbation are applied to the system as follow. At time 1 min, the load connected at Bus 15 is increased by 15% of its nominal value and one minute later, time 2 min, the transmission line connecting buses 14 and 15 is tripped.

Figure 6.12 shows the bus voltage magnitude for the system when the perturbations are applied.

Figure 6.13 depicts the voltage magnitude for Bus 14. The continuous line represents the bus voltage magnitude when the STATCOM is connected, and the dashed line represents the bus voltage magnitude when no STATCOM is connected. It is observed that when the FACTS device is connected to the system, it improves the bus voltage magnitude of the whole system and controls the voltage magnitude of Bus 14 around the value of 0.914 pu, whereas

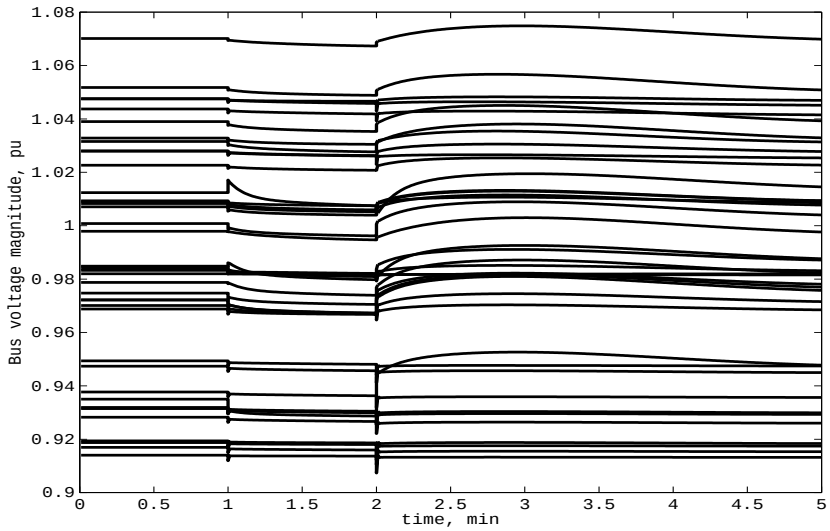

Figure 6.12: *Bus voltage magnitude when STATCOM device is connected.*

when no device is connected the voltage magnitude after the second perturbation reaches a value of around 0.875 pu. Fig. 6.14 shows the voltage magnitude for the power network when no STATCOM controller is placed.

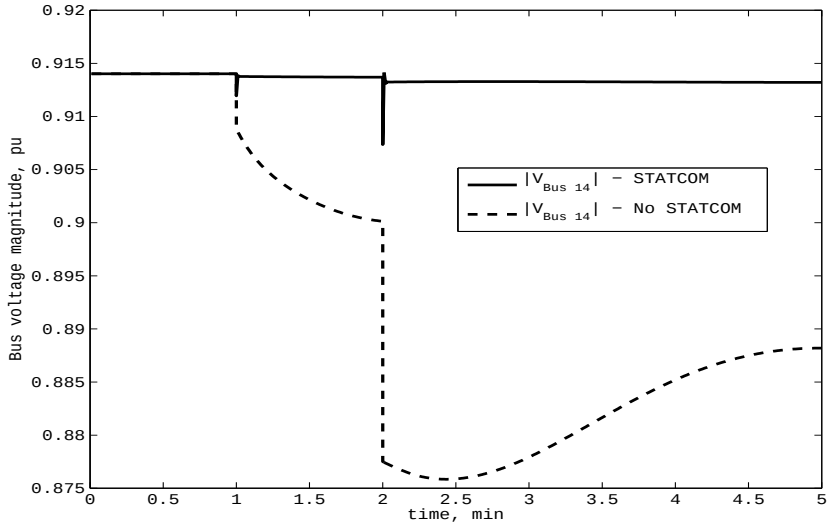

Figure 6.13: *Voltage magnitude comparison at Bus* 14.

Figure 6.14 shows the bus voltage magnitude for the power network when no STATCOM

device is connected.

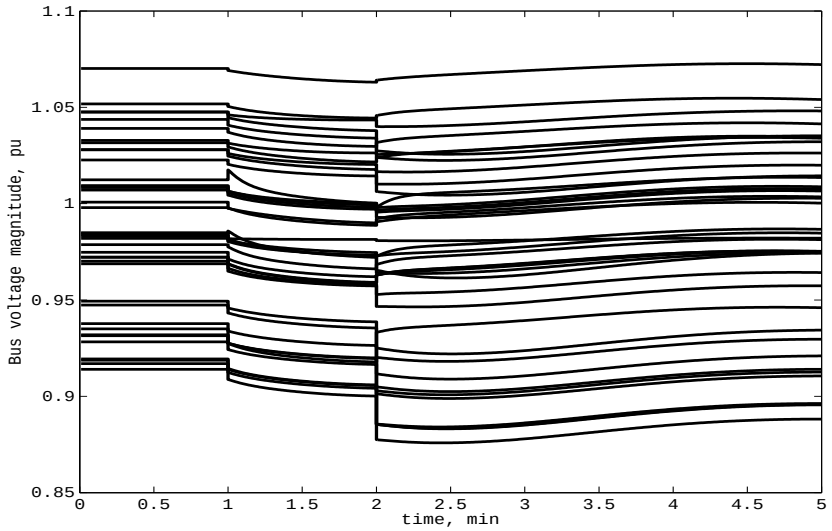

Figure 6.14: *Bus voltage magnitude when no STATCOM device is connected.*

Figure 6.15 shows the reactive power injected by the STATCOM to improve the bus voltage profile of the system and Fig. 6.16 depicts the magnitude of the STATCOM voltage injection.

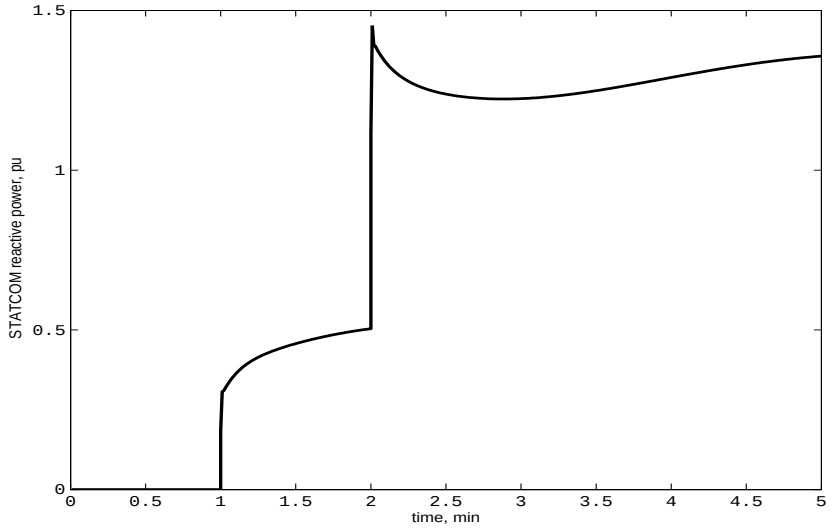

Figure 6.15: *Reactive power injected by the STATCOM.*

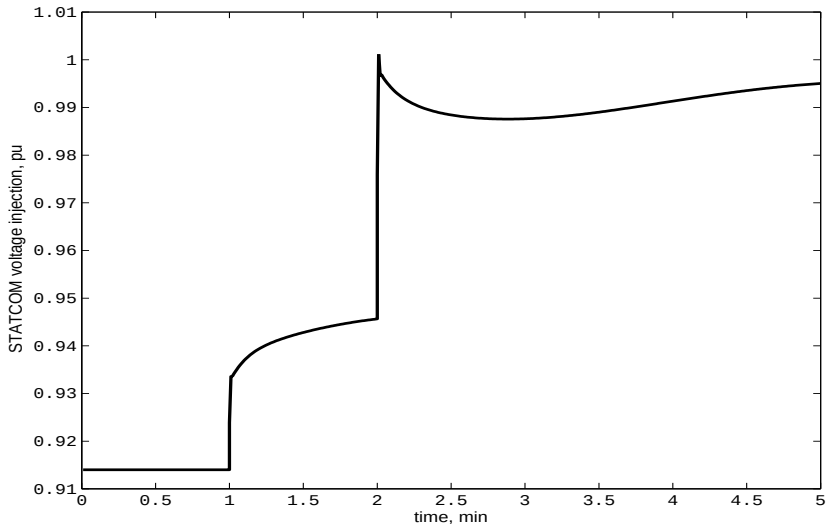

Figure 6.16: *STATCOM voltage.*

It is observed, that while the system remains stable, no reactive power injection by the STATCOM is needed, however when the system is perturbed the FACTS device starts to inject the necessary amount of reactive power to improve the bus voltage magnitude of the system.

6.5 High Voltage Direct Current (HVDC)

Over many years, interest in HVDC technology for bulk power transmission, and asynchronous interconnections has remained strong. Further to the traditional HVDC technology, termed line commutated current (LCC), based on the use of conventional thyristors; two other lines of development in HVDC technology have appeared, capacitor commutated converters (CCC), which is an upgrade of the traditional technology, and voltage source converters (VSC) with insulated gate bipolar transistor (IGBT) and pulse width modulation (PWM) control. In each of these applications, manufactures have taken maximum benefits from the accelerated pace of power electronics technology. It is believed that in a few years time, HVDC-VSC-based systems, will take over a large portion of the traditional HVDC market.

However at present, bulk power DC transmission remains the realm of thyristor-based HVDC technology [Carlsson, 2002].

The advantage of HVDC in long distance transmission is that there is no need to charge the distributed capacitance of the transmission line with alternating voltages, making it a more efficient form of transmission. The drawback is that more expensive terminals at the line ends are required.

The early power converters used mercury arc valves for the AC/DC/AC conversion process. More reliable solid state valves, suitable power transmission applications, appeared in the mid-seventies making the design of HVDC more flexible and responsive to the need of bulk power transmission.

HVDC has a number of characteristics that makes it markedly different from ac-transmission. The most important are summarised below:

- Each station can be connected to AC networks that are not synchronised or do not even have the same frequency.
- Power can be transmitted over very long distances with no need for compensation equipment along the line.
- For comparable power densities, only two conductors are needed (or even one conductor if the ground or the sea is used as return) for HVDC compared to the three conductors required for AC transmission.

6.5.1 Voltage Source Converters - HVDC

A new type of HVDC transmission technology has recently been commercially developed. By using components that can not only switch on the current but also switch it off, has made it possible to build voltage source converters (VSC).

Since the direct current in a voltage source converter is able to flow in either direction, the converter valves it is a requirement that the converter valves should have bidirectional

properties. Thus, a VSC valve is made up of an asymmetric turn off device such as a GTO with a parallel diode connected in anti-parallel.

The VSC-based system is self-commutated, it uses insulated-gate bipolar transistor (IGBT) valves and solid-dielectric extruded HVDC cables. For economic and performance reasons, voltage source converters are often preferred over current source converters for FACTS applications [Hingorani and Gyugyi, 1999].

HVDC-VSC transmission may be beneficial to the overall system performance in a number of fronts. VSCs can rapidly control both active and reactive power independently from one another, and the dynamic support of the ac voltage at each converter terminal improves voltage stability, increasing the power transfer capability of the two ac systems [Bahrman and Johnson, 2007].

The VSC-HVDC technology has the following additional advantages [Reed and Takeda, 2003]:

- Can be used to feed networks with no self generation capacity (black networks);
- Can operate with no communication link between stations;
- No change of voltage polarity when the power direction is reversed. This makes easier to build multi-terminal schemes.
- It uses robust and inexpensive extruded cables for both land and sea applications;
- Small footprint converters that reduce space requirement.

Since ABB [1] introduced its voltage source converter DC-transmission system, named "HVDC Light" in Hellsjön 1997, the rating has increased 100 times, currently standing at 330 MW in the Cross Sound cable connection. A number of projects have now been commissioned [ABB, 2007, Cole et al., 2006] and are showing good operating experience.

[1] Asea Brown Boveri Ltd. (ABB Zurich)

The transmission capacity and converters sizes of the VSC transmission are becoming large enough to also play a role in system stability improvement. Different applications will make good use of the high controllability of active and reactive power, considerably improving system stability [Johansson et al., 2004].

Voltage collapse in another challenging power system application area which may be beneficial from the VSC technology. Inadequate reactive power support from generators may lead to voltage collapse, a situation that can be improved very considerably with the use of VSC technology with its fast response.

One way in which VSC-HVDC technology, can improve the system voltage profile when loads are continuously varied, is by stabilising the ac voltage. The VSC-HVDC may be used to consume reactive power to maintain a specific ac voltage when the ac system is lightly loaded. When the system load equals the "natural load", the ac transmission line neither generates nor consumes reactive power. As the system load increases further, the VSC-HVDC may be set to generate reactive power to support the ac system. By continuous reactive power support from VSC-HVDCs, voltage stability margins are improved [Zhang et al., 2007].

6.6 VSC-HVDC Modelling

The HVDC model consists of two VSC stations, one operating as a rectifier and the other as an inverter. Normally, the rectifier is use to control active power and the inverter is used to control voltage magnitude. However, the converter stations should have control flexibility and they could be set to exert no control. The two converter stations are joined together by a dc line conductor or either back-to-back. Fig. 6.17 shows the application when the HVDC is connected by a dc cable.

The HVDC model proposed here for dynamic power flows simulations is based on the active power balance equation given by,

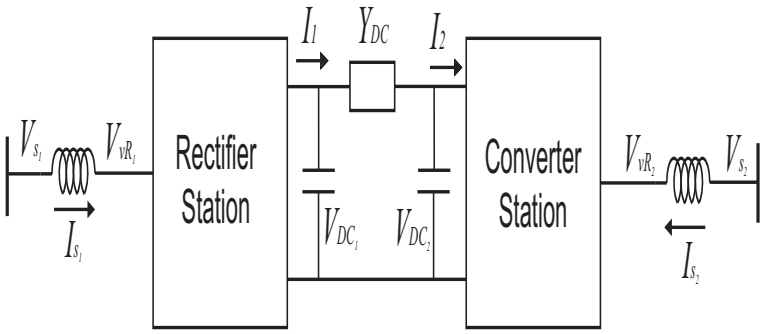

Figure 6.17: *HVDC-VSC transmission link diagram.*

$$\Delta P_{HVDC} = \Delta P_s - \Delta P_r - \Delta P_{loss} \tag{6.6}$$

Fig. 6.18 shows the HVDC control for the rectifier stage, where the following differential equation is derived,

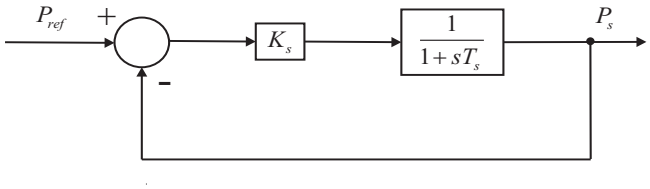

Figure 6.18: *HVDC control block diagram for the rectifier stage.*

$$\dot{P}_s = \frac{K_s\left(P_{ref} - P_s\right)}{T_s} \tag{6.7}$$

where T_s is the rectifier time constant, K_s is the rectifier gain, and the reference power P_{ref} and rectifier sending power P_s are given by,

$$P_{ref} = P_s\left(1 + \frac{1}{K_s}\right) \tag{6.8}$$

$$P_s = \frac{V_s\left(f_k \cos\delta_s - e_k \sin\delta_s\right)}{X_s} \tag{6.9}$$

where for P_s, V_s and δ_s are the rectifier shunt voltage magnitude and phase angle, respectively, e_k and f_k are the real and imaginary part of the voltage at node k respectively, and X_s is the rectifier shunt admittance.

In a similar case, Fig. 6.19 depicts the HVDC control for the inverter stage, giving the following differential equation,

$$\dot{V}_r = \frac{K_r\left(V_{ref} - V_m\right) - V_r}{T_r} \tag{6.10}$$

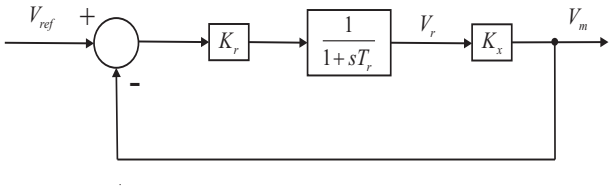

Figure 6.19: *HVDC control block diagram for the inverter stage.*

where T_r is the inverter time constant, K_r is the inverter gain, V_m is the voltage magnitude at node m, V_{ref} is the reference voltage and V_r is the shunt voltage magnitude at the receiving node.

To get a better idea, Fig. 6.20 shows the equivalent diagram for the previous conditions.

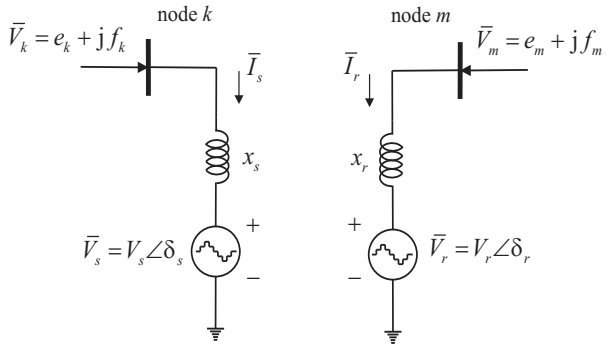

Figure 6.20: *HVDC based VSC equivalent circuit.*

It is important to remark, that for the rectifier stage the state variable is the rectifier sending power P_s and for the inverter side the state variable is the shunt voltage magnitude

V_r.

Finally Eq. 6.6 is redefined as,

$$F_{P_{HVDC}(t)} = F_{P_s(t)} - F_{P_r(t)} - F_{P_{loss}(t)} \tag{6.11}$$

where $F_{P_S(t)}$, $F_{P_r(t)}$ and $F_{P_{loss}(t)}$ are described as follow,

$$F_{P_s(t)} = -P_s \left[1 + \frac{\Delta t}{2T_s}(K_s + 1)\right] \tag{6.12}$$

$$F_{P_r(t)} = \frac{F_{V_r(t)}\left(f_m \cos\delta_r - e_m \sin\delta_r\right)}{X_r} \tag{6.13}$$

$$F_{P_{loss}(t)} = 2\left(\frac{R_{dc}}{{V_s}^2} P_s\right)\ F_{P_s(t)} \tag{6.14}$$

and $F_{V_r(t)}$ is defined as,

$$F_{V_r(t)} = -V_r \left[1 + \frac{\Delta t}{2T_r}\right] - \frac{\Delta t}{2T_r}\ K_r V_m \tag{6.15}$$

In a compact way,

$$F_{P_{HVDC}(t)} = \left(1 - 2\ \frac{R_{dc}}{{V_s}^2} P_s\right) F_{P_s(t)} - F_{P_r(t)} \tag{6.16}$$

6.7 Numerical Evaluation of Power Networks with VSC-HVDC Controller

6.7.1 Test case 4

In this section the HVDC-VSC dynamic behavior is evaluated. As in previous cases, the nine-bus, three-machine power system depicted at Fig. 4.16, is used.

In this test case, an HVDC-VSC is replaced with the transmission line connecting Bus 5

and 7. It will be set to transfer 0.4 pu active power from Bus 5 to Bus 7. The rectifier is set to regulate constant active power flow at its AC terminal, and the inverter is assumed to exert no voltage control. The source of the perturbation is a load increment of 25% at Bus 8 at time 1 min. The simulation is carried out for 5 minutes.

Fig. 6.21 shows the voltage magnitude at all the buses, and Fig. 6.22 depicts the voltage magnitude for the sending and receiving terminals of the HVDC. The continuous line, represents the voltage magnitude injected by the HVDC at the sending node, and the dashed line shows the voltage magnitude injection at the receiving node.

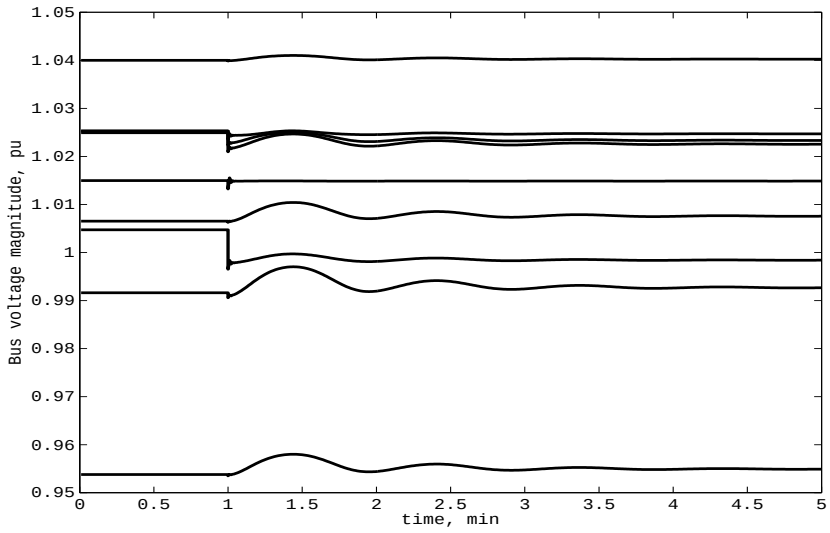

Figure 6.21: *Bus voltage response of the power network.*

Moreover, Fig. 6.23 shows the voltage magnitude at Bus 7, having a value of around 1.015 pu. It is observed that during the transient state, the voltage magnitude injected by the HVDC-VSC terminal, depicted in Fig. 6.22, increases in order to support the voltage magnitude at Bus 7.

The dc-link cable is assumed to contain losses, and it has a resistance value of 0.05 pu. The amount of transferred power is set to 0.40, as depicted in Fig. 6.24, and the power at the receiving end of the HVDC is 0.3934 pu. The transferred power to the receiving bus is

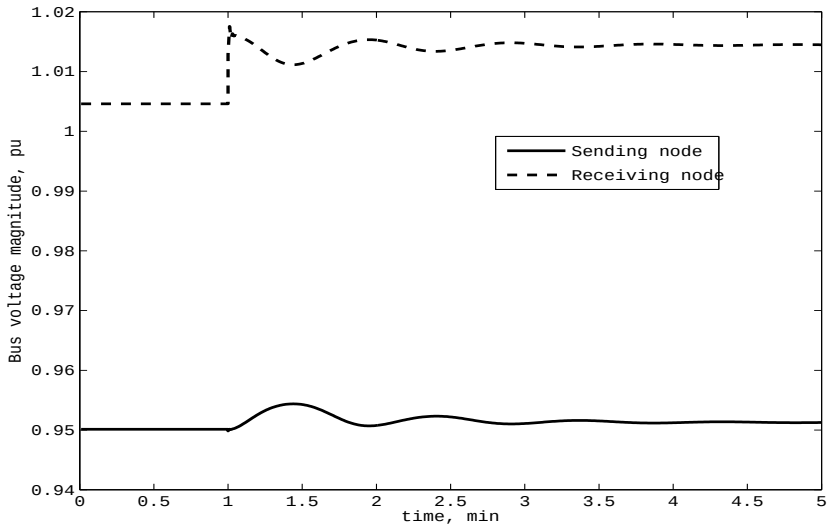

Figure 6.22: *Bus voltage magnitude at HVDC terminals.*

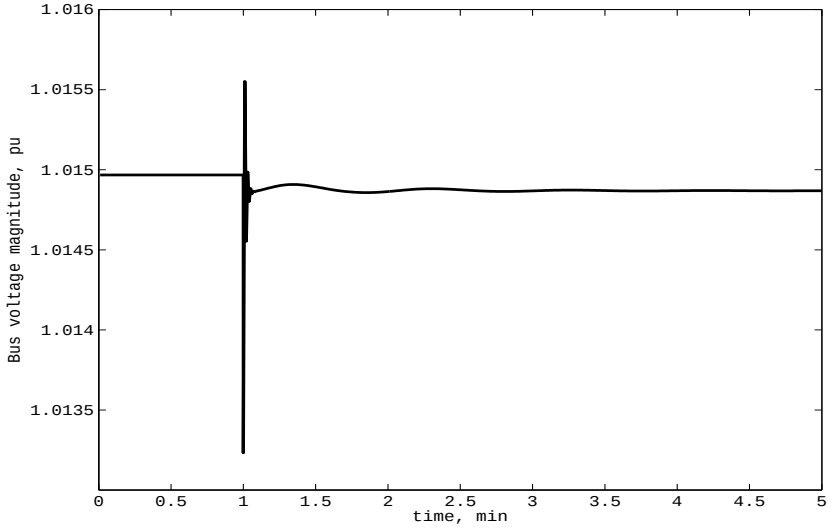

Figure 6.23: *Bus voltage magnitude at Bus* 7*.*

reduced due to the copper losses of the dc-link. It can be observed from the power result in Fig. 6.24 that the power control in the rectifier is very effective in keeping the power at a constant value of 0.4 pu.

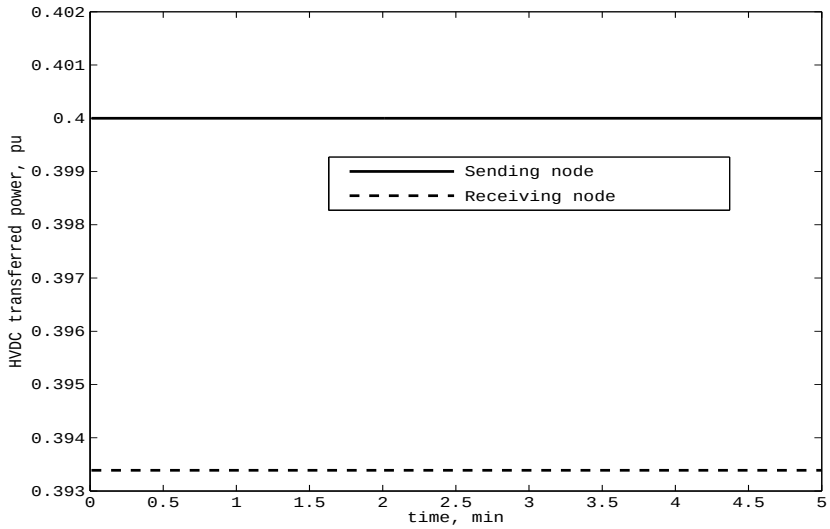

Figure 6.24: *HVDC-VSC transferred power when dc link losses are considered.*

6.8 Summary

This chapter has addressed further developments on the dynamic power flow algorithm. FACTS controllers based on voltage source converters have been developed and implemented into the dynamic power flow algorithm. The main VSC-FACTS controllers described in this chapter are the STATCOM and HVDC-VSC.

Several test cases have been presented. The STATCOM has been used to enhance the voltage at a particular point of the network under both normal and abnormal operation, such as a three-phase fault. Furthermore, this FACTS controller successfully improves the voltage at the weakest bus of the system even when the power network is subjected to a load perturbation. The HVDC-VSC has been set to active power transfer at the rectifier end of the HVDC link, even in situation when a disturbance arises. The HVDC-VSC model implemented is the dynamic power flow program has the flexibility of representing not only point-to-point links but also back-to-back links.

Both VSC-FACTS devices enable a better performance of the whole system under unfavourable conditions.

Chapter 7

Three-Phase Dynamic Power Flows in *abc* Co-ordinates

7.1 Introduction

Worldwide, electrical power is generated, transmitted and distributed in a three-phase fashion. Besides, the possibility of having excessive imbalances between the phase voltages or currents in a three-phase system, has always been a concern to power engineers, due to their detrimental effects on power system operation. In practice, typical power system contains untransposed transmission lines and feeders, single and three-phase unbalanced static shunt loads, single and three-phase dynamic loads such as induction motors and capacitors banks. Generally, power systems are inherently unbalanced because of single-phase loads but also because of the occurrence of asymmetrical spacings between line conductors [Zhang et al., 2005].

When such transmission and load imbalances can no longer be assumed to be negligible, positive sequence modelling and conventional power flows or power system dynamics simulations are not applicable. Instead, detailed three-phase models and solution techniques

must be applied if accurate assessments are to be carried out during dynamic operation of the power system, including the most relevant power plant components such as, synchronous generators and power loads, modelled in phase.

To carry out comprehensive dynamic analyses of unbalanced transmission systems, it is mandatory to have a three-phase dynamic power flow algorithm in *abc* co-ordinates. Likewise its positive sequence counterpart presented in Chapter 4, for the solution of three-phase balanced power systems, the three-phase dynamic power flows can be modelled as a set of non-linear algebraic and differential equations representing the power network, rotating power machinery and controls.

The different static and dynamic elements that comprise the electric power system are modelled in the *abc* frame of reference to develop the three-phase dynamic power flow algorithm in rectangular co-ordinates.

All the relevant power system elements for dynamic power flows analyses, have been described in foregoing chapters; however the dynamic power flow modelling carried out has been positive sequence analyses. Thus, the modelling needs to be extended, in such a way that it is amenable to dynamic power flows studies in *abc* co-ordinates.

7.2 Power System Modelling

7.2.1 Three-phase synchronous machine modelling

The classical theory of synchronous machines for *dq* co-ordinates is well defined [Kimbark, 1948b, Concordia, 1951]. In this thesis, the mathematical theory presented is based on the full *dq*0 co-ordinate system [Park, 1929].

The phase voltages and currents at the terminal of the synchronous generators are, respectively:

$$\begin{aligned} V_a &= V_{t_1} sin(\theta_1) \\ V_b &= V_{t_2} sin(\theta_2 - 120) \\ V_c &= V_{t_3} sin(\theta_3 + 120) \end{aligned} \tag{7.1}$$

and

$$\begin{aligned} I_a &= I_{t_1} sin(\psi_1) \\ I_b &= I_{t_2} sin(\psi_2 - 120) \\ I_c &= I_{t_3} sin(\psi_3 + 120) \end{aligned} \tag{7.2}$$

where

V_t is the bus voltage magnitude at bus terminals.

I_t is the bus voltage magnitude at bus terminals.

θ is defined as the voltage angle.

ψ is defined as the current angle.

Fig. 7.1 schematically describes a three-phase synchronous generator from a circuit theory point of view.

The matrix transformation used to transform the *abc* phase variables into $dq0$ variables is the following one [Park, 1929]:

$$[T_{dq0}] = \frac{2}{3} \begin{bmatrix} \cos\theta & \cos\left(\theta - \frac{2\pi}{3}\right) & \cos\left(\theta + \frac{2\pi}{3}\right) \\ \sin\theta & \sin\left(\theta - \frac{2\pi}{3}\right) & \sin\left(\theta + \frac{2\pi}{3}\right) \\ \frac{1}{2} & \frac{1}{2} & \frac{1}{2} \end{bmatrix} \tag{7.3}$$

In generic form, including voltages and currents, the transformation operations used for referring the stator quantities to the rotor side and viceversa are:

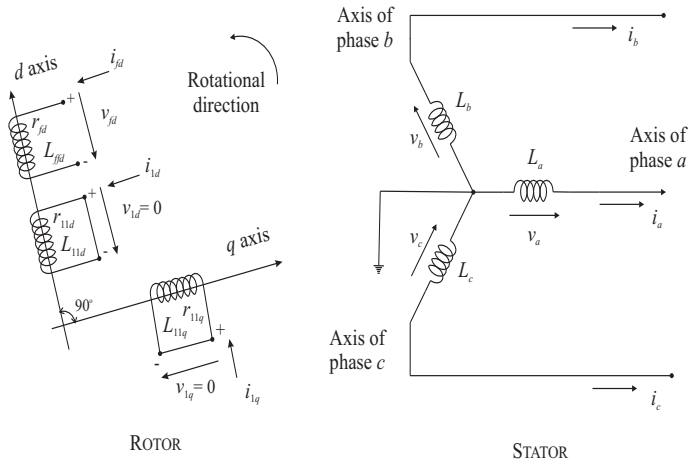

Figure 7.1: *Schematic synchronous machine representation.*

$$[F_{dq0}] = [T_{dq0}]\,[F_{abc}] \tag{7.4}$$

$$[F_{abc}] = [T_{dq0}]^{-1}\,[F_{dq0}] \tag{7.5}$$

Where Eq. 7.5 is referred as to the inverse transformation of Eq. 7.4.

The current component I_0 is taken to produce no space field in the air-gap and, hence, it does not affect the magnetizing rotational field [Kimbark, 1948b]. The two current components that produce field are only the d and q components, hence, for the three-phase synchronous generator implemented in the three-phase dynamic power flow algorithm, with transient saliency and flux decay effects, the following equations are used:

$$|E| = \sqrt{E_d^2 + E_q^2} \tag{7.6}$$

$$\delta = \arctan\left(\frac{V_a \sin\theta_a + I(r_a \sin\psi + (x_q - x_l)\cos\psi)}{V_a \cos\theta_a + I(r_a \cos\psi - (x_q - x_l)\sin\psi)}\right) \tag{7.7}$$

Where the voltage in phase a is taken to be the reference for calculating the internal

voltage angle [Kundur, 1994].

7.2.2 Dynamic three-phase load tap changer model

Three-phase banks of transformers are made up of three single-phase transformers, where the most common winding connections are: star-star, delta-delta and star-delta.

For star-star and delta-delta connected transformers, the relationship between the base voltages and the nominal turns of the primary and secondary sides of the transformer keeps equal for each phase [Kundur, 1994]. Nonetheless, for the star-delta transformer connection, there is a factor of $\sqrt{3}$ involved because of the winding connection. Likewise, a 30° phase shift must be considered between the line-to-line and line-to-neutral voltages.

The dynamic element of the three-phase load tap changer is described by the following differential equation,

$$\dot{T}_k = \frac{1}{H_T}\left(\sqrt{\left(e_k^{\rho}\right)^2 + \left(f_k^{\rho}\right)^2} - V_0\right) \tag{7.8}$$

where H_T is the tap's servomotor inertia, e_k and f_k are the real and imaginary parts of the voltage at the regulated bus, V_0 is the target voltage magnitude and ρ is used to denote phases a, b and c.

The dynamic three-phase load tap changer is discrete, and varies over time as a function of nodal voltages e_k^{ρ} and f_k^{ρ} and the tap step size ΔT_k. Moreover, its pre-defined operating range provide hard limits which can not be violated.

The differential equation that describes the dynamic behaviour of the three-phase load tap changer is transformed into an algebraic equation and appended to the existing set of algebraic equations for a unified solution. Thus, Eq. 7.8 is discretised as follows.

$$\begin{aligned} F_{T_k(t)} - F_{T_k(t-\Delta t)} = T_{k(t)} + \frac{\Delta t}{2H_t}\sqrt{\left(e^{\rho}_{k(t)}\right)^2 + \left(f^{\rho}_{k(t)}\right)^2} - V_0 \\ + T_{k(t-\Delta t)} + \frac{\Delta t}{2H_t}\sqrt{\left(e^{\rho}_{k(t-\Delta t)}\right)^2 + \left(f^{\rho}_{k(t-\Delta t)}\right)^2} - V_0 \end{aligned} \tag{7.9}$$

in compact form, it can be re-written as follows,

$$F_{T_k} = F_{T_k(t)} + F_{T_k(t-\Delta t)} + C_{T_k} = 0 \tag{7.10}$$

where

$$\begin{aligned} F_{T_k(t)} &= T_{k(t)} - \frac{\Delta t}{2H_t}\sqrt{\left(e^{\rho}_{k(t)}\right)^2 + \left(f^{\rho}_{k(t)}\right)^2} \\ F_{T_k(t-\Delta t)} &= -T_{k(t-\Delta t)} - \frac{\Delta t}{2H_t}\sqrt{\left(e^{\rho}_{k(t-\Delta t)}\right)^2 + \left(f^{\rho}_{k(t-\Delta t)}\right)^2} \\ C_{T_k} &= \frac{\Delta t V_0}{H_t} \end{aligned}$$

It is important to mention that a single tap parameter T_k is used for the three-phases in the three-phase primary winding.

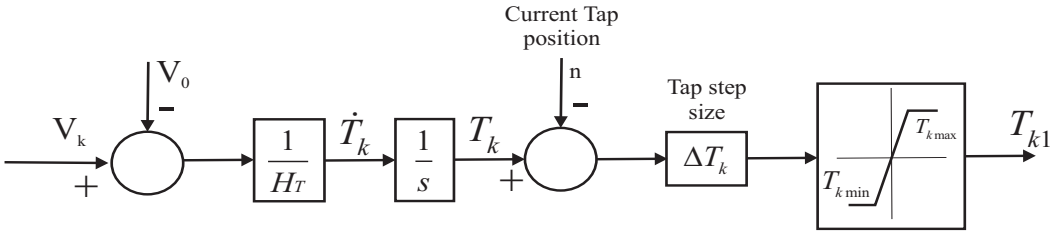

Figure 7.2: *Dynamic load tap changer model.*

The dynamic load tap changer model is depicted at Fig. 7.2, and Fig. 7.3 shows the discrete tap representation for each phase.

The three-phase connection for a solidly grounded star-star winding transformer is de-

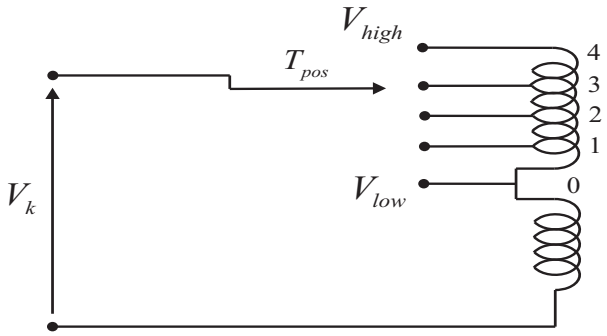

Figure 7.3: *Schematic representation of the discrete tap changer.*

picted at Fig. 7.4 and its nodal matrix representation is,

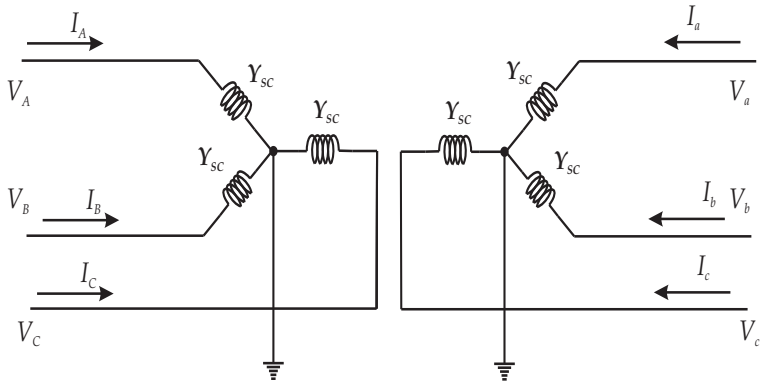

Figure 7.4: *Star-star transformer connection.*

$$\begin{bmatrix} I_A \\ I_B \\ I_C \\ I_a \\ I_b \\ I_c \end{bmatrix} = \begin{bmatrix} Y_{sc} & 0 & 0 & -T_k Y_{sc} & 0 & 0 \\ 0 & Y_{sc} & 0 & 0 & -T_k Y_{sc} & 0 \\ 0 & 0 & Y_{sc} & 0 & 0 & -T_k Y_{sc} \\ -T_k Y_{sc} & 0 & 0 & T_k^2 Y_{sc} & 0 & 0 \\ 0 & -T_k Y_{sc} & 0 & 0 & T_k^2 Y_{sc} & 0 \\ 0 & 0 & -T_k Y_{sc} & 0 & 0 & T_k^2 Y_{sc} \end{bmatrix} \begin{bmatrix} V_A \\ V_B \\ V_C \\ V_a \\ V_b \\ V_c \end{bmatrix} \tag{7.11}$$

In a similar manner, Fig. 7.5 and Fig. 7.6 depict the star-delta and delta-delta transformer

connection, respectively.

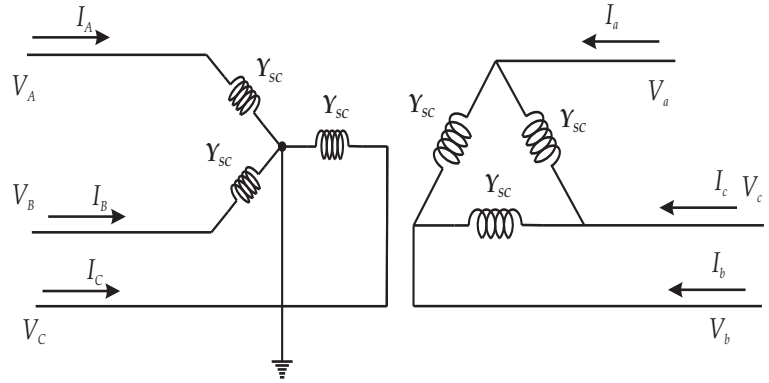

Figure 7.5: *Star-delta transformer connection.*

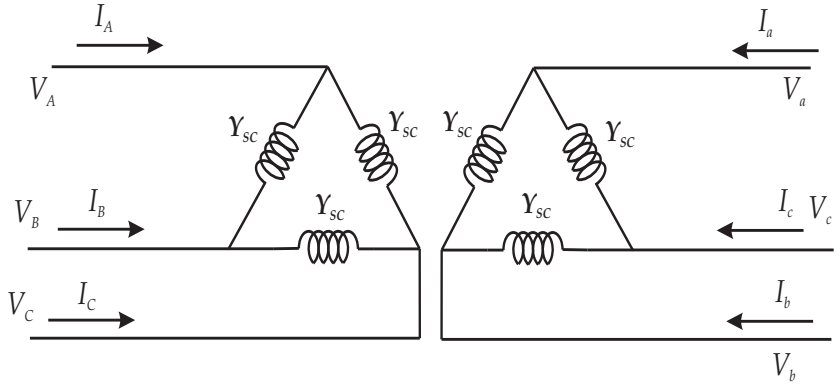

Figure 7.6: *Delta-delta transformer connection.*

The corresponding nodal matrices for this connections are respectively,

$$\begin{bmatrix} I_A \\ I_B \\ I_C \\ I_a \\ I_b \\ I_c \end{bmatrix} = \frac{1}{3} \begin{bmatrix} 2Y_{sc} & -Y_{sc} & -Y_{sc} & -2T_kY_{sc} & T_kY_{sc} & T_kY_{sc} \\ -Y_{sc} & 2Y_{sc} & Y_{sc} & -T_kY_{sc} & -2T_kY_{sc} & T_kY_{sc} \\ -Y_{sc} & -Y_{sc} & 2Y_{sc} & T_kY_{sc} & T_kY_{sc} & -2T_kY_{sc} \\ -2T_kY_{sc} & T_kY_{sc} & T_kY_{sc} & 2T_k^2Y_{sc} & -T_k^2Y_{sc} & T_k^2Y_{sc} \\ T_kY_{sc} & -2T_kY_{sc} & T_kY_{sc} & -T_k^2Y_{sc} & 2T_k^2Y_{sc} & -T_k^2Y_{sc} \\ T_kY_{sc} & T_kY_{sc} & -2T_kY_{sc} & -T_k^2Y_{sc} & -T_k^2Y_{sc} & 2T_k^2Y_{sc} \end{bmatrix} \begin{bmatrix} V_A \\ V_B \\ V_C \\ V_a \\ V_b \\ V_c \end{bmatrix}$$

$$\begin{bmatrix} I_A \\ I_B \\ I_C \\ I_a \\ I_b \\ I_c \end{bmatrix} = \begin{bmatrix} Y_{sc} & 0 & 0 & -T_k Y_{sc}/\sqrt{3} & T_k Y_{sc}/\sqrt{3} & 0 \\ 0 & Y_{sc} & 0 & 0 & -T_k Y_{sc}\sqrt{3} & T_k Y_{sc}/\sqrt{3} \\ 0 & 0 & Y_{sc} & T_k Y_{sc}/\sqrt{3} & 0 & -T_k Y_{sc}/\sqrt{3} \\ -T_k Y_{sc}/\sqrt{3} & 0 & T_k Y_{sc}/\sqrt{3} & 2T_k^2 Y_{sc}/3 & -T_k^2 Y_{sc}/3 & T_k^2 Y_{sc}/3 \\ T_k Y_{sc}/\sqrt{3} & -T_k Y_{sc}/\sqrt{3} & 0 & -T_k^2 Y_{sc}/3 & 2T_k^2 Y_{sc}/3 & -T_k^2 Y_{sc}/3 \\ 0 & T_k Y_{sc}/\sqrt{3} & -T_k Y_{sc}/\sqrt{3} & -T_k^2 Y_{sc}/3 & -T_k^2 Y_{sc}/3 & 2T_k^2 Y_{sc}/3 \end{bmatrix} \begin{bmatrix} V_A \\ V_B \\ V_C \\ V_a \\ V_b \\ V_c \end{bmatrix}$$

where for the previous three-phase nodal matrices,

Y_{sc} represents the transformer short-circuit admittance and T_k defines the tap ratio.

7.2.3 Three-phase power loads

By and large, three-phase power loads are heterogeneous and composed of all categories of individual load devices.

If load components have abundant data and knowing the composition of it at any time of interest on various points of the power system, then it is possible to combine the individual component characteristics to obtain a valid analytical expression for load modelling at the bus.

However, this is not always feasible for stability studies due to the lack of data. In that case, comprise is that the load can be represented in algebraic form with a base power which is a function of voltage either in polynomial or exponential form, with the exception of large motor loads which should be represented in a more detailed manner.

Fig. 7.7 shows the schematic representation of a star-connected, three-phase load with the star point solidly grounded. Fig. 7.8 depicts the schematic representation of a delta-connected load.

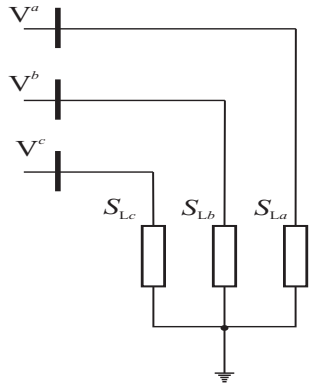

Figure 7.7: *Star-connected load representation.*

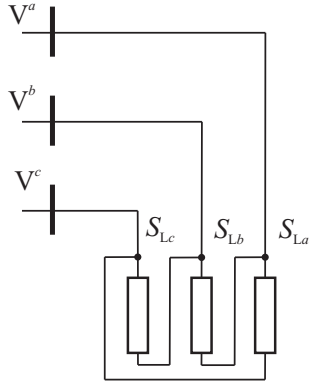

Figure 7.8: *Delta-connected load representation.*

Polynomial/exponential three-phase load model

A three-phase active and reactive power load may be described by a quadratic model given by

$$
\begin{aligned}
S_L^a &= P_0^a \left[a_0 \left(\frac{|V^a|}{|V_0^a|} \right)^2 + a_1 \left(\frac{|V^a|}{|V_0^a|} \right) + a_2 \right] \left[\frac{1}{V^a} \right]^\mu + \mathrm{j} Q_0^a \left[b_0 \left(\frac{|V^a|}{|V_0^a|} \right)^2 + b_1 \left(\frac{|V^a|}{|V_0^a|} \right) + b_2 \right] \left[\frac{1}{V^a} \right]^\nu \\
S_L^b &= P_0^b \left[a_0 \left(\frac{|V^b|}{|V_0^b|} \right)^2 + a_1 \left(\frac{|V^b|}{|V_0^b|} \right) + a_2 \right] \left[\frac{1}{V^b} \right]^\mu + \mathrm{j} Q_0^b \left[b_0 \left(\frac{|V^b|}{|V_0^b|} \right)^2 + b_1 \left(\frac{|V^b|}{|V_0^b|} \right) + b_2 \right] \left[\frac{1}{V^b} \right]^\nu \\
S_L^c &= P_0^c \left[a_0 \left(\frac{|V^c|}{|V_0^c|} \right)^2 + a_1 \left(\frac{|V^c|}{|V_0^c|} \right) + a_2 \right] \left[\frac{1}{V^c} \right]^\mu + \mathrm{j} Q_0^c \left[b_0 \left(\frac{|V^c|}{|V_0^c|} \right)^2 + b_1 \left(\frac{|V^c|}{|V_0^c|} \right) + b_2 \right] \left[\frac{1}{V^c} \right]^\nu
\end{aligned}
\tag{7.12}
$$

where V_0, P_0 and Q_0 are the base voltage and powers of the system. μ and ν will normally vary in the range of 0-2; V_a, V_b and V_c are the three-phase nodal voltage magnitudes at the load point. To represent a power load that to a large extent has a current characteristic, the indices μ and ν are made equal to 1; this load representation varies linearly with voltage. Furthermore, if the system power has the characteristics of an impedance then, μ and ν are made equal to 2; for a constant power load, μ and ν are assumed to be 0.

The matrix expression form for both types of three-phase load connection, star and delta are, respectively:

$$
\begin{bmatrix}
S_{La}/V_a^2 & 0 & 0 \\
0 & S_{Lb}/V_b^2 & 0 \\
0 & 0 & S_{Lc}/V_c^2
\end{bmatrix}
$$

$$
\frac{1}{3}
\begin{bmatrix}
S_{La}/V_a^2 + S_{Lb}/V_b^2 & -S_{Lb}/V_b^2 & -S_{La}/V_a^2 \\
-S_{Lb}/V_b^2 & S_{Lb}/V_b^2 + S_{Lc}/V_c^2 & -S_{Lc}/V_c^2 \\
-S_{La}/V_a^2 & -S_{Lc}/V_c^2 & S_{Lc}/V_c^2 + S_{La}/V_a^2
\end{bmatrix}
$$

The three-phase model representation incorporates the voltage dependency of the load and although it expresses such dependency by only algebraic relationship, such characteristic makes the load model time dependant [IEEE Load Task Force, 1993].

Three-phase induction motor modelling

The AC induction motor is a rotating electric machine designed to operate from a three-phase source of alternating voltage. The stator has three winding displaced from one another by 120°. The most common type of induction motor has a squirrel cage rotor in which aluminum bars are shorted together at both ends of the rotor with aluminium rings. When a three-phase current flows through the three symmetrically placed windings, a sinusoidally distributed air-gap flux generating the rotor current is produced. The interaction of the sinusoidally distributed air gap flux and induced rotor currents produces a torque on the rotor. The mechanical angular velocity of the rotor is lower than the angular velocity of the flux wave in the air-gap by the so called slip.

The induction motor model combines the impedance and the magnetizing branch impedances with the impedances of the three-phase transmission network and only the rotor is taken to be the dynamic element of it, with the air-gap line providing the interface between the two circuits. Thus, the rotor model consists of a first order differential equation where the induction motor slip s is the state variable, and the equations for three-phase active and reactive powers at the air-gap line are:

$$\dot{s} = \frac{1}{2H_{im}} \left(\frac{P_{im}}{1-s} - P_{ag}^{\rho} \right) \tag{7.13}$$

$$P_{ag}^{\rho} = \left(\frac{sR_r}{R_r^2 + s^2 X_r^2} \right) \left((e_{ag}^{\rho})^2 + (f_{ag}^{\rho})^2 \right) \tag{7.14}$$

$$Q_{ag}^{\rho} = \left(\frac{s^2 X_r}{R_r^2 + s^2 X_r^2} \right) \left((e_{ag}^{\rho})^2 + (f_{ag}^{\rho})^2 \right) \tag{7.15}$$

where H_{im} is the induction motor's inertia constant, P_{im} is the mechanical output power, P_{ag}^{ρ} and $Q_{ag}\rho$ are the three-phase active and reactive powers at the air-gap line, e_{ag}^{ρ} and f_{ag}^{ρ} are the three-phase real and imaginary components of the air-gap voltage, R_r and X_r are the rotor's resistance and reactance, and the a, b and c phases of the load are represented by the

superscript ρ.

The differential equation representing the slip s, Eq. 7.13, is discretised making use of the trapezoidal method as follows:

$$s_{(t)} - s_{(t-\Delta t)} = \frac{\Delta t}{2}\left[\frac{1}{2H_{im}}\left(\frac{P_m}{1-s_{(t)}} - P_{ag(t)}\right) + \frac{1}{2H_{im}}\left(\frac{P_m}{1-s_{(t-\Delta t)}} - P_{ag(t-\Delta t)}\right)\right] \quad (7.16)$$

Eq. 7.16 can be split into three algebraic equations separating the terms with respect to t, Δt and the constant parameters. Hence, it can be re-arranged as in the following way.

$$s_{(t)} - s_{(t-\Delta t)} = \frac{\Delta t}{2}\left[\frac{1}{2H_{im}}\left(\frac{P_m}{1-s_{(t)}} - P_{ag(t)}\right) + \frac{1}{2H_{im}}\left(\frac{P_m}{1-s_{(t-\Delta t)}} - P_{ag(t-\Delta t)}\right)\right] \quad (7.17)$$

and in a more compact form,

$$F_s = F_{s(t)} + F_{s(t-\Delta t)} + C_s = 0 \quad (7.18)$$

The three-phase active and reactive power injections at conventional buses are straightforwardly extended to include the three-phase active and reactive powers contributed by all induction motors described by Eqs. 7.14 and 7.15 respectively. Hence, at load buses with induction motors,

$$
\begin{aligned}
&P^a_{(m)} + P^a_{ag(imbus(n))} \\
&P^b_{(m)} + P^b_{ag(imbus(n))} \\
&P^c_{(m)} + P^c_{ag(imbus(n))} \\
&Q^a_{(m)} + Q^a_{ag(imbus(n))} \\
&Q^b_{(m)} + Q^b_{ag(imbus(n))} \\
&Q^c_{(m)} + Q^c_{ag(imbus(n))}
\end{aligned}
\tag{7.19}
$$

for m=1,. . .,nbus and n=1,. . .,nim, where $imbus(n)$ is an array of induction motor-connected buses.

7.3 Dynamic Simulations of Three-Phase Power Networks

7.3.1 Test case 1

The nine-bus, three-machine power system depicted by the one-line schematic diagram of Fig. 4.16, is adopted and extended to carry out three-phase dynamic power flows studies. An unbalanced load perturbation is carried out. At minute 1 the load connected at Bus 6 is reduced by 30, 25 and 20% of its initial value for phase a, b and c respectively. Later on at minute 3, the load connected at Bus 8 is increased by 45, 50 and 55% of its original value for phases a, b and c respectively. The simulation is run for ten minutes. The three-phase power loads are represented by their static load model and the unbalanced values are given at Table 7.1.

Fig. 7.10 shows the three-phase bus voltage magnitude for balanced load reduction of 25% at time 1 min and balanced load increment of 50% at minute 3. Fig. 7.9 depicts the condition where unbalanced load conditions are carried out. For the balanced load condition, the perturbation carried out is the same as for phase b of the unbalanced case. It is taken as

Table 7.1: *Final values for power loads.*

Three phase power loads	
Load Bus 6	Load Bus 8
$S^a = 0.70 + \text{j}0.245$	$S^a = 1.305 + \text{j}0.435$
$S^b = 0.75 + \text{j}0.262$	$S^b = 1.350 + \text{j}0.450$
$S^c = 0.80 + \text{j}0.280$	$S^c = 1.395 + \text{j}0.465$

the starting condition to compare the results for balanced and unbalanced conditions.

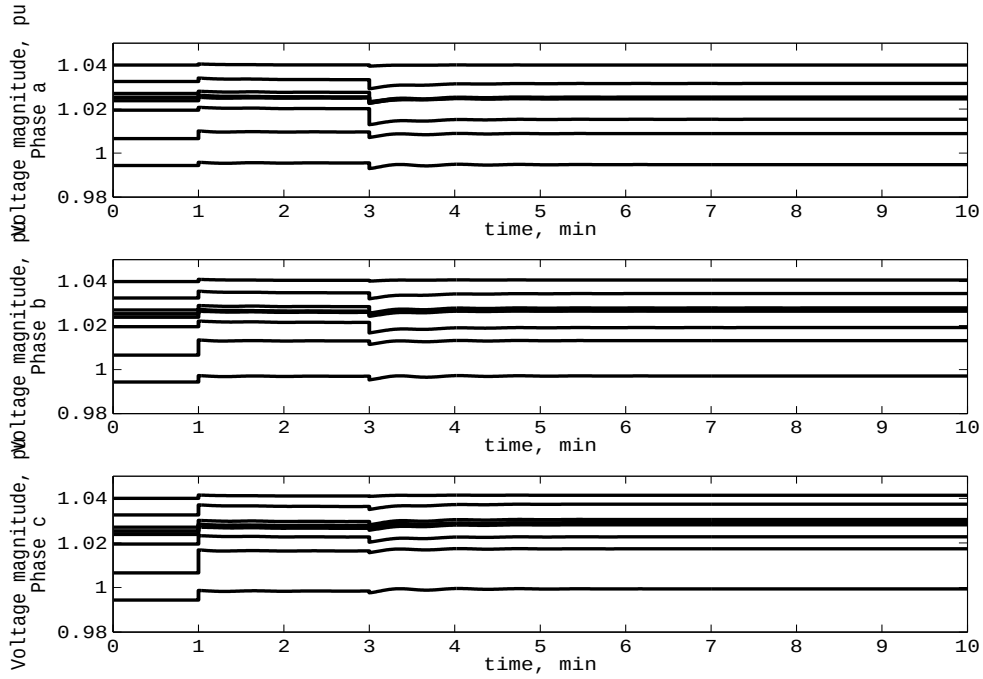

Figure 7.9: *Three-phase bus voltage magnitude under unbalanced loading conditions.*

Figure 7.11 shows the voltage performance at Bus 5. It is appreciated from this figure that the unbalanced conditions does not accentuates considerably the voltage profile, however, there is a voltage difference between the balanced and unbalanced case. The continuous lines represent the balanced load condition, and the dashed lines represent the unbalanced load condition.

Fig. 7.12 and Fig. 7.14 depict the speed and the rotor angle deviation from the syn-

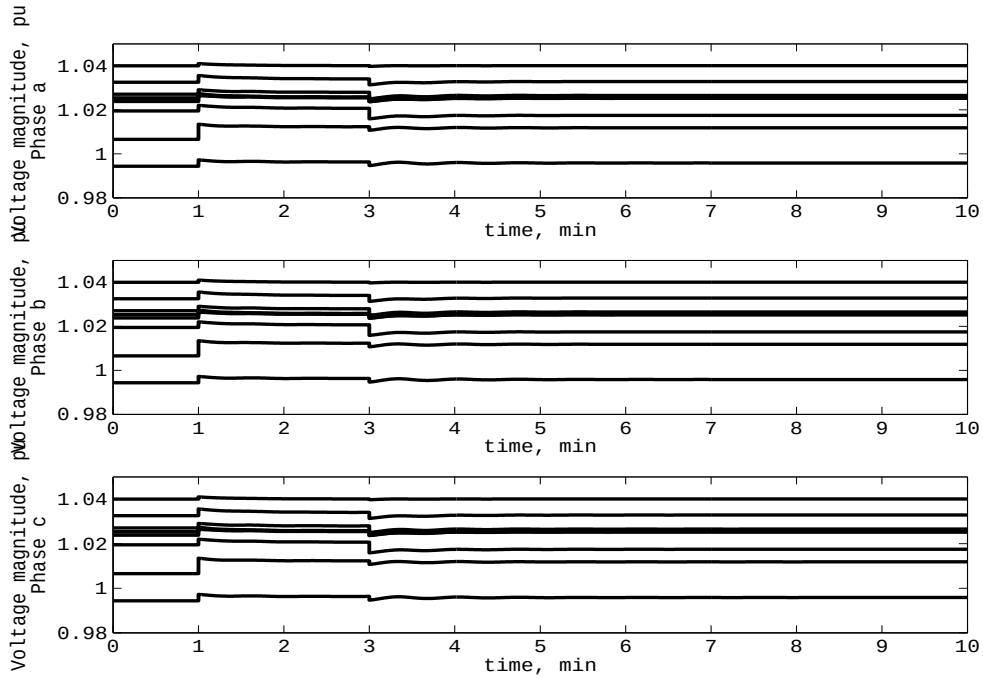

Figure 7.10: *Three-phase bus voltage magnitude under balanced loading conditions.*

chronous generators for the unbalanced case, and Fig. 7.13 and Fig. 7.15 show the same variables response under balanced conditions, respectively.

From the speed and angle deviation figures, it is appreciated that the unbalanced load perturbation do not have an impact on the synchronous generator performance. For both cases, the speed deviation reaches a value around 1.001 at time 3 min, and it settles down to a value very close to the steady-state condition.

Figure 7.16 depicts the angle differences between generators namely, $\delta_{21} = \delta_2 - \delta_1$ and $\delta_{31} = \delta_3 - \delta_1$. After the first load perturbation at time 1 min the angular differences start to decay, and later on at time 3 min, when the second load perturbation takes place, the angular differences still go further down and oscillate for around 2 minutes then becoming stable for the remaining simulation time.

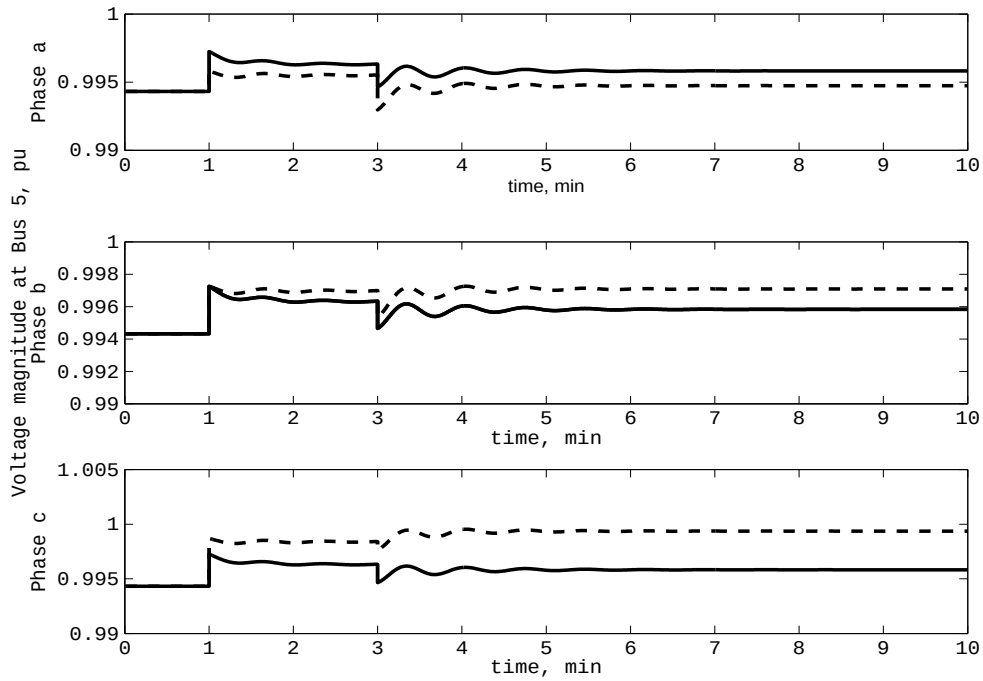

Figure 7.11: *Three-phase voltage magnitude at Bus* 5 *under balanced and unbalanced loading conditions.*

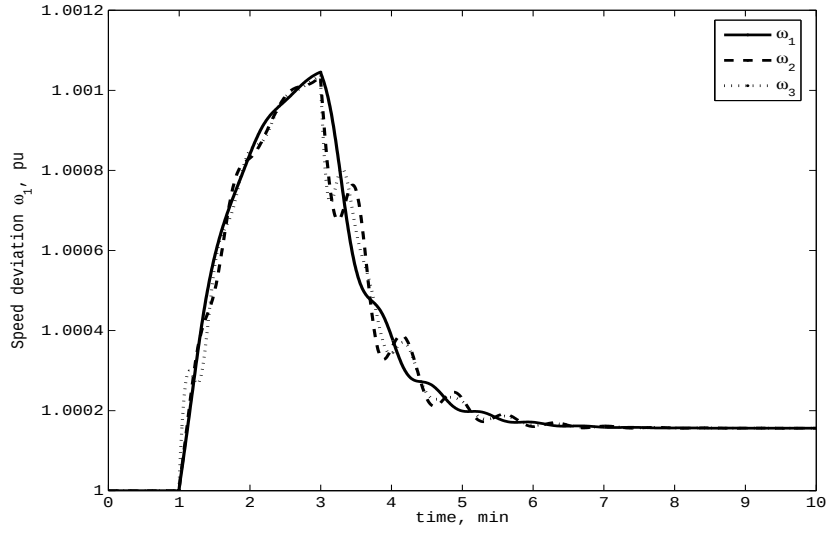

Figure 7.12: *Synchronous generators speed deviation under unbalanced loading conditions.*

7.3.2 Test case 2

To show the flexibility of the three-phase dynamic power flows algorithm, a series fault involving one phase of a transmission line opening is carried out. As in the previous test

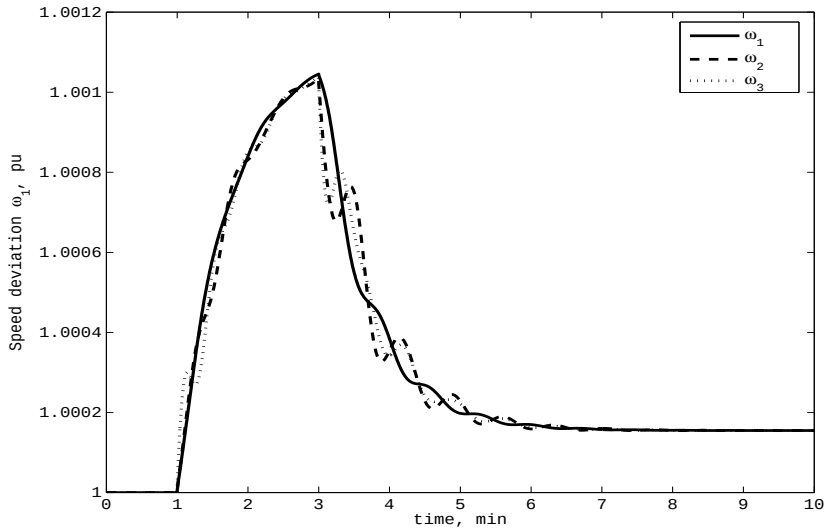

Figure 7.13: *Synchronous generators speed deviation under balanced loading conditions.*

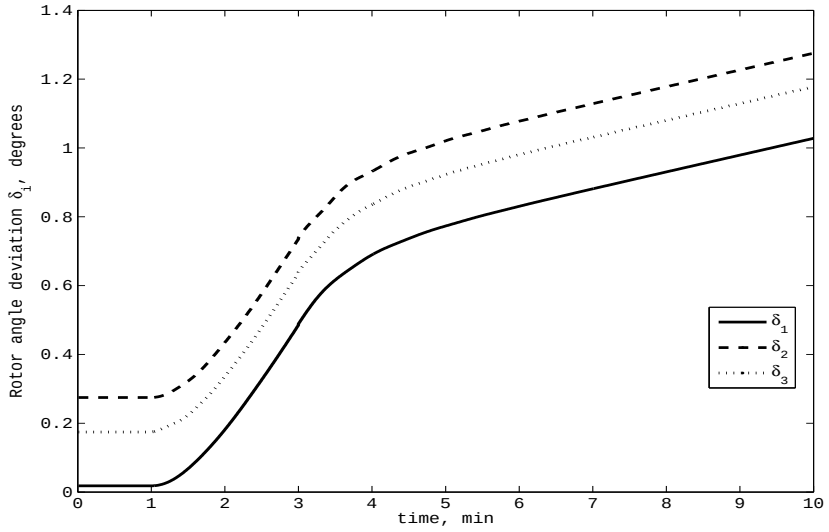

Figure 7.14: *Rotor angle deviation under unbalanced loading conditions.*

case, the three-machine nine-bus power system is used to carry out the study. The phase a of the transmission line which connects buses 5 and 7 is disconnected at time 1 min; as a consequence of this action the bus voltage magnitude of phase a of the system is reduced considerably compared to the voltages in phases b and c. Fig. 7.17 depicts the bus voltage

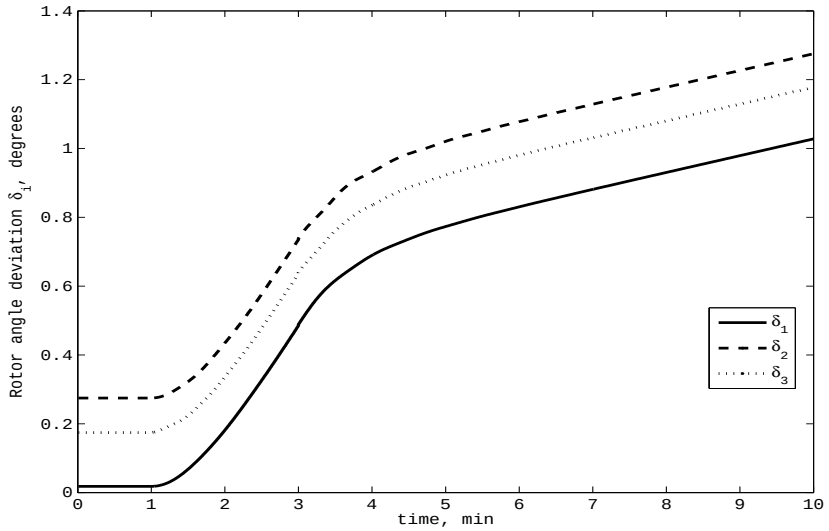

Figure 7.15: *Rotor angle deviation under balanced loading conditions.*

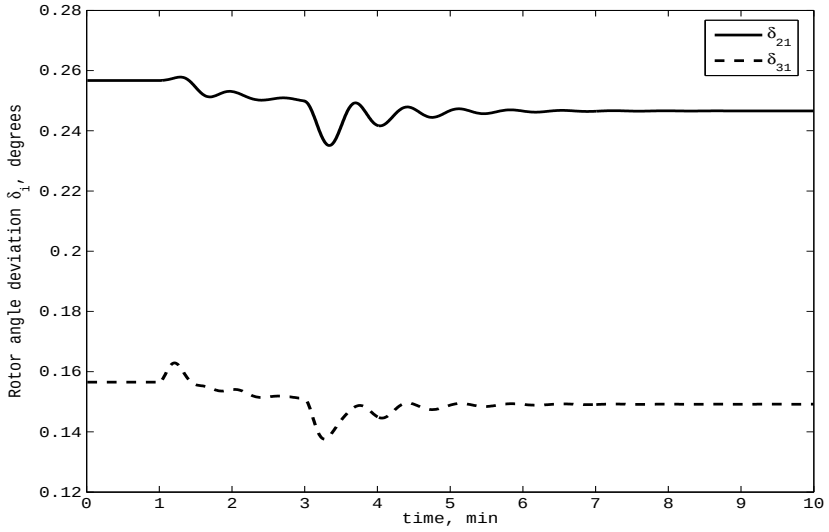

Figure 7.16: *Rotor angle differences under unbalanced loading conditions.*

magnitude of the system under this condition.

It should be noted that although phases b and c of the transmission line remain connected their behaviour is markedly influenced by the tripping of phase a as depicted in Fig. 7.17.

From Fig. 7.17 it is appreciated that at the time the phase a of the transmission line

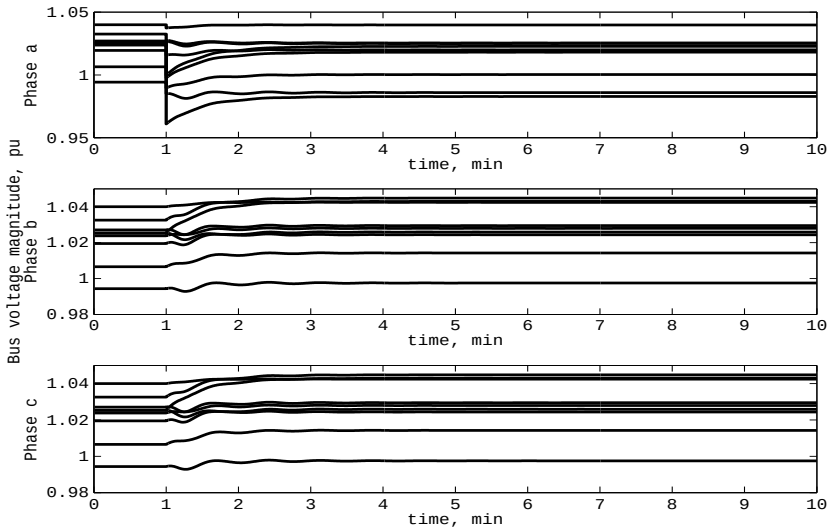

Figure 7.17: *Bus voltage magnitude under unbalanced condition.*

connecting buses 5 and 7 is tripped, the voltage magnitude has a considerable decrement in comparison with the voltage magnitude for phases b and c. The most severe case for the bus voltage magnitude of phase a of Fig. 7.17, is for the voltage magnitude at Bus 6. It reaches a value close to 0.96 pu, whereas for phases b and c the voltage magnitude get a value around 1.02 pu. In general, the voltage magnitude for phase a suffers a decrement while for phases b and c the voltage magnitudes have a slight increment.

Figures 7.18 and 7.19 show the angle differences between generators for the unbalance and balanced simulation case respectively. For both test cases, the angular differences of the machines are not larger enough to produce instability, notwithstanding that their response is oscillatory just after the perturbation but it settles to a new steady-state value.

From Figs. 7.18, 7.19 for rotor angle deviation and Figs. 7.20, 7.21 for generators speed deviation respectively, it is observed that the unbalanced perturbation applied to the power network does affect the synchronous generators response when compared with the balanced assessment. The case when the whole transmission line is tripped, which is a balanced case, the bus voltage magnitude has a more unfavourable response, since this a more severe

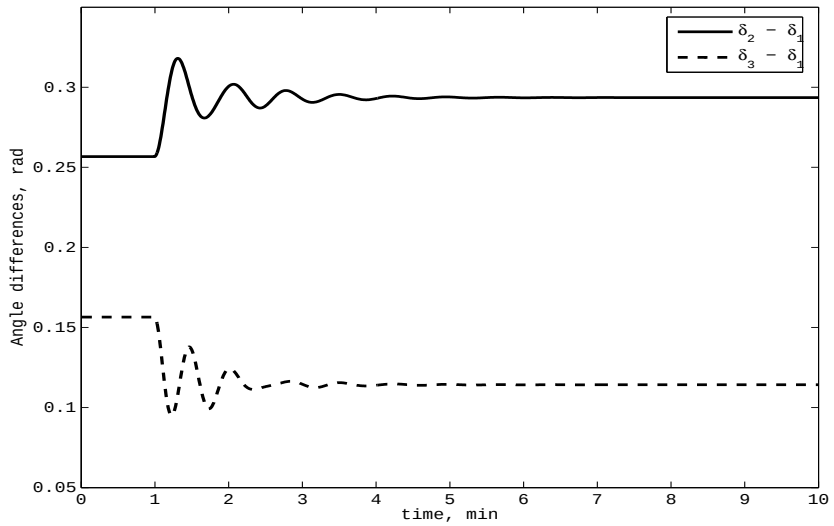

Figure 7.18: *Angle differences under unbalanced condition.*

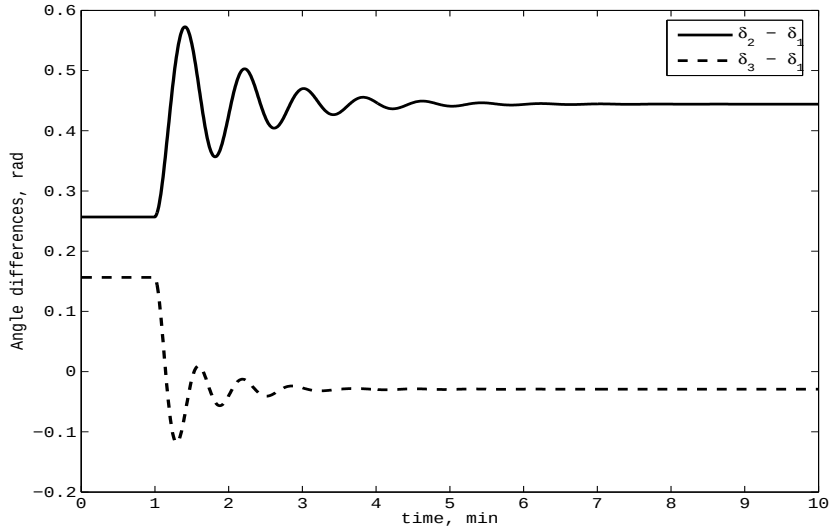

Figure 7.19: *Angle differences under balanced condition.*

perturbation than just the tripping of one phase of the transmission line. Fig. 7.22 shows the bus voltage magnitude for the tripping of the whole transmission line.

It is observed in Figs. 7.20 and 7.21 that the maximum speed deviation is 1.001 pu at time 3 min and then it drops sharply to a value of around 1.00017 pu.

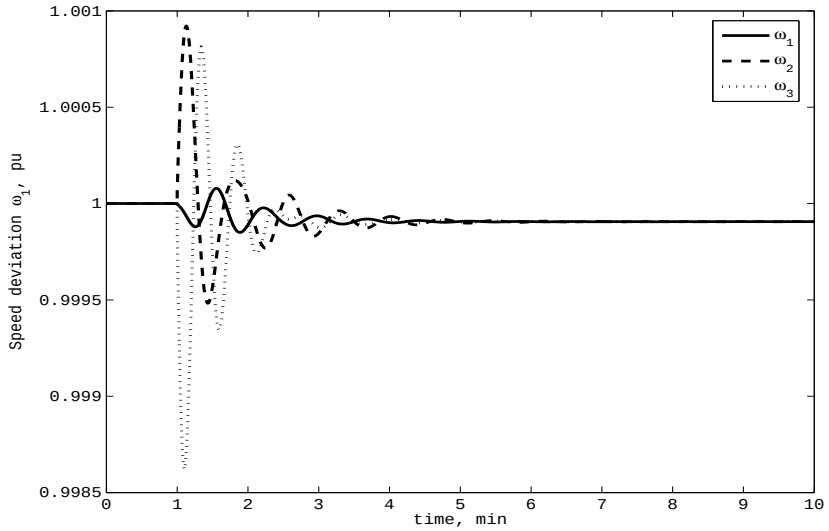

Figure 7.20: *Rotor speed deviation under unbalanced condition.*

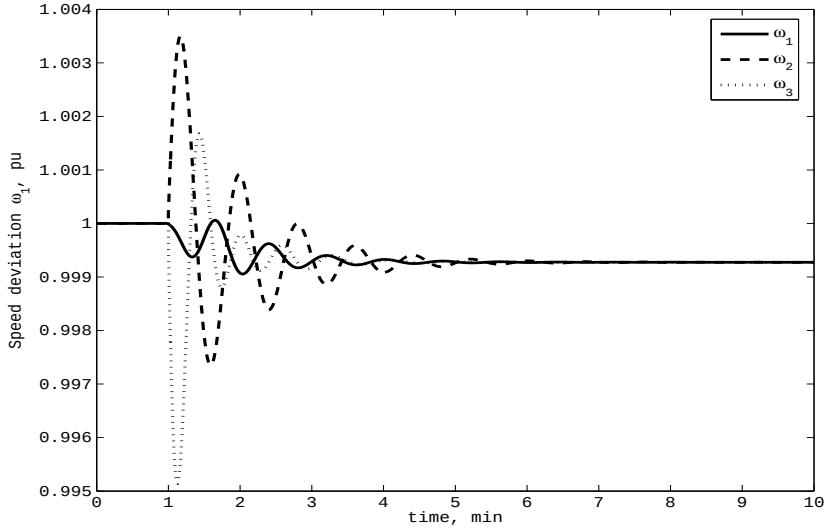

Figure 7.21: *Rotor speed deviation under balanced condition.*

7.3.3 Test case 3

The dynamic behaviour of the three-phase load tap changer transformer is assessed in this section.

A load increment of 20% for phase b of Bus 5 is applied at time 1 min, and later on at

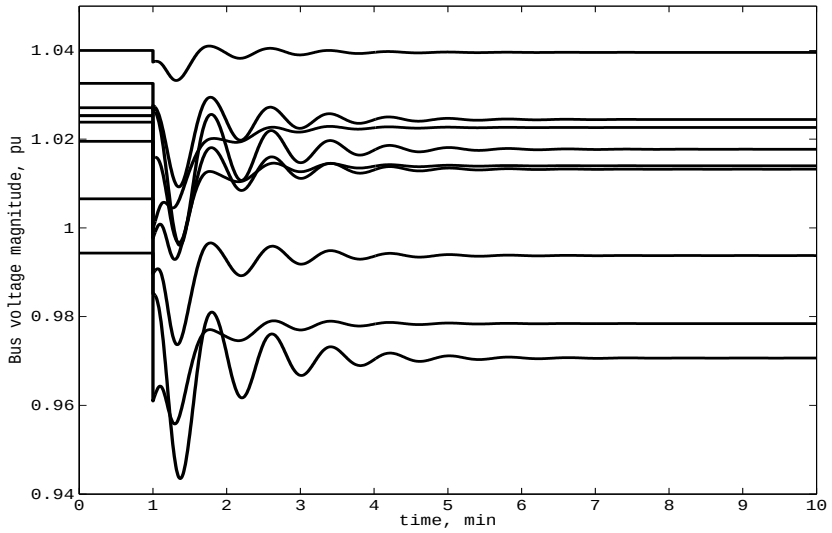

Figure 7.22: *Bus voltage magnitude for phase a under balanced condition.*

time 2 min, the load connected at phase a of the same bus is increased further by 25%. The evaluation time is 10 min.

Figures 7.23, 7.24 and 7.25 show the voltage magnitude for phases a, b and c for the voltage-controlled buses, respectively.

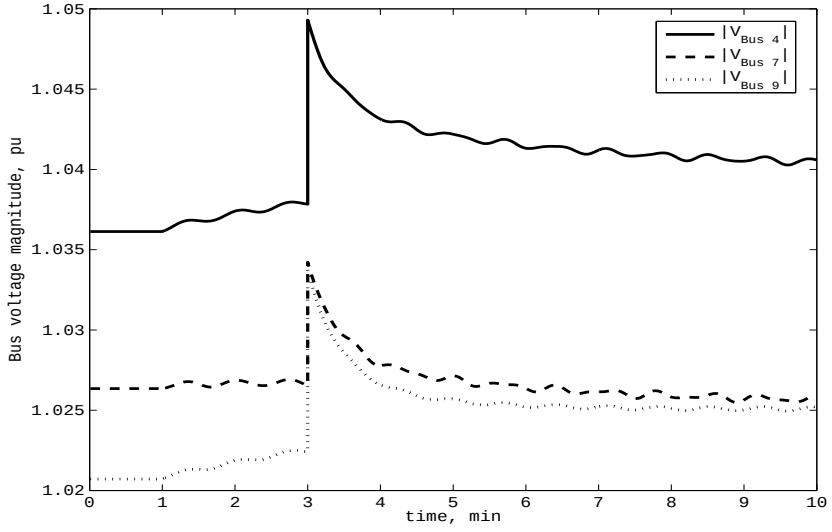

Figure 7.23: *Phase a of the bus voltage magnitude for voltage-controlled buses.*

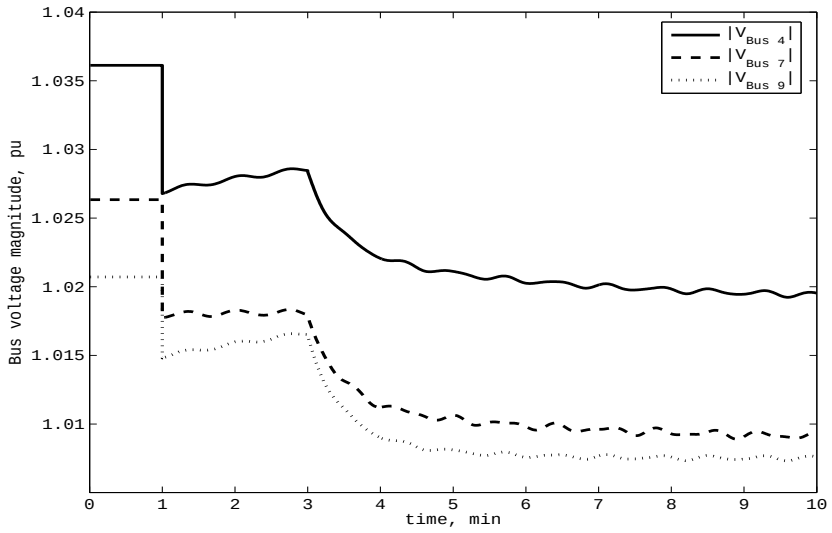

Figure 7.24: *Phase b of the bus voltage magnitude for voltage-controlled buses.*

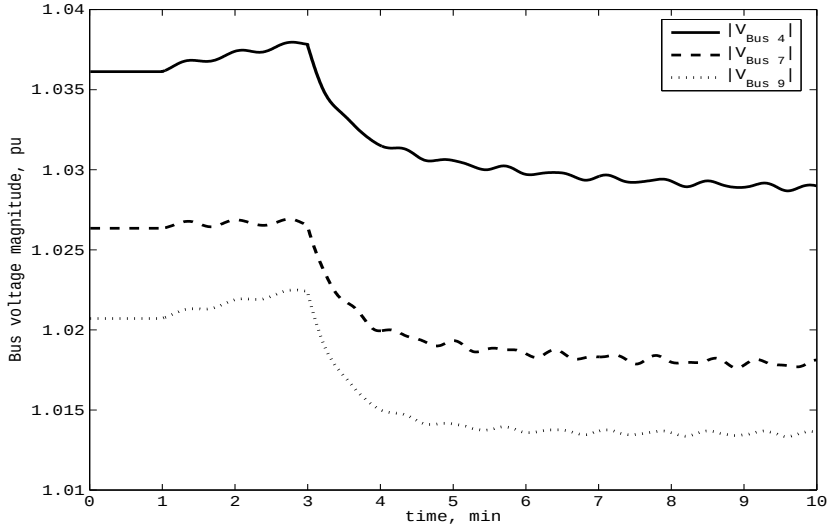

Figure 7.25: *Phase c of the bus voltage magnitude for voltage-controlled buses.*

It is observed in Figs. 7.23 and 7.25 that the voltage magnitude at these points is very well controlled when the first perturbation takes place; furthermore after the second load perturbation takes action, the dynamic load tap changer still controlling the voltage magnitude within a reasonable level. Fig. 7.27 depicts the field voltage magnitude for synchronous

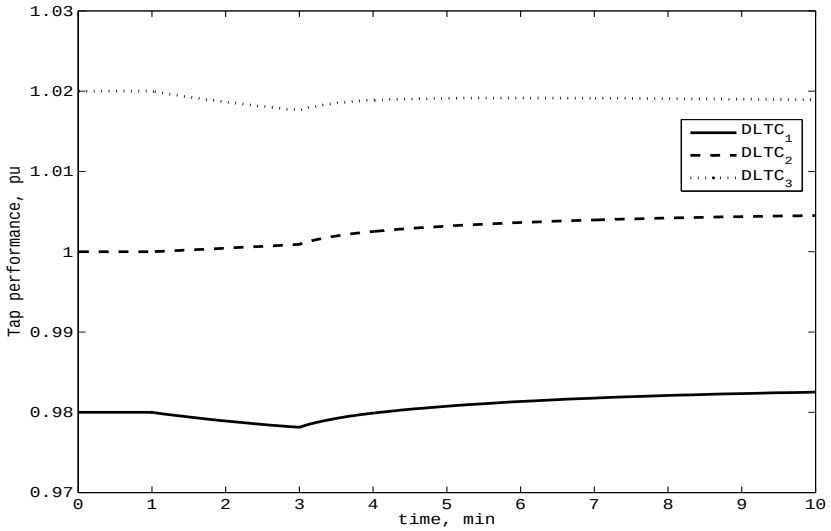

Figure 7.26: *Dynamic load tap changer performance.*

generators and Fig. 7.26 depicts the dynamic load tap changer performance. It is noticed from this figure that the tap ratio T_k is no longer $1:1$ but that it varies according to system requirements for voltage control purposes.

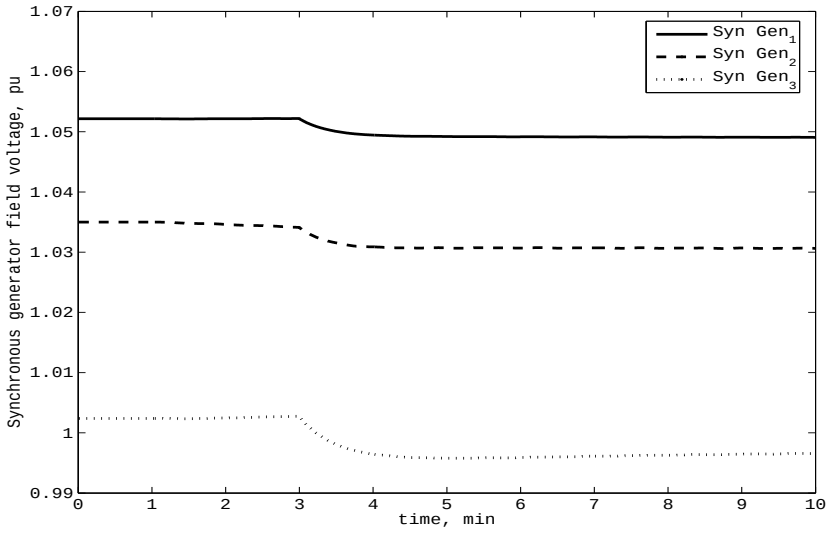

Figure 7.27: *Field voltage magnitude for synchronous generators .*

7.3.4 Test case 4

At this section the three-phase induction motor behaviour is analysed. The same power network used in the last test case is applied to carry out this assessment.

To demonstrate the applicability and versatility of the dynamic power flows tool and the induction motor modelling, the loads of buses 5 and 6 of Fig. 4.16 have been replaced for two large industrial induction motors [Kundur, 1994]. The load connected at Bus 8 remains as an static load. There is a 20% increment of the load of one phase connected to this bus, at time 1 min. The simulation is run for 10 minutes.

Figures 7.28 and 7.29 and Figs. 7.30 and 7.31 the show three-phase active and reactive power consumed by the induction motors at buses 5 and 6, respectively.

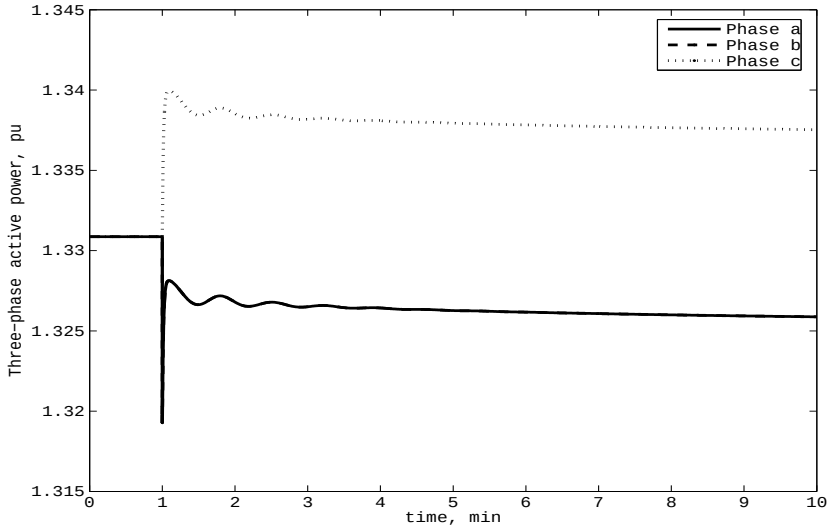

Figure 7.28: *Three-phase active power consumption by the induction motor connected at Bus* 5.

As expected, the three-phase active and reactive powers consumptions of the induction motors are affected by the imbalances. The powers for phases a and b are similar but not for phase c. The voltage magnitude at the induction motor-connected buses is also affected by the load increments and they show a similar behaviour as the consumed powers, as show in Fig. 7.33. The continuous lines represent the voltage magnitude for the induction motor

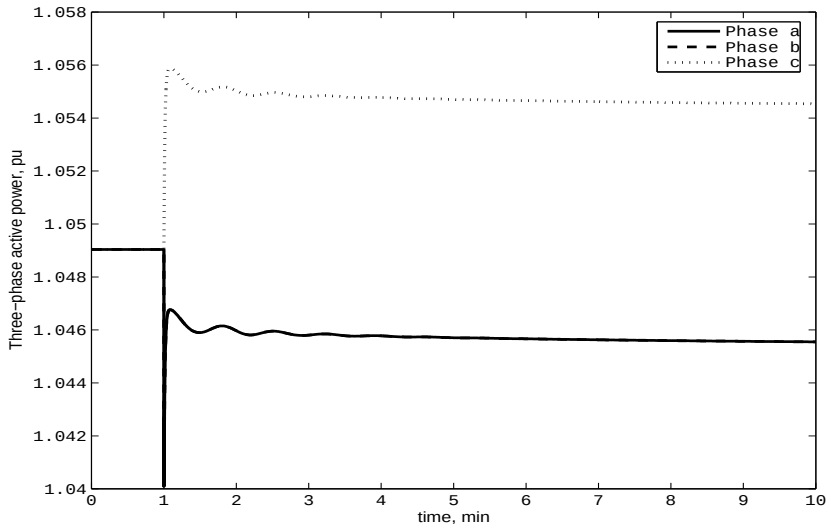

Figure 7.29: *Three-phase active power consumption by the induction motor connected at Bus* 6.

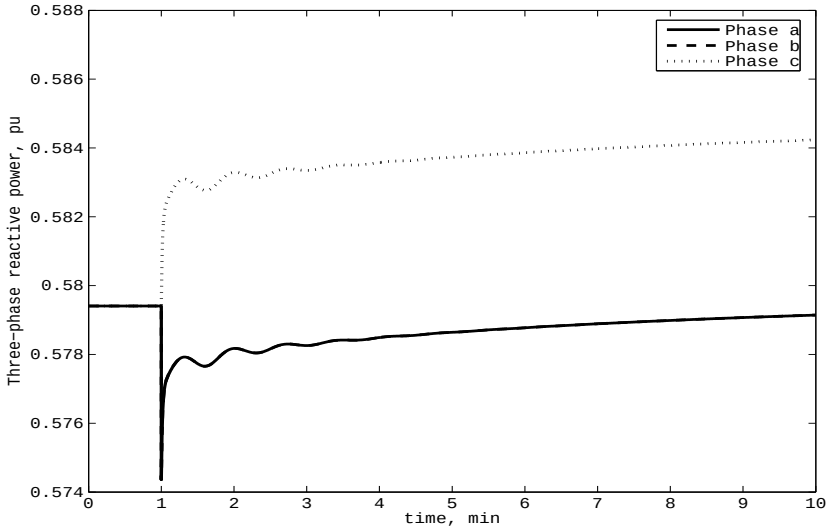

Figure 7.30: *Three-phase reactive power consumption by the induction motor connected at Bus* 5.

connected at Bus 6 and the dashed lines represent the voltage magnitude for induction motor connected at Bus 6. Figs. 7.33(a), 7.33(b) and 7.33(c) depict the voltage magnitude for phase a , b and c respectively.

Fig. 7.32 depicts the slip performance for the induction motor during the transient sim-

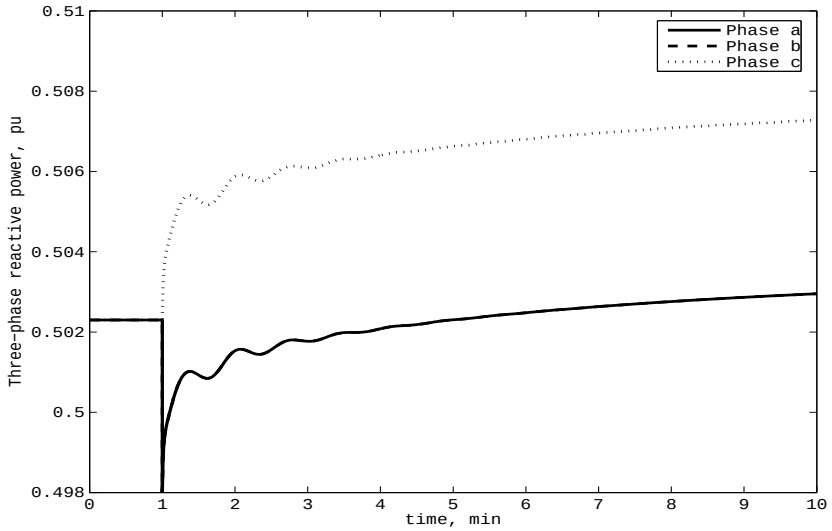

Figure 7.31: *Three-phase reactive power consumption by the induction motor connected at Bus* 6.

ulation.

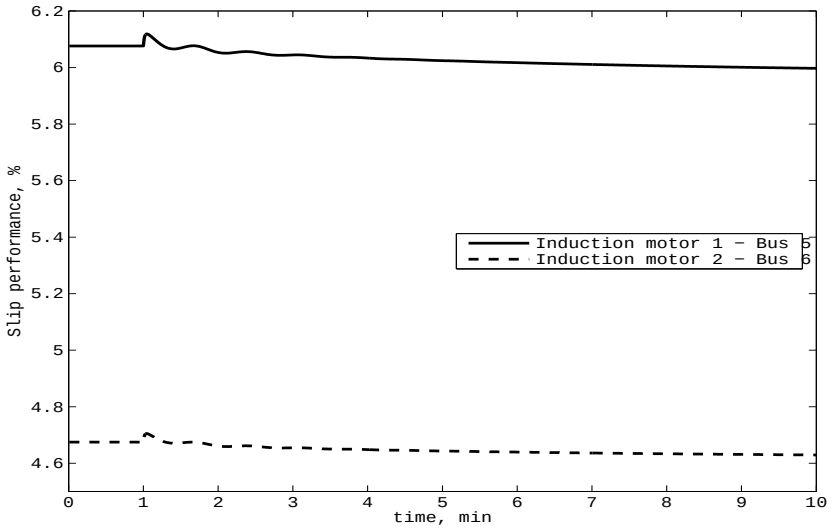

Figure 7.32: *Slip performance for three-phase induction motor.*

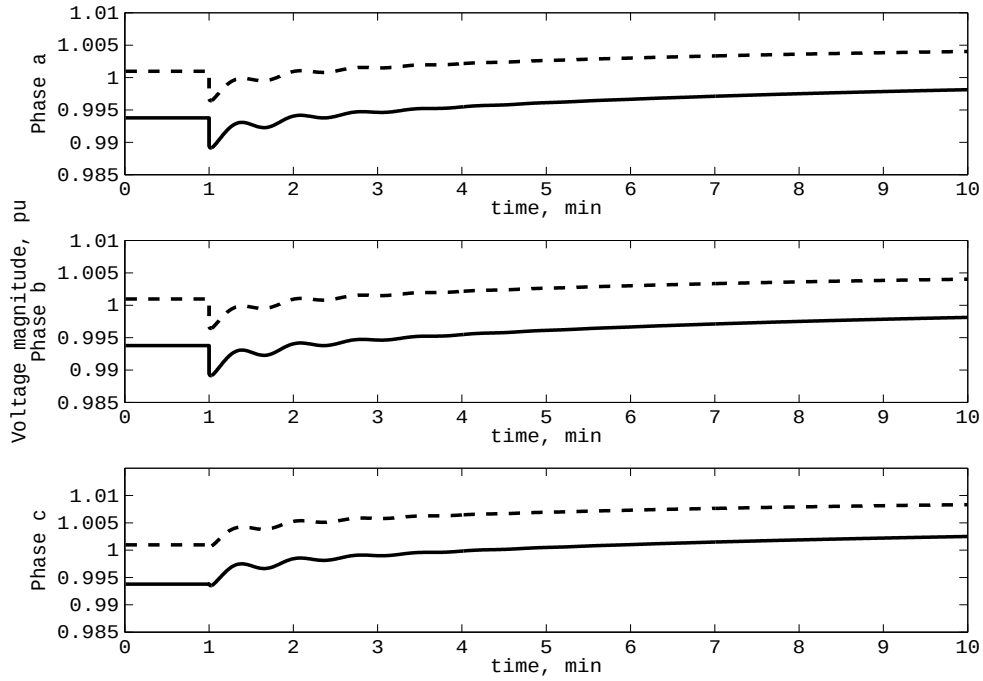

Figure 7.33: *Voltage magnitude for induction motor-connected buses.*

7.4 Summary

This chapter focuses on the three-phase approach in rectangular co-ordinates for the dynamic assessment of power systems.

The dynamic power flows computer program has been extended to carry out three-phase analyses. Likewise, it encompass the three-phase synchronous generator modelled, static and dynamic three-phase load modelling including induction motor load, the dynamic three-phase load tap changer and the unbalanced perturbations to the system to enable the study of a wide range of dynamic phenomena in *abc* co-ordinates of power systems.

The three-phase dynamic model of generating plants is addressed. For the purpose of this research, dynamic stability assessment, mathematical models of the synchronous machine with automatic voltage regulator, turbine, speed-governor and boiler, in the *abc* frame of reference have been developed. A set of ordinary differential equations describing the components are obtained for each generating plant component.

To a large extent the method merges simultaneously the algebraic-differential equation set which represent the power system in *abc* co-ordinates by using repeated linearization and the trapezoidal rule, resulting in a unified frame-of-reference with which to carry out reliable numerical solutions using the Newton-Raphson method for three-phase dynamic simulations of power systems.

Chapter 8

Conclusions

The dynamic assessment of electrical power systems using the Newton-Raphson method represents the main concern in this research work. The goal is to develop suitable dynamic models of power plant components, such as synchronous generators, power loads, VSC-FACTS controllers, and to assess their interaction with the electrical power network.

The solution technique makes use of a simultaneous solution approach which allows for models of rotor saliency, flux decay, non-linear loads and a wide range of control actions to be incorporated within a unified framework. This method is particulary suitable for carrying out long-range dynamic assessments, which is one of the key points of concern of this thesis. This contrast with more traditional solution techniques, namely, partitioned methods, which are primarily aimed at covering short-range simulation studies.

This research work may be seen to consist of three main parts, which are: (i) Steady-state power flows analysis in phase domain co-ordinates, including LCC-HVDC converters with various control modes; (ii) dynamic power flows using a simultaneous solution technique, including electro-mechanical controlled power plant components and VSC-FACTS devices representation; (iii) and three-phase dynamic power flows for carrying out dynamic stability assessments of unbalanced power systems.

From the dynamic simulation studies carried out, it has been observed that inclusion of the load tap-changer transformer has the capability of enhancing system voltage stability. It has also been assessed via modelling and simulation, that the voltage dependency of loads is a matter of great importance in long-term dynamic phenomena and that the load models should reflect such dependency correctly when carrying out long-term dynamic studies. Indeed, the studies carried out show that the most realistic way of load modelling representation during voltage stability assessments is when induction motor loads are modelled explicitly as induction motors and not by static polynomial loads with voltage exponent 1.

The inclusion of VSC-FACTS controllers have shown to contribute effectively to providing dynamic voltage support during steady-state operation, and to enhance power system stability under unfavourable conditions. They have a faster response speeds than those provided by electromechanical devices.

Quantifiable outcome of this research, are software environments for carrying out comprehensive dynamic power flows studies in both positive sequence and in *abc* co-ordinates. Using the generated software, detailed simulations have been carried out in order to assess the dynamic impact of various power plant components on the electrical power network.

Dynamic modelling of the system is amenable to its better understanding, particularly when it undergoes unfavourable conditions.

It is worth adding that with the ever-increasing power of computers, the development of real-time simulators for dispatching and security monitoring issues are finding increasing favour, and that simulation tools using the same philosophy as that applied in this research work may be used as the core of an on-line dynamic security assessment application system.

8.1 Future work

Alongside the developed mathematical models for VSC-FACTS devices and its inclusion into the simultaneous method for carrying out dynamic stability assessments for electrical

power networks, more work needs to be done for including models of additional power electronics controllers such as the UPFC and the TCSC. Modelling of embedded generation technologies should be considered for its incorporation into the dynamic power flow algorithm, including wind farms.

Bibliography

(2007). ABB.

Acha, E., Fuerte-Esquivel, C., Ambriz-Perez, H., and Angeles-Camacho, C. (2004). *FACTS Modelling and Simulation in Power Networks*. John Wiley & Sons, Inc.

Ainsworth, J. D. (1988). Phase-locked oscillator control system for thyristor-controlled reactors. *IEE Generation, Transmission and Distribution*, 135(2):146–156.

Anderson, G., Donaleck, P., Farmer, R., Hatziargyriou, N., Kamwa, I., Kundur, P., Martins, N., Paserba, J., Pourbeis, P., Sanches-Gasca, J., Schulz, R., Stankovic, A., Taylor, C., and Vittal, V. (2005). Causes of the 2003 Major Grid Blackout in North America and Europe, and Recommended Means to Improve System Dynamic Performance. *IEEE Transaction on Power Systems*, 20(4):1922–1928.

Anderson, P. M. and Fouad, A. A. (1997). *Power System Control and Stability*. IEEE Press.

Anrborg, S., Andersson, G., Hill, D., and Hiskens, I. (1998). On Influence of Load Modellling for Undervoltage Load Shedding Studies. *IEEE Transaction on Power Systems*, 13(13):395–400.

Arrillaga, J. (1998). *High Voltage Direct Current Transmission*. IEE Power and Energy Series.

Arrillaga, J. and Arnold, C. P. (1990). *Computer Analysis of Power Systems*. John Wiley & Sons, Inc.

Arrillaga, J. and Callaghan, C. D. (1991). Three phase ac-dc load and harmonics flows. *IEEE Transactions on Power Delivery*, 6:238–241.

Arrillaga, J., Liu, Y. H., and Watson, N. R. (2007). *Flexible Power Transmission. The HVDC Option*. John Wiley & Sons, Inc.

Arrillaga, J. and Watson, N. R. (2001). *Computer Modelling of Electrical Power Systems*. John Wiley & Sons, Inc, second, edition.

Arrillaga, J. and Watson, N. R. (2002). *Power Systems Electromagnetic Transients Simulation*. The IET, first edition.

Bahrman, M. P. and Johnson, B. K. (2007). The ABCs of HVDC Transmission Technologies. *IEEE Power & Energy Magazine*, 5(2):32–44.

Banerjee, S. and Verghese, G. C. (2001). *Nonlinear Phenomena in Power Electronics*. Wiley-IEEE Press.

Carlsson, L. (2002). Classical HVDC: Still continuing to evolve. *Modern Power Systems, MPS Review: Transmission & Distribution*, pages 19–21.

Chapman, S. (1991). *Electric Machinery Fundamentals*. McGraw Hill, Inc, second edition.

Chen, M.-S. and Dillon, W. E. (1974). Power system modeling. *Proceedings of the IEEE*, 62(7):901–915.

Chow, J. H. (1982). *Time-Scale Modeling of Dynamic Networks with Applications to Power Systems*. Springer-Verlag.

Cole, S., Hertem, D. V., Pardon, I., and Belmans, R. (2006). Randstad HVDC. Technical report, Research Group Electa.

Concordia, C. (1951). *Synchronous Machines. Theory and performance.* John Wiley & Sons, Inc.

Concordia, C. and Ihara, S. (1982). Load Representation in Power system Stability Studies. *IEEE Transaction*, PAS-101:969–977.

Corwin, L. and Miles, W. (1998). Impact assessment of the 1977 new york city blackout. Technical report, System Control Inc., Energy Division.

Dommel, H. W. and Sato, N. (1972). Fast transient solutions. *IEEE Transactions on Power Apparatus and Systems*, 91:1643–1650.

Elgerd, O. (1971). *Electric Energy System Theory: An Introduction.* McGraw Hill.

Energy Development and Power Generating Committe of the PES (2003). IEEE Recommended Practice for Excitation System Models for Power System Stability Studies.

Gear, C. W. (1971a). *Numerical Initial Value Problem in Ordinary Differential Equations.* Prentice Hall.

Gear, C. W. (1971b). Simultaneous numerical solution of differential-algebraic equations. *IEEE Transactions on Circuit Theory*, 18:89–95.

Hagajos, L. and Danai, B. (1998). Laboratory measurements and models of modem loads and their effect on voltage stability studies. *IEEE Transactions on Power Systems*, 13(2):584–592.

Harker, B. J. and Arrillaga, J. (1979). 3-phase ac-dc load flow. *IEE Proceedings*, 126:1275–1281.

Hill, D. (1993). Nonlinear Dynamic Load Models with Recovery for Voltage Stability Studies. *IEEE Transaction on Power Systems*, 8(1):166–176.

Hill, D. and Mareels, I. (1990). Stability Theory for Differential/Algebraic Systems with Application to Power Systems. *IEEE Transaction on Circuits and Systems*, 37(11):1416–1423.

Hingorani, N. G. and Gyugyi, L. (1999). *Understanding FACTS. Concept and Technology of Flexible AC Transmission Systems*. John Wiley & Sons, Inc.

IEEE Committee Report (1973). Dynamic Models for Steam and Hydro Turbines in Power System Studies. *IEEE Transactions on Power Apparatus and Systems*, 92:1904–1915.

IEEE Committee Report (1981). Excitation System models for Power System Stability Studies. *IEEE Transactions on Power Apparatus and Systems*, 100:494–509.

IEEE Power Engineering Society (2002). Voltage Stability Assessment: Concepts, Practices and Tools", Final document.

Johansson, S. G., Asplund, G., Jansson, E., and Rudervall, R. (2004). Power System Stability Benefits with VSC DC-Transmission Systems. Technical Report B4-204, CIGRE.

Kassakian, J., Schlecht, M., and Verghese, G. C. (1991). *Principles of Power Electronics*. Addison-Wesley.

Kimbark, E. W. (1948a). *Power System Stability*, volume 1, Elements of Stability Calculation. IEEE Press.

Kimbark, E. W. (1948b). *Power System Stability*, volume 3, Synchronous Machines. IEEE Press.

Knight, U. G. (2001). *Power Systems in Emergencies: From Contigency Planning to Crisis Management*. John Wiley & Sons, Inc.

Kundur, P. (1994). *Power System Stability and Control*. McGraw Hill.

Lapidus, L. and Seinfeld, J. (1971). *Numerical Solution of Ordinary Differential Equations*. Academic Press.

Lehn, P. W. and Iravani, M. R. (1998). Experimental evaluation of STATCOM closed loop. *IEEE Transaction on Power Delivery*, 13(4):1378–1384.

Lehn, P. W. and Iravani, M. R. (2002). Exact modeling of the voltage source converter. *IEEE Transaction on Power Delivery*, 17(1):217–222.

Machowski, J., Bialek, J. W., and Bumby, J. R. (1997). *Power System Dynamic and Stability*. John Wiley & Sons, Inc.

Milano, F. (2005). An open source power system analysis toolbox. *IEEE Transactions on Power Systems*, 20:1199–1206.

Milano, F. (2006). An open source power system analysis toolbox. In *IEEE Power Engineering Society General Meeting*. IEEE.

Milano, F. (2007). Psat version 2.

Morison, G. K., Gao, B., and Kundur, P. (1993). Voltge stability analysis using static and dynamic approaches. *IEEE Transactions on Power Systems*, 8(3):1159–1171.

Nabavi-Niaki, S. A. (1996). *Modelling and Applications of Unified Power Flow Controller (UPFC) for Power Systems*. Ph.d. thesis, University of Toronto.

Nasar, S. and Trutt, F. (1999). *Electric Power Systems*. CRC Press.

Padiyar, K. R. and Kulkarni, A. M. (1997). Design of reactive current and voltage controller of static condenser. *Electrical Power & Energy Systems*, 19(6):397–410.

Park, R. H. (1929). Two-reaction theory of synchronous machines - generalized method of analysis part i. *AIEE Transactions*, 48(2):716–730.

Pavella, M. and Murthy, P. G. (1995). *Transient Stability of Power Systems, Theory and Practice*. John Wiley & Sons, Inc.

Pedra, J., Sainz, L., and Corcoles, F. (2005). Study of aggregate models for squirrel-cage induction motors. *IEEE Transactions on Power Systems*, 20:1519–1527.

Claudio A. Cañizares (1995). On bifurcation, voltage collapse and load modelling. *IEEE Transactions on Power Systems*, 10(1):512–522.

Commission de Régulation de L'énergie (2004). Report on the event of september 28^{th}, 2003 culminating in the separation of the italian power system from the ohter ucte networks. Technical report, Commission de Régulation de L'énergie and Autorità per l'energia elettrica e il gas.

IEEE (2000). Special issues on hybrid systems. *IEEE Proceedings*, 88(7):879–887.

IEEE Load Task Force (1993). Load representation for dynamic performance analysis [of power systems]. *IEEE Transactions on Power Systems*, 8:472–482.

IEEE Power Engineering Review (1991). Northeast blackout of 1965. Technical report, IEEE.

IEEE Task Force on Load Representation (1995). Load models for power flow and dynamic performance simulation. *IEEE Transaction on Power Systems*, 10:523–538.

IEEE Working Group on Power Plant Response to Load Changes (1973). Mw response of fossil fueled steam units. *IEE Proceedings*, PAS-92:455–463.

IEEE/CIGRE Joint Task Force on Stability Terms and Definitions (2004). Definition and classification of power system stability. *IEEE Transactions on Power Systems*, 19(2):1387–1401.

National Grid (2003). Report into the august 28 2003 south london power failure. Technical report, National Grid.

US - Canada Power System Outage Task Force (2004). Final Report on the August 14, 2003 Blackout in the United States and Canada: Causes and Recommendations.

Qin, W., Hwachang, S., and Ajjarapu, V. (2006). Continuation-based quasi-steady-state analysis. *IEEE Transactions on Power Systems*, 21(1):171–179.

Rafian, M., Sterling, M., and Irving, M. (1987). Real-time power system simulation. *IEE Proceedings*, 134(3):209–223.

Rashid, M. H. and Maswood, A. I. (1988). Analysis of three-phase ac-dc converters under unbalanced supply conditions. *IEEE Transactions on Industry Applications*, 24(3):449–455.

Reed, G. and Takeda, M. (2003). Advantages of voltage source converters (vsc) based design concepts for facts and hvdc-link applications. *IEEE Power Engineering Society, General Meeting*, 13:1816–1821.

Sekine, Y. and Ohtsuki, H. (1990). Cascaded Voltage Collapse. *IEEE Transaction on Power Systems*, 5(1):250–256.

Siemens AG Power Transmission and Distribution High Voltage Division (2007). High Voltage Direct Current Transmission - Proven Technology for Power Exchange. available at: www.nyri.us/pdfs.

Smed, E. T. (1989). A new approach to ac/dc power flow. Msc. thesis, Auburn University.

Smith, B. and Arrillaga, J. (1998). Improved three-phase load flow using phase and sequence components. *IEE Generation, Transmission and Distribution*, 145(3):245–250.

Stagg, G. W. and El-Abiad, A. H. (1968). *Computer Methods in Power Systems*. McGraw Hill.

Stevenson Jr, W. (1982). *Elements of Power System Analysis*. McGraw Hill, fourth edition.

Stott, B. (1979). Power systems dynamic response calculations. *IEEE Proceedings*, 67:219–241.

Stott, B. and Alsac, O. (1974). Fast decoupled load flow. *IEEE Transactions on Power Apparatus and Systems*, 93(3):745–751.

Taylor, C. W. (1994). *Power System Voltage Stability*. McGraw Hill.

Tinney, W. F. and Hart, C. E. (1967). Power flows solution by newton method. *IEEE Transactions on Power Apparatus and Systems*, 86(11):1449–1460.

Van Cutsem, T. and Vournas, C. (1998). *Voltage Stability of Electric Power Systems*. Kluwer Academic Publishers.

Weedy, B. M. (1967). *Electric Power Systems*. John Wiley & Sons, Inc.

Williams, P. (1972). *Numerical Computation*. T. Nelson & Sond Ltd.

Wilsun Xu, J. R. M. and Dommel, H. W. (1991). A multiphase harmonic load flow solution technique. *IEEE Transactions on Power Systems*, 6(1):174–182.

Xu, W. and Mansour, Y. (1994). Voltage stability analysis using generic dynamic load models. *IEEE Transactions on Power Systems*, 9(1):479–486.

Zhang, L., Harnefors, L., and Rey, P. (2007). Power System Reliability and Transfer Capability Improvement by VSC-HVDC (HVDC Light). *Security and Realibility of Electric Power Systems*, CIGRE Regional Meeting:1–7.

Zhang, X.-P. (1996). Fast three-phase load flow method. *IEEE Transactions on Power Systems*, 11(3):1547–1554.

Zhang, X.-P., Ju, P., and Handschin, E. (2005). Continuation three-phase power flow: A tool for voltage stability analisys of unbalanced three-phase power systems. *IEEE Transactions on Power Systems*, 20(3):1320–1329.

Appendix A

HVDC Power Equations

A standard six-pulse converter bridge depicted in Fig. A.1 is used to derive the mathematical model for the three-phase HVDC station.

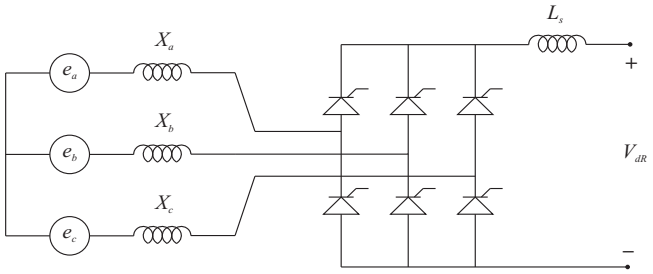

Figure A.1: *Six pulse converter station.*

The three-phase supply voltages to the converter transformer v^a, v^b and v^c are taken to be unbalanced but sinusoidal, as shown in Fig. A.2. The commutation is assumed to be delayed by an angle α with equidistant firing angle control [Arrillaga, 1998], i.e. firing instants occur at successive intervals of 60° following the first voltage crossing.

From Fig. A.2, the rectified voltage V_{dR} is obtained by integration,

$$V_{dR} = \frac{1}{\pi}\int_{\alpha}^{\alpha+\frac{\pi}{3}} \left[-v^{ca}(\theta)\right] d\theta + \frac{1}{\pi}\int_{\alpha+\frac{\pi}{3}}^{\alpha+\frac{2\pi}{3}} \left[v^{bc}(\theta)\right] d\theta + \frac{1}{\pi}\int_{\alpha+\frac{2\pi}{3}}^{\alpha+\pi} \left[-v^{ab}(\theta)\right] d\theta \qquad \text{(A.1)}$$

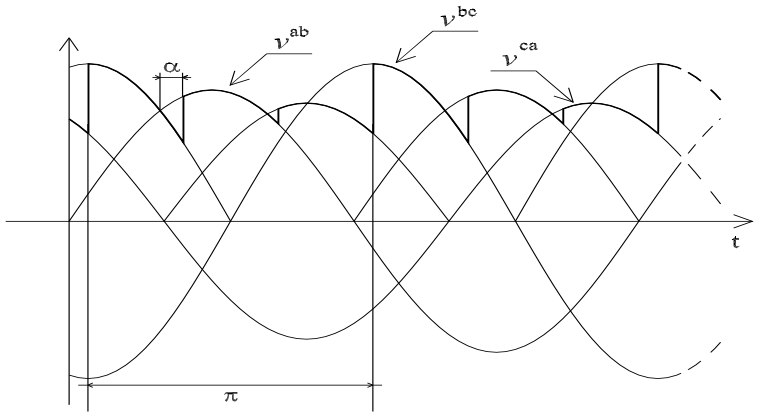

Figure A.2: *Unbalanced converter voltage waveform.*

The voltage V_{dR} is made up of three terms,

$$V_{dR} = V_{dR}^{a} + V_{dR}^{b} + V_{dR}^{c} \tag{A.2}$$

where

$$V_{dR}^{a} = \frac{A\sqrt{2}V^{ab}}{\pi}\left[\cos\left(\alpha + \frac{\pi}{3}\right) - \cos\left(\alpha + \frac{2\pi}{3}\right)\right] \tag{A.3}$$

$$V_{dR}^{b} = \frac{A\sqrt{2}V^{bc}}{\pi}\left[\cos\left(\alpha + \theta^{bc} - \pi\right) - \cos\left(\alpha + \theta^{bc} - \frac{2\pi}{3}\right)\right] \tag{A.4}$$

$$V_{dR}^{c} = \frac{A\sqrt{2}V^{ca}}{\pi}\left[\cos\left(\alpha + \theta^{ca} - \frac{\pi}{3}\right) - \cos\left(\alpha + \theta^{ca}\right)\right] \tag{A.5}$$

giving

$$V_{dR}^{\rho}\frac{A_k\sqrt{2}V_k^{\rho}}{\pi}\cos\left(\alpha + A^{\rho}\right) \tag{A.6}$$

where

$A^a = \theta^{ab} = 0$

$A^b = \theta^{bc} - \frac{4\pi}{3}$

$A^c = \theta^{ca} - \frac{2\pi}{3}$

A similar expression is developed for the inverter,

$$V_{dI}^{\rho} = \frac{A_m \sqrt{2} V_m^{\rho}}{\pi} \cos\left(\gamma + B^{\rho}\right) \tag{A.7}$$

where

$B^a = \varphi^{ab} = 0$

$B^b = \varphi^{bc} - \frac{4\pi}{3}$

$B^c = \varphi^{ca} - \frac{2\pi}{3}$

Taking into account the voltage drop ΔV, the DC voltages of the rectifier and the inverter are:

$$V_{dR}^{\rho} = \frac{A_k \sqrt{2} V_k^{\rho}}{\pi} \cos\left(\alpha + A^{\rho}\right) - \Delta V \tag{A.8}$$

$$V_{dI}^{\rho} = \frac{A_m \sqrt{2} V_m^{\rho}}{\pi} \cos\left(\gamma + B^{\rho}\right) - \Delta V \tag{A.9}$$

where ΔV is defined as,

$$\Delta V = \frac{X_c I_d}{\pi} \tag{A.10}$$

The powers of the inverter and the rectifier are given by the following expressions,

$$P_{dR} = V_{dR} I_d = \sum_{\rho=a,b,c} V_{dR}^{\rho} I_d \tag{A.11}$$

$$P_{dI} = V_{dI} I_d = \sum_{\rho=a,b,c} V_{dI}^{\rho} I_d \tag{A.12}$$

The relations between the currents on the primary side of the three-phase transformers and the direct current I_d, are given by,

$$\begin{aligned} I_k^{\rho} &= A_k k \frac{\sqrt{6}}{\pi} I_d = A_k k I_d \\ I_m^{\rho} &= A_m k \frac{\sqrt{6}}{\pi} I_d = A_m k I_d \end{aligned} \tag{A.13}$$

where k is a constant associated with commutation overlap. For power flow analysis, it can be taken to be $k = 0.995$ [Arrillaga and Arnold, 1990].

The apparent powers are given by,

$$S_k^{\rho} = \frac{V_k^{\rho} I_k^{\rho}}{\sqrt{3}} = \frac{k_1 A_k V_k^{\rho} I_d}{\sqrt{3}} \tag{A.14}$$

$$S_m^{\rho} = \frac{V_m^{\rho} I_m^{\rho}}{\sqrt{3}} = \frac{k_1 A_m V_m^{\rho} I_d}{\sqrt{3}} \tag{A.15}$$

where

$k_1 = \frac{\sqrt{6}}{\pi} k$

Appendix B

Jacobian Matrix Elements

B.1 Jacobian Elements - Partial Derivatives

The Jacobian matrix elements corresponding to the discretised differential equations for the transient synchronous generators model are described as follow.

The non-zero partial derivatives corresponding to the function $F_{\omega(t)}$ are:

$$\frac{\partial F_{\omega(t)}}{\partial \omega} = 1 + KD \tag{B.1}$$

$$\begin{aligned}\frac{\partial F_{\omega(t)}}{\partial \delta} &= 2Kx'_qI_rI_m \sin 2\delta - 2Kx'_dI_rI_m \sin 2\delta + KE'_qI_m \cos\delta \\ &\quad -Kx'_dI_r^2 \cos 2\delta + KE'_dI_m \sin\delta - KE'_qI_r \sin\delta \\ &+KE'_dI_r \cos\delta + KX'_qI_r^2 \cos 2\delta - Kx'_qI_m^2 \cos\delta + Kx'_dI_m^2 \cos 2\delta\end{aligned} \tag{B.2}$$

$$\frac{\partial F_{\omega(t)}}{\partial E'_d} = K\left(I_r \sin\delta - I_m \cos\delta\right) \tag{B.3}$$

$$\frac{\partial F_{\omega(t)}}{\partial E'_q} = K\left(I_r \cos\delta + I_m \sin\delta\right) \tag{B.4}$$

The non-zero partial derivatives corresponding to the function $F_{\delta(t)}$ are:

$$\frac{\partial F_{\delta(t)}}{\partial \omega} = -\frac{dt}{2} \tag{B.5}$$

$$\frac{\partial F_{\delta(t)}}{\partial \delta} = 1 \tag{B.6}$$

The non-zero partial derivatives corresponding to the function $F_{E'_{d(t)}}$ are:

$$\frac{\partial F_{E'_d(t)}}{\partial \delta} = \frac{1}{2dtT'_q}\left(x'_q - x_q\right) - I_r \sin\delta + I_m \cos\delta \tag{B.7}$$

$$\frac{\partial F_{E'_d(t)}}{\partial E'_d} = 1 + \frac{1}{2dtT'_q} \tag{B.8}$$

The non-zero partial derivatives corresponding to the function $F_{E'_{q(t)}}$ are:

$$\frac{\partial F_{E'_q(t)}}{\partial \delta} = -\frac{1}{2dtT'_d}\left(x'_d - x_d\right) + I_r \cos\delta + I_m \sin\delta \tag{B.9}$$

$$\frac{\partial F_{E'_q(t)}}{\partial E'_q} = 1 + \frac{1}{2dtT'_d} \tag{B.10}$$

The Jacobian matrix elements corresponding to the discretised differential equations for power plant components are described as follow.

B.2 Discretised State Variables

The armature resistance and damping coefficient of generator are considered so, the generator power output is therefore of the form,

$$P_e = \frac{r_a\left|E\right|^2}{r_a^2 + x_d^2} - \frac{\left|E\right|\left[r_a\left(e\cos\delta + f\sin\delta\right) + x_d\left(f\cos\delta + e\sin\delta\right)\right]}{r_a^2 + x_d^2} \tag{B.11}$$

The application of the trapezoidal rule to Eq.4.6 and Eq.4.9 are described as follows.

The electromechanical differential equation for the speed is $\dot{\omega} = \frac{\pi f_o}{H}\left[P_m - P_e - D\left(\omega - \omega_o\right)\right]$ so, the application of the trapezoidal rule to this Equation is,

$$\omega_t = \omega_{t-\Delta t} + \frac{\Delta t}{2}\left(\dot{\omega}_{(t)} + \dot{\omega}_{(t-\Delta t)}\right) \tag{B.12}$$

$$F_t(\omega) + F_{t-\Delta t}(\omega) + Cte = 0 \tag{B.13}$$

then,

$$F_{t-\Delta t}\left(\omega\right) = -\omega_{t-\Delta t} - \frac{\Delta t}{2}\left\{\frac{\pi f_0}{H}\left[\left(P_{HP(t-\Delta t)}F_{HP} + P_{IP(t-\Delta t)}F_{IP} + P_{LP(t-\Delta t)}F_{LP}\right) - \frac{r_a\left|E_{(t-\Delta t)}\right|^2}{r_a^2 + x_d^2}\right.\right.$$

$$+ \frac{\left|E_{(t-\Delta t)}\right|\left[-r_a\left(e_{(t-\Delta t)}\cos\delta_{(t-\Delta t)} + f_{(t-\Delta t)}\sin\delta_{(t-\Delta t)}\right)\right.}{r_a^2 + x_d^2} +$$

$$\left.\left.\left.\frac{x_d\left(-f_{(t-\Delta t)}\cos\delta_{(t-\Delta t)} + e_{(t-\Delta t)}\sin\delta_{(t-\Delta t)}\right)\right]}{r_a^2 + x_d^2} - D(\omega_{(t-\Delta t)})\right]\right\} \tag{B.14}$$

$$F_t\left(\omega\right) = \omega_t - \frac{\Delta t}{2}\left\{\frac{\pi f_0}{H}\left[\left(P_{HP(t)}F_{HP} + P_{IP(t)}F_{IP} + P_{LP(t)}F_{LP}\right) - \frac{r_a\left|E_{(t)}\right|^2}{r_a^2 + x_d^2} + \right.\right.$$

$$\left.\left.\frac{\left|E_{(t)}\right|\left[-r_a\left(e_{(t)}\cos\delta_{(t)} + f_{(t)}\sin\delta_{(t)}\right) + x_d\left(-f_{(t)}\cos\delta_{(t)} + e_{(t)}\sin\delta_{(t)}\right)\right]}{r_a^2 + x_d^2} - D(\omega_{(t)})\right]\right\} \tag{B.15}$$

$$Cte = -\frac{\Delta t \pi f_0}{H}\left(D\omega_o\right) \tag{B.16}$$

A similar process is applied to Eq. 4.9, for this Equation we have that,

$$\delta_{(t)} - \delta_{(t-\Delta t)} - \frac{\Delta t}{2}\left(\dot{\delta}_{(t)} + \dot{\delta}_{(t-\Delta t)}\right) = 0 \tag{B.17}$$

where,

$$F_{t-\Delta t}\left(\delta\right) = -\delta_{(t-\Delta t)} - \frac{\Delta t}{2}\omega_{(t-\Delta t)} \tag{B.18}$$

$$F_{t}\left(\delta\right) = \delta_{(t)} - \frac{\Delta t}{2}\omega_{(t)} \tag{B.19}$$

$$C_2 = 2\pi f_0 \Delta t \tag{B.20}$$

For P_g, we have,

$$F\left(P_g\right) = F_t\left(P_g\right) + F_{t-\Delta t}\left(P_g\right) + Cte \tag{B.21}$$

$$P_{g(t)} - P_{g(t-\Delta t)} - \frac{\Delta t}{2}\left(\dot{P}_{g(t)} + \dot{P}_{g(t-\Delta t)}\right) = 0 \tag{B.22}$$

$$P_{g(t)} - P_{g(t-\Delta t)} - \frac{\Delta t}{2}\left\{\frac{1}{T_3}\left(P_{set(t)} - P_{1(t)} - P_{g(t)}\right) + \frac{1}{T_3}\left(P_{set(t)} - P_{1(t)} - P_{g(t)}\right)\right\} \tag{B.23}$$

$$F_{t-\Delta t}\left(P_g\right) = -P_{g(t-\Delta t)} - \frac{\Delta t}{2}\left\{\frac{1}{T_3}\left(-P_{1(t-\Delta t)} - P_{g(t-\Delta t)}\right)\right\} \tag{B.24}$$

$$F_{t}\left(P_g\right) = P_{g(t)} - \frac{\Delta t}{2}\left\{\frac{1}{T_3}\left(-P_{1(t)} - P_{g(t)}\right)\right\} \tag{B.25}$$

$$Cte = -\frac{\Delta t P_{set}}{T_3} \tag{B.26}$$

The discretisation for these elements is like,

$$F\left(E\right) = F_t\left(E\right) + F_{t-\Delta t}\left(E\right) + Cte \tag{B.27}$$

$$E_{(t)} - E_{(t-\Delta t)} - \frac{\Delta t}{2}\left(\dot{E}_{1(t)} + \dot{E}_{1(t-\Delta t)}\right) = 0 \tag{B.28}$$

$$E_{(t)} - E_{(t-\Delta t)} - \frac{\Delta t}{2}\left(\frac{K_A V_{ref} - K_A\sqrt{(e^2_{(t)} + f^2_{(t)})} - E_{(t)}}{T'_{d0}}\right)$$

$$-\frac{\Delta t}{2}\left(\frac{K_A V_{ref} - K_A\sqrt{(e^2_{(t-\Delta t)} + f^2_{(t-\Delta t)})} - E_{(t-\Delta t)}}{T'_{d0}}\right) = 0 \tag{B.29}$$

$$F_t\left(E\right) = E_{(t)} - \frac{\Delta t}{2}\left(\frac{-K_A\sqrt{(e^2_{(t)} + f^2_{(t)})} - E_{(t)}}{T'_{d0}}\right) \tag{B.30}$$

$$F_{t-\Delta t}(E) = -E_{(t-\Delta t)} - \frac{\Delta t}{2}\left(\frac{-K_A\sqrt{(e^2_{(t-\Delta t)} + f^2_{(t-\Delta t)})} - E_{(t-\Delta t)}}{T'_{d0}}\right) \tag{B.31}$$

$$Cte = -\Delta t\left(\frac{V_{ref} K_A}{T'_{d0}}\right) \tag{B.32}$$

The same process is applied to the remaining state variables of the system.

Appendix C

Power Networks Test Data

Following the data for the power system test networks used are depicted. All data is given in per unit on a 100 MW and 400 kV base values of active power and voltage respectively.

Table C.1: *Transmission line parameters: Five-bus test system*

Bus code		Impedance	Line charging
North	South	0.02+ j0.06	0.00+ j0.06
North	Lake	0.08+ j0.24	0.00+ j0.05
South	Lake	0.06+ j0.18	0.00+ j0.04
South	Main	0.06+ j0.18	0.00+ j0.04
South	Elm	0.04+ j0.12	0.00+ j0.03
Lake	Main	0.01+ j0.03	0.00+ j0.02
Main	Elm	0.08+ j0.24	0.00+ j0.05

Table C.2: *Generation: Five-bus test system*

Bus code	MW	MVAR	MVAR limits	Voltage magnitude
North*	–	–	–	1.06
South	40	0	±300	1.00

* Slack bus

Table C.3: *Power loads: Five-bus test system*

Bus code	MW	MVAR
South	40	0
South	45	15
South	40	5
South	60	10

Table C.4: *Power transformers: New England system*

Bus code		R_s	X_s	T_v	U_v
2	30	0.00	0.0181	1.025	1
6	31	0.00	0.025	1.07	1
10	32	0.00	0.020	1.07	1
12	11	0.0016	0.0435	1.006	1
12	13	0.0016	0.0435	1.006	1
19	20	0.0007	0.0138	1.06	1
19	33	0.0007	0.0142	1.07	1
20	34	0.0009	0.0180	1.009	1
22	35	0.0	0.0143	1.025	1
23	36	0.0005	0.0272	1.00	1
25	37	0.0006	0.0232	1.025	1
29	38	0.0008	0.0156	1.025	1

Table C.5: *Transmission line parameters: New England system*

Bus code		Impedance	Line charging
1	2	0.035+ j0.041	0.00+ j0.69
1	39	0.010+ j0.025	0.00+ j0.75
2	3	0.013+ j0.013	0.00+ j0.25
2	25	0.0070+ j0.0086	0.00+ j0.140
3	4	0.0013+ j0.0213	0.00+ j0.2214
3	18	0.0011+ j0.0133	0.00+ j0.2138
4	5	0.0008+ j0.0128	0.00+ j0.1342
4	14	0.0008+ j0.0129	0.00+ j0.1382
5	6	0.0002+ j0.0026	0.00+ j0.434
5	8	0.0008+ j0.0112	0.00+ j0.1476
6	7	0.0006+ j0.0092	0.00+ j0.1130
6	11	0.0007+ j0.0082	0.00+ j0.1389
7	8	0.0004+ j0.0046	0.00+ j0.0780
8	9	0.0023+ j0.0363	0.00+ j0.3804
9	39	0.0010+ j0.0250	0.00+ j1.200
10	11	0.0004+ j0.0043	0.00+ j0.0729
10	13	0.0004+ j0.0043	0.00+ j0.0729
13	14	0.0009+ j0.0101	0.00+ j0.1725
14	15	0.0018+ j0.0217	0.00+ j0.3660
15	16	0.0009+ j0.0094	0.00+ j0.1710
16	17	0.0007+ j0.0089	0.00+ j0.1342
16	19	0.0016+ j0.0195	0.00+ j0.3040
16	21	0.0008+ j0.0135	0.00+ j0.2548
16	24	0.0003+ j0.0059	0.00+ j0.0680
17	18	0.0007+ j0.0082	0.00+ j0.1319
17	27	0.0013+ j0.0173	0.00+ j0.3216
21	22	0.0008+ j0.0140	0.00+ j0.2565
22	23	0.0006+ j0.0096	0.00+ j0.1845
23	24	0.0022+ j0.0350	0.00+ j0.3610
25	26	0.0032+ j0.0323	0.00+ j0.5130
26	27	0.0014+ j0.0147	0.00+ j0.2396
26	28	0.0043+ j0.0474	0.00+ j0.7802
26	29	0.0057+ j0.0625	0.00+ j1.0290
28	29	0.0014+ j0.0151	0.00+ j0.2490

Table C.6: *Generation: New England system*

Bus code	MW	MVAR	MVAR limits	Voltage magnitude
39*	–	–	–	1.0300
30	250	0.0	±250	1.0475
31	573.2	0.0	±300	0.9520
32	650	0.0	±300	0.9831
33	632	0.0	±250	0.9972
34	508	0.0	±250	1.0123
35	650	0.0	±300	1.0493
36	560	0.0	±200	1.0635
37	540	0.0	±300	1.0278
38	830	0.0	±400	1.0265

Table C.7: *Power loads: New England system*

Bus code	MW	MVAR
3	322	2.40
4	500	184
7	233	84
8	522	176
12	8.5	88
15	320	153
16	329.4	32.3
18	158	30
20	680	103
21	274	115
23	247.5	84.6
24	308.6	−92.2
25	224	47.2
26	139	17
27	281	75.5
28	206	27.6
29	283.5	26.9
31	9.12	4.6
39	1104	250

Table C.8: *Transmission line parameters: Three-generators, nine-bus system*

Bus code		Impedance	Line charging
4	5	0.010+ j0.0850	0.00+ j0.176
4	6	0.017+ j0.0920	0.00+ j0.158
5	7	0.032+ j0.0161	0.00+ j0.306
6	9	0.039+ j0.0170	0.00+ j0.358
7	8	0.0085+ j0.0720	0.00+ j0.149
8	9	0.0119+ j0.1008	0.00+ j0.209

Table C.9: *Generation: Three-generators, nine-bus system*

Bus code	MW	MVAR	MVAR limits	Voltage magnitude
1*	–	–	–	1.040
2	163	0.0	±250	1.0253
3	85	0.0	±250	1.0253

Table C.10: *Power loads: Three-generators, nine-bus system*

Bus code	MW	MVAR
5	125	50
6	90	30
8	100	35

Table C.11: *Power transformers: Three-generators, nine-bus system*

Bus code		R_s	X_s	T_v	U_v
1	4	0.00	0.0576	1.040	1
2	7	0.00	0.0625	1.0253	1
3	9	0.00	0.0586	1.0253	1